

Myklebust

MICROBEAM ANALYSIS SOCIETY

PROCEEDINGS

ELEVENTH ANNUAL CONFERENCE

AUGUST 9-13, 1976

**FONTAINEBLEAU HOTEL
MIAMI BEACH, FLORIDA**

Additional copies of these and previous Proceedings may
be obtained from:

Dr. J. I. Goldstein
Metallurgy and Materials Science Department
Lehigh University
Bethlehem, Pennsylvania 18015

ELEVENTH ANNUAL CONFERENCE

OF THE

MICROBEAM ANALYSIS SOCIETY

AUGUST 9 - 13, 1976

FONTAINBLEAU HOTEL

MIAMI BEACH, FLORIDA

PREFACE

This meeting is the 3rd joint meeting of MAS and EMSA. The benefits of an excellent program and a large exhibition have been noted by all. We have begun to operate on a smoother basis. Ray Hart, the EMSA arrangements chairman, has been most cooperative and helpful.

The people who have contributed their efforts to this meeting are listed on a subsequent page. I wish to express my gratitude for their help.

Please mark on your calendar, the dates of August 18-24, 1977 at which time MAS will host the International Congress on X-ray Optics and Microanalysis in Boston.

Paul Lublin
MAS - Arrangements

HONORARY MEMBERS

L. L. Marton
Museum of History & Tech.
Room 5025
Smithsonian Institution
Washington, D. C. 20560

Raymond Castaing
University of Paris
Faculte des Sciences
Orsay, FRANCE

I. B. Borovskii
142432 Chernogolovka Moscow Reg.
Institute of Solid State
Physics Ac. Sc. USSR

Peter Duncumb
Tube Investments Research Labs
Hinxton Hall
Nor. Saffron Walden
Essex, ENGLAND

MICROBEAM ANALYSIS SOCIETY

1976 National Officers

President	Eric Lifshin General Electric R&D Center Schenectady, N.Y.
Past President	John Colby Bell Laboratories 555 Union Boulevard Allentown, Pa.
President Elect	Joseph I. Goldstein Dept. of Met. & Mat. Sci. Lehigh University Bethlehem, Pa.
Treasurer	Don Beaman Dow Chemical Co. Midland, Mich.
Secretary	Harvey Yakowitz 14212 Woodcrest Drive Rockville, Md.

MEMBERS AT LARGE

3 Years	Gordon Cleaver General Electric Co. Vallecitos Nuclear Center Pleasanton, Calif.
2 Years	Oliver Wells IBM Thomas J. Watson Research Center Yorktown Heights, N.J.
1 Year	Eugene White Materials Research Lab Penn. State University University Park, Pa.

MICROBEAM ANALYSIS SOCIETY

COMMITTEES 1976

AWARDS COMMITTEE (all awards - student, Macres, photo exhibit)

L. S. Birks - Chairman

O. Wells

J. Colby

J. Coleman

J. Woodhouse

G. Judd

K. Heinrich

J. Bomback

D. Beaman

J. Taback

MEMBERSHIP

J. I. Goldstein - Chairman

SUSTAINING MEMBERSHIP

D. Beaman - Chairman

J. Taback

LEGAL

P. Lublin - Chairman

STANDARDS

A. Chodos - Chairman

D. Beaman

J. Bomback

EMPLOYMENT SERVICES

J. Woodhouse - Chairman

FUTURE MEETING SITES

P. Lucilin - Chairman

J. Colby

A. Chodos

D. O'Boyle

SECTION LIAISON (speakers tour, section support)

J. Colby - Chairman

D. Wittry

Chairman of Local Sections

INTERNATIONAL USERS LIAISON

E. Lifshin - Chairman

EDUCATIONAL

G. White - Chairman

D. Beaman

D. Brown

J. Goldstein

J. Woodhouse

PUBLICATIONS

J. Goldstein - Chairman

CERTIFICATES & SCROLLS

D. Kyser - Chairman

ELEVENTH NATIONAL CONFERENCE COMMITTEE

Paul Lublin, General Chairman
General Telephone and Electronics
Waltham, Massachusetts

William Kane, Program Chairman
Research and Development Laboratories
Corning Glass Works
Corning, New York

Eric Lifshin, Program Committee
General Electric Corporate Research & Development
Schenectady, New York

Don Beaman, Publications
Dow Chemical Company
Midland, Michigan

Dave Kyser, Photographic Exhibit
International Business Machines
San Jose, California

Lavern Birks, Awards
Naval Research Laboratory
Washington, D. C.

INVITED SPEAKERS

J. W. Colby
Bell Telephone Laboratories
Allentown, Pennsylvania

J. R. Coleman
School of Medicine and Dentistry
University of Rochester
Rochester, New York

E. Elad
Materials Analysis Division
Ortec, Inc.
Oak Ridge, Tennessee

T. E. Everhart
Department of Electrical Engineering and Computer Sciences
University of California
Berkeley, California

J. I. Goldstein
Department of Metallurgy and Materials Science
Lehigh University
Bethlehem, Pennsylvania

W. T. Hatfield
Corporate Research and Development Center
General Electric Company
Schenectady, New York

H. M. Hyman
Solid State Division
RCA Corporation
Somerville, New Jersey

O. Johari
Metals Division
Illinois Institute of Technology
Chicago, Illinois

W. T. Kane
Research and Development Laboratories
Corning Glass Works
Corning, New York

E. Lifshin
Corporate Research and Development
General Electric Company
Schenectady, New York

C. J. McMahon
Department of Metallurgy and Materials Science
University of Pennsylvania
Philadelphia, Pennsylvania

V. Mizuhira
Dept. of Cell Biology, Medical Research Institute
Tokyo Medical and Dental University
Tokyo, Japan

S. J. B. Reed
Department of Mineralogy and Petrology
Cambridge University
Cambridge, England

W. Reuter
Thomas J. Watson Research Center
International Business Machines, Inc.
Yorktown Heights, New York

F. H. Schamber
Tracor Northern, Inc.
Middleton, Wisconsin

D. B. Wittry
Department of Materials Science and Electrical Engineering
University of Southern California
Los Angeles, California

R. Woldseth
Kevex Corporation
Burlingame, California

SUSTAINING MEMBERS -- 1976

ADVANCED METALS RESEARCH CORPORATION
Bedford, Massachusetts

APPLIED RESEARCH LABORATORIES
Sunland, California

BABCOCK & WILCOX COMPANY
ALLIANCE RESEARCH CENTER
Alliance, Ohio

CAMBRIDGE INSTRUMENT COMPANY, INC.
Monsey, New York

CAMECA INSTRUMENTS, INC.
Stamford, Connecticut

COATES & WELTER
Sunnyvale, California

EDAX INTERNATIONAL, INC.
Prairie View, Illinois

ETEC CORPORATION
Hayward, California

INTERNATIONAL SCIENTIFIC INSTRUMENTS, INC.
Mountain View, California

JEOL U.S.A.
Medford, Massachusetts

KEVEX CORPORATION
Burlingame, California

WALTER C. McCRONE ASSOCIATES
Chicago, Illinois

SUSTAINING MEMBERS -- 1976 (cont'd.)

3M COMPANY
St. Paul, Minnesota

NUCLEAR SEMICONDUCTOR
A DIVISION OF UNITED SCIENTIFIC CORP.
Mountain View, California

ORTEC INC.
Oak Ridge, Tennessee

PERKIN-ELMER CORPORATION
Mountain View, California

PHILIPS/EDAX
Mount Vernon, New York

PHYSICAL ELECTRONICS INDUSTRIES, INC.
Eden Prairie, Minnesota

PRINCETON GAMMA-TECH, INC.
Princeton, New Jersey

Q.B.I. INTERNATIONAL
San Francisco, California

CHARLES M. TAYLOR CO.
Stanford, California

TOUSIMIS RESEARCH CORPORATION
Rockville, Maryland

TRACOR NORTHERN
Middleton, Wisconsin

VARIAN ASSOCIATES
Palo Alto, California

THE MAS STUDENT SUPPORT PROGRAM

The encouragement of student participation at the annual meeting is an important objective of the MAS as it was for EPASA which preceded MAS. The registration fee is reduced for student attendees, of course, but the Student Support Program is specifically pointed towards soliciting the presentation of research papers by students at the annual meeting. In addition to being good training for the students, such presentations often bring refreshing new views of theoretical as well as experimental aspects of probe analysis.

The guidelines for the support program are simple:

1. The paper must be co-authored by a bona fide student and his or her professor.
2. It must be of a quality to be accepted by the program committee.
3. It must be presented at the meeting by the student.
4. The professor is asked to attest to the kind and amount of contribution made by the student to each facet of the work presented.

Travel support for the student is furnished by MAS to ensure that his or her attendance will not be an undue financial burden to either the student or the university. The amount of travel support will generally cover round trip economy fare plus partial coverage of food and lodging.

In addition to the student travel support, the MAS administers the annual JEOLCO award for an outstanding student presentation (see accompanying description of the MAS Awards).

ANNUAL AWARDS MADE BY THE
MICROBEAM ANALYSIS SOCIETY

o o o

This award of \$300 was established in 1973 to honor the memory of Dr. Victor Macres, one of the pioneers of electron probe analysis, a dedicated teacher, and a competitive instrument manufacturer. The award is given for the best instrumentation paper presented at the annual meeting. In 1975 the award was made to Oliver C. Wells.

JEOL AWARD

The Japan Electron Optics Laboratory Corporation sponsors this award of \$300 but it is administered by the Microbeam Analysis Society. The award is given for an outstanding student paper presented at the Annual MAS meeting. In 1975 the JEOLCO award was given to John Potosky.

CORNING AWARD

In 1975 the Corning Glass Works established an award of \$300 to the most outstanding contributed paper presented at the annual MAS meeting. The award is administered by the MAS. The 1975 award was made to J. Armstrong and P. Buseck.

MEETING ANNOUNCEMENT

TWELFTH ANNUAL CONFERENCE OF THE MICROBEAM ANALYSIS SOCIETY
AND THE EIGHTH INTERNATIONAL CONFERENCE ON X-RAY
OPTICS AND MICROANALYSIS

Location: Sheraton Boston Hotel
Boston, Massachusetts

Date: August 18-26, 1976

For information concerning this meeting, please contact:

Dr. R. E. Ogilvie
Massachusetts Institute
of Technology
Cambridge, Massachusetts
(617) 253-1000

Dr. D. Wittry
Department of Materials Science
and Electrical Engineering
University of Southern California
Los Angeles, California 90007

(213) 746-2510

PROGRAM

ELEVENTH ANNUAL CONFERENCE

OF THE

MICROBEAM ANALYSIS SOCIETY

PROGRAM

ELEVENTH ANNUAL CONFERENCE OF THE MICROBEAM ANALYSIS SOCIETY

MONDAY 9 AUGUST 1976

TUTORIAL SESSION

Voltaire Room

R. E. Ogilvie, Chairman

8:00 AM Registration

8:45 AM Introductory Remarks by E. Lifshin, President, MAS

TUTORIAL LECTURES

T1 9:00 AM "Statistics of X-ray Analysis", J. I. Goldstein,
Lehigh University

T2 10:30 AM "Making the Choice Between An EDS Equipped SEM and
an Automated Electron Microprobe", J. W. Colby,
Bell Laboratories

12:00 PM LUNCH

T3 2:00 PM "Automation - Making the Hard Decisions", W. T. Kane,
Research and Development Laboratories, Corning Glass
Works.

T4 3:30 PM "The SEM as a Success Analysis Tool for Semicon-
ductor Quality Control", H. Hyman and N. A. Ciampa,
RCA Solid State Division, RCA Corporation

TUESDAY 10 AUGUST 1976

SESSION I - X-RAY ENERGY DISPERSIVE ANALYSIS

Joint MAS-EMSA Session

West Grand Ballroom

P. S. Ong and E. Lifshin, Chairmen

8:00 AM Registration

8:55 AM Introduction of MAS Officers

- 1 9:00 AM INVITED PAPER: "The History of EDS Systems on
Electron Beam Instruments", R. Woldseth, Kevex Corp.
 - 2 9:30 AM INVITED PAPER: "Detector Electronics: Development
and Characteristics", E. Elad, Ortec, Inc.
 - 3 10:00 AM INVITED PAPER: "The X-ray Multichannel Analyzer",
F. H. Schamber, Tracor-Northern
 - 10:30 AM INTERMISSION
 - 4 10:45 AM INVITED PAPER: "Quantitative Energy Dispersive
Analyses", S. J. B. Reed, Dept. of Mineralogy and
Petrology, Cambridge University, Cambridge, England
 - 5 11:15 AM INVITED PAPER: "A Review of the Various Usages of
Energy Dispersive X-ray Analyses in Biology",
V. Mizuhira, Tokyo Medical and Dental University
 - 6 11:45 AM INVITED PAPER: "Applications to Materials Science",
E. Lifshin, General Electric Research Laboratories
 - 12:00 PM LUNCH
-

TUESDAY 10 AUGUST 1976

SESSION II - ENERGY DISPERSIVE SPECTROSCOPY

Joint MAS-EMSA Session

West Grand Ballroom

W. T. Kane, Chairman

- 7 1:30 PM "Elemental Analyses of Thin Films Using Inner Shell
Electron Energy Losses", D. E. Johnson, High Voltage
Microprobe Laboratory, Dept. of Zoology and Labora-
tory of Biophysics, University of Wisconsin;
M. Isaacson, Dept. of Physics and the Enrico Fermi
Institute, University of Chicago
- 8 2:00 PM "The Calculation of Pure Element X-ray Intensities
from Empirically Derived Expressions and Its Applica-
tions to Quantitative SEM/EDS Analysis", N. C. Barbi,
D. P. Skinner and S. Blinder, NL Industries/ICD
Division

- 9 2:15 PM "Quantitative Elemental Analyses of Transparent Particles in the TEM", J. W. Sprys and N. A. Short, Technical Services Engineering and Research Staff, Research, Ford Motor Company
- 10 2:30 PM "Corrections for the Bremsstrahlung Background in EDS Microprobe Analysis of Thick Specimens", Peter Statham, Dept. of Electrical Engineering and Computer Sciences, University of California at Berkeley
- 11 2:45 PM "Beam Switching: A Technique to Improve the Performance of Pulse-Processing Electronics for E.D.S." Peter Statham, Dept. of Electrical Engineering and Computer Sciences, University of California at Berkeley
- 12 3:00 PM "Method for Resolving Overlapping Energy-Dispersive Peaks of an X-ray Spectrum: Application to the Correction Procedure Frame B", C. E. Fiori, R. L. Myklebust and K. F. J. Heinrich, Analytical Chemistry Division, National Bureau of Standards
- 3:15 PM INTERMISSION
- 13 3:30 PM "Modification of Philips EM301 for Optimum EDX Analyses", J. J. Hren, P. S. Ong, P. F. Johnson and E. J. Jenkins, Dept. of Materials Science and Engineering, University of Florida
- 14 3:45 PM "Microchemical Analysis of Thin Metal Foils", N. J. Zaluzec and H. L. Fraser, Dept. of Metallurgy and Mining Engineering, Materials Research Laboratory, University of Illinois
- 15 4:00 PM "Characterization of Cotton Dust by Elemental Analysis", E. Fleming, III, P. Tucker and S. Hersh, School of Textiles, North Carolina State University
- 16 4:15 PM "Recent Applications in Combined Transmission Electron Microscopy and Microanalysis", D. Chescoe, AEI Scientific Apparatus, Ltd., Manchester, England and D. E. P. Beeston, AEI Scientific Apparatus, Inc. Elmsford, N.Y.
- 17 4:30 PM "Energy Dispersive X-ray Measurements of Thin Metal Foil", J. Bentley and E. A. Kenik, Metals and Ceramics Division, Oak Ridge National Laboratories

- 18 4:45 PM "Evaluation of Gold Zinc Alloys for Use as
Quantitative Microprobe Standards", R. B. Bolon,
M. Ciccarelli and E. Lifshin, General Electric
Research Laboratories (PAPER WITHDRAWN)
- 19 4:45 PM "Errors Introduced in Eliminating or Extrapolat-
ing Standards", John C. Russ, EDAX Laboratories
-

WEDNESDAY 11 AUGUST 1976

SESSION III - QUANTITATIVE MICROANALYSIS

French Room

A. A. Chodos, Chairman

- 20 8:45 AM INVITED PAPER: "Present and Future Possibilities
9:00 for Local Chemical Analysis of Solids Based on
Physical Techniques", D. B. Wittry, Dept. of
Materials Science and Electrical Engineering,
University of Southern California
- 21 9:15 AM INVITED PAPER: "Low-Energy Photoionization Cross
9:30 Section from Proton-Induced X-ray Spectroscopy",
A. Lurio, Wilhad Reuter and Johann Keller, IBM
Thomas J. Watson Research Center
- 10:00 Break*
- 22 9:45 AM "Experimental X-ray Mass Attenuation Coefficients
10:15 Between the M_I and M_V Absorption Edge of Rhenium",
W. J. Steele and Jack M. Johnson, Lawrence Liver-
more Laboratory, University of California at
Livermore
- 23 10:00 AM "Prediction of X-ray Intensities from Small Parti-
10:30 cles by a Monte Carlo Calculation", R. L. Myklebust,
D. E. Newbury and K. F. J. Heinrich of the National
Bureau of Standards, Chemistry A121; and H. Yakowitz
of the National Bureau of Standards, Materials B114
- 24 10:15 AM "X-ray Excitation Depth in the 2 to 5 KeV Electron
10:45 Energy Range", W. Reuter, J. D. Kuptsis and A.
Lurio, IBM Thomas J. Watson Research Center
- ~~10:30~~ AM INTERMISSION

- 25 10:45 AM "Quantitative X-ray Analysis of Thin Films in
11:00 the Electron Microscope", J. I. Goldstein,
Metallurgy and Materials Science Dept., Lehigh
University and G. W. Lorimer and G. Cliff,
Metallurgy Dept., University of Manchester,
England
- 26 11:00 AM "Analytical Model for the Depth Distribution of
11:15 Direct X-ray Generation in the Target Bombarded
by Electrons", Kurt F. J. Heinrich, Analytical
Chemistry Div., National Bureau of Standards
- 27 11:15 AM "An Overview of the Glass Standards Program for
11:30 Microanalysis at the National Bureau of Standards",
C. E. Fiori, K. F. J. Heinrich, R. B. Marinenko,
M. M. Darr, D. H. Blackburn, D. E. Newbury and
J. A. Small, Institute for Materials Research,
National Bureau of Standards
- 28 11:30 AM "Evaluation of Formulas for Ionization Cross
11:45 Section in Electron Probe Microanalysis",
David T. Kyser, IBM Research Laboratory, San
Jose, Calif.
- 29 11:45 AM "Progress in the Measurement of Relative X-ray
12:00 Line Intensities", K. F. J. Heinrich, C. E. Fiori,
and R. L. Myklebust, National Bureau of Standards
- 12:00 AM LUNCH
-

WEDNESDAY 11 AUGUST 1976

SESSION IV-A - ADVANCED PHYSICAL INSTRUMENTATION

Joint MAS-EMSA Session

French Room

J. Silcox, Chairman

- 30 2:00 PM INVITED PAPER: "The Mechanisms of Secondary Elec-
tron Emission", T. E. Everhart, University of
California, Dept. of Electrical Engineering and
Computer Sciences
- 31 2:30 PM INVITED PAPER: "Applications of Photoelectron
Microscopy", William J. Baxter, Research Labora-
tories, General Motors Corp.

- 32 3:00 PM "Considerations in Making Stereomicrographs
With the Scanning Electron Microscope -
Positioning the Stereowindow", Earl R. Walter,
Research and Development Dept., Union Carbide
Corp.
- 33 3:15 PM "Resolution Test for the SEM", R. A. Ploc,
Atomic Energy of Canada, Ltd., Chalk River
Nuclear Laboratories
- 3:30 PM INTERMISSION
- 34 3:45 PM "Accurate Microcrystallography in the SEM Using
Electron Backscattering Patterns", J. A. Venables,
C. J. Harland and R. bin-Jaya, University of
Sussex, School of Mathematical and Physical
Sciences, Falmer, Brighton, England
- 35 4:00 PM "Proposed Scheme for a Directional Low-Loss
Detector", Oliver C. Wells, IBM Thomas J. Watson
Research Center
- 36 4:15 PM "Quantitative Microanalysis by Electron Energy
Loss Spectrometry", R. F. Egerton, Dept. of
Physics, University of Alberta, Edmonton,
Canada and C. J. Rowwouw and M. J. Whelan, Dept.
of Metallurgy, University of Oxford, Oxford,
England
- 37 4:30 PM "Observation of Direct Non-Vertical Interband
Transitions in Al and Si by Electron Energy-Loss
Spectroscopy", C. H. Chen and J. Silcox, School
of Applied and Engineering Physics, Cornell
University
- 38 4:45 PM "Operational and Instrumental Considerations for
the Development of a Planetary SEM-EDA", A. L.
Albee, J. R. Anderson and A. A. Chodos, California
Institute of Technology
-

WEDNESDAY 11 AUGUST 1976

SESSION IV-B - LATE BREAKING DEVELOPMENTS

Pasteur Room

C. Gordon Cleaver, Jr., Chairman

THURSDAY 12 AUGUST 1976

SESSION V - SURFACE ANALYSIS TECHNIQUES

French Room

J. Colby, Chairman

- 39 8:45 AM INVITED PAPER: "The Use of Auger Electron Spectroscopy to Study Impurity-Induced Intergranular Fracture in Steel", C. J. McMahon, Dept. of Metallurgy and Materials Science, University of Pennsylvania
- 40 9:15 AM "Revised Calculation of Oxygen Concentration in the LTE Model", J. D. Brown and A. P. vonRosentiel, Metallinstituut, TNO, Apeldoorn, The Netherlands
- 41 9:30 AM "Secondary Ion Yields of Metals and Oxides of Ti Through Zn", Ian M. Steele, T. N. Solberg, J. V. Smith, Dept of the Geophysical Sciences, University of Chicago, and I. D. Hutcheon and R. N. Clayton, Enrico Fermi Institute, University of Chicago
- 42 9:45 AM "Local Thermal Equilibrium Analysis of Secondary Ion Mass Spectra from Multi-Element Glasses", D. E. Newbury, R. L. Myklebust and K. F. J. Heinrich, Analytical Chemistry Div., National Bureau of Standards
- 43 10:00 AM "Phase Analysis in Steel by Secondary Ion Spectroscopy", P. H. Maitrepierre, R. Namdar-Irani, J. Rofes-Vernis, B. Thomas, and G. Henry, The Institut de Recherches de la Siderurgie (IRSID), Cedex, France
- 10:15 AM INTERMISSION
- 44 10:30 AM "Sensitively Effects in the Analysis of Ni-Cr-Fe Alloys by IMMA", J. D. Brown, Metaalinstituut TNO and the University of Western Ontario, London, Canada; D. J. Gras, A. P. vonRosentiel, and B. H. Kolster, Metaalinstituut TNO, Apeldoorn, The Netherlands
- 45 10:45 AM "Ion-Microscope Characterization of Carburized Thoriated-Tungsten Wire Cathodes", B. F. Phillips and J. A. Amy, Electron Optics Laboratory (Code 30333), Naval Weapons Support Center

- 46 11:00 AM "High Mass-Resolution Ion Microprobe Analysis",
S. J. B. Reed, J. V. P. Long, J. N. Coles and
D. M. Astill, N.E.R.C. Ion Probe Unit, Dept. of
Mineralogy and Petrology, University of Cambridge,
England
- 47 11:15 AM "Scanning Auger Micro-Analysis of Particles",
R. L. Gerlock and N. C. MacDonald, Physical
Electronics Industries
- 48 11:30 AM "Thin Film Studies with the QMAS; Metalurgical
and Electronic Applications", T. A. Whatley and
R. D. Fralick, Applied Research Laboratories
- 49 11:45 AM "Surface Analysis of Insulators by SIMS", J. A.
Leys, 3M Company, Central Research Laboratories;
and G. R. Sparrow, 3M Company, Analytical Systems
- 12:00 AM LUNCH

THURSDAY 12 AUGUST 1976

SESSION VI-A - MATERIALS APPLICATIONS

Pasteur Room

P. Lublin, Chairman

- 50 2:00 PM INVITED PAPER: "Use of Electron Beam Instruments
in Applied Materials Studies - An Overview",
Om Johari, Metals Division, IIT Research
Institute
- 51 2:30 PM "Energy Dispersive X-ray Identification of Rock
Forming Aluminosilicates", Arthur B. Merkle,
Dept. of Geology, University of Nebraska-Lincoln
- 52 2:45 PM "Organic Coating Thickness Measurement", John C.
Russ, EDAX Laboratories
- 53 3:00 PM "Interaction of a Glass-Based Nuclear Waste
Simulant and Natural Rock", P. F. Hlava and W. F.
Chambers, Sandia Laboratories
- 54 3:15 PM "Electron Microprobe Studies of Metal-Ceramic
Brazed Joints", W. F. Chambers and P. F. Hlava,
Sandia Laboratories
- 3:30 PM INTERMISSION

- 55 3:45 PM "A Preliminary Investigation of the Fouling of Catalyst Pellets by Residual Oils and Tars", R. H. Packwood, Physical Metallurgy Research Laboratories, Canadian Centre for Mineral and Energy Technology, Dept. of Energy, Mines and Resources, Ottawa, Canada; M. Ternan and B. I. Parsons, Energy Research Laboratory, Canadian Centre for Mineral and Energy Technology, Dept. of Energy, Mines and Resources, Ottawa, Canada
- 56 4:00 PM "Limitations of Microprobe Analysis of Angle-Lapped Multilayered Specimens", M. V. Mitchell and J. N. Ramsey, IBM Corporation
- 57 4:15 PM "Real Time Cathodoluminescent Spectroscopy", A. Sicignano, Philips Laboratories, Briarcliff Manor, N.Y.
- 75 4:30 PM "Investigation of Deep Levels in ZnSe Using Electron and Photon Excitation", C. J. Wu and D. B. Wittry, Dept. of Materials Science, University of Southern California
- 76 4:45 PM "Microanalysis of Sodium Exposed Stainless Steel Specimens", A. P. vonRosenstiel, H. B. Zeedijk, and B. H. Kolster, Metaalinstituut TNO, Apeldoorn, The Netherlands
- 77 5:00 PM "Electron Beam Furnace Melting Control by the Use of an Energy Dispersive Spectrometer", F. Borile, E. Olzi, and G. Turisini, CNR-LTM, Via Induno, 10 - Cinisello B., Milano, Italy
-

THURSDAY 12 AUGUST 1976

SESSION VI-B - BIOLOGICAL APPLICATIONS

Lafayette Room

C. Lechene, Chairman

- 58 2:00 PM INVITED PAPER: "Electron Probe Studies of Calcium Transport", J. R. Coleman, University of Rochester, School of Medicine and Dentistry
- 59 2:30 PM "Electron Probe Analysis of Limiting Transepithelial Inorganic Ion Concentrating Differences Across the Rat Proximal Tubule", R. R. Warner and C. P. Lechene, LHRN, Harvard Medical School

- 60 2:45 PM "Comparison of Scanning Transmission and Back-scattered Electron Imaging in the SEM, Using Heavy Metal Stained Sections of Biological Tissue", Phillip B. DeNee, Appalachian Laboratory for Occupational Safety and Health, National Institute for Occupational Safety and Health; and Richard G. Frederickson, Dept. of Anatomy, School of Medicine, West Virginia University Medical Center
- 61 3:00 PM "Electron Probe Study of the Urinary Concentrating Mechanism. Elemental Cortico-Papillary Gradient in Frozen Hydrated Rat Kidney", C. P. Lechene and J. V. Bonventre, Harvard Medical School, LHRRB
- 3:15 PM INTERMISSION
- 62 3:30 PM "Calcium in Goblet Cells of the Small Intestine", Bernard P. Halloran and James R. Coleman, Dept. of Radiation, Biology and Biophysics, University of Rochester, School of Medicine and Dentistry
- 63 3:45 PM "Volume Changes in Freeze-Dried Tissue", F. Duane Ingram and Mary Jo Ingram, Dept. of Internal Medicine, University of Iowa; and Arthur R. Spurr, Dept. of Vegetable Crops, University of California
- 64 4:00 PM "Aluminum, Zinc and Lead in Arterial Calcifications of Human Brain", S. Duckett, Jefferson Medical College-Philadelphia - (USA); and P. Galle, Dept. de Biophysique de la Faculte de Medecine de Creteil - (France)
- 65 4:15 PM "Dynamic Effects on Quantitation in the Electron Probe Analysis of Mineralized Tissues", John W. Edie, Dental Research Lab., University of Iowa; and Paul L. Glick, V.A. Hospital and College of Dentistry, University of Iowa
- 66 4:30 PM "An Ultra-High Vacuum SEM for Microanalysis of Ultrastructure of Thin Specimens", Lloyd V. Sutfin, Dept. of Orthopaedic Surgery, Harvard Medical School, Children's Hospital Medical Center
- 78 4:45 PM "Use of Energy Dispersive X-ray Techniques for Detection and Identification of Immunochemically Stained Tumor Viruses", W. J. Hamilton, Jr., Developmental Electron Microscopy Lab, Frederick Cancer Research Center (Litton Biometrics, Inc.)

FRIDAY 13 AUGUST 1976

SESSION VII - AUTOMATION AND INSTRUMENTATION

French Room

W. F. Chambers, Chairman

- 67 9:00 AM INVITED PAPER: "Microprobe Automation - Past, Present and Future", W. T. Hatfield, General Electric Research and Development Center
- 68 9:30 AM "Computer Applications to Multiple User Microprobe Systems", G. G. Yagunoff, T. A. Baillieul and W. A. Ranson, Geological Dept., University of Massachusetts
- 69 9:45 AM "A Programmable EPMA Controller Using a Micro-Processor", Minoru Fujisawa and Koh Kirata, JOEL LTD., Tokyo, Japan
- 70 10:00 AM "Krisel Control Automation Plus MAC 5 (ETEC) Microprobe Used in Teaching and Research in Geosciences", H. O. A. Meyer and D. L. Hawkins, Department of Geosciences, Purdue University
- 10:15 AM INTERMISSION
- 71 10:30 AM "An Artifact in X-ray Micro-Analysis Secondary X-rays Emitted from the Specimen Chamber, A Study in the Case of Thin Specimen Analysis", P. Galle, C. Conty and A. Boissel, Department de Biophysique de la Faculte de Medecine de Creteil and CAMECA
- 72 10:45 AM "Low Magnification X-ray Mapping Without Defocusing Using a Crystal Spectrometer; Crystal Performance Characteristics", C. Conty, Cameca Instruments Co., Paris, France (PAPER WITHDRAWN)
- 73 11:00 AM "Minimum Detection Limits in an Automated Microprobe Analysis", Joseph D. Geller, J.O.E.L.
- 74 11:15 AM "The Design, Performance and Applications of a 100 kV Field Emission STEM", I. R. M. Wardell, V. G. Microscopes, Ltd., Sussex, England
- 11:30 AM End of Session

ELEVENTH ANNUAL CONFERENCE

OF THE

MICROBEAM ANALYSIS SOCIETY

TUTORIALS

T1A

Statistics of X-ray Analysis

J. I. Goldstein

Metallurgy and Materials Science Department

Lehigh University, Bethlehem, Pa.

The X-ray analyst is often asked, is this sample homogeneous, did you detect a given element in this sample, what is the precision of this analysis or perhaps do these two areas of the sample have the same composition? To answer these questions the analyst must be able to plan his analytical X-ray procedures considering such items as the number of points per sample, the analysis time, the method of measuring continuum background, etc., before beginning an analysis. Luckily X-ray production is statistical in nature (random in time, but with a fixed mean value). Therefore by using relatively straight forward statistical analysis techniques, many of the above questions can be answered directly and analytical X-ray procedures can be planned before the analysis is begun.

Fundamental Statistics

The distribution of the number of determinations of X-ray counts from one point on a sample vs. the number of X-ray counts N for a fixed time interval can be closely approximated by a continuous normal (Gaussian) distribution. The Gaussian curve has a mean value of N called \bar{N} and the standard deviation is the square root of the mean ($\sigma_c = \bar{N}^{1/2}$). The standard σ_c is the irreducible minimum for the X-ray emission process. As Liebhafsky et al.⁽¹⁾ have pointed out, the actual standard deviation of the experiment S_c is given by

$$S_c = \left[\sum_{i=1}^n (N_i - \bar{N})^2 / (n-1) \right]^{1/2} \quad (1)$$

T1B

where N_i is the number of X-ray counts for each determination i and the mean or average number of X-ray counts,

$$\bar{N} = \sum_{i=1}^n N_i / n \quad (2)$$

where n is the number of determinations of i . In practical analysis S_c rarely equals σ_c .

Usually the true average or mean number of X-ray counts m is unknown. As discussed by Youmans⁽²⁾ the Student's t is a statistic that permits an estimation of m and is given by

$$t = (\bar{N} - m) / (S_c / \sqrt{n}) \quad (3)$$

Student t values actually allow one to estimate a range of values for the average number of X-ray counts at some probability level. This probability level $1-\alpha$, means that one can expect only some fraction α (.05 or .01 for example) of the measured values N_i to lie outside the range t . The Student's t value decreases as the number of measurements n increases. Student t values, $t_{n-1}^{1-\alpha}$, for various degrees of freedom $(n-1)$ are given in Table I.⁽³⁾ For a given probability level, $1-\alpha$,

$$m = \bar{N} \pm t_{n-1}^{1-\alpha} S_c / n^{1/2} \quad (4)$$

and the term $t_{n-1}^{1-\alpha} S_c / n^{1/2}$ is the confidence limit for the true average number of X-ray counts m .

The analysis of the difference of two means, such as \bar{N}_1 and \bar{N}_2 , is a common problem in statistics.⁽⁴⁾ We are interested here in whether the difference $\bar{N}_1 - \bar{N}_2$ is zero or not. The Student's t distribution can again be employed since it gives the probability of exceeding the observed difference of the two means. Two means which are almost equal, have similar

statistical variations. If one determines two means \bar{N}_1 and \bar{N}_2 by n repetitions of each measurement taken for the same fixed time interval, then these two values are significantly different at a certain probability level $1-\alpha$ if

$$\bar{N}_1 - \bar{N}_2 \geq \sqrt{2} t_{n-1}^{1-\alpha} S_c / n^{1/2} \quad (5)$$

The statistical equations (1-5) can be applied to specific problems in X-ray analysis.

Homogeneity

The measured range of homogeneity $W_{1-\alpha}$ in wt% for a probability level $1-\alpha$ can be obtained using Eqn. 4 where

$$\pm W_{1-\alpha} = \pm \frac{C}{\bar{N}} (t_{n-1}^{1-\alpha} S_c / n^{1/2}) \quad (6)$$

The wt% of the element of interest is C and the average number of counts accumulated at each measurement is \bar{N} . The level of homogeneity $W_{1-\alpha} / C$ in % is given by

$$\pm \frac{W_{1-\alpha}}{C} = \pm (t_{n-1}^{1-\alpha} S_c / n^{1/2}) \frac{100}{\bar{N}} (\%) \quad (7)$$

It is important to note that it is difficult to measure the same level of homogeneity as the concentration C decreases since S_c / \bar{N} increases as \bar{N} decreases.

Analytical Sensitivity

Analytical sensitivity involves the ability to distinguish between two compositions C_1 and C_2 of the same element that are nearly equal. The measurements are made on two different areas of a sample. Using Eqn. 5, the difference in concentration ΔC for n measurements of N_1 and N_2 for the same time interval is

T1D

$$\Delta C = C_1 - C_2 \geq \sqrt{2} t_{n-1}^{1-\alpha} S_c / n^{1/2} \left(\frac{C_1}{\bar{N}_1 - \bar{N}_B} \right) \quad (8)$$

The terms \bar{N}_1 and \bar{N}_B are the average number of X-ray counts and the average number of background continuum X-ray counts, respectively, for the desired element in one of the two areas of interest. In this case S_c is essentially the same for either measurement \bar{N}_1 or \bar{N}_2 . For a given probability level $1-\alpha$, ΔC must exceed the value on the right hand side of Eqn. 8 or the two compositions C_1 and C_2 are indistinguishable.

Ziebold⁽⁵⁾ has shown that the analytical sensitivity for a 95% probability level can be approximated by

$$\Delta C = C_1 - C_2 \geq \frac{2.33 C \sqrt{\bar{N}_1}}{n^{1/2} (\bar{N}_1 - \bar{N}_B)} \quad (9)$$

This approximation disregards the effect of various instrumental errors.

If \bar{N}_1 is much larger than \bar{N}_B , Eqn. (9) can be rewritten as

$$\Delta C = C_1 - C_2 \geq 2.33 C / (n \bar{N}_1)^{1/2} \quad (10)$$

and the analytical sensitivity in percent that can be obtained is given as

$$\Delta C / C (\%) = 2.33 (100) / (n \bar{N}_1)^{1/2} \quad (11)$$

Although the analytical sensitivity improves with decreasing concentrations, the X-ray intensity \bar{N}_1 decreases directly with the reduced concentration. Therefore longer counting times become necessary in order to retain a low sensitivity level. Eqn. 11 is useful for predicting necessary procedures to obtain the analytical sensitivity desired in a given measurement.

TIE

Trace Element Analysis

At a low concentration range sometimes referred to as the trace element range, \bar{N}_1 is not much larger than \bar{N}_B . The analysis requirement in trace element analysis is to detect significant differences between the sample and the continuum background generated from the sample. The detectability limit for trace element analysis is governed by the minimum value of the difference $\bar{N}_1 - \bar{N}_B$ that can be measured with statistical significance.

By analogy with Eqn. 5, which gives the analysis of the difference of two means, we can define the detectability limit, $(\bar{N}_1 - \bar{N}_B)_{DL}$, for trace analysis as

$$(\bar{N}_1 - \bar{N}_B)_{DL} \geq \sqrt{2} t_{n-1}^{1-\alpha} S_c / n^{1/2} \quad (12)$$

where S_c is essentially the same for both the sample, \bar{N}_1 , and background, \bar{N}_B , measurement. If we assume that the X-ray calibration curve of intensity vs. composition is expressed as a linear function, then C , the unknown composition, can be related to \bar{N}_1 by the equation

$$C = \left[\frac{\bar{N}_1 - \bar{N}_B}{\bar{N}_S - \bar{N}_{SB}} \right] C_S \quad (13)$$

where \bar{N}_S and \bar{N}_{SB} are the mean counts for the standard and the continuum background for the standard, respectively, and C_S is the concentration in wt% of the element of interest in the standard. The detectability limit, C_{DL} the minimum concentration that can be measured, can be calculated by combining Eqns. 12 and 13 to give

$$C_{DL} = \left(\frac{C_S}{\bar{N}_S - \bar{N}_{SB}} \right) \left(\sqrt{2} t_{n-1}^{1-\alpha} S_c / n^{1/2} \right) \quad (14)$$

TIF

The relative error or precision in a trace element analysis is equal to

$$C/C_{DL} \quad (5)$$

Ziebold has shown that the detectability limit can be approximated by

$$C_{DL} \geq 3.29a/(n \tau P \cdot P/B)^{1/2} \quad (15)$$

where τ is the time of each measurement, n is the number of measurements, P is the pure element counting rate, P/B is the peak to background ratio of the pure element, and a is the Ziebold-Ogilvie⁽⁶⁾ constant for a given sample. It is clear from Eqn. 15 that the detectability limit can be decreased by raising the peak intensity, analysis time and peak to background ratio.

Experience on many different types of samples, obtained by performing repeated analyses in small areas, refocusing at each point, and counting for 10-100 sec. per point, demonstrates that S_c is usually equal to $2(\bar{N})^{1/2}$. Using this experimental observation Eqns. 8 and 14 can be greatly simplified. If one estimates or measures \bar{N} for a given sample, one can use Eqns. 8 and/or 14 to determine the optimum analytic procedures to use in order to obtain a desired sensitivity or detectability limit. This procedure is described in detail by Goldstein et al.⁽⁷⁾

Table I Values of Student t Distribution
for Probability Levels, $1-\alpha$, of 0.95 and 0.99.⁽³⁾

n	$n-1$	$t_{n-1}^{.95}$	$t_{n-1}^{.99}$
2	1	12.71	63.66
3	2	4.304	9.92
4	3	3.182	5.841
8	7	2.365	3.499
12	11	2.201	3.106
16	15	2.131	2.947
30	29	2.042	2.750
∞	∞	1.960	2.576

References

1. H. A. Liebhafsky, H. G. Pfeiffer and P. D. Zeman, Anal. Chem. 27, p. 1257 (1955).
2. H. L. Youmans, "Statistics for Chemistry," C. E. Merrill Pub. Co., Columbus (1973).
3. E. L. Bauer, "A Statistical Manual for Chemists," 2nd Ed., Academic Press, New York (1971).
4. R. A. Fisher, "Statistical Methods for Research Workers," Hafner Pub. Co. (1950).
5. T. O. Ziebold, Anal. Chem., 39, p. 858 (1967).
6. T. O. Ziebold and R. E. Ogilvie, Anal. Chem., 36, p. 322 (1964).
7. J. I. Goldstein, H. Yakowitz, D. Newbury, E. Lifshin, J. Colby and J. Coleman, "Practical Scanning Electron Microscopy, Electron and Ion Microprobe Analysis," Plenum Press, New York (1975).

MAKING THE CHOICE BETWEEN AN EDS EQUIPPED SEM
AND AN AUTOMATED ELECTRON MICROPROBE

by

J. W. Colby
Kevex Corporation
Burlingame, California

The choice between a full electron microprobe equipped with wavelength dispersive spectrometers (WDS) and a scanning electron microscope (SEM) equipped with an energy dispersive spectrometer, (EDS) is one with which an increasing number of laboratories find themselves faced. The resulting choice is thus a compromise and depends primarily on whether one is interested in high quality, high resolution electron images or highly accurate, highly precise chemical analysis. This, at present, is the least subtle difference between the two alternatives. There are other factors which may also govern the choice, and these will be elucidated upon during the presentation. It is this author's belief that a good laboratory should have access to both types of instruments even though one may not be able to fully utilize all capabilities of both or may not be able to justify both on the basis of full-time usage. For example, if one must obtain analysis for light elements such as boron, carbon, nitrogen, etc., or if one is interested in the valence state of the chemical constituents, the best EDS

system in the world could not provide such information. On the other hand, if one is interested in analyzing glasses with highly mobile species, such as potassium, sodium, etc., then it behooves one to obtain an analysis for all constituents as rapidly as possible, with as low a beam current as possible. In such cases the EDS is clearly superior. Many other cases can and will be cited during the presentation which govern the choices to be made.

AUTOMATION
MAKING THE HARD DECISION

W. T. Kane

Research and Development Laboratories
Corning Glass Works
Corning, New York 14830

The automation of microbeam instruments has at least a ten-year history and sessions on the subject at M.A.S. annual conferences have been given since then. One might think that by this time the whole matter might be rather cut and dried, but to the contrary, the tools and methods of computer automation have been changing at almost an exponential rate and the options available for instrument control have grown very wide. At one extreme, complete, ready-to-run "Turnkey" microprobe analyzers and SEMs are offered by a number of manufacturers which include the instrument, computer, interfacing logic and software. On the other extreme are the hardy adventurers with microcomputer chips, blank circuit boards and wire wrap guns who automate literally from "scratch". Before one can make an intelligent choice in this spectrum of automation options, why an automated instrument is needed, should be clearly understood. Some rationals for automating are the following:

1. to reduce analytical cost (\$/sample),
2. to speed data acquisition and reduction,
3. to improve precision and/or accuracy of analysis,
4. to reduce the level of skill and training necessary to operate the instrument,
5. to perform analyses which are not possible and/or practical using manual methods,
6. to serve as a test bed for automation research,
7. to serve as a laboratory status symbol, and
8. some or all of the above.

In addition, the probable mix of problems to be handled should be identified as well as possible as no two laboratories have identical requirements. Optimum system design for environmental, metallurgical, geological and materials research, for example, are different. The important point here is that the goals that automation are expected to accomplish must be clearly identified before the specification of a system. These goals then serve as benchmarks against which any potential system should be weighed.

The next major hurdle is the selection of a system which best fulfills the identified needs. System is stressed since the interfacing, the controlling computer and the software form critical links in the automation chain as defects or limitations in any one can lead to failure of the whole.

1. The Instrument

One month of automated operation can easily equal 5 years of manual use and thus the mechanical parts of the instrument should be designed with automation in mind. Particular attention should be paid to the ruggedness and durability of scanning crystal spectrometers and the sample stage. The stress and wear of high speed stepping motor drive can rapidly cause severe backlash and vibration problems which can totally defeat automated operation in the stage and spectrometers originally designed for manual control.

The electronic components which are to be controlled must include provisions for accepting either digital or low level analog control signals from the interface. For example, if the high voltage supply is to be controlled, inputs for voltage selector, filament voltage and bias control as well as an output to allow the monitoring of filament voltage must be included as all are necessary. When specifying a new system, it is wise to include control input and output options for all functions that it may be desired to control even if immediate implementation is not planned. These options are relatively inexpensive and usually quite difficult to install in the field.

2. The Interface

The interface is the black box which makes possible the interchange of commands and data between the instrument and the computer. It usually includes computer-controlled switches (output registers), instrument status indicators (input registers), Analog to Digital Converters (ADC's), Digital to Analog Converters (DAC's), Stepping Motor Controllers, Scalers, Clocks, and Data Mode Converters (BCD to Binary or Binary to BCD, etc.) Early interface designs tended to be simple, inflexible, "stupid" and expensive, and be warned - many currently available still are. An inflexible interface has a fixed ("hard wired") design which makes it difficult and expensive to change or expand the control of the instrument. A "stupid" interface puts the major load of controlling the instrument on the computer software and that, as we shall see later, is where the real money is. "Simple" and "expensive" are of course self explanatory but that they may accompany each other is not. Put directly, the interface is commonly a box containing several hundred dollars worth of components which is sold for as much as twenty thousand dollars. As such, the interface is an extremely profitable component and can be the focus of a very hard sell.

On the other hand, a variety of modular "smart" interfaces are available at moderate cost. Modular units often of proprietary modified NIM (Nuclear Instrumentation Module) design or based upon CAMAC (a nonproprietary internationally accepted standard for interfacing) make it quite simple to change or expand the control of the instrument by adding or changing modules. In addition, the individual modules are often capable of performing rather complex functions in response to simple commands from the computer. For example, stepping motor control modules are available which will accelerate a motor to a computer selected speed then deaccelerate and stop when a desired number of steps have been taken, and then signal the computer that execution is complete. This sort of "smart module" leads to very important simplifications in the control computer programming which, in turn, substantially reduces system cost and increases the ease of changing control algorithms.

3. The Computer

A number of excellent minicomputers with many peripheral device options and powerful software operating systems are available at competitive prices. This is a highly competitive market and increases in computing power accompanied by substantial price reductions have been occurring at an almost unbelievable pace. The result has been that the cost of the computer and mass storage hardware has become a much smaller portion of overall system cost. The cost of high speed memory, for example, has dropped by a factor of ten in the last six years. At the same time, powerful real-time operating software systems including high level language interpreters and compilers, editor programs, subroutine libraries and convenient utility programs which a few years ago were available only for million dollar class machines are available for almost all mini's with either floppy or cartridge disc support.

As a consequence, the hardware compromises made on the basis of cost (limited memory for the CPU, no mass storage devices, no printing or plotting capability, and low speed I/O devices) really no longer apply. However, the cost of programming a stripped down minicomputer and the inconvenience of using it are prices which are paid after installation and they can be very high indeed.

4. Software

The current user of minicomputers has contact with three fundamental varieties of software; assembler languages, compiler languages, and interpretive languages. It is important to understand the distinctions between them.

Assembler languages are specific to a single variety of computer and are very close to the actual binary machine code. In general, a single assembler instruction is equivalent to a single

machine instruction although sophisticated assemblers may have macro-instructions which represent frequently used groups of machine instructions. The use of an assembler language requires that the programmer have an intimate knowledge of the architecture of the computer. Programs written in assembler tend to run faster and occupy less high speed storage than equivalent routines in the higher level languages. Until recently, control programs involving dynamic interaction between the computer and the instrument (interrupt level programming) were necessarily written in assembler. On the negative side these machine specific languages are notoriously difficult to use and require large amounts of skilled programmer time to write and debug. In practice it takes 20 times as long to debug an assembler language routine as it does to write it and a recent estimate of programming cost was \$10 per instruction.

Compiler languages such as FORTRAN IV, FORTRAN Plus, FORTRAN V, and PL1 are usually not specific to a single computer and are written in a relatively simple algebraic code which is translated by a special utility program called a compiler into machine code. A single line of compiler language coding will generate up to hundreds of machine instructions. On most minicomputers, disc mass memory is required for compilation. The machine code generated by the compiler program is usually somewhat slower and less economical of high speed memory than assembler but programming and debugging are at least an order of magnitude cheaper and faster. No particular knowledge of the internal workings of the computer are required. Interpretative languages (BASIC, BASIC Plus CLASS®, etc.) are written in a simple algebraic format like the compiler languages. The program as written is loaded into high speed memory with a special interpreter program which converts the raw code to machine language and executes it line by line. Since the original program as written is stored, it is very easy to correct or change. As might be expected such programs run considerably slower and occupy substantially more high speed storage than do compiled programs.

Recent versions of both compiler and interpretive languages for most minicomputers include provisions for dynamically interactive control programming. Since assembler languages are necessarily machine specific there can be no standard languages. The higher level languages which are machine independent can be standardized. ANSI FORTRAN IV and BASIC can be used on many varieties of minicomputers with little or no change for computation although some modifications may be necessary in the use of subroutine library calls which permit interrupt handling.

Given the best of starting conditions, i.e., a powerful minicomputer, a "smart" interface, a large high speed memory (32K words), a fast mass storage device (floppy or cartridge disc), and a powerful high level programming language, the writing of control software for an automated microprobe or SEM is a substantial

undertaking. Under these conditons, the control software for the Corning automated microprobe took 5-man months of skilled programmer time. This represented an internal cost of \$17,300 without consideration of the overhead costs of a very expensive capital investment not earning its keep. The estimated cost of implementing the same control program in assembler language is over \$200,000 and 50-man months. The cost in money and time of attempting to program this control software with 8K of memory and without a disc-based operating system is almost incomprehensible. Had we started the programming with an "inexpensive" computer and a hardwired interface, we would necessarily have considerably simplified and compromised the control program at the cost of significant accuracy and precision of analysis and even so the cost of the software would approach the total hardware cost. In short, five cents saved in hardware expense can very easily result in a dollar of software cost.

5. Selecting a System

A number of options for systems selection are available. Most probe and SEM manufacturers can supply complete automated systems including control and data reduction software. At first glance, it would appear much easier to simply pay and let them do the engineering. However, it is very important that one ask the same questions about a "Turnkey" system concerning the instrument, the interface, the computer and the software that would be asked in designing your own. A number of these systems have software which is written in assembler language, minimal computer configurations and very inflexible interfaces. In such cases, make sure that the whole system closely parallels your analytical needs for changes in the software or the instrument control configuration are apt to be difficult and very expensive. Always ask for a complete user list from the manufacturer and then make some inquiries at random. Half a dozen telephone calls may well tell you more about a packaged system than twenty pounds of sales brochures. For example, some very inflexible interfaces have been packaged in unpowered NIM crates to give the appearance of modular construction. If in doubt ask the man that owns one - better yet, ask a number of them.

Another approach is to have the automation supplied and installed by a company specializing in interfacing. In this case, the interface and computer as well as operating system software are supplied, but the control and data reduction software may be the responsibility of the purchaser. A "smart" interface, a computer with a disc operating system and a reasonably good programmer then become quite important. Again, ask the vendor for a list of users and in the phone poll also ask if the user will share any or all of his control software. Many users will happily help newcomers avoid reinventing the wheel.

The references provided by Bill Hatfield in Paper No. 67 of these proceedings represents both a history and a view of the

current state of the art in automating electron beam instruments. The authors of most of the listed papers are alive and living in front of functional automated instruments. Many of them will happily answer intelligent questions and might welcome a lab visit to show off their marvelous machines. If you are about to spend several hundred thousand dollars of your company's or Uncle Sam's money, a few dollars spent on the phone and in lab visits may be a very wise investment.

General References

Hatfield, W. T., "Microprobe Automation - Past, Present and Future", Paper No. 67, Proc. of the 11th National Conference of the Microbeam Analysis Society, Miami, Florida (1976).

Kay, R. H., Ploetzeneder, H. D., and Gritter, R. J., "Cost Effectiveness of Computerized Laboratory Automation," Proc. of the IEEE, Vol. 63, No. 10, pg. 1495-1502, October, 1975.

CAMAC, A Modular Instrumentation System for Data Handling, United States Atomic Energy Commission, TID 25875 (Revision July 1972) (From U. S. Government Printing Office, Washington, D. C. 20402.)

THE SEM AS A SUCCESS ANALYSIS TOOL FOR SEMICONDUCTOR
QUALITY CONTROL

T4A

by H.M. HYMAN and N.A. CIAMPA
RCA CORPORATION , SOLID STATE DIVISION
SOMERVILLE , NEW JERSEY

There is surely no question or doubt , that within the semiconductor world of electrons , atoms and molecules , even the smallest human insights towards their behavior patterns during processing failures --- can lead to success in the future !

I also submit that failure analysis for yield improvement is actually only one part of the story. The real world in the semiconductor business today demands that we recognize any technical deficiencies in our products , demonstrate a high degree of cosmetic and electrical performance capability , and that we use every skill , tool , or means at our disposal , to equal or surpass the quality of the competition .

I can best describe the impact of the scanning electron microscope within our industry , by saying that it has proven to be one of the most efficient, versatile , and valuable means for the failure and --- more important -- the success evaluation of our production and advanced development technologies.

The first section of this video tape presentation briefly reviews some of the basic design considerations , principles, and accessory features of the SEM employed at this facility.

Continuing then with our theme of successful product engineering --- We begin with considerations of the starting material -- the Silicon Wafer ! Whether it be a single crystal substrate , laminate structure or epitaxial material , we are essentially concerned that ;

- (a) It be free of gross surface imperfections or contaminants
- (b) Have proper orientation and dopant distributions
- (c) Contain a minimum of internal crystal defects, damage or stress.

All of the factors mentioned so far , and many of those that will be considered , cannot be resolved simply by using an S.E.M.! I will illustrate many of the applications for which the SEM is ideally suited in a production environment , but certainly there are other means for more efficient and informative investigations of specific material properties. They also need to be employed to complement the SEM and to maintain a more complete control program. (For example --- transmission electron microscopy, Auger surface analysis, spark-source mass spectrometry, X-Ray diffraction, ion microprobe analysis and numerous types of electrical evaluations.

This section of the presentation deals with the starting materials and processing of our elaborate semiconductor device fabrication scheme , and illustrates some of the anomalies which are observed .(Examples -- dislocations , stacking faults, orange-peel effect, contamination)

The next stage of processing would normally involve the high temperature deposition of an epitaxial silicon layer on either the starting silicon material or possibly a sapphire substrate wafer. In some cases a polysilicon layer may be grown instead for certain device purposes. The quality of this layer is the single most important factor in the whole device fabrication scheme for integrated circuits. (Examples -- Craters , hillocks, misorientation, temperature problems)

The next series of operations common to almost all device fabrication schemes involves , high temperature oxidation , photoresist masking, oxide etching , high temp dopant diffusions and a number of surface preparations . These steps are usually repeated 4 or 5 times during the course of fabrication. Now we are essentially concerned that we have introduced a minimum of surface or processing defects, maintained good physical alignment of components, and that we have proper oxide, silicon window or photoresist edge integrity. (Examples -- Arsenic whiskers, antimony rosettes , phosphorous diffusion damage, boron pitting, photoresist defect problems , oxide etching and edge definition effects)

We now consider the final steps for the wafer fabrication in T4C wafer form , namely metallization , alloying, metal definition , polysilicon or metal interconnects, and glass surface passivation. We have now reached the point of no return in the processing of the device wafer and our success analysis is 90% complete --- if all has gone well --- otherwise our failure analysis is just beginning.

The emphasis now is on proper metal continuity, good electrical contact, satisfactory component isolation, freedom from obvious surface defects, proper alignment of circuit functions, and the appearance of reliability.(Examples - various acceptable, marginal and unacceptable metallization and interconnect conditions)

After inspection and packaging , we now have a completed transistor or integrated circuit , which to no one's surprise , will sometimes fail in the elaborate final test conditions or after special procedures such as burn-in, temperature cycling , stress evaluation, or operating life. We must then logically concentrate on the analysis of our failures !Considering the complexity of the processing involved , it is expected that some very strange things will happen on occasion to devices that appear perfectly normal before they are sealed in the final package. (Examples - Disappearing aluminum metal , electro-migration, metal extrusions)

Whereas quite often the failure symptoms are easily visible in the SEM once the unit has burned out or degraded sharply ,it is far more important to have adequate diagnostic tools available to investigate potential problems before they occur . For that purpose we may want to consider some entirely different modes of SEM operation --- namely voltage contrast, electron beam induced current (with and without bias) , or energy dispersive X-Ray analysis.

One of the most valuable of the auxillary modes is commonly referred to as Voltage Contrast ! It may be simply described as a modification of the collection efficiency of secondary electrons in the normal mode of SEM operation. When the surface of a conductor is externally biased with either a positive or negative potential , the low energy secondary electron ejection efficiency, which produces the SEM picture, is altered sufficiently so that there is a significant change in contrast. More negative areas appear relatively bright compared to positive areas. The effect is usually enhanced by operation at low accelerating potentials (1 - 10) , and is sensitive to approximately 2-3 volts bias. In resistor structures it may be possible to discern 0.5 volt differences where there is a good reference point ,

This technique then allows us to view potential differences on a device surface which has been electrically activated in either an operating or reverse bias mode. The most promising applications for this technique are in ;

- (1) The location of metal stripe opens - even when they are covered with passivation layers.
- (2) The location of contact points to the substrate or other components which are not functioning or highly resistive.
- (3) The evaluation of junction properties such as isolation, diffusion boundaries, pipe defects, mask defects, shorts, and cross-section measurements. (Examples - Voltage contrast effects on various power , linear and MOS semiconductor devices)

Another very essential mode of operation for proper device diagnostics is the EBIC or electron beam induced current mode. When the electron beam of the SEM penetrates the silicon at a P/N junction site, it creates hole-electron pairs to a depth dependent on the beam energy. Carriers generated within the depletion region or close to it, will be swept across the junction by the built-in field---- holes toward the P side and electrons toward the N side. This gives rise to a small current flow of the order of 10 to the minus of 10 amps, which is then amplified and can be used to modulate the brightness of the CRT.

(Examples - EBIC effects on various semiconductor device structures)

T4E

Another mode of operation , which has been previously mentioned , and really comes in handy for special problems , is the energy- dispersive X-Ray microprobe accessory. (Examples - Particle identification problem and evaluation of silver migration during stress testing)

The final part of this presentation will be a display of dynamic operational voltage contrast effects on three different C/Mos integrated circuits. They were taped directly from the SEM T.V. monitor and were activated with an external pulse generator and battery power supplies. The effect that is visible is the change in potentials of the metal stripes and component regions as the devices operate. Obviously it provides a powerfull yet simple means for the comparison of good and failure units , without the need for complex electrical test equipment.

Example 1 - C/MOS Watch Circuit containing 17 Flip-Flops, 4 inverters and 4 power transistors --- operating just as it would in a wrist watch.

Example 2 - C/MOS Heart Pacer Circuit Chip -- a very complex system involving many inter-related functions coordinated to produce the desired effect

Example 3 - C/MOS 18 stage static shift register - simulated as it would operate in a computer with stored information.

ELEVENTH ANNUAL CONFERENCE

OF THE

MICROBEAM ANALYSIS SOCIETY

PROCEEDINGS

THE HISTORY OF EDS SYSTEMS ON ELECTRON BEAM INSTRUMENTS

R. Woldseth

KeveX Corporation, Burlingame, California

The marriage of the electron column instrument and the x-ray energy spectrometry system for the purpose of microanalysis truly represents a unique technological synthesis. In the best sense, the result has been a constructive symbiotic relationship, beneficial to the development and use of both components.

A 1976 historical review of this relationship and its development could perhaps fill volumes -- and a review of the pertinent literature reveals that indeed it has -- however, our aim here is to be somewhat less ambitious. What is the essence of the development and progress that we have seen over the short decade that has passed since the first reporting of its combined use in 1968? ¹⁾

In a capsule statement, the viability of the energy dispersive detection technology for these and other applications is associated with a few key factors:

- a. Sufficient energy resolution for element emission line separation and identification
- b. High detection efficiency over energy range of interest
- c. Adaptability to general and specific requirements as relating to its function as an accessory to a parent instrument, and to those aspects that are unique to microanalysis
- d. Reliability

The developmental history of its association with the electron column parent system may most readily be traced by a definition of the general and specific requirements. Anyone in close association with the use or manufacturing of the solid state detector systems for these purposes very quickly formulates the ideal detector system (the concept) embodying the above points:

1. "Infinite" (delta-function) energy resolution
2. 100% intrinsic (absorption) detection efficiency
3. 4-Pi geometrical detection efficiency (sometimes)
4. Must be interfaced to the parent instrument without occupying any space, requiring no sacrifices in imaging performance (preferably doing topographical mapping and x-ray mapping simultaneously without sacrifices in either).

The everwidening acceptance and use of this tool reflects a development that still is somewhat short of the phantom transducer as broadly defined above. However, in terms of the general requirements as stated in points a. - d., considerable progress is represented.

One of the earliest reviews of the technology was made by Aitken and Woo as early as 1970 ²⁾, at the Symposium on Energy Dispersion X-Ray Analysis. This Symposium had a format quite similar to these tutorial sessions, and might serve as an excellent reference point for all the discussions from the detector transducer through the processing electronics and on into the multiple problems and approaches associated with quantitative analysis.

Viewed from six years down into the future, the views and evaluations as offered by Aitken and Woo in 1970 have held up remarkably well. Anyone who may have been looking for fundamental break-throughs have perhaps been disappointed. The progress, while in my view no less significant, has come through a systematic exploring, probing, and general practical use of these systems; and they are perhaps less apparent than those at certain other points in the system. The Si (Li) detector is still the king in the field of characteristic x-ray analysis as the best compromise of the requirements summarized in Table 1. Table 2 lists the properties of other semiconductor materials that are used and/or could be considered as candidates for these applications. However, the sum total of all considerations still leaves the field to Si (Li) as the most universally applicable and generally best performing transducer.

The question is invariably raised as to what the prospects are for further improvements in the energy resolution of the Si (Li) detector. It has always been appreciated that certain fundamental limitations do exist, as represented in the generally well known relation governing the resolution, expressed in terms of the full width half maximum (FWHM) of the ideal Gaussian line shape:

$$\text{FWHM} = \sqrt{(2.35 \ F \ \epsilon \ E)^2 + (\text{FWHM})_{\text{noise}}^2}$$

The quest for the better mousetrap potentially involves any and all of these parameters. The competitive semiconductor materials as listed in Table 2 are here fundamentally represented in the effective quantum efficiency ϵ , which is the average energy required for an electron - hole pair generation in the material, and the theoretically expectable but empirically derived Fano factor, the latter imposing a limitation to the applicability of purely statistical considerations in the energy transfer process. No major factor can be identified at the present time to materially change the general conclusions drawn by Aitken and Woo in 1970, yielding the asymptotic trend in detector resolution (Fig. 1). The trend that has been discernible over the past few years can best be identified in fine point improvements affecting the "intrinsic term" in the relation above (the "black magic" of detector manufacturing) along with comparable fine points affecting the noise term, and in improved capabilities of routine production of the "state of the art" product. Presently this lies in the neighborhood of 140 eV FWHM at 5.9 keV, with the asymptotic limit still somewhere around 100 eV.

Perhaps a more significant development can be found in the improved "plumbing" capabilities in detector cryostat packaging. The combined, sometimes contradicting requirements as suggested in the "ideal" configuration above has brought about the development of remarkably compact detector cryostat configurations, adapting to the limited access/small space conditions of most parent instruments (Fig. 2). All this while attempting to meet the request for favorable take-off angle and good geometrical efficiency. This type of system adaptability is perhaps best reflected in the adjustable cryostat, where the above parameters may be controlled by adjusting the sample-to-detector distance under vacuum. Other approaches, such as the "in the polepiece" detector placement, may be equally significant.

Another extension of the total detection capability has been introduced on a limited scale; i.e., the so-called window-less detector. By reducing the effective entrance window absorption, this formulation extends the detection/analysis capability to elements with emission lines below 1 keV. However, the associated burden placed on the user to preserve the detector integrity vis-a-vis contamination, reproducible performance, etc., has implicit limitation with regard to universal use.

Without claiming to have touched all bases in this "Status 1976" overview, may we still step back and ask "what's new"? Compared to other developments to the total system capability, the "progress" may appear minor. This would, however, be underestimating the importance of detail in a complex system. To that extent one should not be allowed to forget that the detector properties makes it all possible. And perhaps the greatest compliment to capability, quality, reliability and performance may be found in the fact that the front end of the system is taken for granted. Nothing could better characterize a mature and established technology - Sic progress and Status 1976.

- 1) R. Fitzgerald et al., Science, Vol. 159, No. 3814, p. 528 (1968)
- 2) D. W. Aitken, E. Woo: "The Future of Silicon X-Ray Detectors", ASTM Special Technical Publication 485

TABLE 1. TRANSDUCER REQUIREMENTS FOR HIGH RESOLUTION PHOTON SPECTROMETERS

Characteristic	Requirement
Energy Gap	$> 1 \text{ eV}$
ϵ	2-5 eV
F (Fano Factor)	< 0.3
Free Carrier Concentration	$< 10^{10}/\text{cm}^3$
Trapping sites	$< 10^{12}/\text{cm}^3$
Carrier Mobility	$> 100 \text{ cm}^2/\text{Volts-sec}$
Contacts	One ohmic and one injecting
Electric Field	$> 10^3 \text{ V/cm}$ (material dependent)

TABLE 2. PROPERTIES OF SEMICONDUCTOR MATERIALS
FOR RADIATION DETECTORS

Semi-conductor	Energy Gap (eV) at 300°K	Electron Mobility ($\text{cm}^2\text{volt}^{-1}\text{sec}^{-1}$) at 300°K	Hole Mobility ($\text{cm}^2\text{volt}^{-1}\text{sec}^{-1}$) at 300°K	Electron lifetime in p-type (sec)	Hole lifetime in n-type (sec)
Silicon (Z = 14)	1.08	1500	500	3×10^{-3}	3×10^{-3}
Germanium (Z = 32)	0.67	3800	1800	10^{-3}	10^{-3}
Gallium-Arsenide (Z = 31, 33)	1.43	8500 to 10^5	420	10^{-7}	10^{-7}
Cadmium-Telluride (Z = 48, 34)	1.5	100	100	4×10^{-5}	$> 10^{-5}$
Indium-Antimonide (Z = 49, 51)	0.17	78000	750	$\sim 10^{-7}$	$\sim 10^{-7}$
Mercuric-Iodide (Z = 53, 80)	4.2	80	5	10^{-4}	$\sim 5 \times 10^{-6}$

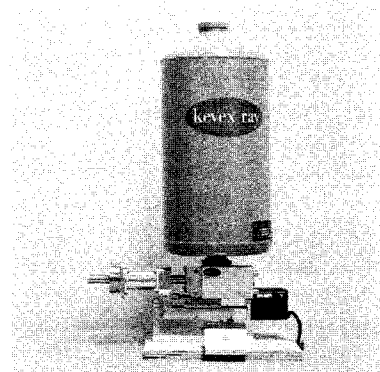
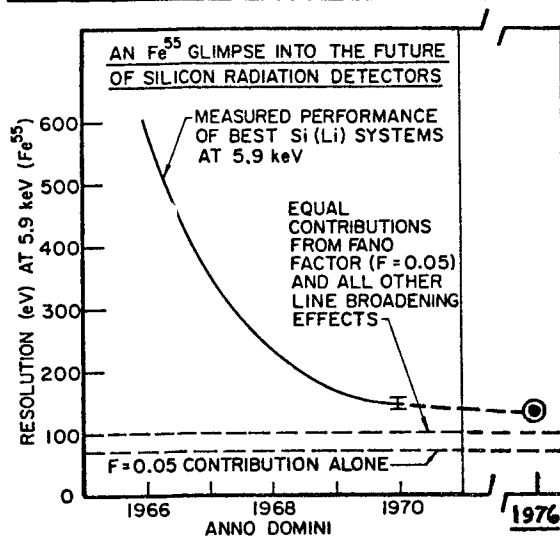


Fig. 1 The Resolution Evolution

LINEAR ELECTRONICS IN MICROANALYSIS SYSTEMS

E. Elad

ORTEC, Inc., Materials Analysis Division, Oak Ridge,
Tennessee 37830

The purpose of this review paper is to discuss the functions and performance limitations of the linear modules, namely the preamplifier and the amplifier, in an energy dispersive microanalysis system. This paper will be tutorial in nature, but will include the major developments in linear electronics in the last several years.

The primary functions of a preamplifier-amplifier combination are to amplify the minute charge signals from the silicon detector with minimum noise degradation of their contents, and to prepare them for the pulse-height sorting process performed by the multi-channel analyzer. Preamplifier configurations, both pulsed and continuous, will be described. Noise effects and count-rate limits will be analyzed. Relationships between detector and preamplifier parameters will be explained.

Detailed description of the noise filtering process by a pulse amplifier will be given. Performance parameters of amplifiers such as throughput rate, deadtime effects, count-rate induced peak-shift integrity, and others will be defined and analyzed. Baseline restoration, pole-zero cancellation, pile-up rejection, and other major amplifier-related functions will be outlined and discussed.

THE X-RAY MULTICHANNEL ANALYZER

F. H. Schamber

Tracor Northern, Inc., 2551 W. Beltline Hwy., Middleton, WI 53562

The multichannel analyzer (MCA) is a necessary instrument for the effective utilization of a solid-state X-ray detector. The designation MCA is commonly applied to any instrument which can accumulate a digitized spectrum within an internal storage memory; each individual storage "channel" of this memory represents the amplitude of a discrete data point of an acquired spectrum. The functions of a multichannel analyzer can be broken down into 3 major divisions:

1. data acquisition
2. display and readout
3. data manipulation and reduction

The most important acquisition mode for X-ray spectroscopy is known as Pulse Height Analysis (PHA). In this analysis mode the fast, random pulses generated by the front-end detector electronics (detector, pre-amplifier, amplifier) are sorted by amplitude via a specialized analog to digital converter (ADC) and corresponding channels of the analyzer memory are incremented for each event. Since the amplitude of an input pulse is directly proportional to the energy of a detected X-ray, the number of counts which are collected in each channel represent the number of X-rays of corresponding energy. Thus, a PHA spectrum represents the distribution of X-ray intensity (number of counts) versus energy (channel number).

Another mode of acquisition available in most commercial analyzers is known as Multi Channel Scaling (MCS). During consecutive time intervals the number of X-rays which are detected within a particular energy window are counted in successive channels of memory. If the energy window is set to include a characteristic peak of a particular element and the channel advance is externally synchronized with the sweep of the electron beam across the sample, one obtains a "line profile" which depicts the spatial distribution of the selected element across the sample surface. Refinements of this technique permit the electron beam and the channel advance to be precisely synchronized and thus permit repetitive high-speed scans.

Effective visual presentation of the acquired data is important when qualitative judgments are to be made, or when photographs are to be used in reports. Modern instruments make extensive use of overlap displays, moveable cursors, elemental peak markers and alphanumeric display labeling. Video display techniques have been introduced to permit relatively inexpensive large screen displays and color displays are also available.

The ability to preserve spectral data for long periods of time is important in many applications. Magnetic storage media provide reliable,

high density storage and rapid operation. Magnetic tape cassettes have been used extensively in past years with flexible diskettes growing in popularity due to their higher access speed.

A significant trend has been the extensive computerization of the X-ray analyzer. This trend was initially motivated by the recognition that peak area determination of silicon-detector spectra required careful treatment of bremsstrahlung continuum, and frequently, the ability to resolve overlapping peaks. In the past several years a great deal of effort has been directed towards the development of efficient, reliable techniques for spectral data reduction. This effort, coupled with the availability of sophisticated, low-cost minicomputers, has brought on-line data reduction within the reach of a majority of X-ray analysts. The advantages of computerization, however, are not confined to quantitative analysis. The enhanced versatility of a computerized instrument, the provisions for automated and unattended operation, and the ability to be user-programmed for unique applications make the computerized multichannel analyzer a popular choice for semi-quantitative and purely qualitative applications as well.

Today's X-ray analyzer is technically adequate for the data rates and resolution of modern silicon detectors and no major technological advances in data acquisition capability seem imminent. Looking towards the future, the greatest changes in analyzer technology appear likely to be in the areas of price and convenience features, primarily due to the impact of low cost solid-state memories and microprocessor devices.

QUANTITATIVE ENERGY-DISPERSIVE ANALYSIS

S.J.B.Reed

Department of Mineralogy & Petrology, Downing Place,
Cambridge CB2 3EW, England.

INTRODUCTION. Quantitative analysis is possible with an E.D. system, provided its performance is adequate (stability especially). Such a system may be fitted to an electron probe, SEM, TEM, or STEM and used for the analysis of either thick or thin specimens, of which the former are considered primarily here, though in many respects the procedures discussed are equally applicable to thin specimens. Elements in the range $Z = 11-30$ are primarily of interest (i.e. those with K peaks in the energy range 1-10 keV), though heavy elements with L or M peaks in this energy range can be treated by the methods discussed as well.

PEAK IDENTIFICATION. Often the analyst knows the elements present in the specimen. If not, a procedure for identifying peaks in the recorded spectrum is necessary. Various mathematical techniques are available for this purpose (e.g. cross-correlation with a gaussian). Observed peaks can be identified by reference to a list of peak energies.

COUNTING STATISTICS. It is desirable to collect about 10^6 counts in the whole spectrum: this gives a relative s.d. of $<1\%$ for concentrations above a few %, and a detection limit (3 s.d. of background) below 0.1% (except Na). Instrumental factors usually limit count-rate to $\sim 10^4$ counts/s, thus the analysis time is typically about 2 minutes.

DEAD TIME. E.D. systems have a large dead time (e.g. 40 μ s), and the count-rate for different specimens may vary considerably. The conventional 'live time' clock corrects the total spectrum for dead-time losses, but an additional correction is required to correct peak intensities for the counts displaced to a higher energy by pile-up (coincidence). This can be done electronically, but each system should be tested for linearity over the intended range of count-rates.

PILE-UP. Electronic pile-up rejection eliminates most of the spurious coincidence pulses which would otherwise appear in 'sum peaks'. However, very close coincidences cannot be detected, also part of the spectrum generally falls below the threshold of the rejection system (e.g. ~ 1.25 keV). Thus sum peaks still appear if too high a count-rate is used, and errors may occur when a sum peak is close to a characteristic peak. In principle sum peaks could be removed mathematically, but this is difficult to do rigorously.

ESCAPE PEAKS. Si escape peaks can cause errors similarly. The escape peak intensity is in the range 0.1-1% of the parent peak (1,2). Escape peaks can be stripped from the recorded spectrum channel by channel as a preliminary step in spectrum treatment (3).

COUNT-RATE LIMITATIONS. Peak shift and broadening are liable to occur at high count-rates, and are undesirable in quantitative analysis. Such effects can be tolerated within limits if each spectrum is recalibrated on the basis of the position of known peaks, but otherwise only about 10 eV shift and 2 eV broadening is acceptable, and the working count-rate should be chosen with this in mind. Peak shift and broadening can also be caused by extraneous influences (e.g. microphonics), which should be guarded against.

SPECTRUM STRIPPING. In quantitative analysis we wish to extract from the spectrum (consisting of the accumulated counts in each channel) the intensity (area) of each peak of interest, free from the influence of overlapping peaks, continuum background, and instrumental artefacts. Conventional 'ZAF' corrections are then applied, as in W.D. analysis.

K α OVERLAP. At low Z (<18) overlap between adjacent K α peaks is significant, though with good detector resolution (<180 eV at 5.9 keV) the effect is not too serious and can be corrected by one of the following methods.

OVERLAP COEFFICIENTS. Raw peak intensities can be obtained simply by summing the counts in groups of channels straddling the peaks. Overlap can then be calculated by means of coefficients representing the fraction of each peak that 'spills over' into the adjacent peak (3,4). The coefficients may be determined empirically (e.g. by measuring the Mg K α intensity above background on a pure Al specimen). The observed peak intensities in the 'unknown' spectrum are corrected iteratively. In general the correction is only important for elements differing by one in Z, but the 'shelf' which occurs on the low energy side of the peak owing to incomplete charge collection in the detector results in detectable overlap for atomic numbers 2 or 3 below the element in question (4). This method has been extensively tested on silicates (5).

Overlap coefficients may be calculated, given a suitable peak-shape function. The simple gaussian function is scarcely adequate on account of the low energy shelf, and more complicated expressions are preferable (6). It should be noted that the form of the shelf varies from detector to detector. Also the calculated peak shape should take into account any broadening that occurs as a function of count-rate.

ITERATIVE SPECTRUM STRIPPING. In this method a gaussian or other suitable peak function, scaled according to the estimated peak height, and assigned a width appropriate to the energy concerned, is subtracted channel by channel from the recorded spectrum (7). Each peak is treated thus in turn, and the whole procedure is repeated until no detectable peaks remain. The estimate of peak height can be obtained by subtracting from the sum of the counts in a group of channels centred on the peak the sum of an equal number of channels disposed symmetrically on each side. When the difference is zero it is assumed that the peak has been completely stripped, and the amount taken away equals the required peak area. This method has the advantage of requiring no explicit background correction, given that the background is not strongly curved.

LEAST SQUARES FITTING. Another approach is to build up a synthetic spectrum by adding together contributions from all the elements present and obtaining the least squares best fit to the recorded spectrum. The pure element spectra may be calculated or empirical, the advantage of the latter being that instrumental characteristics are taken into account automatically. In the case of silicate analysis pure oxide spectra may be used (8). It is desirable to limit the fitting procedure to the relevant parts of the spectrum and ignore the smooth (continuum) regions (9). This method has been applied successfully to complex spectra of sulphides containing heavy elements (10). Least squares fitting using pure element spectra is not strictly rigorous with respect to the continuum background, but in practice this is usually not a serious drawback.

K β OVERLAP. In some procedures K β peaks are taken into account automatically (e.g. if experimental pure element spectra are used to synthesise the spectrum). Alternatively it is possible to generate synthetic K β peaks for fitting or stripping, given the K β /K α intensity ratio, which is now known

more accurately than hitherto (11,12). Strictly the difference in absorption of K_{β} and K_{α} radiation should be taken into account, though usually the effect of this is small. Whatever correction method is used a large K_{β} peak inevitably reduces the accuracy and raises the detection limit of the interfered-with element. Elements around $Z=24$ are worst affected.

L AND M SPECTRA. Specimens containing heavy elements ($Z > 30$) present additional difficulties on account of the greater complexity of L and M spectra and the greater probability of interference. However, in principle the methods described can be extended to cope with this.

BACKGROUND. The continuum background is much more important than in conventional (W.D.) analysis, firstly because of the relatively low peak to background ratio, and secondly because it is often difficult to find regions of the spectrum truly representative of the continuum in order to measure background, especially at low energies where the peaks are crowded (e.g. Na-Mg-Al-Si). Some procedures (iterative stripping, least squares fitting) automatically take account of background, though not with complete rigour.

FREQUENCY FILTERING. This is another technique which does not require explicit correction for background. The component of the spectrum with low spatial frequency (background) is filtered out leaving the peaks, which have a relatively high frequency content (13). Limitations of this, and other, techniques are discussed in detail by Statham (7). It has not been shown that frequency filtering is comparable with other methods for quantitative analysis in difficult cases such as a small peak lying between two large ones.

CALCULATION OF CONTINUUM SHAPE. If the shape of the continuum is known, the background at any point can be estimated, given a measured value at a point where there are no peaks. Empirical background formulae can be used (14,15), or the shape can be calculated from first principles, for example using Kramers' law with factors for absorption in the specimen itself, the detector window, and dead layer (16). Closer fits have been obtained with modified versions of Kramers' law (17,18,19). Recent theoretical work shows that Kramers' law underestimates the continuum intensity at low energies, and modified expressions have been proposed (20,21). Also the depth distribution of continuum production in the specimen is not the same as for characteristic X-rays, and a modified absorption correction is required (20,21). In the case of thin (EM) specimens continuum formulae for thick specimens are not suitable.

BACKGROUND AS A FUNCTION OF Z. An alternative procedure for background subtraction is to use the spectrum from a reference standard to give the shape, and apply a scaling factor to allow for differences in Z . For example carbon, in the form of graphite or diamond, gives a spectrum free of peaks which may be used as the reference spectrum (4,8). According to Kramers the continuum intensity is proportional to Z , but more recently it has been shown theoretically to vary as $Z^{1.2}$ to $Z^{1.37}$ (22,23) and experimental work has confirmed the inadequacy of Kramers' law in this respect (4,24). It is desirable to allow for the different self-absorption in standard and specimen though sometimes this step is omitted (8).

'NO STANDARDS' ANALYSIS. In conventional (W.D.) analysis it is necessary to have a standard for each element and refer all peak intensities from the specimen to those from the standards. This approach is also commonly used in E.D. analysis, but owing to the good day-to-day stability obtained with a correctly functioning E.D. system it is necessary to refer to the standards much less frequently. With a constant probe current quantitative analysis

can in principle be carried out using stored calibration factors, obviating the need to record standard spectra every day. In practice it is desirable to use a standard of some kind to allow correction for minor day-to-day changes in instrumental conditions (25). For minor elements it is sometimes convenient to make use of the fact that the sensitivity of the detector is a smoothly-varying function of Z, allowing calibration factors to be interpolated, thereby avoiding the need for any standard at all for such an element(4).

REFERENCES.

1. Reed, S.J.B.: J.Phys.E 5, 582 (1972).
2. Dyson, N.A.: Nucl.Instr.Meth. 114, 131 (1974).
3. Reed, S.J.B. & Ware, N.G.: X-ray Spectrom. 2, 69 (1973).
4. Smith, D.G.W.: 10th M.A.S. Conf. (1975).
5. Reed, S.J.B. & Ware, N.G.: J.Petrol. 16, 499 (1975).
6. McNelles, L.A. & Campbell, J.L.: Nucl.Instr.Meth. 127, 73 (1975).
7. Statham, P.J.: X-ray Spectrom. 5, 16 (1976).
8. Gehrke, R.J. & Davies, R.C.: Anal. Chem. 47, 1537 (1975).
9. Schamber, F.H.: 8th E.P.A.S.A. Conf., paper 85 (1973).
10. Corlett, M.I. & McDonald, M.: 9th M.A.S. Conf., paper 23 (1974).
11. Smith, D.G.W., Reed, S.J.B. & Ware, N.G.: X-ray Spectrom. 3, 149 (1974).
12. Slivinsky, V.W. & Ebert, P.J.: Phys.Rev. A5, 1581 (1972).
13. Russ, J.C.: 7th E.P.A.S.A. Conf., paper 76 (1972).
14. Plant, G. & Lachance, G.: 8th E.P.A.S.A. Conf., paper 13 (1973).
15. Short, J.M.: Proc.IITRI SEM Conf., 106 (1973).
16. Ware, N.G. & Reed, S.J.B.: J.Phys.E 6, 286 (1973).
17. Lifshin, E.: 9th M.A.S. Conf., paper 53 (1974).
18. Lifshin, E., Ciccarelli, M.F. & Bolon, R.B.: in Practical Scanning Electron Microscopy (ed. J.Goldstein & H.Yakowitz), Plenum, New York, p.263 (1975).
19. Fiori, C.E., Myklebust, R.L., Heinrich, K.F.J. & Yakowitz, H.: Anal.Chem. 48, 172 (1976).
20. Reed, S.J.B.: X-ray Spectrom. 4, 14 (1975).
21. Statham, P.J.: X-ray Spectrom., in press.
22. Rao-Sahib, T.S. & Wittry, D.B.: in Proc. 6th Internat. Conf. on X-ray Optics & Microanalysis (ed. G.Shinoda et al.), Univ. of Tokyo Press, p.131 (1972).
23. Rao-Sahib, T.S. & Wittry, D.B.: J.Appl.Phys. 45, 5060 (1974).
24. Smith, D.G.W., Gold, C.M. & Tomlinson, D.A.: X-ray Spectrom. 4, 149 (1975).
25. Russ, J.C.: 9th M.A.S. Conf., paper 22 (1974).
26. Cliff, G. & Lorimer, G.W.: J.Microsc. 103, 203 (1975).

A REVIEW OF THE VARIOUS USAGES OF ENERGY DISPERSIVE X-RAY ANALYSIS IN BIOLOGY

V.Mizuhira

Department of Cell Biology, Medical Research Institute, Tokyo Medical and Dental University, Yushima, Bunkyo-Ku, Tokyo 113, Japan

The electron microscope fitted with an electron probe X-ray microanalyzer is a unique method for detecting the fine distribution of elements in fine structure by using a very small electron beam spot. The characteristic X-ray energy or wave length of the element can be ascertained by the aid of energy dispersive or wave length dispersive X-ray detectors with an amplifier and a display system. The energy dispersive type, which is a nuclear diode Si-detector (NDS), has very high inherent efficiency in detecting X-rays as compared to the wave length dispersive type detector. The NDS type detector system analyzes the elements from sodium to uranium simultaneously within a very short time. These characters are very useful for biological applications, although NDS has some characteristic demerits which cause difficulty in the identification of superimposed spectra, as will be described later.

We have devised a new "analytical electron microscope" (AEM) for the same purpose. The AEM is basically composed of a JEM 100-C transmission electron microscope fitted with a scanning device (ASID-4), side-entry goniometer stage (SEG) and an energy dispersive type X-ray microanalyzing unit (EDAX-707B), as shown in Fig.1. The electron images are taken by the SEM, STEM and TEM electron images. Then a very small part of the image can be analyzed by a combination of the ASID and EDAX systems, such as spot X-ray pulses, line X-ray pulses and X-ray pulse image analysis superimposed on the original electron image (Figs. 5a, b; 7). SEM or STEM images are made with the accelerating voltage at 10 to 40 KeV, or sometimes 60 to 100 KeV, at $n \times 10^{-10}$ Amp(A). X-ray analysis is carried out at 10 to 40 KeV and $n \times 10^{-9 \sim 10}$ A. The specimens are tilted at 25° to 45° degrees using an SEG.

As basic experiments, we examined the S/N ratios which are the characteristic X-ray energy intensity versus the white X-ray intensity under various conditions. Judging from our basic experiments, the biological specimens must be supported on a carbon film deposited on a carbon grid or a carbon plate, and must be analyzed with a low accelerating voltage in the range of 10 to 40 KeV, as shown in Fig. 2.

As briefly noted above, sometimes it is necessary to separate the overlapping X-ray energy spectra, such as the Cd-L line and the U-M line; Sb-L and Ca-K; and, S-K and Hg-M or Pb-M lines. These X-ray lines overlap each other so perfectly that they can not be identified. We succeeded in identifying the overlapping spectra using computer system, the EDAX-707B-EDIT system, on the X-ray luminescence analyzer. In this experiment, we used mixed standard samples, cadmium chloride and uranyl acetate mixture; potassium antimonate and calcium chloride; and mercury chloride and ferric ammonium sulfate mixture. We succeeded in separating and identifying each element from the combined X-ray energy spectrum as shown in Figs. 3 & 4. In Fig.3, we found that an energy shift of approximately 40 to 60 eV to the right side was observed in the combined spectra in the case of Sb-L and Ca-K, and of Cd-L and U-M. But the original value was recovered after the subtraction procedure of the mixed elements (Fig. 4).

In some cases, we obtained improved colour analysis of the SEM or STEM images by superimposing the X-ray data on Kodak high speed Ektachrome film. For this, a combination of coloured plastic filter plates are used over a display cathode-X-ray tube, and to make a multiple exposure.

"Epon" is not the best embedding medium for it contains much chlorine. It is very important to find good embedding media as well as fixation methods for soluble ions. The glutaraldehyde-urea resin quick embedding method (Pease, 1972; Yarom, 1974) is very simple and requires only two hrs from fixation to polymerization. Of course, it does not contain chlorine or other elements. Since the procedure is very short and simple, a part of many light elements,

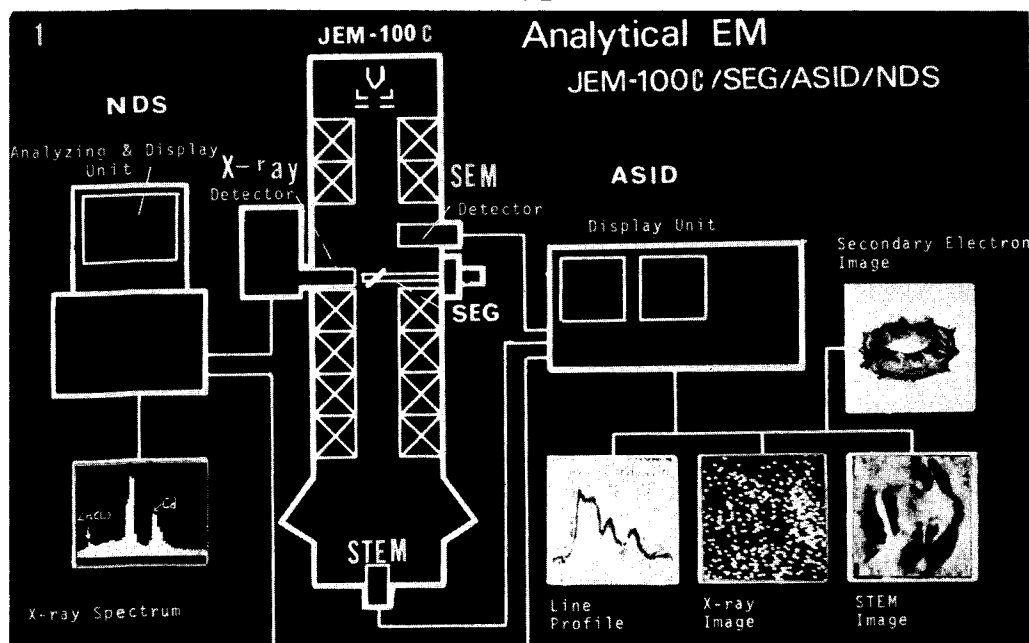


Fig. 1. Diagram of an analytical electron microscope

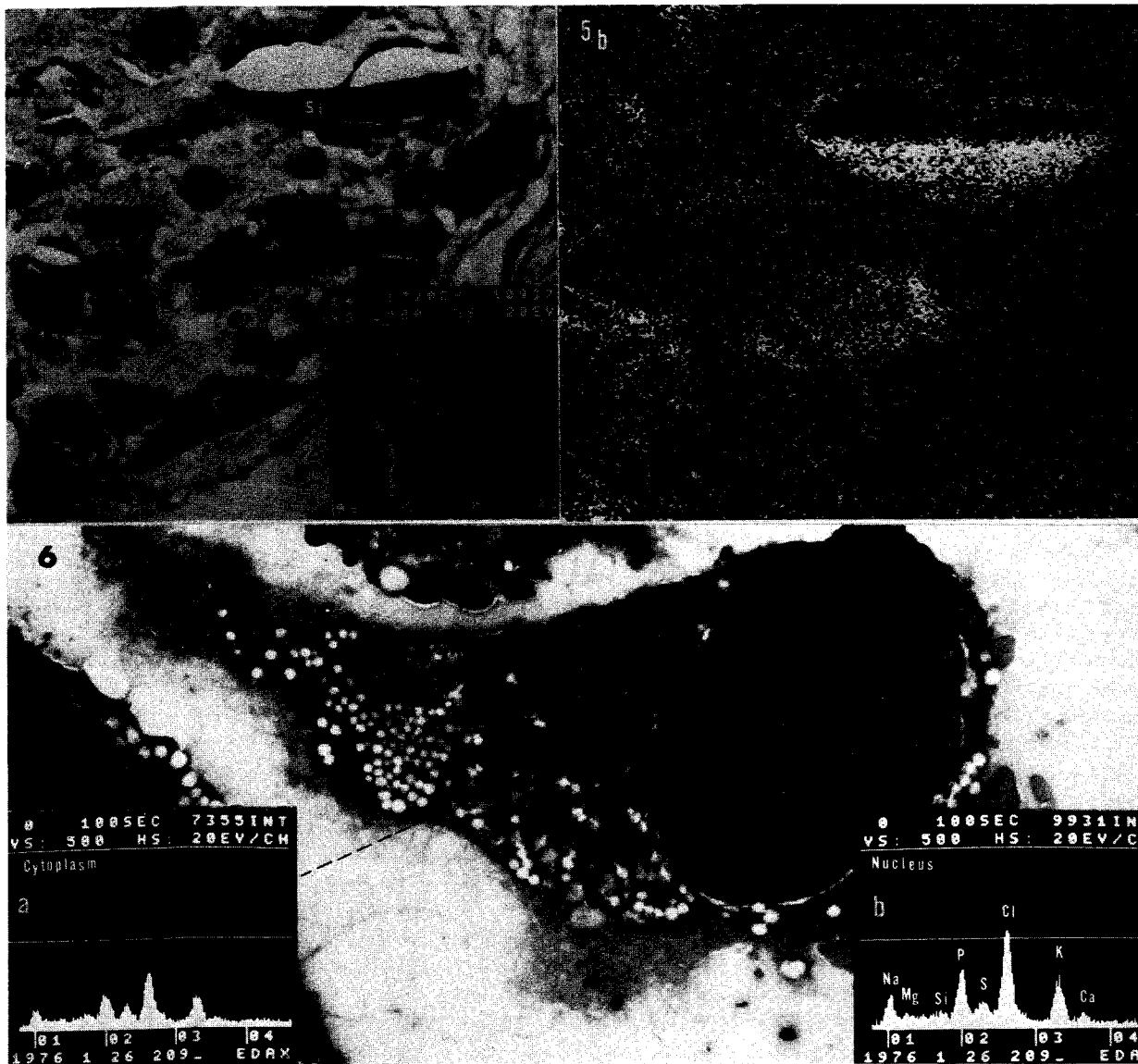
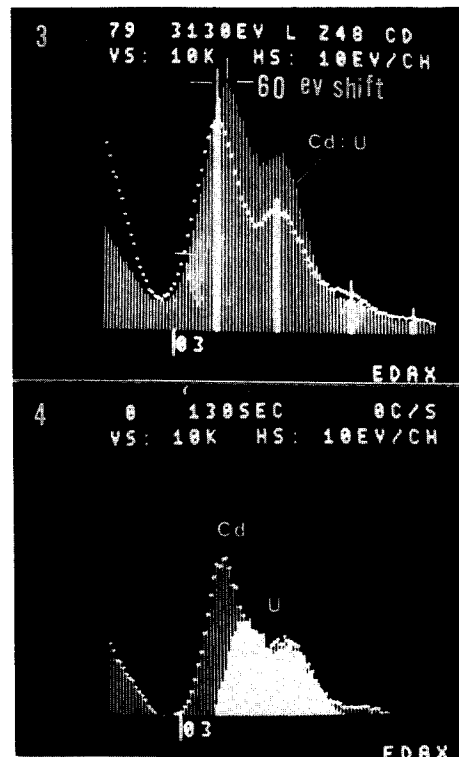
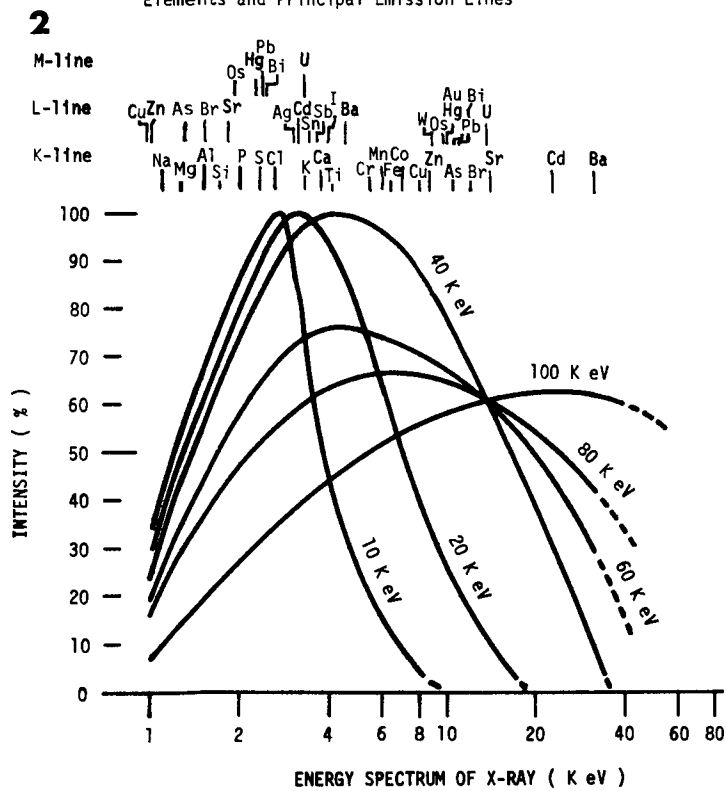
such as Na^+ , Mg^{++} , Cl^- , K^+ , or Ca^{++} remain in the embedded tissue section, although some technical problems are still encountered.

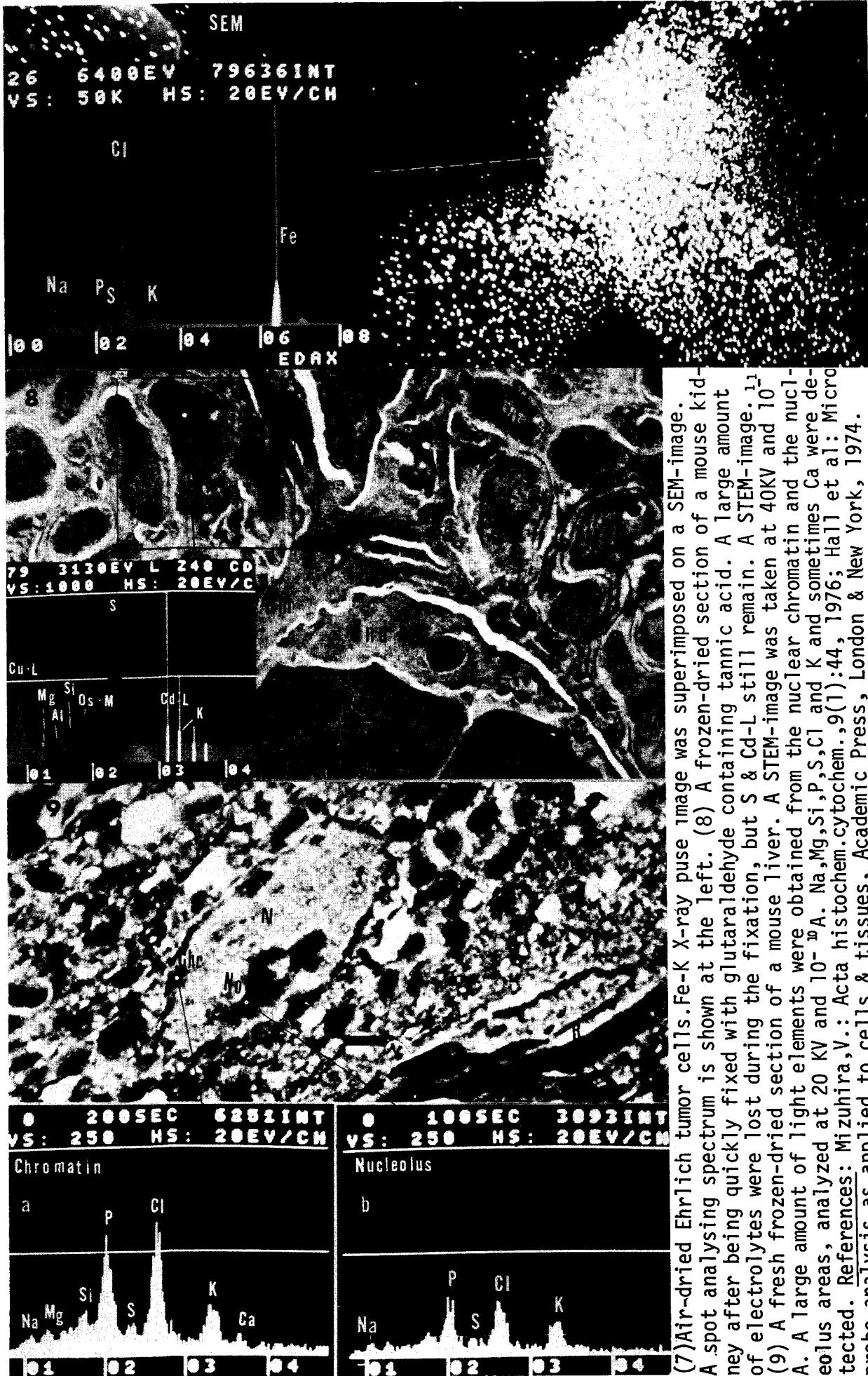
The best results with physiological electrolytes in biological samples can be obtained with fresh air-dried (Figs. 6 & 7) or fresh frozen-dried sections (Figs. 8 & 9). A speedily fixed (10 min) frozen-dried section was nearly as good as the fresh air-dried or fresh frozen-dried sections (Fig. 8), but a large amount of ions were lost during the short fixing procedure. We have improved the fresh frozen-dried sectioning method: the small pieces of fresh tissue are fixed with acrolein-gas for ten min, then they are touched to a copper rod at the temperature of liquid nitrogen.

The frozen tissue blocks are stored in the liquid nitrogen. The freed blocks are cut with an LKB-Cryokit at -70 to -100°C , mounted on a carbon film with a carbon grid, and then dried in a small container with a molecular sieve, gradually raising the temperature to room temperature. The dried sections are treated with osmium vapor for 10 min. Then the sections are analyzed after carbon coating, or directly analyzed with no osmium treatment.

These acrolein and osmium gas fixation methods promise good results in both cell fine structures and X-ray analysis. The STEM-image system is also very useful for obtaining good electron contrast in low contrast fresh frozen-dried sections. The conditions for obtaining a good STEM-image of low contrast fresh frozen-dried sections are found to be almost equivalent to the value of the accelerating voltage and the illuminating current for the X-ray energy detection. An accelerating voltage of 20 to 40 KeV at approximately $n \times 10^{-10} \sim 11$ A is required. Under this condition, the spot is not very small, about 1000 to 2000 \AA in diameter, compared to the size of the normal STEM-image spot. In the osmium-fixed and heavy-metal-stained sections, we can obtain very sharp and high resolution STEM-images at $n \times 10^{-13}$ A using a spot size of less than 100 \AA . If the experimental conditions are the same and constant, one can obtain a quantitative X-ray analysis of elements. It is also necessary to compare the various X-ray energy counts of the same element and the same nuclear lines (K, L, M). When a light element is combined with a heavy metallic element, such as in calcium antimonate, the X-ray counts of Ca-K will be increased by the excitation of the secondary or the scattered electron beam from the heavy element. It is necessary to make clear the correlation between the original X-ray counts and the additional secondary counts. It is very useful and helpful to obtain the quantitative results by the aid of a computer system, including the elemental identifications, as described above. At the present time, we supposed the final X-ray analysing resolution will be 10^{-13} m / spot size. Dr. Y. Futaesaku cooperated in this report.

Elements and Principal Emission Lines





THE APPLICATION OF ENERGY DISPERSIVE
ANALYSIS TO PROBLEMS IN MATERIALS SCIENCE
REQUIRING HIGH SPATIAL RESOLUTION

Eric Lifshin

General Electric Company
Corporate Research and Development
P.O. Box 8
Schenectady, New York 12301

The ability to perform chemical analysis at a submicron level is of great interest to the metallurgist and ceramist, for at this scale microstructural and compositional effects often profoundly influence the physical, chemical, and electrical properties of materials. Use of the electron microprobe analyzer was a dramatic step forward in microchemical analysis, but it is interesting to note that since its introduction in the fifties⁽¹⁾ the limit of one to two micron spatial resolution for quantitative analysis of polished bulk specimen has basically stayed the same. This restriction was first generally associated with electron beam size and the quality of scanning or coaxial light optical imaging systems. However, when the scanning electron microscope (SEM) became commercially available in the mid-sixties it was well recognized that even when extremely fine electron probes (200\AA) were used that the penetration and scattering of the electron beam within a specimen defined the volume of x-ray production. Numerous Monte Carlo calculations and experimental measurements demonstrated that at operating voltages consistent with reasonable peak to background ratios that this volume is rarely less than one micron.^(2,3,4) The question of x-ray signal strength was also raised because as an electron probe size diminishes the corresponding probe current decreases drastically⁽⁵⁾. Eventually a point is reached where the x-ray signal measured with a crystal diffraction spectrometer is too small to be measured over a time period compatible with instrument stability requirements.

In the late sixties, this difficulty was largely overcome with the introduction of energy dispersive spectrometers (EDS) on SEM's. Their high collection efficiency relative to crystal diffraction spectrometers and ability to measure all detectable energies, essentially simultaneously, made it possible to obtain reasonable x-ray spectra in a few minutes even at probe diameters less than 500Å. The penetration problem remained, however, and even unambiguous qualitative analysis of submicron structure requires that the sample consists of well separated particles on or in an innocuous background material. General examples include dispersed particles on carbon substrates or inorganic deposits in biological materials.^(6,7) An alternative approach which has been tried, when possible, is extraction replication. This technique is not easily used with all materials nor can it be applied to the study segregation effects.

It appears, therefore, that the examination of thin specimens may be the most desirable approach to fine structures analysis. Recently many combined transmission electron microscopes (TEM) and scanning transmission electron microscopes (STEM) have been equipped with EDS systems. These microscopes offer an excellent opportunity to combine high resolution imaging systems (50Å<) with selected area microdiffraction and elemental analysis capability. A major experimental difficulty with this approach, which can also occur with SEM's and electron microprobe analyzers, is the undesirable effects of electron beam scattering and the x-ray fluorescence of electron column components. The result is the excitation of nonselected regions of a specimen or the direct entrance of unwanted x-ray or electrons into the detector introducing spurious peaks in observed spectra.⁽⁹⁾ Furthermore, the issue of signal strength cannot be ignored, since a large percentage of 100kV or higher voltage electron probes penetrate the specimen without energy loss and consequently do not generate x-rays. It is clear that considerable research during the next few years will be directed at the utilization of higher brightness electron sources, the elimination of unwanted signals, and the development of new models for the quantitative analysis of thin films.

- 1) Castaing, R. (1951), PhD Dissertation, University of Paris.
- 2) Cosslett, V.E. and Thomas, R.N. (1966), The Electron Microprobe (J. McKinley et. al. editors), Wiley, New York, p 248.
- 3) Bishop, H.E. (1966) PhD Dissertation, Cambridge University.
- 4) Bolon, R.B. and Lifshin, E. (1973), Proceedings of the Sixth Annual Scanning Electron Microscope Symposium, IITRI, Chicago, p 285.
- 5) Smith, K.C.A. (1956), PhD Dissertation, University of Cambridge.
- 6) Maggiore, C.J. and Rubin, I.B. (1975), Proceedings of the Sixth Annual Scanning Electron Microscope Symposium, IITRI, Chicago, pp 129-135.
- 7) Coleman, J.R. (1975), Practical Scanning Electron Microscopy, (Goldstein, J. and Yakowitz, H., editors), Plenum, New York, pp 491-527.
- 8) Bolon, R.B. and McConnell, M.D., (1976), Proceedings of the Ninth Annual Scanning Electron Microscope Symposium, IITRI, Chicago, pp 163-170.

ELEMENTAL ANALYSIS OF THIN FILMS USING INNER SHELL ELECTRON ENERGY LOSSES

D. E. Johnson* and M. Isaacson**

*High Voltage Microscope Laboratory, Department of Zoology and Laboratory of Biophysics, University of Wisconsin, Madison, Wisconsin

**Department of Physics and the Enrico Fermi Institute, University of Chicago, Chicago, Illinois

The use of electron energy loss spectroscopy (ELS) for elemental analysis of thin films holds considerable promise. This technique has definite advantages in comparison with energy dispersive X-ray spectroscopy (EDS) for two fundamental reasons. First, the detection sensitivity is independent of the fluorescence yield, since for each inner shell excitation an energy loss electron exists as opposed to only a finite probability that an excitation will result in a X-ray emitted. Second, the information carrying energy loss electrons are contained in a small solid angle about 0° scattering angle as opposed to the resulting X-rays which are emitted uniformly over 4π steradians. This means that a large fraction of the energy loss electrons can be detected (up to ~90%) compared to only a small fraction (~1%) of the emitted X-rays with an EDS system.

In addition to the two fundamental differences between ELS and EDS indicated above, several practical aspects should also be noted. For example, background and extraneous peaks due to stray electrons striking pole pieces, specimen holders, etc. are not a problem for ELS since only electrons scattered into relatively small angles can enter the electron spectrometer. Also, with the high energy resolution possible in ELS (~0.5 eV) there is no problem distinguishing adjacent peaks and equally as important, fine structure can be observed at the leading edge of inner shell energy loss peaks providing information on chemical binding states. Finally, the use of higher incident electron energies (>50 kV) can be advantageous. Principally, as the energy of the incident electrons is increased, the collection efficiency for a given energy loss is increased due to smaller scattering angles. This then allows thicker specimens to be analyzed with increased sensitivity. On the other hand, for EDS, the sensitivity actually decreases for energies >50 kV. (1)

In an attempt to exploit the apparent potential of this energy loss elemental analysis technique several groups (2,3,4) are now continuing the original work of Hillier and Baker (5). Our own research in this field has concentrated in two main areas (6). First, we have developed the necessary formalism to describe elemental analysis using energy loss electrons and to predict for this technique, such quantities as the minimum detectable mass and the minimum detectable concentration. Our analysis predicts, for example, detection of concentrations of at least an order of magnitude smaller using ELS than using EDS. These predictions are for K-shell excitations and for elements of $Z < 20$. This same analysis also predicts minimum detectable masses of up to several orders of magnitude smaller using ELS than using EDS. For example, a minimum detectable

mass of 10^{-22} gms of carbon is predicted. Second, in an instrument with known limitations in collection efficiency, we have verified the basic correctness of the predictions for minimum detectable concentrations for all elements, Li through F. We have also detected masses as small as 10^{-20} gms. of carbon.

To fully confirm the usefulness of ELS for elemental analysis, considerable experimental work remains to be done particularly in an instrument designed specifically for ELS analysis (e.g. an electron spectrometer with large acceptance angle and a parallel data collection system). Two important areas being investigated are the use of L and M shell excitations of higher Z elements where the fluorescence yield is again very low, and the use of the increased sensitivity of ELS to allow elemental analysis at high spatial resolution ($<100\text{\AA}$) for example, in a field emission STEM.

1. Russ, J. C.: SEM/1976 (O. Johari and I. Corvin, eds.) (1976).
2. Wittry, D. B., Ferrier, R. P., and Cosslett, V. E.: Brit. J. Appl. Phys. 2, 1967 (1969).
3. Egerton, R. F., and Whelan, M. J.: Proc. 8th Int. Congress on Electron Microscopy, Canberra, 1, 384 (1974).
4. Colliex, C., and Trebbia, P.: Proc. EMAG Conf., Bristol (1975).
5. Hillier, J., and Baker, R. F.: J. Appl. Phys. 15, 663 (1944).
6. Isaacson, M., and Johnson, D.: J. of Ultramicroscopy 1, 33 (1975).

This work was supported in part by the Energy Research and Development Administration.

THE CALCULATION OF PURE ELEMENT X-RAY INTENSITIES FROM
EMPIRICALLY DERIVED EXPRESSIONS AND ITS APPLICATION
TO QUANTITATIVE SEM/EDS ANALYSIS

N.C. Barbi, D.P. Skinner, and S. Blinder
NL Industries/ ICD Division
Hightstown, N.J. 08520

INTRODUCTION

It has been demonstrated that the measured x-ray intensities from pure elements in an EDS system will give rise to a smooth curve when plotted as a function of atomic number for a given series of lines and analytical conditions¹. Moreover, these curves are reproducible. If the curves are modeled by mathematical expressions, one can scale the appropriate expression to account for intensity differences due to variations in incident beam current and calculate the required set of pure element intensities. The advantages of using such a technique are:

1. A complete set of high quality standards is not required since unavailable pure element intensities may be calculated from measurements made on other reliable pure element standards.
2. The time of analysis is considerably shortened. This can be a double advantage if the SEM exhibits short term instability. In some cases, only two measurements may be required (unknown and one standard), affording less opportunity for instability to occur during the analysis, compared to the normal multi-standard technique.

The disadvantage is a decrease in ultimate attainable accuracy due to:

- 1) a lack of perfection in the original curve fit on which subsequent calculations are based; and
- 2) slight variations of voltage and take-off angle, which would alter curve shape.

RESULTS

Figure 1 shows pure element intensity curves for K and L lines at 16kV and 41° take-off angle. Each curve fit has been split into two regions. The initial segment of the curves ($Z \leq 24$ for K lines; $Z \leq 47$ for L lines) is fit with an equation of the type:

$$I_i = C \frac{K_1}{K_2 - K_1} [\text{Exp} (-K_1(Z_i - Z_0)) - \text{Exp} (-K_2(Z_i - Z_0))]$$

Where I_i is the intensity for element with atomic number Z_i and K_1 , K_2 and Z_0 are constants.

For K Lines of $Z \geq 24$, a third degree polynomial is used and for L lines of $Z \geq 47$, a straight line is employed. Only standards of proven homogeneity (in composition and surface) were used to develop the curves. Table I shows the accuracy of prediction for K lines at 16kV over a five month period. Chromium was selected as a single standard and used to scale the expression for calculations of the new pure element intensities. The choice of chromium as a single standard for 16kV was based on its reliability (homogeneity) and the fact that it is the point of intersection of the two functions used to describe the data. Iron is used for a K line standard at 25 kV. It can be noted from Table 1 that the accuracy is generally better than 5%.

Curves have been derived for K and L lines at 15 and 25 kV (nominal) for carbon-coated and uncoated standards at 41° take-off angle. A standards calculation subroutine has been interfaced to Frame B² to perform quantitative or semiquantitative analysis. The option exists to calculate the scaling factor from any number of standards, or to bypass the subroutine to perform a normal multi-standard analysis. The subroutine logic is as follows:

1. Atomic number and intensities for each K and L line standard must be entered. Voltage, take-off angle and elements to be analyzed are passed to the subroutine from the main program.
2. A code must be entered to indicate whether standards (and unknown) are carbon coated or uncoated.
3. The subroutine then calculates, using the appropriate expression, an "old" value for each measured standard. The new input value and "old" calculated value are ratioed to provide a scale factor. In cases where more than one standard is used, an average scale factor is calculated.
4. Each expression is then multiplied by its corresponding scale factor and all required pure element intensities are calculated for the present analysis.

An example of results obtained on Type 304 stainless steel, using 26kV and Fe as a single K-line standard is given in Table II.

DISCUSSION OF RESULTS

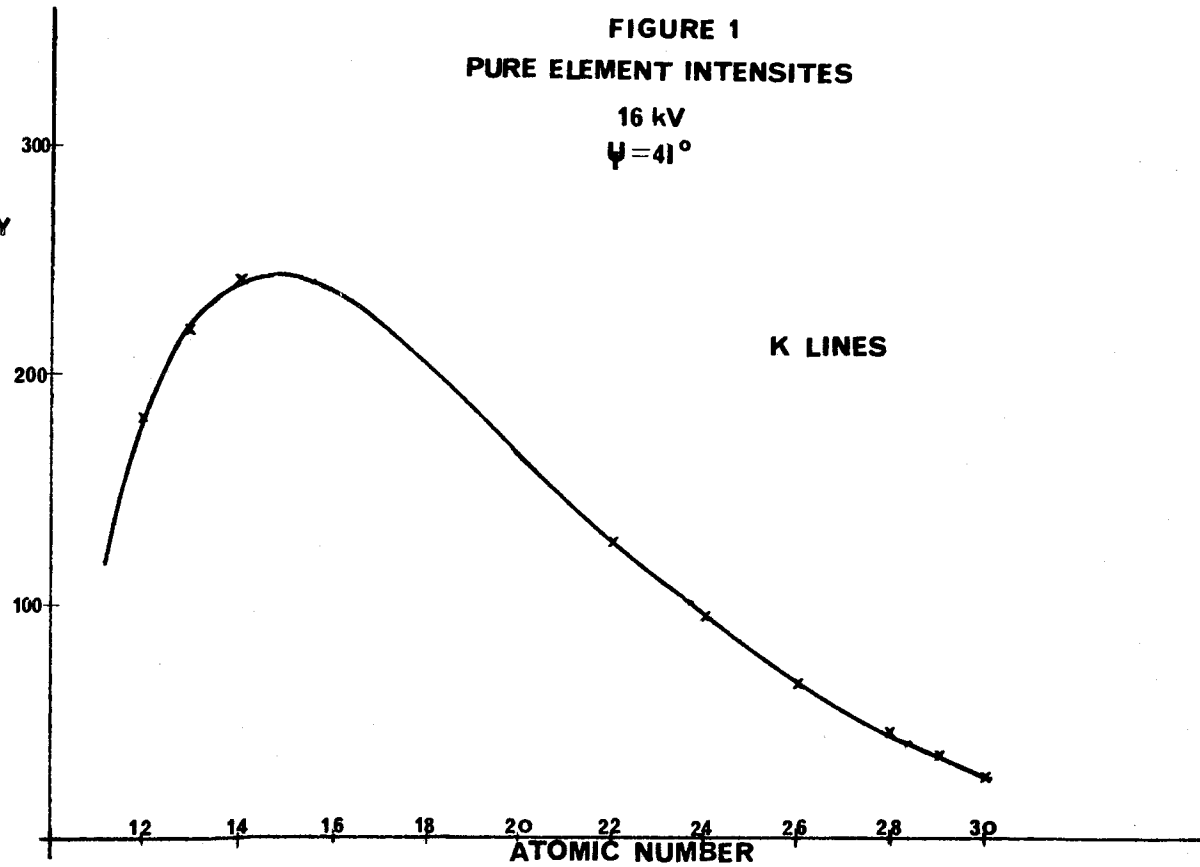
The empirical curves such as presented in Figure 1 can be predicted with reasonable accuracy on a theoretical basis³. This allows freedom in choice of accelerating voltage and take-off angle. However, the empirical technique, applied at two commonly used voltages such as 15 and 25 kV, should be more reliable for a specific microscope. Such parameters as detector efficiency and other constants need not be estimated, and certain other variables will cancel out with the empirical approach.

To check the curves in the critical region from $Z=14$ to $Z=22$, where no reliable standards were available, reverse calculation through the ZAF program is planned for appropriate compounds. The curves may then be modified for future analyses.

FIGURE 1
PURE ELEMENT INTENSITIES

16 kV
 $\psi = 41^\circ$

INTENSITY
 $\times 10^{-3}$



INTENSITY
 $\times 10^{-3}$

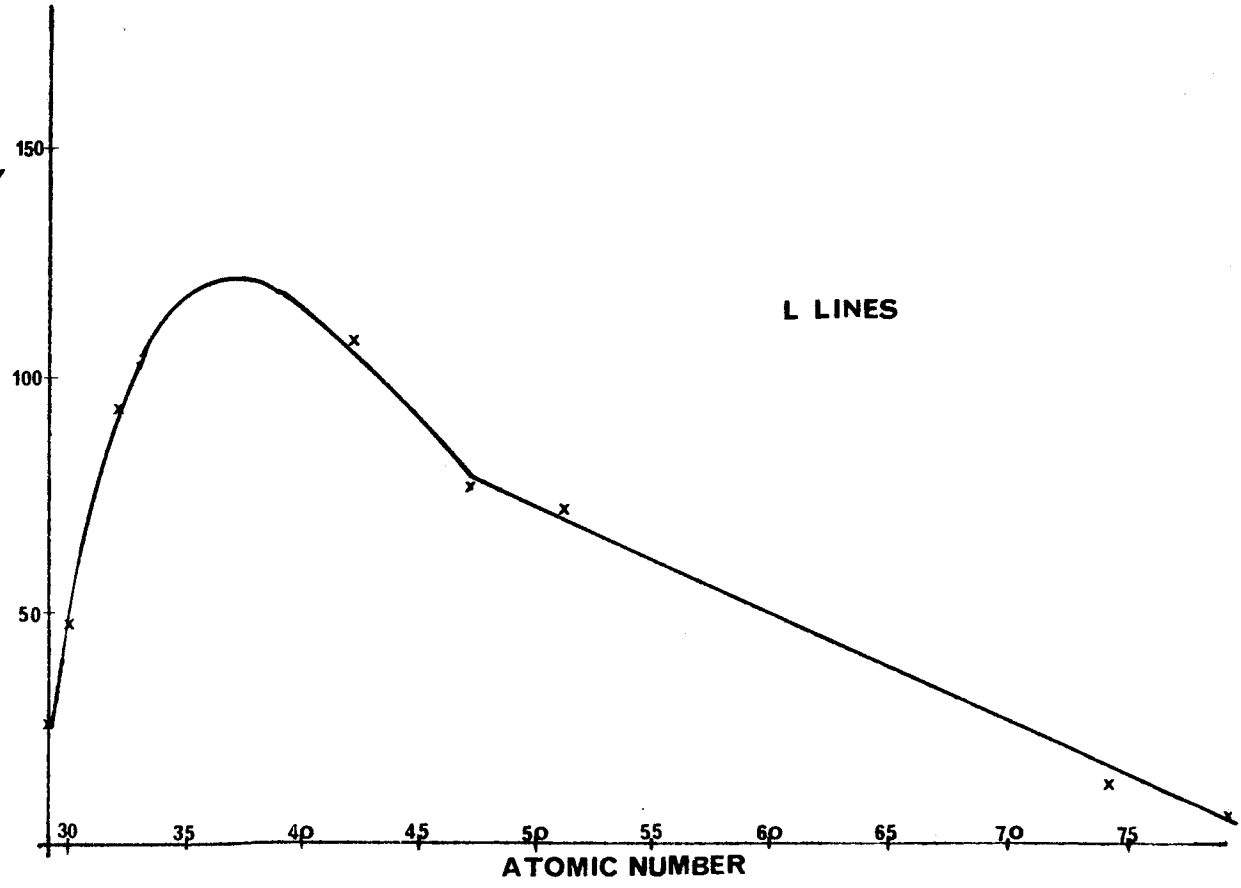


TABLE I

Reproducibility of the Pure Element Intensity Curve
at 16kV over a 5 Month Period*

<u>Z</u>	<u>THREE MONTH DATA</u>			<u>FIVE MONTH DATA</u>		
	<u>Calculated</u> <u>I(X10⁻³)</u>	<u>Measured</u> <u>I(X10⁻³)</u>	<u>Error (%)</u>	<u>Calculated</u> <u>I(X10⁻³)</u>	<u>Measured</u> <u>I(X10⁻³)</u>	<u>Error (%)</u>
12	254.6	249.5	2.0	137.0	140.7	2.6
13	317.1	299.5	5.9	169.3	177.4	4.6
14	344.8	334.7	3.0	184.5	191.6	3.7
22	182.7	185.6	1.5	99.3	99.9	0.6
24	-----USED FOR SCALING INTENSITIES-----					
26	93.9	95.3	1.4	50.2	50.6	0.8
28	61.9	63.3	2.3	33.1	32.7	1.2
29	48.2	50.6	4.7	25.8	25.9	0.4
30	35.3	35.8	1.5	18.8	18.8	0.0

* Empirical relationship derived 9/75; Three month data taken
12/75; Five month data taken 2/76.

TABLE II

Analysis of 304 Stianless Steel using Frame B and Fe
as a Single Standard at 25 kV

	<u>TRUE CONCENTRATION</u>	<u>CALCULATED CONCENTRATION</u>
Si	0.52	0.75
Cr	18.54	19.1
Mn	1.47	1.9
Fe	69.6	68.6
Ni	9.4	9.1

REFERENCES

- [1]. F. Blum and M.P. Brandt, "The Evaluation and Use of a Scanning Electron Microscope Combined with an Energy Dispersive X-ray Analyzer for Quantitative Analysis", X-ray Spectrometry, 2, 1973, 121-124.
- [2]. C. Fiori, R. Myklebust, K. Heinrich, and H. Yakowitz, National Bureau of Standards, Washington, D.C. Based on FRAME (NBS Tech. Note 796).
- [3]. J. Russ, "Quantitative Microanalysis with Minimum Pure Element Standards", Proceedings of the 9th Annual Conference, Ottawa, Canada, 1974, 22.

QUANTITATIVE ELEMENTAL ANALYSIS OF "TRANSPARENT" PARTICLES IN THE TEM

J. W. Sprys and M. A. Short

Technical Services, Engineering and Research Staff - Research,
Ford Motor Company

The quantitative elemental analysis of small particles can be performed in the transmission electron microscope by use of an energy dispersive X-ray detector and multichannel analyzer. As recently suggested by Cliff and Lorimer (1), Equation 1

$$I_1/I_2 = k_{1,2}(C_1/C_2) \quad (1)$$

is used to determine a calibration curve of X-ray intensities relative to silicon for the accurate chemical analysis of thin particles. In this equation, I_1 and I_2 are the measured characteristic X-ray intensities of the two elements in question, C_1 and C_2 are the weight fractions and k is a proportionality constant. Absorption, atomic number and fluorescence corrections in transparent particles are assumed to be negligible at an electron accelerating voltage of 100 keV.

When characteristic X-ray intensities of several elements are measured simultaneously with an energy dispersive system, the ratios of the intensities are independent of the electron beam current. Determination of a calibration or sensitivity curve relating the constant k of Equation 1 to the characteristic K, L and M X-ray energies of the elements allows the calculation of the concentration ratios of elements present in a material of unknown composition. Cliff and Lorimer show a curve for k as a function of the energy of the K_α radiation of elements up to zinc. The purpose of the present work is to extend the K curve and to include data relating k to the L and M characteristic X-ray energies of the elements up to lead. As in the earlier work, the thickness of the materials used to obtain these curves was within the limits outlined by Cliff and Lorimer, but differed in that many standards (mainly silicides) were used instead of a series of minerals.

Measurements were made using a Philips EM 300 electron microscope equipped with a goniometer stage, a Kevex lithium drifted silicon detector and amplifier and a Northern NS 750 multichannel analyzer. Each standard material was crushed and ground and dispersed on carbon films prepared on nylon grids. A specially designed sample holder, described elsewhere (2), which gave no extraneous radiation was used to support the sample being examined. Characteristic radiations were obtained using 100 keV electron excitation and variable beam currents. All particles contributing to the data were visibly transparent to 100 keV electrons and no particles larger than 0.1 microns in projected cross section were used. All data points were obtained from particles of compounds of silicon with the exception of the point obtained for lead. The point for lead was obtained mathematically from Equation 2

$$k_{Pb,Si} = k_1 \times k_2 = \left(\frac{C_{Cr}}{C_{Si}} \cdot \frac{I_{Si}}{I_{Cr}} \right) \times \left(\frac{C_{Pb}}{C_{Cr}} \cdot \frac{I_{Cr}}{I_{Pb}} \right) \quad (2)$$

using the k_1 obtained for a $CrSi_2$ compound and the k_2 obtained for $PbCrO_4$.

A part of the results of this work is shown in Figure 1. An initial duplication of the curve obtained by Cliff and Lorimer indicated close agreement between their results obtained using minerals and data obtained by us using

silicides. Additional points for K radiation were found and curves for L and M characteristic radiations were determined. These curves have been used to analyze particulate materials.

REFERENCES

1. G. Cliff and G. W. Lorimer, "The Quantitative Analysis of Thin Specimens," Journal of Microscopy, Vol. 103, Pt. 2, March, 1975, pp. 203-207.
2. J. W. Sprys, "Specimen Holder for Energy Dispersive X-Ray Analysis in the Transmission Electron Microscope," Rev. Sci. Instrum., Vol. 46, No. 6, June, 1975, pp. 73-74.

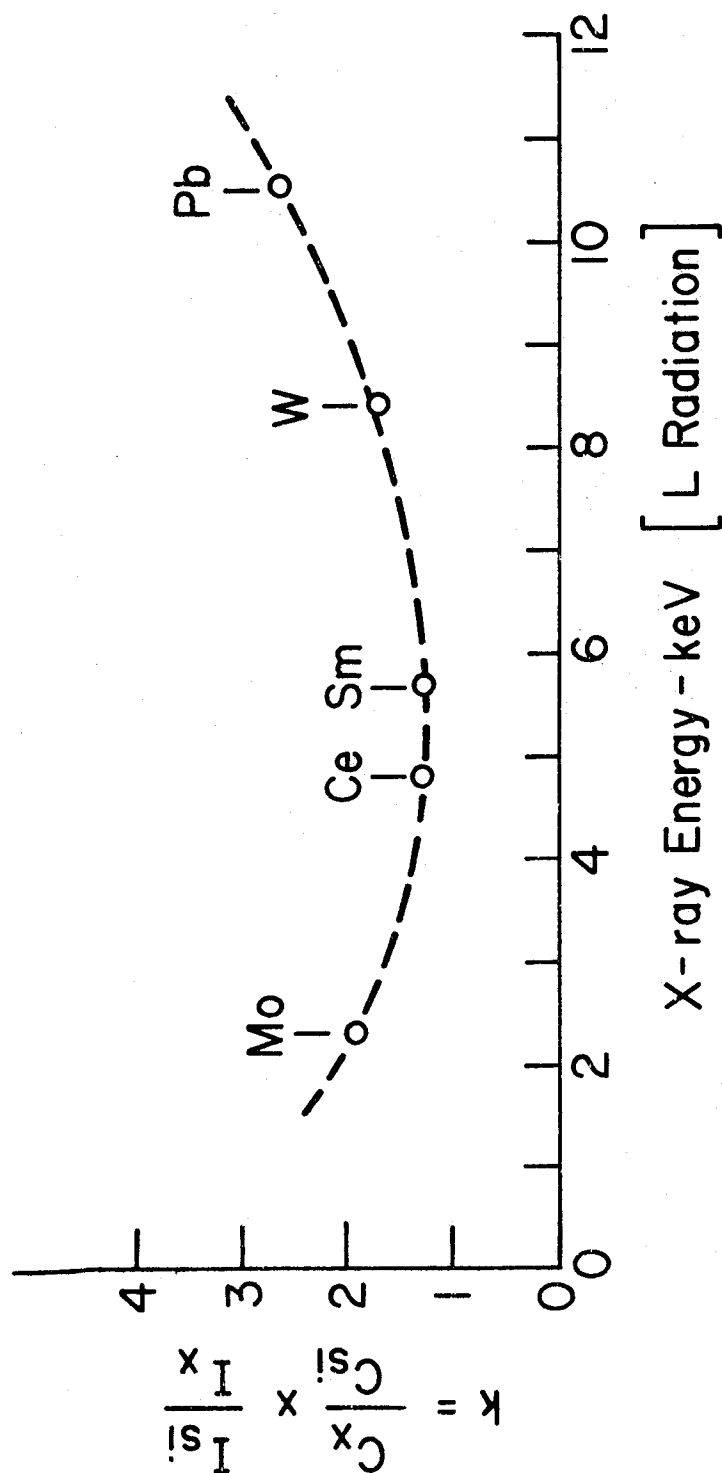


Figure 1. k as a function of L characteristic X-ray energy.

CORRECTIONS FOR THE BREMSSTRAHLUNG BACKGROUND
IN EDS MICROPROBE ANALYSIS OF THICK SPECIMENS

Peter Statham

Dept. Electrical Engineering & Computer Sciences,
University of California, Berkeley.

ooo00ooo

In this presentation, emphasis will lie in 'explicit' procedures which involve subtraction of a suitably-shaped curve from the spectrum. The distinction is drawn with 'implicit' techniques which reduce the influence of the background by some mathematical device in the course of peak deconvolution, as discussed in ref.1 .

In an attempt to clarify some of the remarks below, the background $B(E)$ at an energy E is considered as the sum of a number of components but parameters like the detector solid angle are ignored when they only produce a uniform scaling of the whole spectrum and do not affect the shape of the background:

$$B(E) = e_d \cdot l_q [D (I_{E,\theta} \cdot f(\chi)_{\text{cont.}} + I_{\text{stray}}) + I_w] + P_n + S_q$$

The heart of this expression is the bremsstrahlung intensity, $I_{E,\theta}$, which is affected by backscatter and is anisotropic (there is also a slight effect produced by the conductive carbon coating). The absorption correction $f(\chi)$ is similar to that for characteristic radiation but is slightly smaller. The remaining components represent instrumental deficiencies which are not all necessarily significant in a given system. I_{stray} is stray radiation which is generated by backscattered electrons and fluorescence; its influence is noted by Rao-Sahib and Wittry (ref.2) and it may be reduced by careful collimation and by coating the excited surfaces with a low Z material such as graphite. D is the attenuation caused by the detector entrance window; since the constituent layers of beryllium, gold and silicon are unlikely to be of uniform thickness (z_i), for a detector of active area A ,

$$D = \int_x \int_y [\sum_i \exp(-\mu_i^0 z_i)] dx dy / A$$

In the energy range below 10keV, the possibility of an x-ray photon passing right through the detector is negligible so there is only one attenuation term shown here. I_w represents bremsstrahlung excited within the entrance window by backscattered electrons; it typically represents a few percent of the observed continuum (ref.3) and is most significant at low energies. e_d is the efficiency of pulse detection; in the presence of noise there is the chance that a pulse may sit on a negative noise pulse, thus failing to reach the threshold, and the probability is greater for small pulses (e.g. see ref.4). l_q represents non-linearity in the detector response produced for example by the escape effect. P_n accounts for the 'continuum' produced by pile-up and also for any electronic distortion. S_q represents the effects of poor charge collection in the detector which are manifest as 'escape peaks' and a 'shelf' or low-energy tail below each major peak in the spectrum.

The somewhat bewildering array of instrumental effects would seem to make accurate prediction virtually impossible but with the incorporation of additional empirically-determined variables, theoretical formulae can be used as a basis for the background function. However, it is still usually necessary for the user to do a number of experiments to find the necessary parameters and this is something of a disadvantage.

PUBLISHED FORMULAE

Ware and Reed(ref.5) use the expression

$$B(E) \propto \frac{(E_0 - E)}{E} \cdot f(\chi)_{\text{char.}} \exp(-\sum_1 \mu_i \rho_i z_i) + F(E) \quad 1.$$

and find that $F(E)$ is sufficiently independent of specimen composition in silicate minerals that it can be determined at discrete peak positions for all elements in a once-off calibration procedure. In an attempt to remove the 'fudge factor' $F(E)$, Lifshin(ref.6) proposes

$$B(E) \propto \frac{(a(E_0 - E) + b(E_0 - E)^2)}{E} \cdot f(\chi)_{\text{char.}} \exp(-\sum_1 \mu_i \rho_i z_i) \quad 2.$$

This has the advantage that, after correcting for absorption, the parameters a and b can be found for any spectrum by fitting to two peak-free background points, as shown by Fiori et al (ref.7), and no calibration procedure is required. However, in both methods(1) and (2), the detector window thickness parameters have to be optimised so that the remaining degrees of freedom ($F(E)$ or a & b) can satisfactorily correct for instrumental deficiencies and inaccuracies in the theory. Furthermore, peak-free background points are not trivial to find and sum peaks (e.g. (AlK+AlK), (MgK+SiK) are close to argon K position) and peak tailing (S above), complicate the selection. Smith et al (ref.8) get round these difficulties by using the ratio of spectra (to eliminate D) and devising an automatic method for scaling which uses the full spectrum (this does however require that the full spectrum be calculated which takes time). Their method still involves a fairly extensive calibration procedure, in which the exponent n in the expression

$$\frac{B(E)_1}{B(E)_2} = \frac{Z_1^n}{Z_2^n} \cdot \frac{f(\chi)_1}{f(\chi)_2} \cdot \frac{R_1}{R_2} \quad 3.$$

is determined as a function of E and E_0 , and as such bears some similarity with Ware and Reed's technique where $F(E)$ is in fact tabulated rather than fitted to a function.

Their is no doubt that the expressions (1), (2) and (3) are very useful for background corrections but invariably, some skill is required by the user in order to implement them: optimisation of the window thickness parameters is required in (1) and (2), detailed fitting is required in (3) and calibrations are required for (1) and (3). It would thus be convenient if Ware and Reed's $F(E)$ and Smith et al's n were in fact universally applicable. Unfortunately, $F(E)$ depends on the window attenuation term and both $F(E)$ and n correct for instrumental effects and are somewhat sensitive to geometry, so this is unlikely.

ABSORPTION AND ANISOTROPY

In all the above methods, the $f(\chi)$ has been derived from formulae applicable to characteristic radiation although all authors acknowledge that the continuum absorption correction should be (slightly) different. Furthermore, anisotropy is usually ignored because random scattering in a thick sample would be expected to make the bremsstrahlung spectrum insensitive to geometry. Monte Carlo calculations have been performed (ref.3) to indicate the extent to which these assumptions are valid.

The results of absorption correction calculations are shown in table 1 ; the ratio of correction factors for continuum and characteristic radiation is computed because this can be done to high accuracy and if the characteristic correction is known then the continuum correction can be obtained. The final column in table 1 shows that the ratio of two 'Philibert type' formulae predicts the ratio to within 2% in all cases i.e.

$$\frac{f(\chi)_{\text{cont.}}}{f(\chi)_{\text{char.}}} = \frac{(1 + \chi/\sigma_2)(1 + \frac{h}{1+h} \chi/\sigma_2)}{(1 + \chi/\sigma_1)(1 + \frac{h}{1+h} \chi/\sigma_1)} \quad 4.$$

where $\sigma_1 = \frac{4 \times 10^5}{E_o^{1.65} - E_c^{1.65}}$, $\sigma_2 = \frac{4.5 \times 10^5}{E_o^{1.65} - E_c^{1.65}}$ and $h = 1.2 \left(\frac{A}{Z^2} \right)$.

(The use of the reduced σ value for $f(\chi)_{\text{cont.}}$ was suggested by Reed(ref.9) following a single calculation and the results in table 1 show the prediction to be quite good in general as it turns out.) The continuum absorption factors at 1.5keV for Ti, Mn and Cu specimens are respectively 0.4, 0.3 and 0.2. $f(\chi)_{\text{cont.}}$ is roughly 5% less than $f(\chi)_{\text{char.}}$ for $f(\chi)=0.5$ and roughly 10% less for $f(\chi)=0.2$. With these facts in mind it is clear that the empirical parameters in formulae (1), (2) and (3) and optimisation of window thickness parameters must implicitly correct for inaccuracies in the $f(\chi)$ expression. If $f(\chi)_{\text{cont.}}$ is to be computed using the ratio in eqn.4, $f(\chi)_{\text{char.}}$ should be found using a formula which is better than the Philibert expression for small $f(\chi)$ (e.g. the Andersen and Wittry formula which is implemented by Rao-Sahib and Wittry in ref.2).

The results for anisotropy are shown in fig.1 for two geometries: normal incidence, 40° T.O.A. (e.g. electron microprobe) and 45° incidence, 45° T.O.A. (e.g. S.E.M.). What is most important about these results is that it appears that with a change in geometry, the intensity distribution may alter by typically 5 to 10% across the energy range 1 to 10keV. The implication is that the empirical parameters in (1), (2) and (3) may not be universally applicable, even if all instrumental deficiencies are eliminated, because of the dependence on geometry.

IMPROVED THEORETICAL PREDICTIONS

Calculations on the bremsstrahlung intensity from a thick specimen have now been performed by a number of authors (refs.2,3,9,10,11,12) and the general conclusion is that the Kramers' expression, $Z(E_o - E)/E$, is incorrect as regards the shape of the continuum. Reed(ref.9) suggests that $(E_o - E)/E^{1.21}$ is an improvement for E_o between 15 and 20keV and Z between 13 and 29 and this type of modification has been extended(ref.3) to account for variations in Z and geometry so that the complete

theoretical prediction is

$$B(E) \propto D \cdot \frac{(E_o - E)}{E^{1+a+b}} \cdot f(\chi)_{\text{cont.}} \quad 5.$$

with a and b given by table 2 (note that the backscatter correction is contained within the intensity expression and a and b are not the same as in eqn.2). The comparison of (5) with experiment is shown in fig.2. There is clearly a marked improvement over equation(1) (without the F(E) factor) although the agreement is imperfect below 3keV. This feature is commonly found with attempts to fit the background and is probably due mainly to inaccuracies in D and $f(\chi)_{\text{cont.}}$ (only the standard Philibert formula is used in fig.2). In order to eliminate D and reduce the dependence on $f(\chi)$, the ratio of two spectra can be predicted; just as in the usual style of microprobe analysis, a background spectrum can be used as a standard for comparison and as an added benefit, the effects of $e_d, I_q, I_{\text{stray}}$ and I_w are considerably reduced. Thus in fig.3 various 'standard' backgrounds are used to predict a number of specimen backgrounds on multiplication by

$$\frac{E_{\text{standard}}^{a+b}}{E_{\text{spec.}}^{a+b}} \cdot \frac{(1 + \chi/\sigma)(1 + \frac{h}{1+h} \chi/\sigma)}{(1 + \chi/\sigma)(1 + \frac{h}{1+h} \chi/\sigma)} \text{standard.} \quad 6.$$

where $\sigma = \sigma_1$ of eqn.4. The interfering characteristic peaks in the standard spectra would normally be removed by interpolation, but in the regions away from peaks the agreement is in general good to well within 10% of the background which corresponds to an absolute error of around 0.1% concentration in quantitative analysis.

CONCLUSIONS

It is very desirable to have a background correction which does not involve a great deal of preparation on the part of the user. The author of ref.3 obviously would say that equation 6 applied to a spectrum from a standard with \bar{Z} fairly close to that of the specimen (or a carbon spectrum as in ref.8) is the best way to generate the correct background shape. However, the equation is not perfect because a and b are only roughly determined, only $E_o = 20\text{keV}$ is covered and as mentioned above, a better expression for $f(\chi)_{\text{cont.}}$ could be obtained through use of the ratio (4) and a better $f(\chi)_{\text{char.}}$ formula. Nevertheless, the use of a background standard spectrum $f(\chi)_{\text{char.}}$ is highly recommendable and gives good results, even with the existing formula (fig.3). Smith *et al* (ref.8) handle some of the shortcomings but use $f(\chi)_{\text{char.}}$ instead of the more correct $f(\chi)_{\text{cont.}}$. It is probably impractical for the average user to do the sort of extensive fitting performed in ref.8 but if some investigators were to repeat this type of analysis using $f(\chi)_{\text{cont.}}$ a universal background correction could be devised for all users provided the following guidelines are followed:

1. Minimise $I_{\text{stray}}, I_w, P_n, S_q$ and evaluate contributions. Make sure conductive coating is thin and same thickness for all samples.
2. Correct all spectra for backscatter (ref.12) and with $f(\chi)_{\text{cont.}}$.

3. Find a formula $I(E, E_0, Z)$ which enables accurate prediction of ratios of spectra.
4. Publish $I(E, E_0, Z)$ together with the geometry for which it was obtained and the estimate of the instrumental deficiencies in 1.

The general user would then be responsible for minimising I_{stray} , I_w , P_n and S_q , using similar thickness carbon coatings on samples and recording a standard background spectrum with good counting statistics. By referring to $I(E, E_0, Z)$ in the literature for the relevant geometry, the spectrum for any specimen could be calculated to high accuracy.

This last outline is for a practical correction scheme which would be universally applicable. Although exact theoretical prediction of the intensity would be fundamentally attractive, uncertainties in radiation cross sections, electron retardation and D tend to limit the attainable accuracy. Without further basic information of this type, perhaps the best that can be expected is an expression like (1), with $(E_0 - E)/E^{1+a+b}$ instead of $(E_0 - E)/E$ for example, where the 'fudge' factor $F(E)$ is substantially reduced.

REFERENCES

1. P.J. STATHAM, X-Ray Spectrom. 5, 16 (1976).
2. T.S. RAO-SAHIB, D.B. WITTRY, J. Appl. Phys. 45, 5060 (1974).
3. P.J. STATHAM, paper submitted to X-Ray Spectrom. Jan. 1976.
4. K. KANDIAH, in Proc. 8th Nat. Conf. Electron Probe Analysis, New Orleans, paper 32 (1973), also chap. 24 in "Physical Aspects of Electron Microscopy and Microbeam Analysis", Eds. B. Seigel & D.R. Beaman, Wiley, 1975.
5. N.G. WARE, S.J.B. REED, J. Phys. E. 6, 286 (1973).
6. E. LIFSHIN, Proc. 9th. Ann. Conf. Microbeam Analysis Society, Ottawa, paper 53 (1974).
7. C.E. FIORI, R.L. MYKLEBUST, K.F.J. HEINRICH, H. YAKOWITZ, Anal. Chem. 48, 172 (1976).
8. D.G.W. SMITH, C.M. GOLD, D.A. TOMLINSON, X-Ray Spectrom. 4, 149 (1975).
9. S.J.B. REED, X-Ray Spectrom. 4, 14 (1975).
10. E. STORM, Phys. Rev. A 5, 2328 (1972).
11. D.B. BROWN, J.V. GILFRICH, M.C. PECKERAR, J. Appl. Phys. 46, 4537 (1975).
12. T.S. RAO-SAHIB, D.B. WITTRY, in Proc. 6th. International Conf. X-Ray Optics and Microanalysis, Eds. G. Shinoda et al, University Press, Tokyo, p.131 (1972).

TABLE 1

Element	Radiation Energy keV	AOI	TOA	Monte-Carlo	
				$\frac{f(\chi)_{xy}}{f(\chi)_{char}}$	$\frac{f(\chi)_{Ph}}{f(\chi)_{Ph}}$
Aluminium (Z = 13)	1.5	0°	40°	.986	.977
	2.0	0°	40°	.940	.921
	1.5	45°	45°	.988	.985
	1.6	45°	45°	.926	.913
Titanium (Z = 22)	1.5	0°	40°	.935	.928
	4.5	0°	40°	.994	.993
	5.0	0°	40°	.963	.966
	8.0	0°	40°	.985	.990
	4.5	45°	45°	.996	.995
	5.0	45°	45°	.970	.976
Manganese (Z = 25)	5.9	0°	40°	.995	.995
	6.6	0°	40°	.973	.977
	5.9	45°	45°	.997	.996
	6.6	45°	45°	.981	.985
Copper (Z = 29)	1.5	0°	40°	.902	.899
	3.0	0°	40°	.971	.964
	4.5	0°	40°	.987	.986
	8.04	0°	40°	.996	.996
	9.0	0°	40°	.979	.987
	8.04	45°	45°	.997	.997
	9.0	45°	45°	.986	.992
Gold (Z = 79)	2.12	0°	40°	.957	.955
	2.5	0°	40°	.918	.929
	2.12	45°	45°	.966	.967
	2.5	45°	45°	.935	.943

Comparison of the absorption correction $f(\chi)_{xy}$ for the continuum with that for characteristic radiation, $f(\chi)_{char}$.

The final column is computed using the formula in equation 4 where

$$\chi = \mu \operatorname{cosec} \psi$$

and $\operatorname{cosec} \psi = 1.556$ for normal incidence, 40° take-off-angle and $\operatorname{cosec} \psi = 1$ for 45° incidence, 45° T.O.A.

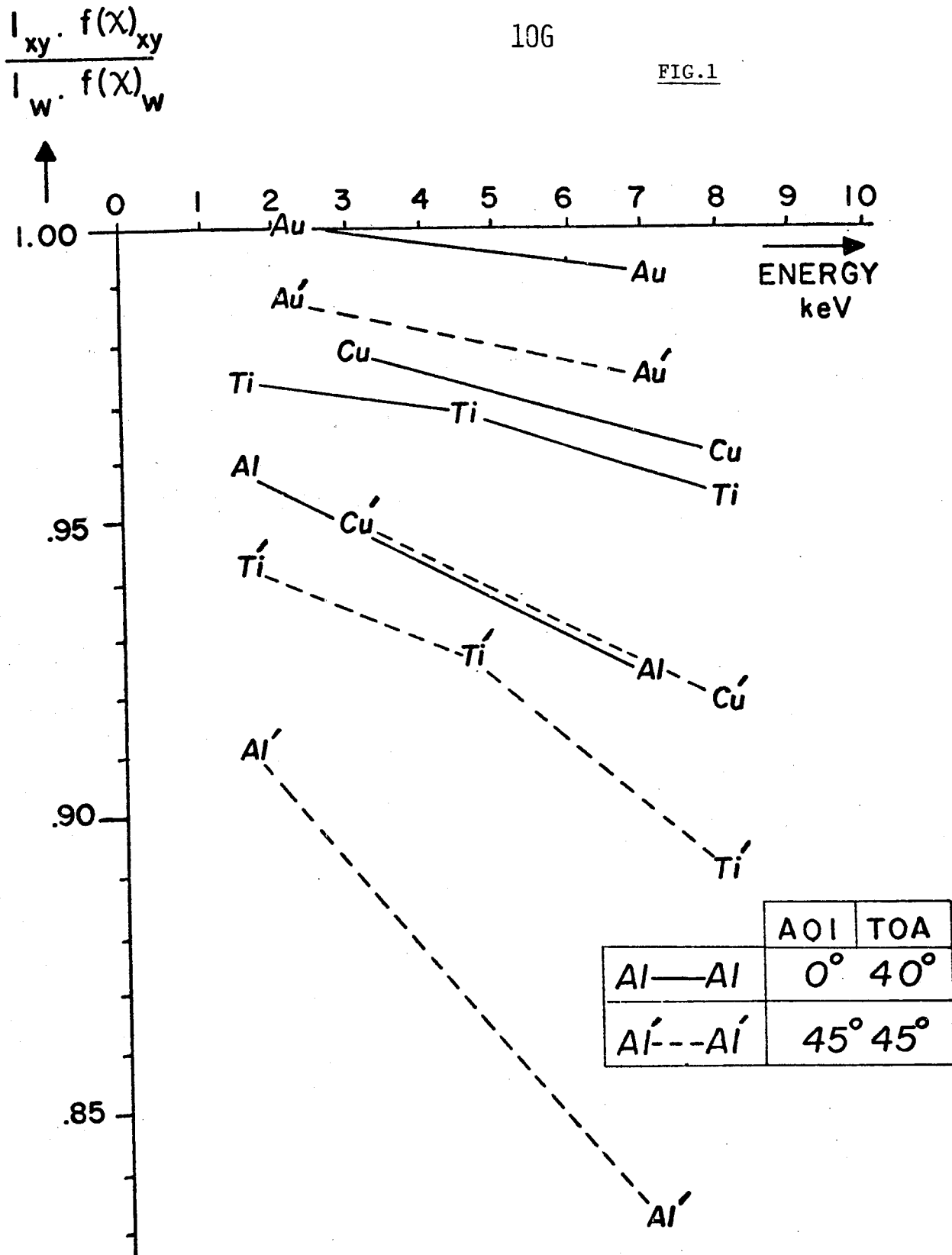
In all cases, $E_0 = 20$ keV.

TABLE 2

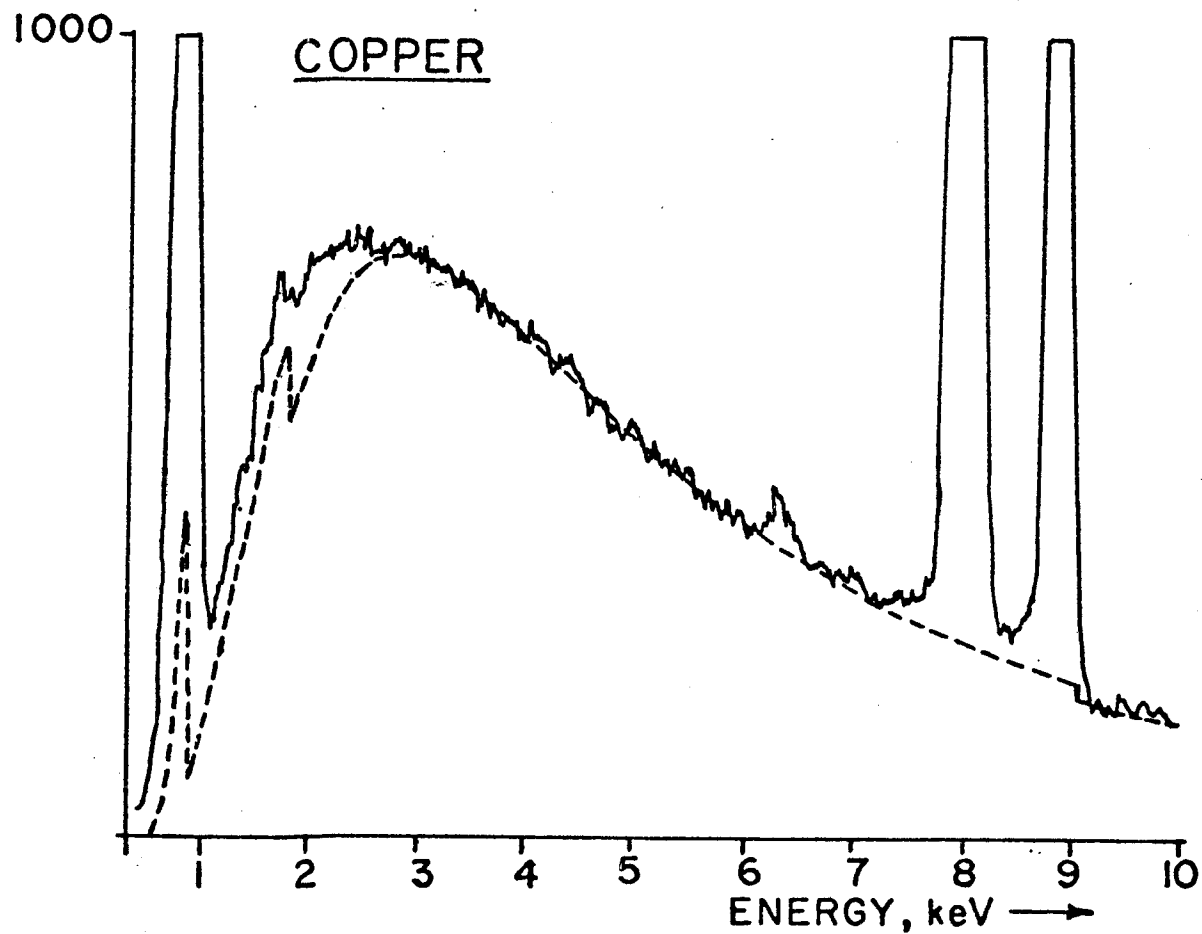
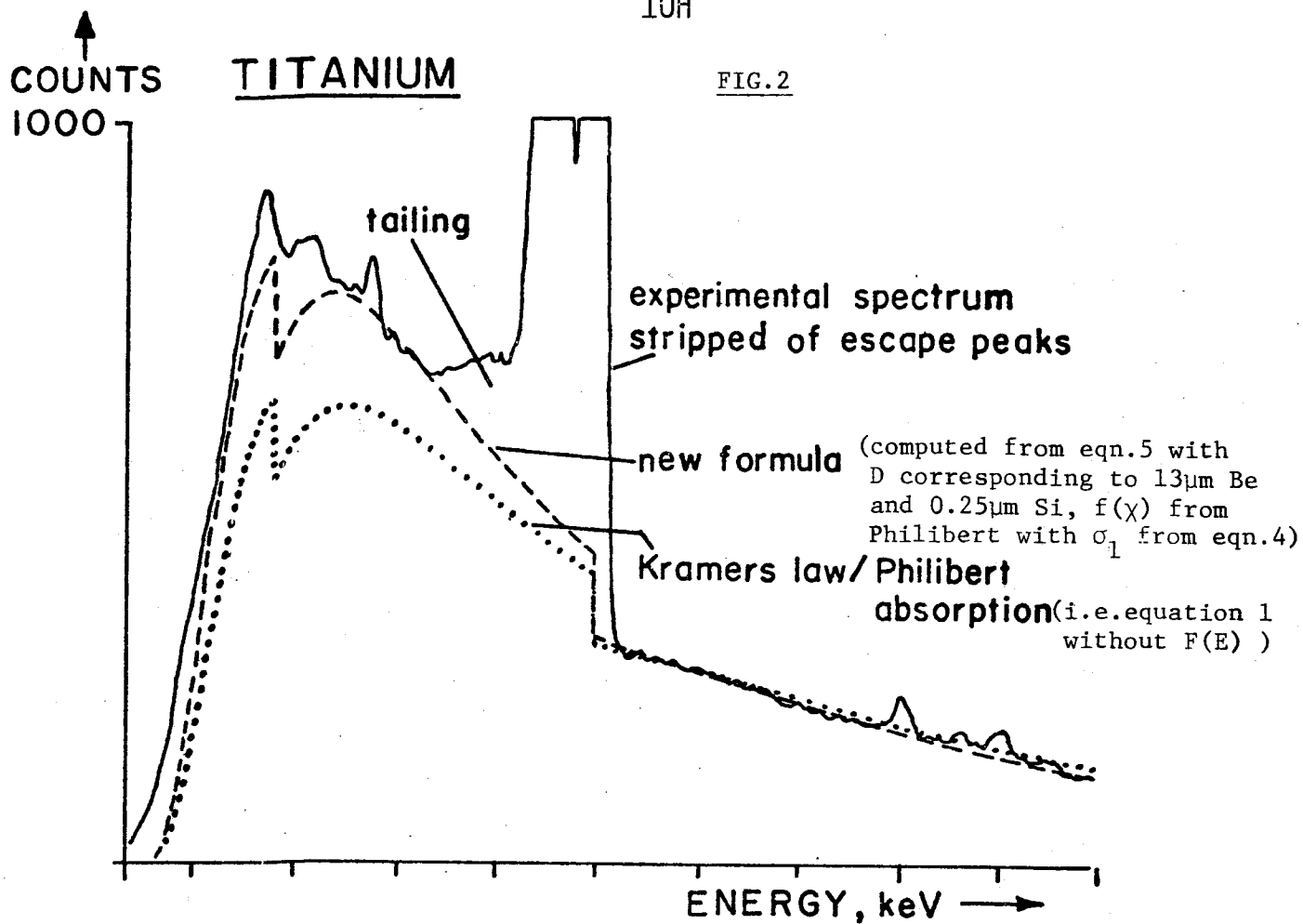
Z	a	0°, 40°	45°, 45°
		b	b
13	.26	.02	.06
22	.23	.01	.04
25	.23	.01	.02
29	.18	.01	.02
79	.15	.006	.01

Values of the exponents a and b in equation 5. This table applies to $E_0 = 20$ keV.

FIG.1



The effect of including anisotropy in the calculations for the observed bremsstrahlung intensity from a thick specimen. Data is shown by element symbols and related points are joined by straight lines for clarity. I_{xy} = Intensity computed with anisotropy included in cross sections, I_w is computed using isotropic cross sections, $f(X)_{xy}$ is the absorption correction for I_{xy} and $f(X)_w$ is the same for I_w .



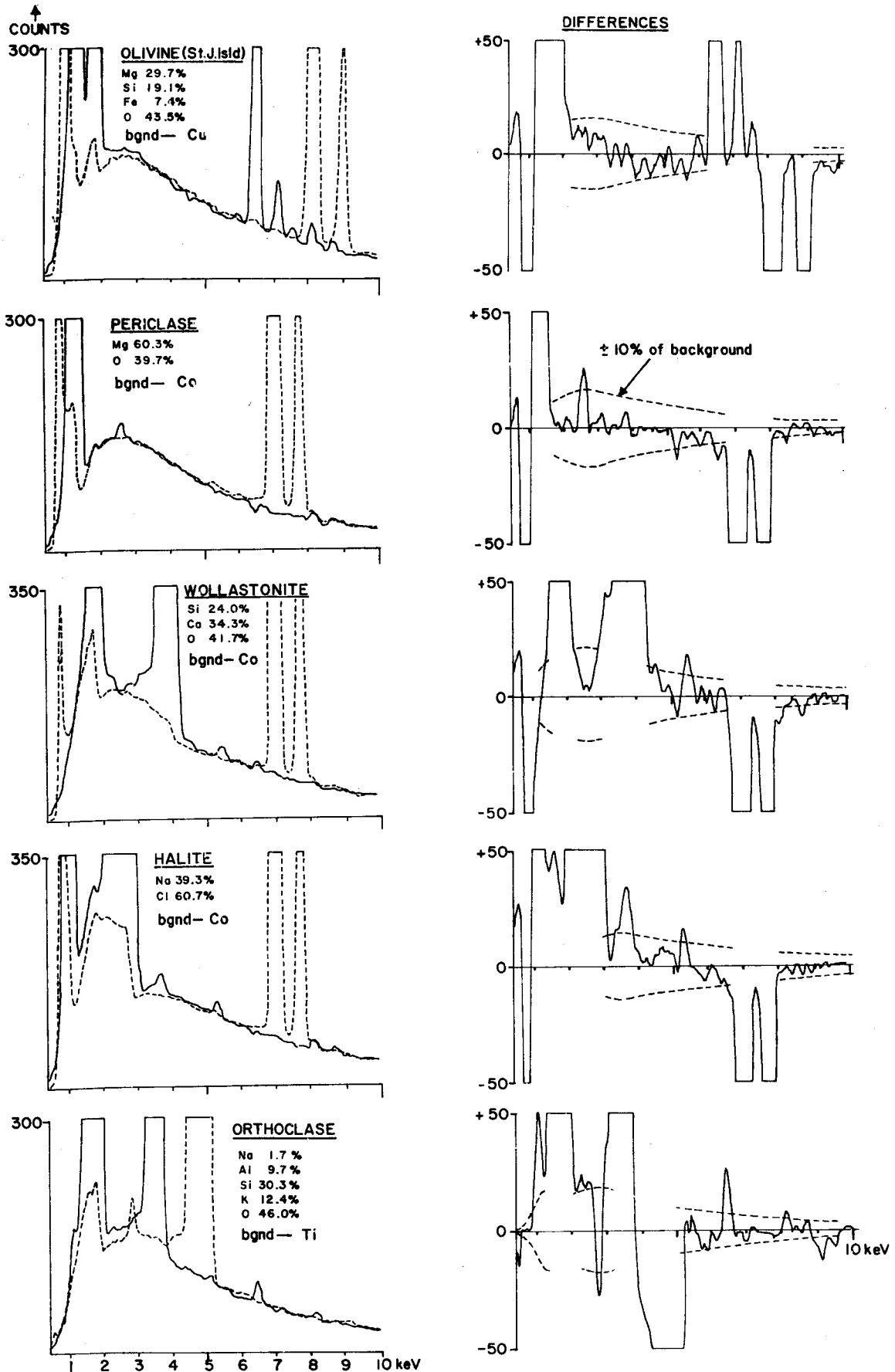


FIG.3 Dashed curves are obtained by multiplying the spectra from samples labelled 'bgnd--' by equation 6. Spectra are shown in full lines and the differences are shown on an expanded vertical scale so that the predictions can be evaluated.

BEAM SWITCHING:

a technique to improve the performance of
pulse-processing electronics for E.D.S.

Peter Statham

Dept. Electrical Engineering & Computer Science,
University of California , Berkeley .

ooo00ooo

Electronic designers do their best under the constraints of resources money and time to produce a good processing unit (PPU) for pulses from a solid-state detector. The primary aim is to obtain a measure of pulse height, to an accuracy of a fraction of a percent, for every pulse from the detector. However, two fundamental phenomena are paramount in affecting the performance of the very best of designs, namely electronic noise and the statistical scatter in arrival times of x-ray photons from a specimen excited by a continuous electron beam current.

In order to improve the signal-to-noise ratio, pulses from the pre-amplifier must be filtered or smoothed but the output pulse must still have a reasonably flat peak to facilitate measurement. Whether passive, active, or time-variant filters are used, there are certain features which are common to all and these may be described in terms of fig.1 .

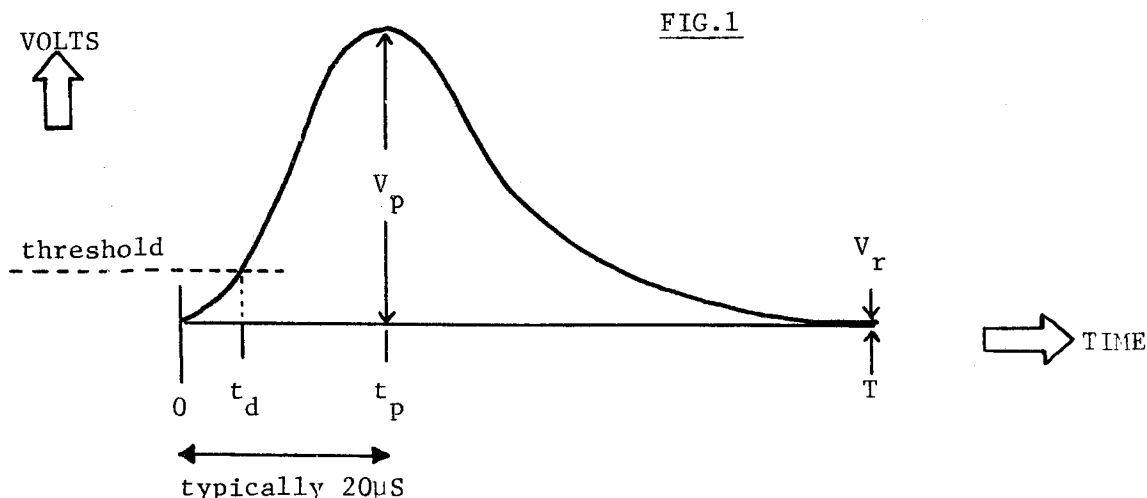


Fig.1 shows a pulse, after shaping in the measurement channel, which resulted from a single photon arriving at the detector at time zero. The pulse is detected when it rises above a threshold voltage at time t_d . (t_d will clearly vary depending on the height of the pulse in relation to the threshold which is usually fixed.) At the 'peaking time', t_p , the pulse height, V_p , is measured. (After this point, a shaping time-constant would be switched in a time-variant shaper.) When the pulse has decayed significantly (e.g. $|V_r| < 0.001 V_p$ for 1000-channel precision) a second pulse could be processed: the electronics is thus 'ready' and T could be called the 'total pulse length' or the 'dead time per pulse'.

If a second pulse arrives at any time before T it cannot be measured accurately and the logics must tell the PPU to wait a further period T for the second pulse to decay; this updating process could clearly continue indefinitely at very high count rates and corresponds to 'extendable dead time'. If a second pulse arrives before t_d , the present measurement has to be aborted in addition to the updating.

In order to see whether a second pulse has arrived, it is common to employ an auxillary short-time-constant channel as a 'pile-up inspector' (time-constants typically $< 1\mu\text{S}$ so that t_d is small). The signal-to-noise ratio is much worse than in the measurement channel and as a result some small second pulses may be missed because the threshold level has to be set high enough to exclude noise (refs.1,2).

The above description points to inherent problems when the PPU is faced with a stream of pulses where the probability of x pulses arriving in any interval t secs for an average input rate of n PPS is

$$\frac{(n.t)^x}{x!} \exp(-n.t)$$

i.e. the Poisson distribution. The updating process results in many pulses not being measured ('lost') and many pulse measurements (e.g. those of 'A' in fig.2) being aborted. As the input rate is increased, the processing efficiency decreases and the characteristic acceptance curve for normal operation is shown in fig.3.

Thus, in normal operation there are the following drawbacks :

1. There is a maximum output rate dictated by the finite interval required for smoothing to reduce the signal-to-noise ratio. For maximum output only about 1/3 of the input pulses are actually measured so much of the beam current is in fact wasted in producing photons which are never measured.
2. Baseline fluctuations arise because of the cumulative effects of residual voltages like V_r . The consequent peak broadening and distortion may be reduced by baseline restoration circuits but these usually have to be optimised for a particular count rate and are rarely perfect.
3. Pile-up inspection, though effective for large pulses, can be imperfect for low-energy pulses. Furthermore, the minimum separation that can be resolved depends on the relative heights of the overlapping pulses which makes mathematical correction to the final spectrum very difficult. Of course, there is a much greater problem in systems without protection!

THE BEAM SWITCHING TECHNIQUE

A comparatively simple piece of instrumentation can greatly improve the performance of even the most sophisticated PPU's. All that is required is a method to switch the electron beam (and hence x-ray photons) off as soon as a pulse has been detected so that the pulse can then be measured with no possibility of interference. The beam is switched back on again after T (fig.1) when the electronics is ready to process another pulse.

To implement this sequence, logical signals are required from the PPU corresponding to t_d and T of fig.1 and these are in turn used to turn the electron current on and off. Jaklevic et al (ref.3) derived a 100V signal to pulse the grid in an x-ray tube used for X.R.F. analysis; turn-on took $0.2\mu\text{S}$ and the uncertainty in turn-off time was $< 0.5\mu\text{S}$. Statham et al (ref.4)

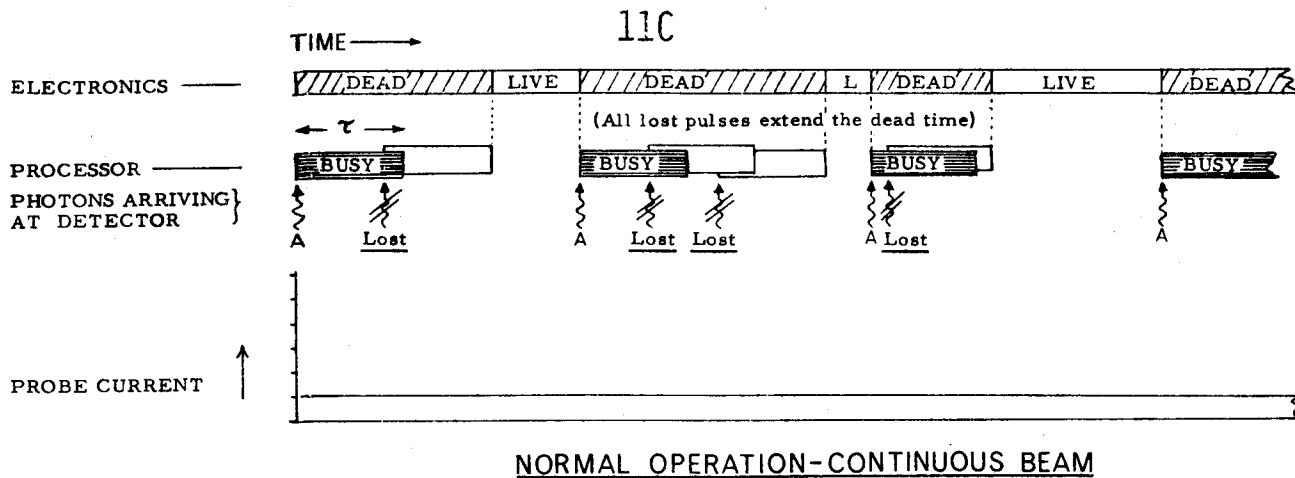


FIG. 2

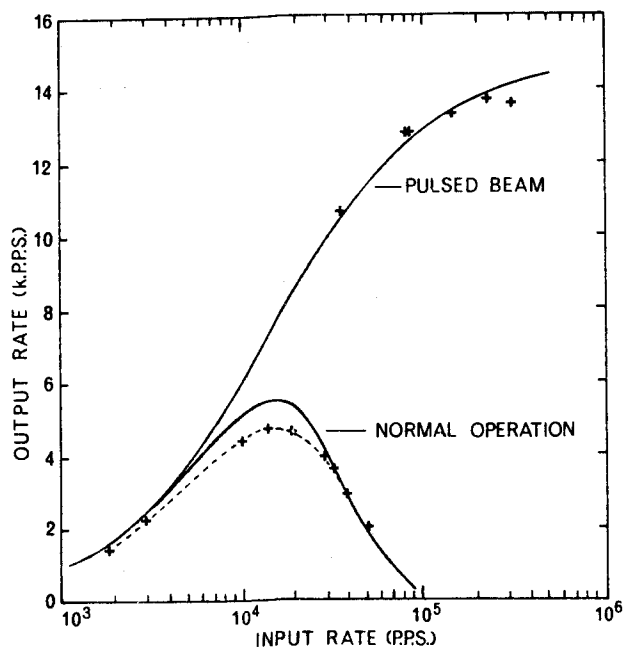
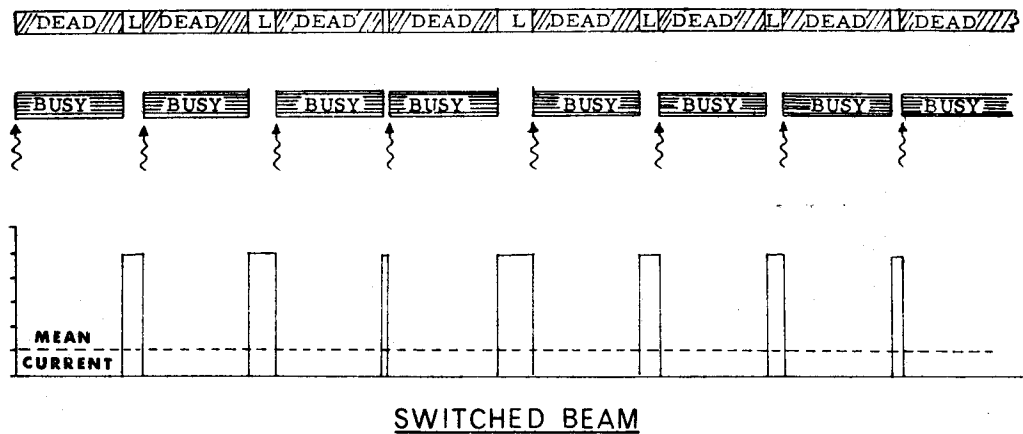
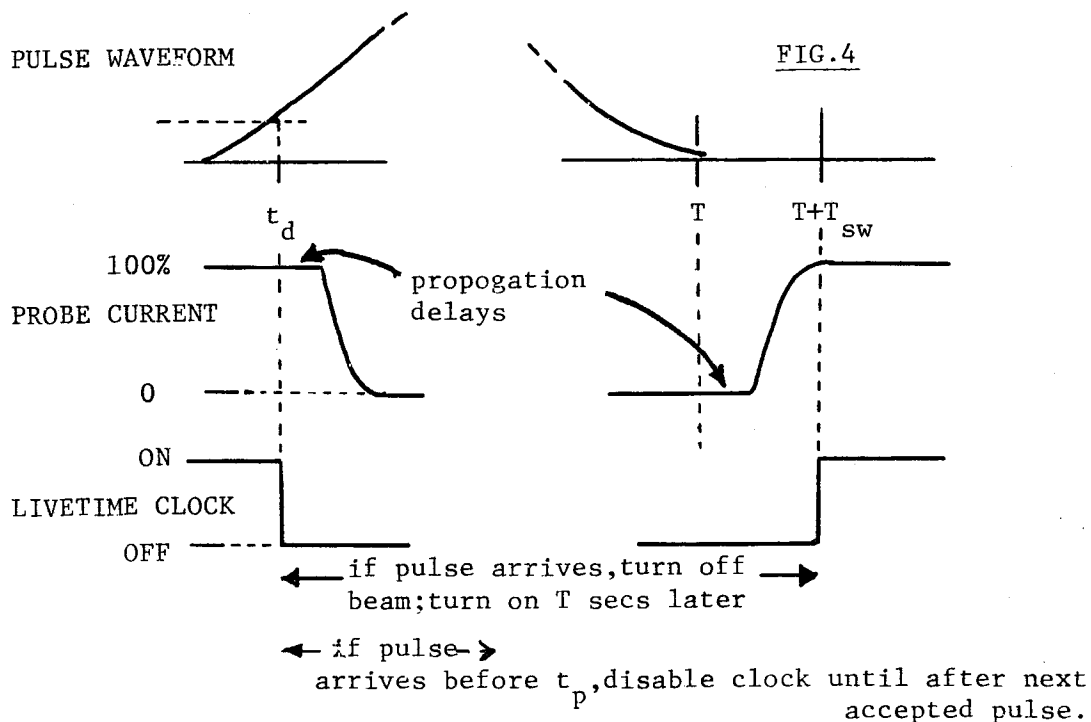


FIG. 3

Acceptance curves for switched and continuous-beam operation. Experimental results are shown by + and apply to a processor with $T=67\mu\text{S}$. The dotted line lies below the curve representing $R_o = R_i \exp(-R_i T)$ because of the lost events such as A in fig. 2. The upper curve is given by the equation $R_o = R_i / (1 + R_i T)$ which relates the output rate, R_o , to the input rate, R_i .

worked with an electron probe and achieved a switching time of about 30ns for a 20kV beam by deflecting it on and off an earthed aperture using a 20V control voltage derived from the PPU logic . Although a very fast switching time is desirable it is not essential and a commercial electron beam instrument may already have a beam-blanking facility which could be usefully employed in this technique.

Ideally, in the small but finite interval while the beam is being turned off or turned on, current should not reach areas of the specimen outside the analysed point; this has to be tested by experiment by applying intermediate control voltages to the switching device. Grid modulation may involve defocusing which produces such stray current and also can upset the current stability of the electron probe. A parallel plate or magnetic deflection system is apt to move the probe spot during the switching interval unless double deflection is employed or the deflector is positioned close to the cross-over point between condenser and objective lenses. However, despite such problems, good results can be obtained with subtle control of the switch timing as shown below.



In fig.4 the timing of the beam switch is shown in relation to the pulse waveform. At t_d , the beam is turned off as fast as possible in order to eliminate pile-up (especially with 'alien' pulses from photons produced outside of the analysed spot). If the switching is slow, a pile-up inspector will still be useful but in any case, the livetime clock should be switched off. At time T , the beam is turned on again but there is a chance that a pulse may arrive to be processed in the turn-on interval and this could be 'alien' to the area being analysed; the problem is clearly worst when analysing a small inclusion with a composition differing greatly from its surrounding matrix. Even if the probe does not move or defocus during the switching interval, the current takes time to reach a maximum and the 'on'

current is ill-defined. Therefore, if serious quantitative analysis is contemplated, the following timing sequence is arranged:

The beam is switched on at T but the logic (pile-up inspector) must continue to reject any pulses which arrive before time $T+T_{sw}$, where T_{sw} is the time for the probe current to reach its full sw value. At sw the instant $T+T_{sw}$ the livetime clock is turned on and the system awaits the next pulse. A pulse which arrives during $T \rightarrow T+T_{sw}$ must switch the beam off and cause the PPU to wait a further sw time T before turning on the beam, as in the usual reject situation.

If the logic is arranged in this manner, no further modifications need be made to the livetime clock or processor. In a system where the current is not completely turned off after t_d the PPU will reject the few pulses which may arrive, just as it would under continuous beam conditions. (N.B. When a pulse arrives before t_d , thus aborting the measurement, the livetime clock would not be enabled^p until another pulse has been successfully measured in a scheme which corrects for the aborted pulse (e.g. ref.5). The intervals marked 'live' in fig.2 would not be correct in such a system of livetime correction.)

PERFORMANCE

The behaviour of a system which has the beam switching option can be now understood with reference to fig.2. For comparison, the lower diagram corresponds to the same mean probe current, although the 'on' current is much higher. The PPU is working much more efficiently and the photon arrival is more periodic, since no multiple overlaps ever occur. In another comparison, the acceptance curve in fig.3 shows how the output rate is increased when the beam switch is connected, even though the 'on' current is kept the same; the rise in output rate is accompanied by a drop in mean current compared to the continuous beam case. The maximum output rate approaches $1/T$ and is typically about 4 times the maximum that can be obtained with a continuous beam with the same processing time constant. However, it requires large 'on' currents to achieve close to the maximum output rate and although the mean current is still no greater than would be used under normal operation, there is a greater pile-up problem and the livetime intervals are short and difficult to measure accurately (see fig.2). Finally, with beam switching, the input pulse rate as measured at the PPU is equal to the output rate, provided that no rejects occur as would be the case with a fast switch.

RESULTS

The experimental results shown here were obtained in conjunction with a Harwell detector and time-variant PPU (refs.6,7). The rejection logic differs slightly in function from that described above but Deighton(ref.8) describes it in detail and calculates the acceptance rates for both the Harwell system and the 'model' rejection system discussed above. Full details of the beam switching assembly, electronic circuitry and inter-connections appear in ref.9 and are available on request from the author. The protection against 'alien' pulses has been evaluated and proved effective under extreme conditions(ref.4). Also, the feasibility of quantitative analysis near the high output rate limit, $1/T$, has been demonstrated(ref.4). With a continuous beam giving an input rate of 20kPPS the output rate was 4.5kPPS and the f.w.h.m and position of the $MnK\alpha$ peak were 181.0eV and 591.44 channels respectively. When the beam was

switched with an 'on' current giving 82kPPS, output rate was 12.7kPPS and the width and position were 181.3eV and 591.59 channels. Even when switching an 'on' current corresponding to 314kPPS (output rate 13.4kPPS), the width and position were 182.3eV and 591.64 channels and pile-up effects probably made a large contribution to the changes which are slight nevertheless.

POTENTIAL ADVANTAGES

1. High Accumulation Rates

Perhaps the most transparent advantage is the high data accumulation rate that can be achieved. In fig.3 the maximum rate approaches $1/67\mu\text{S}$ or 14.9kPPS, for a 'peaking time' of $20\mu\text{S}$. Moreover, after modifying the range switch on the PPU, T was reduced to $45\mu\text{S}$ (peaking time still $20\mu\text{S}$) with virtually no deterioration in resolution, and this corresponds to an output rate of 22kPPS. The factor of 4 improvement over continuous beam operation gives a factor of 2 in terms of statistical precision for the same accumulation time. This may be important for x-ray mapping but since detection limits in quantitative analysis are limited to about 0.1% by inaccuracies in spectrum processing and enough counts can be recorded in typically 100secs to attain this, there is an argument in saying that the modification is not worth the effort, at least with the turn around time of most present day spectrum processing procedures.

2. Better PPU performance

The strength of the technique in fact lies in the general improvement in most features of PPU performance. The main feature to recognise is that to achieve the same output rate, the switched beam mode not only operates with a smaller mean current, but the on current is also less than with a continuous beam. Since most deficiencies in the PPU are a function of the input count rate, it is clear why the performance should be better. For example, the behaviour of a baseline restorer degrades with increase in count rate thus producing peak shift and broadening (e.g. see ref.10). Since for a given output rate, beam switching directly reduces the number of pulses the BLR has to correct for, there is an obvious reason for improvement and even when the switching is pushed to its limit, a BLR tends to operate better with the more periodic pulse train than it would with a Poisson distribution with the same mean rate (ref.3). One difficulty that is often encountered is the effects of charge retention (and subsequent leakage) in trapping centres after opto-electronic charge restoration. Under normal conditions, the dead time penalty for waiting for such charge to decay may be too high a price to pay for the slight improvement in performance. With a switched beam however, not only could T be extended significantly with little penalty, but the actual number of restore operations is reduced.

3. Electronic Noise

If the probe current is adjusted to obtain the maximum output rate then a little calculation in conjunction with fig.3 shows that if the same current were switched, T could be extended by a factor of 2.3 and the output rate would be the same. That is, longer shaping time constants could be used to reduce electronic noise.

4. Pile-up Protection

Switching the beam in principle affords better protection for a given count rate than any pile-up inspector. The time resolution is actually given

by the sum of t_d (fig.1), the preamplifier slew delay, signal propagation delay and the t_d delay involved in turning off the current. In the present case this came to between 0.26 and 1.26 μ S depending on the size of the pulse and although this can be matched by the best rejectors, mathematical pile-up corrections are easier to devise than for an inspector where the pulse-pair resolution is a strong function of the relative heights of the pulses (ref.9). Furthermore, the possibility of pile-up rejection for low-energy (1 keV) pulses that would be missed by a fast inspection channel may be valuable for thin-windowed or windowless EDS systems.

Since the degree of pile-up is a function of the 'on' current, the percentage for a given output rate can be reduced by a factor of 2 with a switched beam, even if the same pulse-pair resolution is assumed. This is because it only requires about half the 'on' current to achieve the maximum output rate that may be obtained with a continuous beam (fig.3).

In short, although beam switching makes high accumulation rates possible, perhaps the major feature is that it makes life so much easier for the PPU that the performance of any EDS system could benefit from the addition of a beam switching device.

REFERENCES

1. S.J.B. REED, J. Phys. E 5, 997 (1972).
2. K. KANDIAH, Proc. 8th National Conference, Electron Probe Analysis Society of America, New Orleans, Paper 12 (1973).
3. J.M. JAKLEVIC, F.S. GOULDING, D.A. LANDIS, IEEE Trans. Nucl. Sci. NS-19(3), 392 (1972).
4. P.J. STATHAM, G. WHITE, J.V.P. LONG, K. KANDIAH, X-Ray Spectrom. 3, 153 (1974).
5. J. BARTOSEK, J. MASEK, F. ADAMS, J. HOSTE, Nucl. Instrum. & Meth. 104, 221 (1972).
6. K. KANDIAH, Nucl. Instrum. & Meth. 95, 289 (1971).
7. K. KANDIAH, A.J. SMITH, G. WHITE, 2nd ISPPRA Nuclear Electronics Symp., Stresa, Italy, Paper 2.9, in IEEE Trans. Nucl. Sci. NS-22, 2058 (1975).
8. M.O. DEIGHTON, Nucl. Instrum. & Meth. 103, 1 (1972).
9. P.J. STATHAM, "X-Ray Energy Spectrometry", Ph.D Thesis, Cambridge, England (1975).
10. N. KARLOVAC, T.V. BLALOCK, IEEE Trans. Nucl. Sci. NS-22, 457 (1975).

A Method for Resolving Overlapping Energy-Dispersive Peaks
of an X-ray Spectrum; Application to the Correction
Procedure FRAME B

C. E. Fiori, R. L. Myklebust and
K. F. J. Heinrich
Analytical Chemistry Division
National Bureau of Standards
Washington, D. C. 20234

Abstract

The correction procedure FRAME B was developed for electron probe microanalysis with a lithium-drifted silicon detector [1]. The mass fractions of the elements contained in a specimen are computed by utilizing the summed contents of small blocks of adjacent channels (regions of interest) of a multi-channel analyzer. The program was developed for on-line operation on a small computer. FRAME B, as originally described, did not provide a method of resolving overlapped peaks. We have developed a simple method to remove this limitation. To determine the degree of interference we calculate the line width as a function of line energy. We assume that the line profiles are Gaussian, modified by the effects of incomplete charge collection. Interfering lines which have not been measured are calculated from the knowledge of relative generated line intensities.

The method, as developed so far, corrects for the mutual interference of one $K\alpha$ or $L\alpha$ peak to another $K\alpha$ or $L\alpha$ peak, for the interference with the $K\alpha$ peak of one element by the $K\beta$ peak of another element, and for the interference of the escape peak of an analytical line of one element with the analytical line of another element. The mechanics of the method are shown in figure 1.

12B

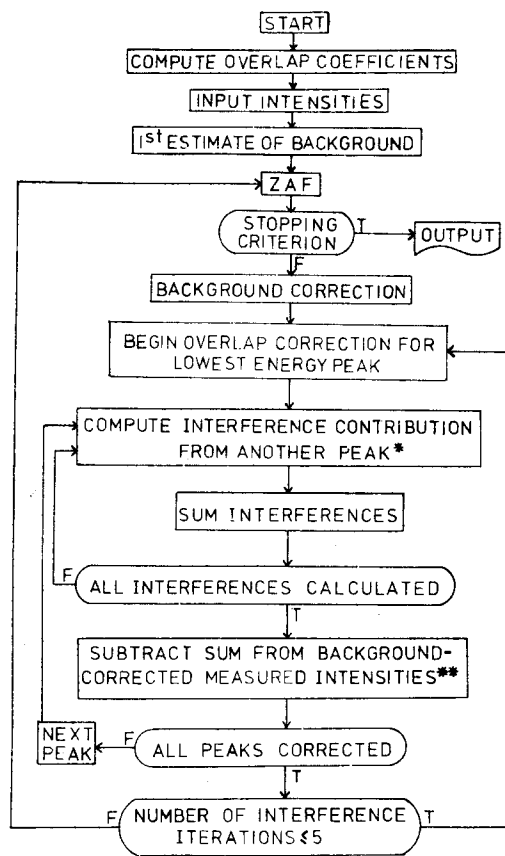


Figure 1. Flow chart of the overlap correction procedure.

*The interference contribution to a peak A from a neighboring peak B is computed by multiplying the current estimate of the intensity of peak B by the overlap coefficient of peak B on A. The intensity of peak B used here is the current estimate of peak intensity, corrected for overlaps in previous loops. If the interfering line is not a measured one, the overlap contributions are here corrected for differences in absorption within the target.

**The intensity of peak A is, throughout the iteration, the measured intensity, corrected for background only. In the iterative procedure, mutually interfering peaks are corrected for the effect of each one on the other.

The overlap coefficient predicts the contribution of a peak to the region of interest of another peak with which it interferes. If the interfering peak has not been measured, the overlap coefficient also includes the ratio of intensity of this peak to a measured peak of the same element. Overlap coefficients are obtained by formal integration of the peak shape function of the interfering lines over each region of interest of the interfered lines. The overlap coefficients are calculated for generated intensities, outside of any iterative loop, and converted to emitted intensities when the interference contributions are calculated within the interference iteration loop. Since the integrations are performed outside of any loop, the proposed method adds little computation time. FRAME B, with the inclusion of the proposed method, requires approximately 12K words of core for up to ten elements. The program is available in either FORTRAN IV or BASIC.

Reference

1. Fiori, C. E., Myklebust, R. M., Heinrich, K. F. J. and Yakowitz, H., 10th Annual Conference of Microbeam Analysis Society, Las Vegas, Nevada, paper 20 (1975).

MODIFICATION OF PHILIPS EM 301 FOR OPTIMUM EDX ANALYSIS

J. J. Hren, P. S. Ong, P. F. Johnson and E. J. Jenkins

Department of Materials Science and Engineering, University of Florida,
Gainesville, Florida 32611

It is well recognized that the incorporation of STEM into commercial electron microscopes offers potential advantage for EDX analyses as well. The microscope requirements for high resolution EDX are severe for even qualitative compositional measurements of regions excited by electrons beams approximately 100 Å diameter. We report here on some modifications of a Philips EM 301 equipped with STEM and an Ortec Model 6200 EDX system aimed at improving the EDX capability.

Geiss and Huang (1) earlier reported similar studies on metallic alloy films. Our intention is to look at low solute concentrations in both crystalline and amorphous materials, including biological specimens. Thus, we are especially concerned about ultimate sensitivity and resolution for compositional measurements. In turn, these goals dictate special attention to sources of background and secondary excitation.

We believe we have achieved significant progress toward our goals with the following modifications:

1. Following Geiss and Huang (1), the crystal detector has been moved (Fig. 1) to the position formerly occupied by the cold finger.
2. The cold finger has been rebuilt from nearly pure aluminum and a graphite columnator has been mounted in it. Suitable adapters were constructed for the auxiliary port and to extend the cold finger assembly (Fig. 2). Alignment can be achieved optically with the column broken. The detector is positioned with 0.5 mm of the cold finger, but must be electrically isolated.
3. A specimen holder has been constructed (Fig. 3) with a tip of nearly pure Al and with a flat unobstructed side facing the detector. This tip is also isolated from ground and may be used to measure the absorbed specimen current.
4. Shielding of the pole pieces is accomplished with pure aluminum sheet and thick condensor apertures are employed during measurements. The latter is critical, since thin, self-cleaning apertures serve as an efficient X-ray source.

With the above modifications, we have minimized systematic background contributions (e.g., from the grid and specimen holder) to a point significantly less than the peaks of interest. This has been demonstrated in many studies undergoing preparation for publication (2) (e.g., see Fig. 4).

Since the specimen holder is electronically isolated the specimen current can be accurately measured to about 10^{-11} A, providing reproducible spot counting. This feature is especially important in the determination of compositional gradients (2).

1. R. H. Geiss and T. C. Huang, IBM Report, RJ 1574, April 23, 1975.
2. J. J. Hren, P. F. Johnson, S. R. Bates and L. L. Hench, submitted to 34th Ann. EMSA Meeting (1976).

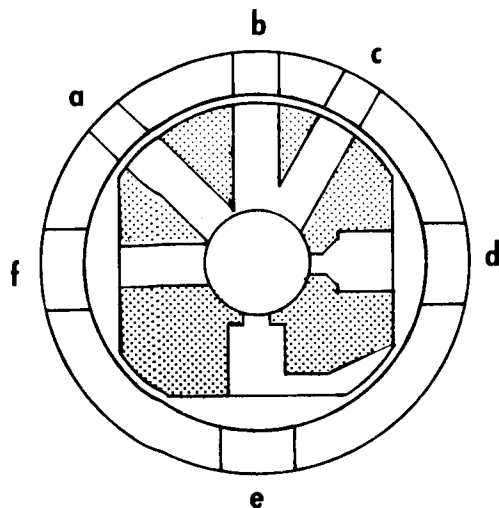


FIG. 1. Schematic of modified EM-301 goniometer stage. The cold finger, mounted in port a, is thermally isolated from the column and goniometer by Teflon point contact positioning bearings. The goniometer EDX detector, port b, was drilled to accept the detector. The remaining ports are unmodified; they are: c-vacuum port; d-specimen and x-translation port; e-objective apperture port; and f-y-translation port.

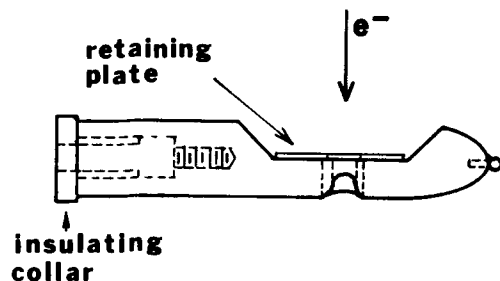


FIG. 3. High purity Al specimen holder. Only the tip is shown. The specimen is mounted through the bottom and is held in place by the retaining plate and a "c" ring (not shown). Note that the hole for transmitted electrons was drilled parallel to the plane of the drawing, and redrilled at 45°, providing a full transmitted image when the specimen is tilted toward the detector. The tapped hole allows for attaching the specimen current lead.

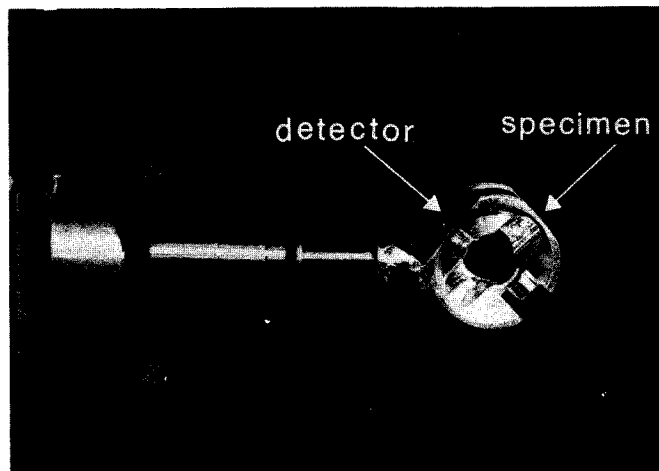


FIG. 2. A new cold finger was designed and fabricated of 99.99 + % Al. The design incorporates a graphite x-ray columnator against which the detector is placed. The detector must be electrically isolated from the columnator.

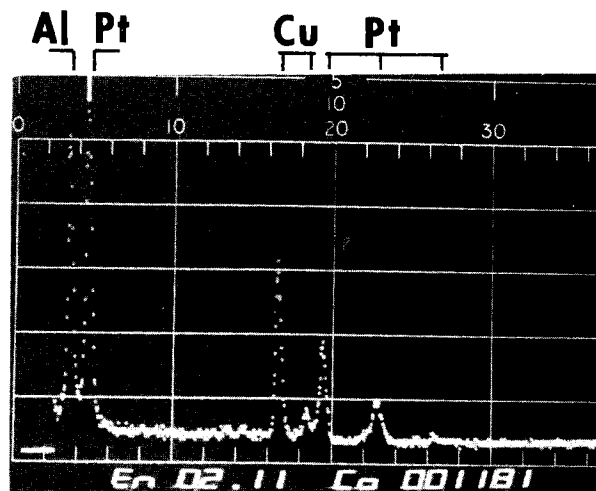


FIG. 4. Spectrum of Pt in neural tissue. Note that the Pt-Mα peak is significantly larger than either the AlK or CuKα peaks.

MICROCHEMICAL ANALYSIS OF THIN METAL FOILS

N. J. Zaluzec and H. L. Fraser

Department of Metallurgy and Mining Engineering, and the Materials Research Laboratory, University of Illinois at Urbana-Champaign, Urbana, Illinois 61801.

Several techniques^{1,2,3,4} have been developed for quantitative x-ray microanalysis of thin metal foils. These techniques usually provide relative elemental concentrations, and assume that for a "thin" homogeneous alloy of elements A and B, the ratio of intensity (I) of any two characteristic x-ray peaks (e.g. $I_A^{K\alpha}/I_B^{K\alpha}$) should be independent of specimen thickness. Recently, Fraser et al.,⁵ conducted experiments using a highly ordered alloy (β -NiAl) to investigate this assumption, and indeed showed that in electron transparent regions of the foils there was a marked variation in the ratio of the K α peaks of Ni and Al, respectively. The results given by Fraser et al.,⁵ are summarized in Fig. 1. It can be seen that the variation in the intensity ratio may be considered in two parts, one involving an initial decrease, the other a subsequent increase in this ratio with increasing foil thickness. It seemed reasonable to attribute the second part of this variation to preferential absorption of Al K α x-rays. However, no explanation for the initial decrease in intensity ratio was given. It is important to understand the origin of such variations in thin parts of a foil, since it is these areas that are often most suitable for microchemical analysis. This paper presents the results of a study aimed at understanding the initial decrease in intensity ratio.

It was not possible to predict this effect by consideration of factors such as backscattering, fluorescence by the continuum generated in the sample, absorption effects, etc., so the possibility of x-rays being generated in the foil by radiation other than the incident electron beam was considered. Thus, with the microscope correctly aligned for the recording of x-ray spectra,* the electron beam was positioned just off the edge of a foil of NiAl. A spectra containing a relatively large NiK α peak and a negligibly small AlK α peak was recorded. The experiment was repeated but this time with a lead foil over the condenser aperture to prevent electrons reaching the specimen, and still spectra were recorded (again containing similar Ni and AlK α peaks). These observations are consistent with x-ray generation in the sample caused by high energy bremsstrahlung created primarily at the condenser aperture.

*A JEOL JSEM 200 coupled with an Ortec energy dispersive analyzer was used as described previously.⁵

Such radiation will excite x-rays from the specimen as a whole, and thus, has serious implications as to the feasibility of micro-area chemical analysis.

A brass liner having a diameter of 2 mm was inserted into the top pole piece of the objective lens and this was found to reduce the level of x-ray counts produced by bremsstrahlung to an extremely low level. The variation in intensity ratio with foil thickness when bremsstrahlung effects are accounted for is shown in Fig. 2. While it is apparent that the initial decrease in intensity ratio is now absent, it is still important to note that a variation in this ratio still exists in regions of a foil which are electron transparent. Thus, care must be taken when applying the established techniques for reducing intensity data to relative concentrations.

We acknowledge many useful discussions with John B. Woodhouse. This work was supported in part by the USERDA under contract #E(11-1)-1198.

References

1. Philibert, J. and Tixier, R.: NBS special pub #298 Quantitative Electron Probe Microanalysers, p. 13.
2. Cliff, G. and Lorimer, G. W.: Pro. 5th Europ. Conf. on E.M. (1972), 136.
3. Jacobs, M. H. and Baboroska, J.: Ibid, 140.
4. Duncumb, P.: J de Microscopie 7, (1965), 581.
5. Fraser, H. L., Zaluzec, N. J., Woodhouse, J. B., and Sis, L. B.: 33rd Ann. Proc. of EMSA (1975), 106.

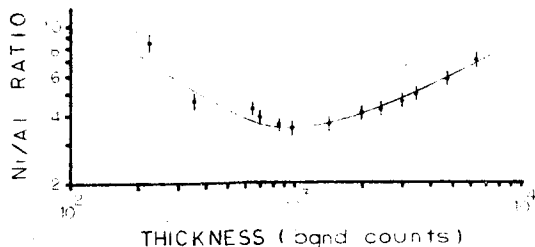


Figure 1. Measured intensity ratio of Ni/Al versus thickness (measured in background counts). Accelerating voltage 200 KeV.

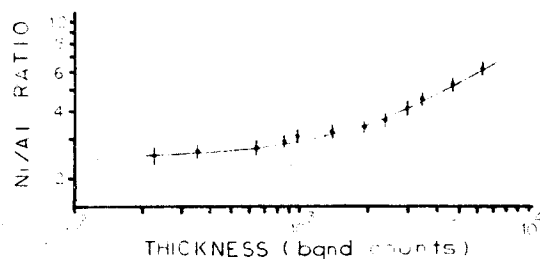


Figure 2. Intensity ratio of Ni/Al versus thickness (measured in background counts); data corrected for bremsstrahlung effects, see text. Accelerating voltage 200KeV.

CHARACTERIZATION OF COTTON DUST BY ELEMENTAL ANALYSIS

E. Fleming III, P. Tucker, and S. Hersh

School of Textiles, North Carolina State University, Raleigh, North Carolina 27607

Cotton dust has been identified as one of five common substances present in the workplace that are significant health hazards to industrial workers. The material reported here is part of a larger program being conducted by the School of Textiles to identify the etiological agent(s) causing byssinosis and to characterize the dust associated with cotton processing (1-3). The early results quickly verified that there are large amounts of both soluble and insoluble inorganic matter in cotton dusts.

Electron diffraction patterns were obtained from dust samples collected directly on carbon-coated grids from the air and from water dispersed samples collected by a filtration system located in a model cotton card room (4). Identification of these diffraction patterns has not yet been completed because our attention has now focused on examining the water extractable components of cotton dusts with a newly acquired EDS-SEM system. Discussions of the EDS examination of these extracts constitute the major part of this paper.

By interpretation of the spectral display, 9 elements (Na, Mg, Al, Si, Cl, K, Ca, Fe, Cu) were identified in water extracts of cotton bract. The identification was difficult for the less significant emission peaks because of the large number of peaks in the 0 to 10 kV range as shown in Figure 1.

Crystals (~ 1 mm on edge) were grown from the viscous water extract of the bracts. The composition of these crystals was determined to be KCl. A photomicrograph of a typical crystal is shown in Figure 2 with a superimposed "map" of dots representing potassium. Similar maps were obtained for chlorine. Figure 3 provides a spectral display of the "unknown" specimen as represented by the histogram and known KCl by the superimposed dots. An excellent match is evident. Since materials can be purified by crystallization, it was evident that this process could become a major aid in identifying other compounds. Crystals of compounds which are present in much smaller concentrations than KCl were grown on glass slides to the order of 0.05 mm on edge. Typically four or five quite different morphologies occur. Upon viewing such a preparation between crossed polars, dendrites, spherulites and small equant crystals are observed; some are birefringent while others are not. Typical spherulites in an early state of growth are shown in Figure 4. Since all these different crystalline structures grew under the same environmental conditions, it is reasonable to assume that most of them are of different compounds. Current efforts are being directed to identifying these compounds.

This study was supported by the U. S. D. A. with funds made available by Cotton Incorporated. The authors are grateful for this support and wish to thank Dr. Carl Bryan for providing the samples of water extracts.

References:

1. Fornes, R. E., Gilbert, R. D., and Sasser, P., "Inorganic Content of Cotton Dusts and Plant Parts," accepted for publication in Textile Research J.

2. Hersh, S. P., Rochow, T. G., Tucker, P. A., and Farwell, F. W., "Mineralogy of Airborne Dust in a Cotton Card Room," accepted for publication in Textile Research J.
3. Fornes, R. E., Kleinfelter, M. K., and Hersh, S. P., "Particle Size Analysis of Cotton Dusts Using Scanning Electron Microscopy," to be presented at the 1976 Textile Engineering Conference of ASME, Charlotte, N. C., September 1976.
4. Hersh, S. P., Fornes, R. E., and Caruolo, E. V., "Respirable Dust Levels Developed While Processing Cotton in a Model Card Room" in Cotton Dust (H. Ayer, Ed.), American Conference of Governmental Industrial Hygienists, Cincinnati, Ohio, 1975, p. 376.



Fig. 1. Spectral display of EDS analysis of water-extracted cotton dust showing multiplicity and possible confounding of emission peaks

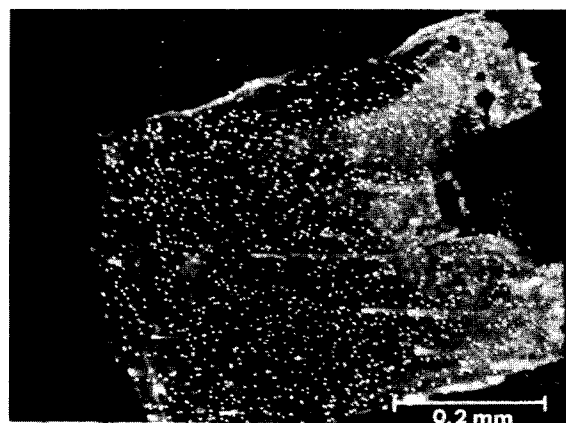


Fig. 2. X-ray emission map for potassium from "unknown" crystal

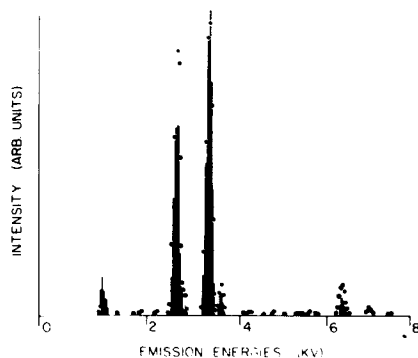


Fig. 3. Spectral display of an EDS analysis from unknown crystal and known KCl. Histogram depicts "unknown" crystal with superimposed dots representing the known KCl

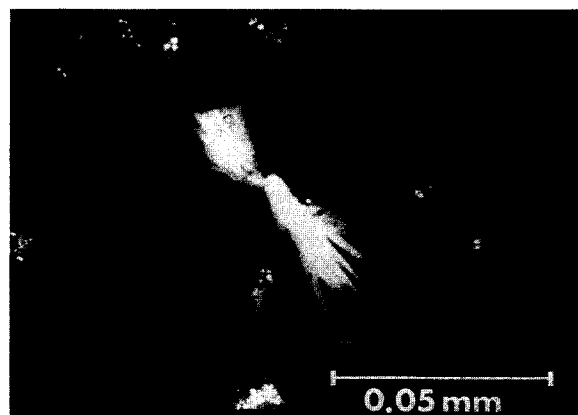


Fig. 4. Photomicrograph of micro-crystals grown from the water-extracted cotton dust

RECENT APPLICATIONS IN COMBINED TRANSMISSION ELECTRON MICROSCOPY AND MICROANALYSIS

Miss D. Chescoe and Dr. B.E.P. Beeston

AEI Scientific Apparatus Limited, Barton Dock Road, Urmston, Manchester, England and AEI Scientific Apparatus Inc., 500 Executive Boulevard, Elmsford, New York, 10523, U.S.A.

An AEI CORA has recently been used to examine a wide number of applications mainly in the biological field. This instrument with its unique double field condenser/objective lens combines the normal accepted high resolution performance of a transmission electron microscope with X-ray analysis of areas down to a 250°A in diameter.

Environmental pollution is one field in which this technique excels. Although the dangers of handling asbestos are well known and stringent controls operate in industrial use, an individual can be at risk in domestic use, especially when handling some of the home repair kits. Certain spackling compounds were examined by dispersing a small quantity in distilled water and drying down onto a carbon coated grid. As can be seen from the micrograph Fig 1a many fibres exist, similar in appearance to asbestos. The characteristic spectrum (Fig 1b) and diffraction pattern were taken and compared with known asbestos fibres; and in this case found to be chrysotile asbestos.

Identification of fibres by, say, dimension ratio methods and appearance without X-ray analysis can lead to misinterpretation. In a specimen extracted from an osteo-arthritic knee joint, a fibre similar in appearance to amosite asbestos was observed (Fig 2a). Analysis revealed this to contain Calcium and Phosphorus, indicating a Calcium Phosphate crystal (Fig 2b).

The small probe of CORA can be particularly useful. A sample of tissue taken from a patient who had received gold injections was examined to determine the presence of gold. To lower background radiation from the tissue the specimen was ashed by the technique described by Henderson and Griffiths.¹ Several adjacent particles were found and analysis showed one to contain gold, and the other iron, presumably from the red blood cells, as can be seen by comparing the two spectra in Fig. 3.

Apart from examining particles, physiological changes are readily observed. In the study of Chromatin condensation in spermatogenesis, a several fold increase in phosphorus during development indicates the DNA is becoming condensed and more tightly coiled. (Fig 4)

These and other recent applications together with some comments on specimen preparation for analysis will be discussed in more detail.

References

1. W.J. Henderson & K. Griffiths. Shadow Casting and Replication Ed. M.A. Hayat. Principles and Techniques of Electron Microscopy, Biological Applications. Vol. 2 pp 151 - 193. Van Nostrand and Rheinhold, New York.



Fig. 1a
Dispersion of spackling compound

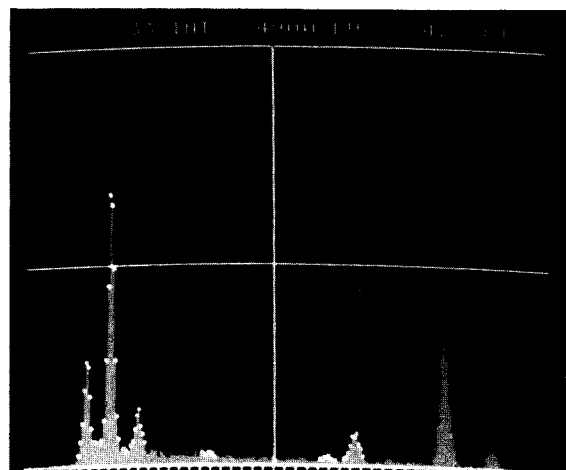


Fig. 1b
Spectrum from fibre



Fig. 2a
Fibrous looking particle

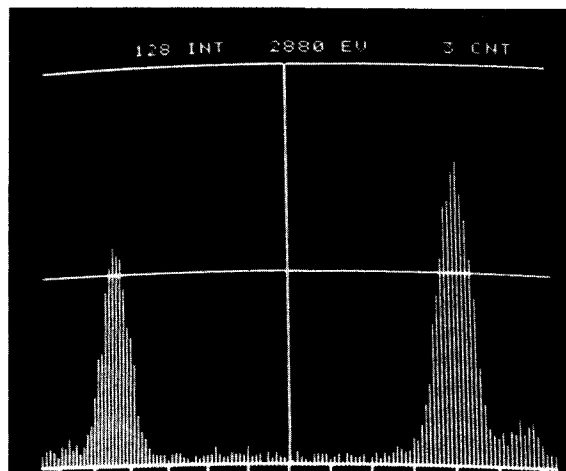


Fig. 2b
Spectrum from particle

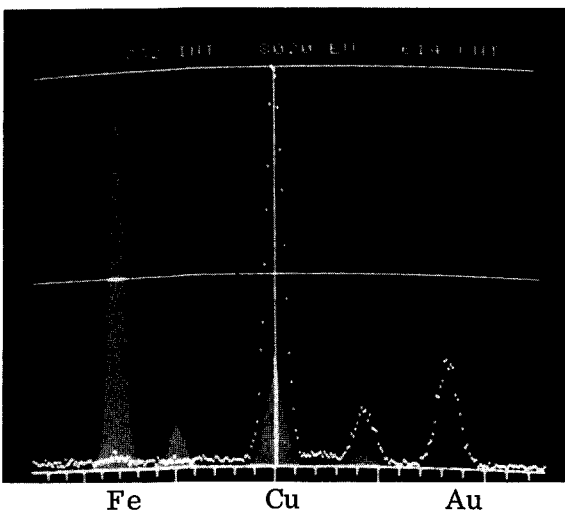


Fig. 3 Comparison spectra of adjacent particles of iron and gold in ashed specimen

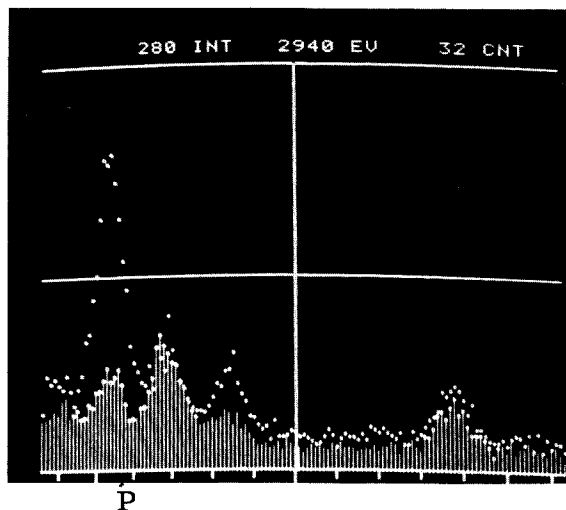


Fig. 4 Comparison spectra of phosphorus in immature and mature nuclei

ENERGY DISPERSIVE X-RAY MEASUREMENTS OF THIN METAL FOILS*

J. Bentley and E. A. Kenik

Metals and Ceramics Division, Oak Ridge National Laboratory
Oak Ridge, Tennessee 37830

Instruments combining a 100 kV transmission electron microscope (TEM) with scanning transmission (STEM), secondary electron (SEM) and x-ray energy dispersive spectrometer (EDS) attachments to give analytical capabilities are becoming increasingly available and useful. Some typical applications in the field of materials science which make use of the small probe size and thin specimen geometry are the chemical analysis of small precipitates contained within a thin foil and the measurement of chemical concentration profiles near microstructural features such as grain boundaries, point defect clusters, dislocations, or precipitates. Quantitative x-ray analysis of bulk samples using EDS on a conventional SEM is reasonably well established, but much less work has been performed on thin metal foils using the higher accelerating voltages available in TEM based instruments. We present here some preliminary results of x-ray intensities measured as a function of foil thickness for two pure metals and one solid solution alloy obtained with such a system.

The instrument used was a JEM 100C TFM (120 kV maximum) equipped with the ASID-4D scanning attachment and a Kevex 5100 EDS. The TEM is equipped with a side entry goniometer and the x-ray detector is introduced through the pole piece at the plane of the specimen. The x-ray count rate is optimized (and the background and Cu peaks from the specimen holder minimized) by tilting the specimen through $\sim 45^\circ$ about the specimen rod axis and $\sim 25^\circ$ about the orthogonal tilt axis. Disks of aluminum, 316 stainless steel, and iridium were thinned using conventional techniques. The foils were set at the Bragg condition (120 kV) for a low order reflection and observed in the STEM mode. The illumination and collector angles were both $\sim 1.5 \times 10^{-2}$ rad. X-ray spectra were recorded for successively thicker areas by counting (~ 30 s) in the spot scan mode with the probe positioned on successive bright thickness fringes. The procedure was repeated for 80, 40, and 20 kV positioning the beam alongside the small contamination spots visible in the STEM (or SEM for 40 and 20 kV) image. The thickness measurements were checked in a CTEM image and found to agree with those from the STEM image, although the contrast of the fringes was greater in the CTEM image. The integrated peak intensities with background subtracted were measured for the K_{α} line (Al and Fe) and the M line (Ir) and are shown plotted as a function of foil thickness for the three specimens and four accelerating voltages in Figure 1. Repeated measurements in foils $\sim 5 \mu\text{g}$ thick indicated errors of $< 5\%$ in x-ray intensity and $< 1/4 \mu\text{g}$ in the foil thickness.

The essential feature of Figure 1 is that all the plots are linear. The extrapolated values of intensity at zero thickness are all slightly positive and agree reasonably well with those measured with the probe positioned in the hole and presumably arise from electrons scattered out of the main beam by apertures, etc. The linear behavior shown in Figure 1, even to large values of thickness, shows that absorption of x-rays in the foil is not important, even for low energy x-rays in high Z materials. A "viewable"

*Research sponsored by the Energy Research and Development Administration under contract with the Union Carbide Corporation.

image, even at voltages as high as 120 kV, is therefore still an adequate criterion in determining the applicability of a linear relationship between x-ray intensity and concentration, which significant absorption would invalidate. It can be shown that the results are in fact consistent with calculations using appropriate self-absorption coefficients for x-rays.

It was originally thought possible to gain some insight into the size of the excited x-ray emission volume of the foil, but the results are not unambiguous. For thin foils and high incident electron energies, little spreading of the beam is expected to occur and so in the absence of other effects the diameter of the excited volume should be slightly larger than the probe diameter. Fluorescence excited by Bremsstrahlung produced by passage of the beam through the foil was considered as possibly contributing to a large excited volume, but a simple geometrical argument shows that the intensity of fluorescence so produced is proportional to the square of the foil thickness. Although this effect surely occurs, the linear behavior in Figure 1 suggests that its contribution to the total intensity is small for the foil thicknesses studied.

Finally, the linearity of the x-ray intensity as a function of foil thickness suggests that this property could be used in foil thickness measurement applications.

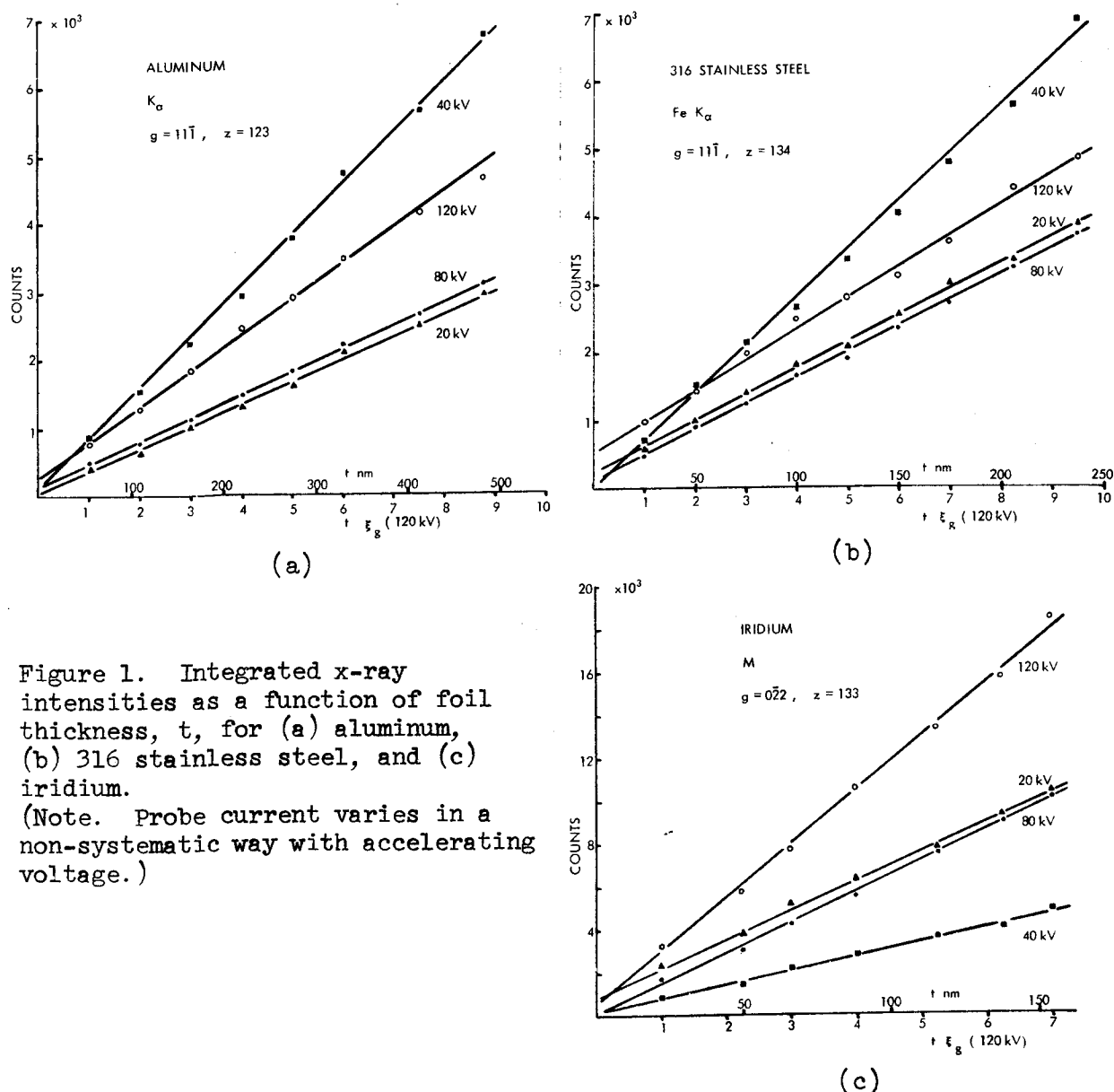


Figure 1. Integrated x-ray intensities as a function of foil thickness, t , for (a) aluminum, (b) 316 stainless steel, and (c) iridium. (Note. Probe current varies in a non-systematic way with accelerating voltage.)

ERRORS INTRODUCED IN ELIMINATING OR EXTRAPOLATING STANDARDS

John C. Russ
EDAX Laboratories
Prairie View, IL 60069

Reducing the classic dependence on pure standards is desirable because it reduces the time needed to perform analysis, and relaxes the dependence on SEM stability. The time savings results directly from reducing the number of samples and standards that need to be introduced and their spectra recorded. The stability and reproducibility of the SEM is most seriously tested when standards must be introduced for analysis requiring the beam to be turned off. It is also a problem in some instruments which do not have highly stable beam currents over a period of minutes.

The basic method to calculate an effective pure element intensity for an element of interest by extrapolating from another measured element has been described.¹ It is a relatively simple function of atomic number and geometry, but since the calculation involves approximations both in the models and fundamental constants, the extent of extrapolation that can be considered "safe" must be questioned. In principle, the method would allow the use of no standards at all by calculating relative excitation of each element and normalizing the total of the elements to 100%.

As a relatively simple case, consider the alloy of Cr-Co shown in Table 1.² The elements are both analyzed by their $K\alpha$ lines, which are close together in energy, so that they are both excited well, and at reasonably high energies so that internal self absorption and spectrometer losses are small. The table values show the results, with and without normalizing the answers to 100% (shown in parentheses) of ZAF-corrected values. Particularly after normalizing there is no major additional error introduced by using either single element as a standard, or no standard at all.

Table 1

<u>Element</u>	<u>Given Chem.</u>	<u>Measured Intensity*</u>	<u>Pure Intensity*</u>	
Cr	56.23	4.322	7.176	
Co	43.45	1.910	4.927	
Standard:	<u>Both</u> <u>Pure</u>	<u>Cr</u> <u>Only</u>	<u>Co</u> <u>Only</u>	<u>None</u>

<u>Element</u>				
Cr	57.85(57.04)	57.40(57.63)	59.59(57.66)	(56.98)
Co	43.58(42.96)	42.20(42.37)	43.74(42.34)	(43.02)

* Counts/second - picoamp, 25 kV

A more difficult situation arises when different shells are used in the extrapolation, or when a large energy difference (or Z-number difference) is present. As an example, Table 2 shows data from analysis of a Cu-Au alloy.³ Both the Au-L α and Au-M α were used. Relatively large errors are introduced, particularly when the Au-M α line is used. Normalization to 100% (shown in parentheses) again improves the results.

Table 2

<u>Element (line)</u>	<u>Given Chem.</u>	<u>Measured Intensity</u>	<u>Pure Intensity</u>	
Cu (K α)	65.0	6.393	9.787	
Au (L α)	35.0	0.891	3.112	
Au (M α)		1.701	6.240	
Standard:	<u>Both</u> <u>Pure</u>	<u>Cu</u> <u>K</u>	<u>Au</u> <u>L</u>	<u>Au</u> <u>M</u> <u>None</u>

<u>Element</u>					
Cu (K)	64.05 (65.48)	64.06 (67.33)	70.15 (67.40)	85.75 (67.62)	(67.39)
Au (L)	33.78 (34.52)	31.08 (32.67)	33.92 (32.60)	40.08 (32.38)	(32.61)
Cu (K)	64.05 (64.80)	64.07 (70.86)	70.16 (70.15)	85.74 (69.85)	(70.29)
Au (M)	34.80 (35.20)	26.35 (29.14)	29.33 (29.49)	37.00 (30.15)	(29.72)

Since these examples used major elements and lines, for which we normally expect good accuracy after conventional ZAF correction, the loss in accuracy due to extrapolation or elimination of standards can be seen directly. The greater the energy or Z-number range involved, particularly if different shells are involved, the greater the error.

For minor elements the errors introduced by counting statistics, background and peak overlap removal, are significant limitations on the accuracy of the final results. In these cases the errors introduced by extrapolation may be more acceptable. The use of a few pure standards, well distributed in energy and/or Z-number, or even the complete elimination of standards, represents an acceptable compromise between accuracy and practicality for a useful fraction of microanalysis applications.

REFERENCES

1. Russ, J. C., "Quantitative microanalysis with minimum pure element standards", Proceedings of Ninth Annual Conference, Microbeam Analysis Society, Ottawa, Canada, 1974, p. 22a-22c.
2. Samples - courtesy of Fran Planinsek, University of Denver, Denver, Colorado.
3. Samples - courtesy of John Precht, Hughes Aircraft, Torrance, California.

PRESENT AND FUTURE POSSIBILITIES FOR LOCAL CHEMICAL
ANALYSIS OF SOLIDS BASED ON PHYSICAL TECHNIQUES

D.B. Wittry

Department of Materials Science
and Electrical Engineering
University of Southern California
Los Angeles, California 90007

Many techniques and associated instruments have been developed over the past 25 years to provide a chemical analysis of surface layers or of localized regions of a solid specimen. The principal techniques developed or refined in this period include electron probe x-ray microanalysis (EPMA), electron spectroscopy in transmission electron microscopy (ES-TEM), electron spectroscopy for chemical analysis (ESCA), Auger electron spectroscopy (AES or SAM), sputtered ion mass spectroscopy (SIMS), laser-probe optical emission spectroscopy, nuclear backscattering spectroscopy and ion scattering spectroscopy (ISS).

By examples, it will be shown that some microanalytical techniques depend on spatial localization by focussing the exciting beam (microprobe methods) or by focussing the emitted radiation (selected area methods). Depth resolution can sometimes be improved by utilizing signals that have a small escape depth or by using specimens of small thickness.

The relative and absolute detection limits of some of these newer techniques will be compared with older techniques including conventional optical emission spectroscopy, mass spectrometry, x-ray fluorescence spectroscopy, neutron activation analysis, etc.

Recognizing the advantages and limitations of present techniques, it is possible to predict which of the many available analytical techniques will be of principal importance in the future.

LOW ENERGY PHOTOIONIZATION CROSS SECTIONS FROM
PROTON INDUCED X-RAY SPECTROSCOPY

Allen Lurio, Wilhad Reuter and Johann Keller

IBM Thomas J. Watson Research Center
Yorktown Heights, New York 10598

ABSTRACT: We describe a new and reliable experimental technique for the measurement of photoionization cross sections in the soft x-ray region. A film of the absorber is evaporated onto a polished substrate. When a proton beam from our 3 MeV Van de Graaf accelerator is incident onto this target, characteristic x-rays from the substrate are produced. From the intensity ratio of the substrate radiation with and without the absorber, and the measured film areal density, the photoionization cross section can be directly calculated. The intensity change in the substrate radiation due to the energy loss of the protons in passing through the absorber was at most 3.5% and this correction is easy to measure or calculate. For each film the areal density was measured by non-destructive Rutherford backscattering analysis and also by analytical chemistry methods. Results will be given for the mass absorption coefficient of a number of metals for boron K α , carbon K α , Ni L α and Al K α radiation. We conclude that the technique can yield reliable photoionization cross sections in the soft x-ray region and that, at least in the cases studied, solid-state absorption can be accurately described by the free-atom-absorption theory. More experimental work would be required to allow the extension of this conclusion into the absorption edge region where larger deviations between theory and experiment can be expected.

EXPERIMENTAL X-RAY MASS ATTENUATION COEFFICIENTS
BETWEEN THE M_I AND M_V ABSORPTION EDGE OF RHENIUM

Wayne J. Steele and Jack M. Johnson

Lawrence Livermore Laboratory, University of California
Livermore, California 94550

ABSTRACT

Experimental values obtained for x-ray mass attenuation coefficients between the M_I and M_V absorption edges of rhenium are presented below. Also presented is a brief discussion of the experimental procedure.

Introduction

Situations frequently arise during microprobe analysis of alloy systems in which it is desirable to use certain characteristic lines that are between the M_I and M_V absorption edge of the absorber.

An example would be the advantageous use of $M\beta$ rhenium instead of $M\alpha$ rhenium in the analysis of tungsten-rhenium alloys, in this case $M\beta$ tungsten interferes with $M\alpha$ rhenium characteristic radiation. Another example is the analysis of yttrium-rhenium alloy systems. In this case the mass attenuation coefficient when $L\alpha$ yttrium is attenuated by rhenium is not very well known since $L\alpha$ yttrium characteristic radiation lies between the M_{IV} and M_V absorption edge of rhenium.

Procedure

Thirty-four characteristic radiations between $L\alpha$ antimony (3.439λ) and $M\alpha$ tantalum (7.25λ) were used. These were generated from the pure element standards at 20 keV at approximately 30 nA specimen current with rhenium foils (varying in thickness from 1500 to 3000 Å) used as absorbers.

Since rhenium foils are difficult to make free of oxide, an effective foil thickness was determined experimentally by measuring the attenuation of twelve different characteristic radiations from eight different elements below

the M_I and above the M_V absorption edge. Heinrich's¹ mass attenuation coefficients were used to determine the effective thickness, using the following formula.

$$I = I_0 e^{-\mu \rho x}$$

The foils were then mounted on an adapter ring. The adapter was spring loaded to an arm extending through one of the ports on the microprobe. This configuration made it relatively easy to move the foil between the x-ray source and the electron trap on the spectrometer. When securely in place, the adapter fits over the electron trap. To minimize drift effects, three 10 s counts were taken for each characteristic radiation of interest with the foil removed, and immediately following, another three 10 s counts were taken with the foil in place. This was repeated five times for each characteristic radiation of interest. To minimize possible effects of the electron beam on the pure element standards, and hence the x-ray source, the specimen stage was translated $\sim 2 \mu\text{m}$ following each 10 s counting period.

The measured thicknesses were then used to calculate the mass attenuation coefficients for four foils of significantly different thickness. These (μ) values were then averaged for each radiation and are listed in Table 1. Also listed in Table 1 are appropriate σ values for each radiation as calculated from the (μ) values of each foil. The σ were calculated using the expression

$$\sigma = \sqrt{\frac{\sum_{i=1}^n (\mu - \bar{\mu})_i^2}{n-1}}$$

Table 2 is a list of μ values of elements that might be encountered in microanalysis where characteristic radiation lies between the M_I and M_V absorption edge of rhenium.

Figures 1 and 2 illustrate the scatter of μ values of elements whose characteristic radiation lies between the M_I and M_V absorption edge of gold and rhenium along with the values obtained experimentally.

Table 1. Summary of Derived Mass Attenuation Coefficients

	λ (Ref 4)	μ	σ
$\mu(\text{Re}, \text{SbL}\alpha)$	3.44	1453	61
$\mu(\text{Re}, \text{SnL}\alpha)$	3.60	1615	58
$\mu(\text{Re}, \text{CdL}\beta_1)$	3.738	1775	20
$\mu(\text{Re}, \text{AgL}\beta_1)$	3.934	1963	39
$\mu(\text{Re}, \text{CdL}\alpha)$	3.96	2022	8
$\mu(\text{Re}, \text{AgL}\alpha)$	4.15	2252	40
Re M_I absorption edge	4.227		
$\mu(\text{Re}, \text{RhL}\beta_1)$	4.365	2469	26
$\mu(\text{Re}, \text{PdL}\alpha)$	4.37	2422	39
$\mu(\text{Re}, \text{RhL}\alpha)$	4.60	2793	13
$\mu(\text{Re}, \text{RuL}\beta_1)$	4.6206	2832	36
Re M_{II} absorption edge	4.6210		
$\mu(\text{Re}, \text{RuL}\alpha)$	4.84	2926	43
$\mu(\text{Re}, \text{BiM}\beta)$	4.909	3038	47
$\mu(\text{Re}, \text{PbM}\beta)$	5.076	3231	54
$\mu(\text{Re}, \text{BiM}\alpha)$	5.12	3295	56
$\mu(\text{Re}, \text{MoL}\beta_1)$	5.177	3368	41
Re M_{III} absorption edge	5.234		
$\mu(\text{Re}, \text{PbM}\alpha)$	5.30	3140	43
$\mu(\text{Re}, \text{S K}\alpha)$	5.37	3179	32
$\mu(\text{Re}, \text{MoL}\alpha)$	5.41	3222	57
$\mu(\text{Re}, \text{NbL}\beta_1)$	5.492	3363	57
$\mu(\text{Re}, \text{AuM}\beta)$	5.624	3435	64
$\mu(\text{Re}, \text{NbL}\alpha)$	5.73	3555	40
$\mu(\text{Re}, \text{AuM}\alpha)$	5.84	3748	40
$\mu(\text{Re}, \text{PtM}\alpha)$	6.05	3919	41
$\mu(\text{Re}, \text{P K}\alpha)$	6.16	3797	33
$\mu(\text{Re}, \text{Y L}\beta_1)$	6.212	3784	38
$\mu(\text{Re}, \text{IrM}\alpha)$	6.27	3329	51
Re M_{IV} absorption edge	6.33		
$\mu(\text{Re}, \text{Y L}\alpha)$	6.45	2502	80
$\mu(\text{Re}, \text{ReM}\beta)$	6.504	1739	8
Re M_V absorption edge	6.560		
$\mu(\text{Re}, \text{ReM}\alpha)$	6.729	1370	31
$\mu(\text{Re}, \text{W M}\beta)$	6.797	1370	41
$\mu(\text{Re}, \text{W M}\alpha)$	6.98	1506	8
$\mu(\text{Re}, \text{TaM}\beta)$	7.023	1512	8
$\mu(\text{Re}, \text{SiK}\alpha)$	7.13	1598	8
$\mu(\text{Re}, \text{TaM}\alpha)$	7.252	1646	34

Table 2. Table of Interpolated Mass Attenuation Coefficients

	λ (Ref 4)	μ
$\mu(\text{Re}, \text{ClK}\alpha)$	4.73	2830
$\mu(\text{Re}, \text{S K}\beta)$	5.03	3190
$\mu(\text{Re}, \text{TlM}\beta)$	5.349	3060
$\mu(\text{Re}, \text{HgM}\alpha)$	5.65	3440
$\mu(\text{Re}, \text{P K}\beta)$	5.796	3650
$\mu(\text{Re}, \text{PtM}\beta)$	5.828	3675
$\mu(\text{Re}, \text{ZnL}\beta_1)$	5.836	3680
$\mu(\text{Re}, \text{IrM}\beta)$	6.038	3890
$\mu(\text{Re}, \text{ZnL}\alpha)$	6.07	3850
$\mu(\text{Re}, \text{OsM}\beta)$	6.267	3350
$\mu(\text{Re}, \text{OsM}\alpha)$	6.49	1325

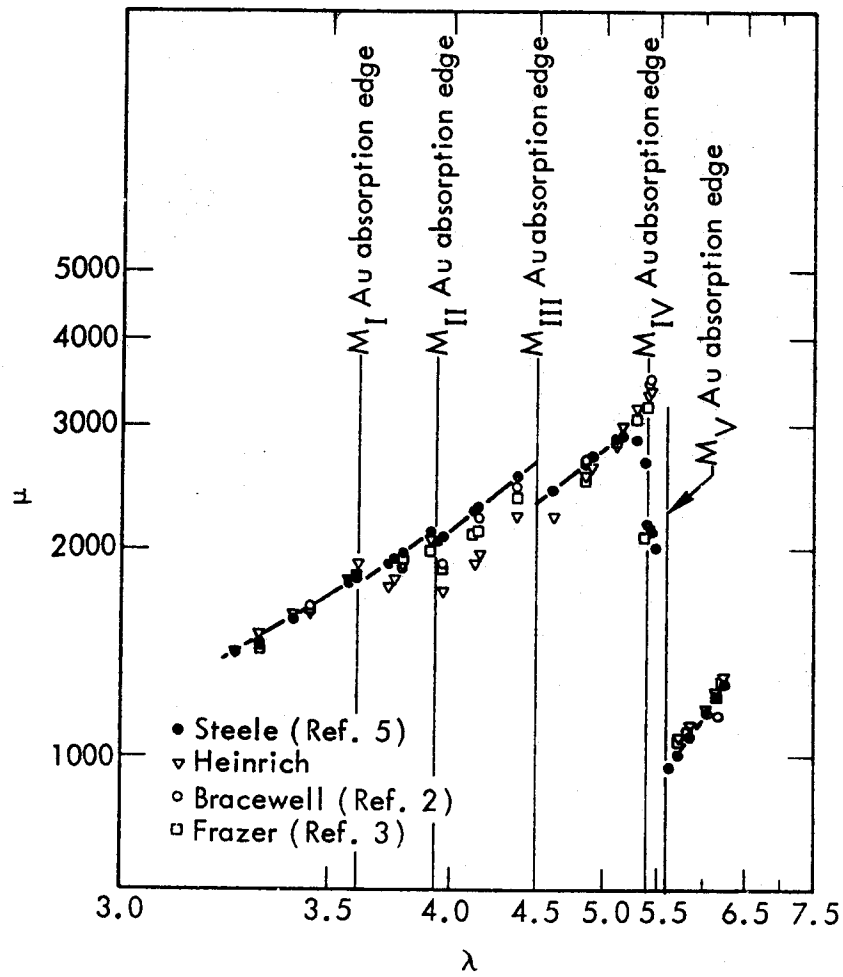


Figure 1. Gold

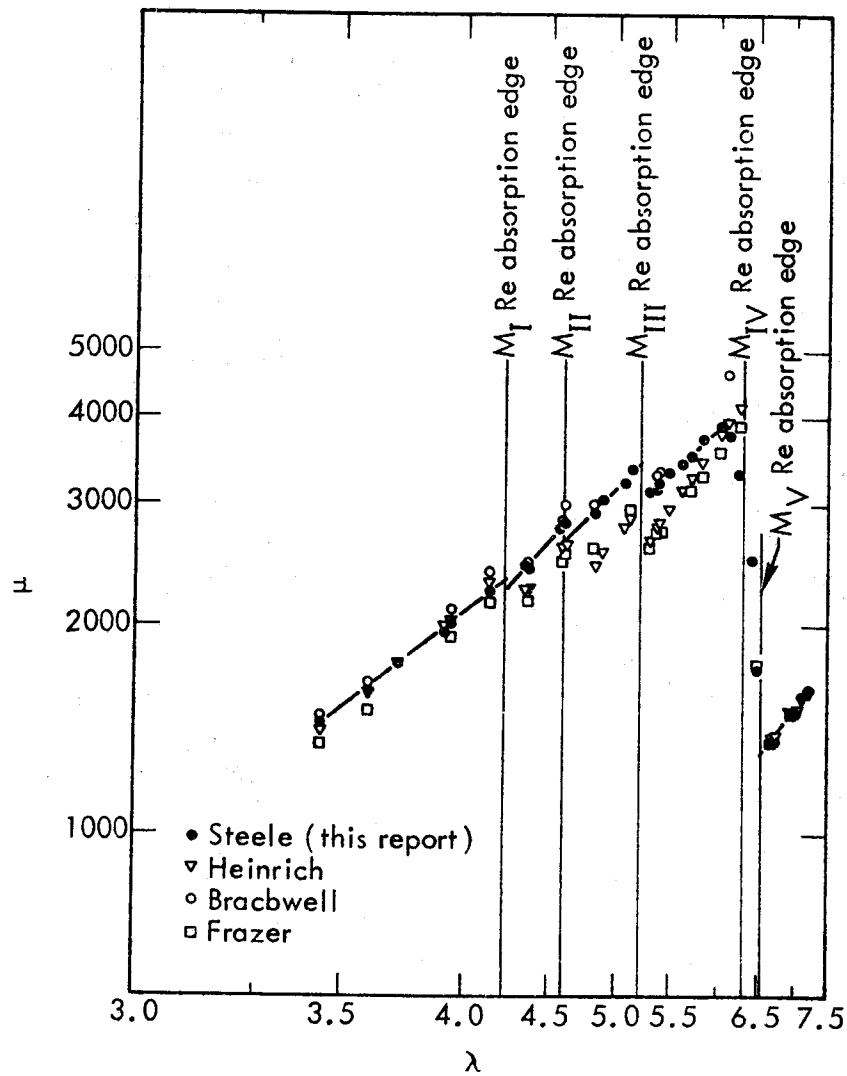


Figure 2. Rhenium

References

1. T. D. McKinley, K.F.J. Heinrich, and D. B. Wittry, Eds, *X-Ray Absorption Uncertainty, the Electron Microprobe*, John Wiley & Sons, Inc, N.Y., 1966.
2. J. Frazer, *A Computer Fit to Mass Absorption Coefficient Data*, Institute for the Study of Matter, Univ of Calif, La Jolla, SIO Ref No. 67-29, 1967.
3. B. L. Bracewell and W. J. Veigele, "Tables of X-Ray Mass Attenuation Coefficients for 87 Elements at Selected Wavelengths," in E. L. Grove and A. J. Perkins, Eds, *Developments in Applied Spectroscopy*, 9, pp 357-400, Plenum Press, 1971.
4. J. A. Bearden, *X-Ray Wavelengths*, John Hopkins Univ, NYO-10586, 1968.
5. W. J. Steele, *Experimental X-Ray Mass Attenuation Coefficients Between the M_I and M_V Absorption Edge of Gold*, Lawrence Livermore Laboratory, UCRL 75503.

Acknowledgements

The authors wish to thank Ronald Reno for fabricating the rhenium foils, Charles Hugenberg for designing and fabricating the necessary hardware, and Perry Studt for statistical evaluation of the data.

Work performed under the auspices
of the U.S. Energy Research &
Development Administration under
contract No. W-7405-Eng-48.

NOTICE

"This report was prepared as an account of work sponsored by the United States Government. Neither the United States nor the United States Energy Research & Development Administration, nor any of their employees, nor any of their contractors, subcontractors, or their employees, makes any warranty, express or implied, or assumes any legal liability or responsibility for the accuracy, completeness or usefulness of any information, apparatus, product or process disclosed, or represents that its use would not infringe privately-owned rights."

Prediction of X-ray Intensities from Small Particles
by a Monte Carlo Calculation

R. L. Myklebust, D. E. Newbury and K. F. J. Heinrich
Analytical Chemistry Division

and

H. Yakowitz
Metallurgy Division
National Bureau of Standards
Washington, D. C. 20234

Abstract

A number of Monte Carlo programs for obtaining information of interest to x-ray microanalysts and scanning electron microscopists have been discussed by several investigators [1,2]. Since the classical theory of quantitative electron probe microanalysis does not apply to the analysis of small particles, we have used a Monte Carlo method to compute the electron scattering and x-ray emissions from spherical and cylindrical particles.

The NBS Monte Carlo program employs a multiple scattering model that is similar in principle to that of Curgenven and Duncumb [3]. There are two important differences in the scattering model between the two programs. In the NBS program, the electron step length varies directly as the electron energy, while in the Curgenven-Duncumb program, equal step lengths were used regardless of electron energy. The second difference involves the multiple scattering angle computation. Curgenven and Duncumb used:

$$\tan\left(\frac{\beta}{2}\right) = \frac{F_i}{E_i} \left(\frac{1}{\sqrt{R_L}}\right) \quad (1)$$

where β is the scattering angle, E_i is the electron energy, F_i is an adjustable parameter fitted so that the program will compute the correct backscatter coefficient for a flat specimen, and R_L is a random number between 0 and 1. This equation truncates the angular distribution of β to a minimum value

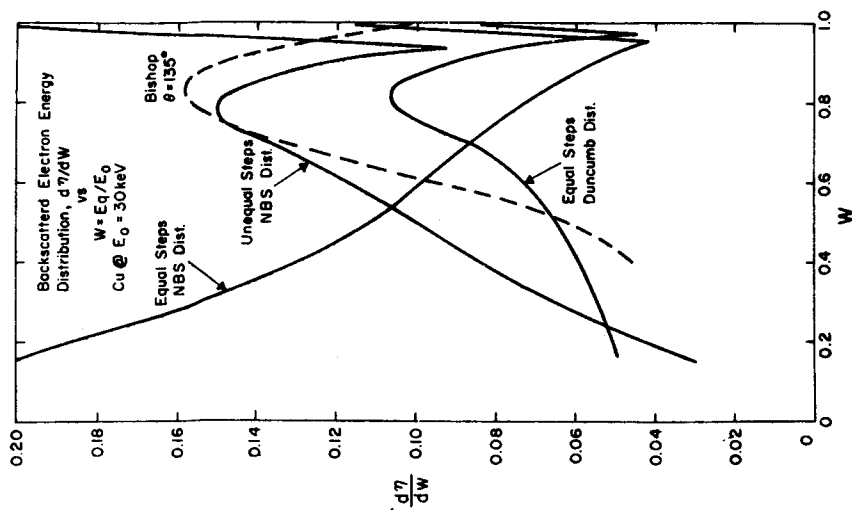


Figure 1. Backscattered electron energy distribution calculated with various step lengths and scattering parameters; experimental data of Bishop [4].

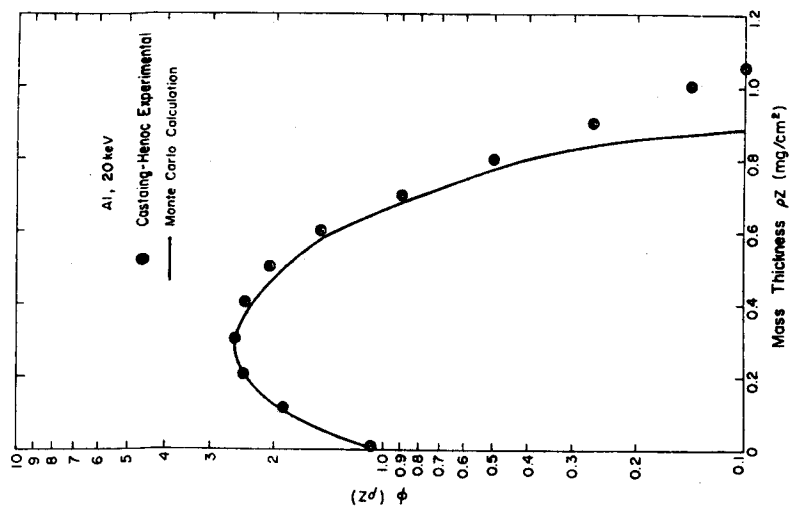


Figure 2. Depth distribution, $\phi(z)$ versus z , for aluminum with a beam energy of 20 keV; experimental data of Castaing and Hénoc [5].

of about 10° to 15° depending on the value of F_i . We have modified equation (1) as follows:

$$\tan\left(\frac{\beta}{2}\right) = \frac{F_i}{E_i} \left(\frac{1}{\sqrt{R_L}} - 1 \right). \quad (2)$$

The energy distributions of the backscattered electrons produced by the different methods is shown in figure 1. Both methods produce too many backscattered electrons in the first step; however, both produce satisfactory results for x-ray emission. A complete description of the NBS Monte Carlo program will appear in the Proceedings of the Workshop on Monte Carlo Calculations in Electron Probe Microanalysis and Scanning Electron Microscopy, to be published in 1976 [1].

The generation of x-rays by electrons is an inefficient process yielding only one characteristic photon for every 1,000 to 10,000 primary electrons. For Monte Carlo computations, this inefficiency may be circumvented by considering the probabilities of x-ray excitation as appropriate fractions of a photon to be excited for each electron scattering event. The x-ray cross-sections are summed at the depths in the specimen where they are generated to produce a distribution in depth of x-ray generation (see figure 2). A numerical integration of this distribution as a function of depth yields the number of photons generated per steradian per electron. Some results are shown in figure 3, with the experimental results of Green [6]. A second summation of the same cross-sections is performed as a function of the path length for an x-ray leaving the specimen in the direction of the detector. The generated x-rays are absorbed along the path out of the specimen:

$$I' = I e^{-\mu_\ell S} \quad (4)$$

where I' is the emitted x-ray intensity, I is the generated x-ray intensity at each increment of path length, μ_ℓ is the

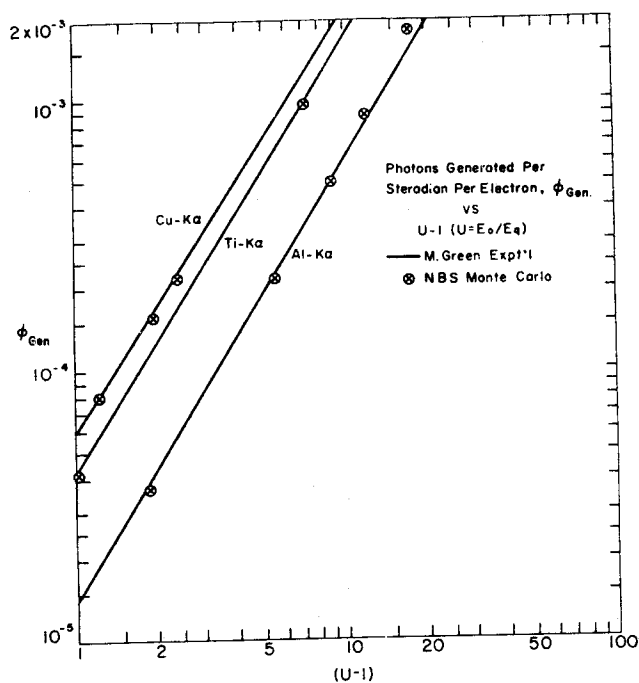


Figure 3. Photons generated per electron as a function of beam overltage; experimental data of Green [6].

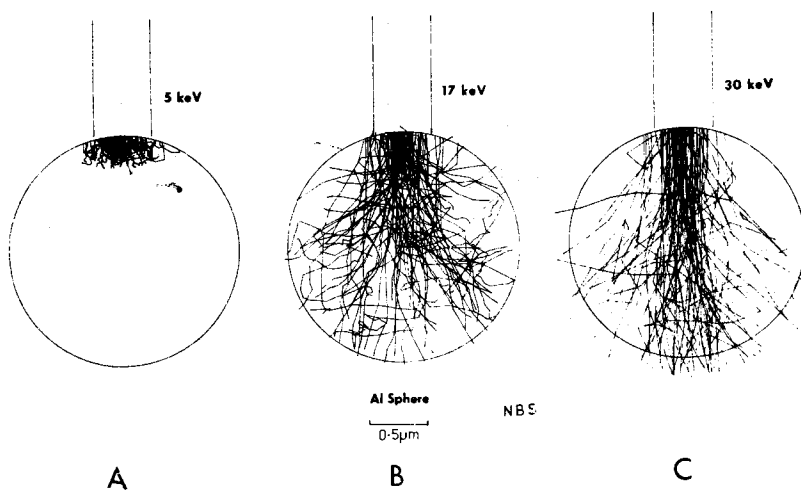


Figure 4. Electron trajectories in 2 μm aluminum spheres at three difference beam energies.

linear absorption coefficient, and s is the path length out of the specimen. This procedure produces a distribution in depth of emitted x-rays which is then numerically integrated to obtain the number of photons emitted per steradian per electron.

The particle size and shape, and the accelerating potential of the beam determine the number of x-rays emitted from a specimen. Figure 4 shows the electron trajectories in 2 μm diameter aluminum spheres at three different beam voltages, with a Gaussian beam 0.5 μm in diameter. The number of x-rays generated will be reduced when the volume of material normally excited by the electron beam exceeds the particle size as is the case in b and c in figure 4. This is demonstrated by the emission of $\text{AlK}\alpha$ x-rays from aluminum spheres relative to bulk aluminum, and is shown in figure 5 as a function of sphere diameter [7].

The number of x-rays emitted will also be affected by the path length necessary to leave the specimen towards the detector. The position of the detector in relation to the particle has a very large effect on the emitted x-ray intensity. Figure 5 shows the emission of $\text{SiK}\alpha$ from Fe-3.22% Si alloy particles relative to the emission from a bulk specimen of the same composition at two detector positions. It is evident from this figure that it is undesirable to position a detector 90° from the beam diameter when analyzing small particles. Many scanning electron microscopes have this configuration. While tilting eliminates this problem for flat specimens, it has no effect on spherical particles.

Monte Carlo calculations can thus provide a powerful and flexible approach to particulate analysis. Any particle geometry can be considered. Analysis is based on the generation of working curves where the independent variable is a particle dimension and the dependent variable is the emitted x-ray intensity normalized by the intensity for a bulk standard.

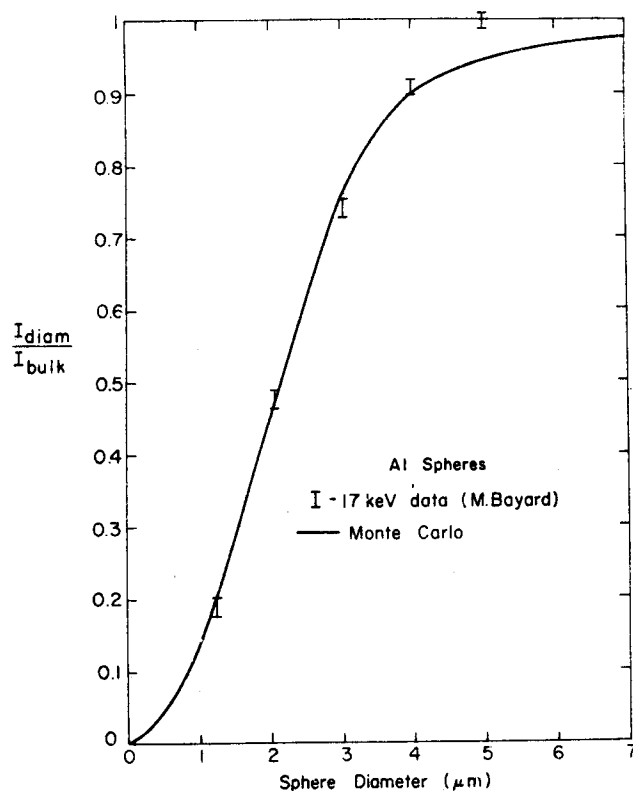


Figure 5. Intensity ratio $I_{\text{Diam}}/I_{\text{Bulk}}$ versus diameter for aluminum spheres, beam energy 17 keV; experimental data of Bayard [7].

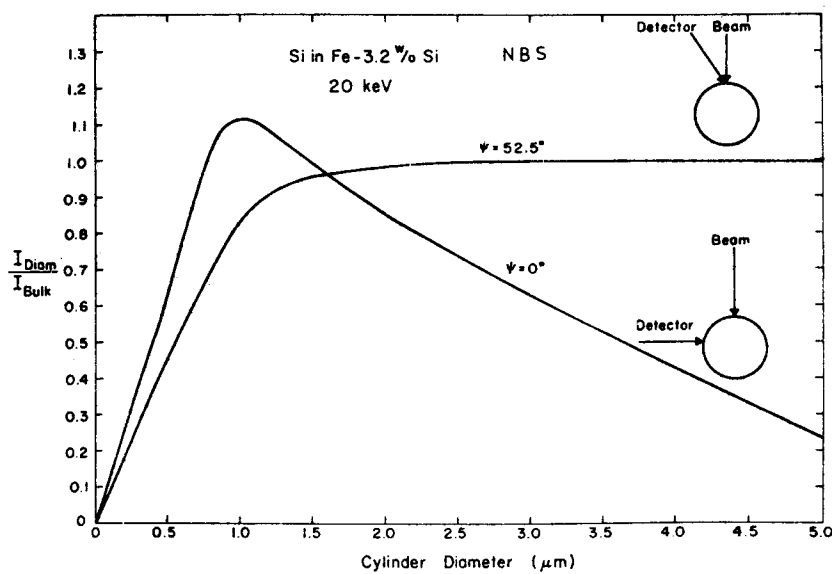


Figure 6. Effect of take-off angle on the intensity ratio $I_{\text{Diam}}/I_{\text{Bulk}}$ for silicon K-radiation from an Fe-3.22% Si alloy needle.

References

1. Heinrich, K. F. J., Yakowitz, H., and Newbury, D. E., eds., Proc. of the Workshop on Monte Carlo Calculations in Electron Probe Microanalysis and Scanning Electron Microscopy, to be published as an NBS Special Publication.
2. Bolon, R. B. and Lifshin, E. in SEM/1973, Proceedings of the 6th Annual SEM Symposium, Johari, O. and Corvin, I., eds. (IIT Research Institute, Chicago, Ill.) p. 286 (1973).
3. Curgenven, L. and Duncumb, P., Simulation of Electron Trajectories in a Solid Target by a Simple Monte Carlo Techniques, Tube Investments Research Laboratories, Report No. 303, (Hinxton Hall, Saffron Walden, Essex, England) (1971).
4. Bishop, H. E. in X-ray Optics and Microanalysis, IV International Congress on X-ray Optics and Microanalysis, Orsay, France, Castaing, R., Deschamps, P., and Philibert, J., eds. (Hermann, Paris), p. 153 (1966).
5. Castaing, R. and Hénoc, J. in X-ray Optics and Microanalysis, IV International Congress on X-ray Optics and Microanalysis, Orsay, France, Castaing, R., Deschamps, P., and Philibert, J., eds. (Hermann, Paris), p. 120 (1966).
6. Green, W., Thesis, University of Cambridge (1962).
7. Bayard, M. in Microprobe Analysis, Andersen, C. A., ed. (Wiley, New York), p. 323 (1973).

X-RAY EXCITATION DEPTH IN THE 2 TO 5 KeV ELECTRON ENERGY RANGE

W. Reuter, J. D. Kuptsis and A. Lurio

IBM Thomas J. Watson Research Center
Yorktown Heights, New York 10598

ABSTRACT: The continuing trend towards miniaturization in the electronic industry imposes severe demands on microanalytical techniques. Frequently encountered problems in electron probe microanalysis are the analysis of thin composite films and the determination of concentration profiles of impurities or dopants in angle lapped samples. In such cases one wants to limit the x-ray excitation to the near surface region. The literature offers the experimentalist a multitude of choices for the estimation of the electron range in a target at a given energy E_0 . These estimates fluctuate by as much as a factor of two depending on the experimental or theoretical definition of the electron range. Most meaningful for the electron microprobe spectroscopist is the effective x-ray excitation depth for which very few data have been published at electron energies below 5 KeV. We determined experimentally the effective excitation depth in thin metal films evaporated onto various substrates. The mass deposition was determined by Rutherford backscatter spectroscopy and chemical analysis. We measured the x-ray intensity of the characteristic film radiation normalized to the radiation from a thick standard as a function of the primary beam energy. The extrapolation of this curve to the saturation level of the intensity ratio at low energies yields a primary energy for which the film thickness represents the effective excitation range. For the electron energy range of interest in this study particular attention was given to the preparation of clean and oxide free films and standards. The standard was a "thick" film prepared under conditions (e-beam evaporation, 10^{-7} torr) identical to those used in the preparation of the thin film. The oxygen content was determined on films deposited on carbon using Rutherford backscatter spectroscopy and was usually found to be negligible.

One would expect that the effective x-ray excitation depth would agree best with the depth at which the most probable energy is reduced to the

critical excitation energy. Castaing¹ proposed the range relation

$$\rho x [\mu\text{g}/\text{cm}^2] = 3.3 (E_o^{1.7} - E_c^{1.7}) A/Z$$

where E is given in KeV. This relationship is based on a deceleration law first proposed by Williams as his best fit to the most probable energy loss measured in mica by White and Millington,² later modified by Webster³ extending the law to higher atomic number targets and finally modified by Castaing to adapt to electrons in the 10-30 KeV range. In its present form the relation is in good agreement with Terrill's⁴ and Cosslett's⁵ experimental data on most probable energy losses in thin films ranging from beryllium to gold. The effective excitation range reported here is indeed in good agreement with Castaing's proposed range equation. Much shorter ranges are estimated if one uses the Thompson Widdington law or defines the range in terms of the extrapolated electron transmission.

-
1. R. Castaing, Adv. in Electronics and Electron Physics, L. Morton, Ed., Academic Press, New York, 317 (1960).
 2. P. White and G. Millington, Proc. Roy. Soc., A, 120, 701 (1928).
 3. P. L. Webster, W. W. Hansen and F. B. Duvenek, Phys. Rev. 43, 839 (1933).
 4. H. M. Terrill, Phys. Rev., 22, 101 (1923).
 5. V. E. Cosslett and R. N. Thomas, Brit. J. Appl. Phys., 15, 1283 (1964).

QUANTITATIVE X-RAY ANALYSIS OF THIN FILMS
IN THE ELECTRON MICROSCOPE

J. I. Goldstein,^{*} G. W. Lorimer⁺ and G. Cliff⁺

^{*}Metallurgy and Materials Science Dept., Lehigh University, Bethlehem, Pa. 18015

⁺Metallurgy Department, University of Manchester, Manchester, England

Cliff and Lorimer⁽¹⁾ have shown that if the primary X-rays generated in the specimen are neither absorbed nor cause X-ray fluorescence, then the following expression:

$$\frac{I_1}{I_2} = k_{12} \frac{C_1}{C_2} \quad (1)$$

where I_1 and I_2 are the measured characteristic X-ray intensities from elements 1 and 2, C_1 and C_2 are the weight fractions of the two elements in question and k_{12} is a factor which can be determined from thin film standards, can be used to carry out quantitative analysis. The thin foil limit or specimen thickness, where X-ray absorption and fluorescence become significant, is to a first approximation greater than the limit where a specimen is sufficiently thin to carry out conventional 100 kV transmission electron microscopy. If this thin foil criterion is satisfied, the intensity ratio I_1/I_2 is also independent of specimen thickness.

Measurements were carried out using the EMMA-4 instrument fitted with a Kevex energy dispersive detector. All analyses were obtained at 100 kV with a probe current of 2-5 nA and a beam diameter of 100-150 nm. Characteristic Fe, Ni and P X-ray peaks and appropriate continuum background levels were integrated using a Kevex series 6000 data processor. Two binary Fe-Ni and one ternary Fe-Ni-P calibration standards were used. The bulk compositions are 35.3 ± 0.54 wt% Ni, remainder Fe and 50.2 ± 0.32 wt% Ni, remainder Fe. The bulk composition of the Fe-Ni-P standard is 2 wt% Ni, 2 wt% P, and 96 wt% Fe. This alloy was heat treated at 750°C for approximately one month in order to produce a two phase alloy containing a b.c.c. α phase of 1.99 ± 0.04 wt% Ni, 0.90 ± 0.04 wt% P and a phosphide (Ph) phase of 2.97 ± 0.10 wt% Ni and 15.6 ± 0.25 wt% P.⁽²⁾

Measurements of $I_1 = I_{Ni}$ and $I_2 = I_{Fe}$ were obtained from ion thinned specimens of the two binary alloys. From the intensity measurements and known compositions, a value of $k_{12} = k_{NiFe}$ from Eqn. 1 was calculated. The thickness

of the specimen was obtained at each analysis point using the method of Lorimer et al.⁽³⁾ This method consists of measuring the separation between contamination spots from the top and bottom of the thin specimen after the sample is tilted through a known angle. Figure 1 shows the variation of k_{NiFe} with specimen thickness for the 35 and 50 wt% Ni alloys. Average error limits in the determination of the k ratio and foil thickness are also given. At a thickness $\geq 0.7 \mu\text{m}$ the specimen is no longer transmission thin to the conventional 100 kV electron microscope.

It can be observed from Figure 1 that k_{NiFe} increases with increasing foil thickness above $0.45 \mu\text{m}$. This variation is primarily caused by X-ray absorption. For a 50-50 Ni-Fe alloy the maximum loss of Ni K_{α} intensity by absorption is 1.7%, 8.1% and 11.9% for foil thicknesses of 0.1, 0.5 and 0.75 microns. The corresponding Fe values are much smaller, 1%, 3% and 4%. Consideration of absorption effects show that the ratio $I_{\text{Ni}}/I_{\text{Fe}}$ should decrease with increasing thickness for the same alloy. According to Eqn. 1, the value of k_{NiFe} should also increase.

Lorimer, et al.⁽³⁾ have pointed out that except for very thin foils, it is necessary to know the specimen thickness in order to correct if necessary the weight fraction ratios obtained using Eqn. 1. Our results for a $0.5 \mu\text{m}$ thick specimen show an increase in k_{NiFe} of 1.3% for the 35 wt% Ni alloy and 3.9% for the 50 wt% Ni alloy over the values given by Cliff and Lorimer.⁽⁴⁾ The practical effect of using the newly determined k_{NiFe} values for quantitative analysis is however small. Using the new k_{NiFe} values from the 50-50 Fe-Ni standard leads to an increase of only 1.3 wt% Ni (2.5% relative) at the 50 wt% Ni level. The results of this study indicate that for all practical purposes the effect of thickness below the transmission thin limit can be neglected for the Fe-Ni system.

Calculations of P contents in the phosphides of the ternary standard using Eqn. 1 and the k_{PNi} and k_{PFe} from Cliff and Lorimer⁽⁴⁾ gave values between 12.5 and 13.0 wt%. These P contents are well below the known values of 15.6 wt%. Measurements of P in phosphides from two meteorites Coahuila and Dayton gave values ≤ 10 wt%. The phosphide regions analyzed in these meteorites were thicker than the surrounding metal matrix and in some cases approached the transmission thin limit. The absorption coefficient of $\text{P}_{K_{\alpha}}$ in the Fe-Ni phosphide is over 4 times that of $\text{Ni}_{K_{\alpha}}$ in the FeNi phosphide. For the phosphide the maximum loss of P intensity by absorption is 12%, 47% and 61% for film thicknesses of 0.1, 0.5 and 0.75 microns. Since the ratio $I_{\text{P}}/I_{\text{Fe}}$ or $I_{\text{P}}/I_{\text{Ni}}$ decreases with increasing

thickness for the same alloy, the appropriate value of k_{PNi} and k_{PFe} in the standard and meteorite samples is significantly higher than the Cliff and Lorimer k values obtained from very thin films.

In summary it appears that for characteristic X-ray lines where the mass absorption coefficient for the material of interest is generally less than $200 \text{ cm}^2/\text{g}$ and the specimen is transmission thin, the Cliff and Lorimer⁽⁴⁾ method is applicable. For X-ray lines where the mass absorption coefficient is greater than $200 \text{ cm}^2/\text{g}$, e.g. $P_{K\alpha}$ in Fe-Ni, the k values must be known as a function of thickness or a separate absorption calculation must be made after the specimen thickness is measured.

References:

1. Cliff, G. and G. W. Lorimer, (1972), in the Proc. Fifth Eur. Congr. Electron Micros., Manchester, p. 140, Institute of Physics, London.
2. Norkiewicz, A. S. and J. I. Goldstein, (1975), Met. Trans. A, 6A, 891.
3. Lorimer, G. W., G. Cliff and J. N. Clark, (1975), to be published in the Proc. of EMAG 75 Meeting, Bristol, Institute of Physics, London.
4. Cliff, G. and G. W. Lorimer, (1975), J. Microscopy, 103, 203.

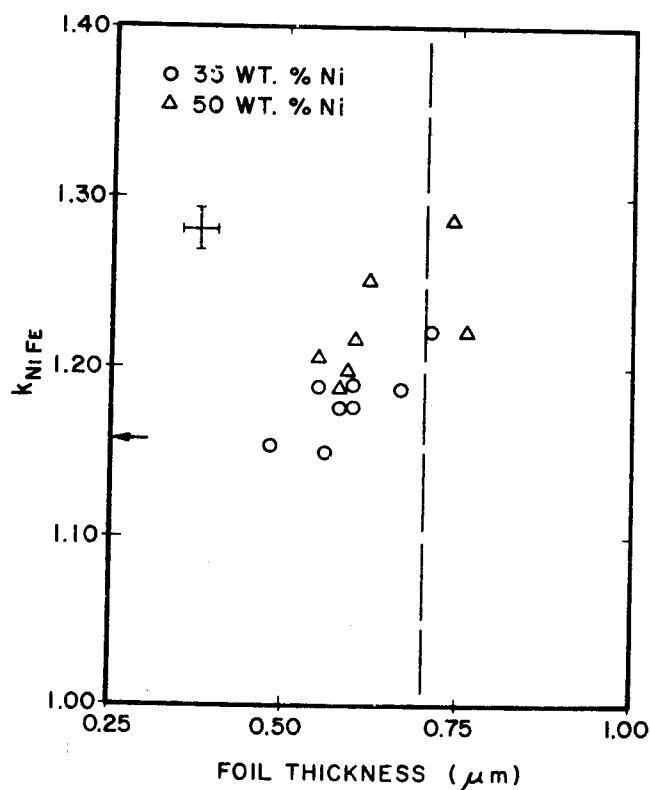


Figure 1: Variation of k_{NiFe} with foil thickness for two Fe-Ni alloys.

Analytic Model for the Depth Distribution of Direct X-ray Generation in the Target Bombarded by Electrons

Kurt F. J. Heinrich
Analytical Chemistry Division
National Bureau of Standards
Washington, D. C. 20234

Abstract

The dependence of the ionization depth distribution $\phi(z)$ on the operating potential can be eliminated by dividing the depth coordinate z (g/cm^2) by the factor $\gamma \equiv (V_o^{1.65} - V_q^{1.65})$, in which V_o is the operating potential and V_q the critical excitation potential for the radiation of interest. If the intensity is scaled so that the area under the $\phi(z)$ curve is equal to one, then the experimental curves for aluminum, with Mg-tracer [1], are virtually identical for all operating voltages, and other experimental $\phi(z)$ curves also have comparable dimensions.

The match of curves from diverse target materials improves if the normalized depth parameter x also contains the ratio of atomic number and atomic weight:

$$x = \frac{Z}{A} \frac{1}{\gamma} z.$$

We have elsewhere [2] proposed the following form for the primary absorption function:

$$f_p = (1 + a\gamma\chi)^{-2}$$

in which $\chi \equiv \mu \text{csc} \psi$ is the well-known absorption parameter, and a is a numerical constant of the order of 1.2×10^{-6} (g/cm^2). The inverse Laplace transform of this function is (model 1):

$$\phi(x) = a^{-2} x e^{-x/a}$$

with x being the normalized depth. This function matches the shape of the experimental $\phi(z)$ curves quite well, but

like Philibert's simplified expression [3], it indicates zero x-ray generation at zero specimen depth.

This feature causes errors in the absorption correction when f_p is small (<0.3). The problem can be overcome easily by shifting the x coordinate by a parameter δ so that the value of $\phi(0)$ fits appropriately. We obtain (model II):

$$\phi(x) = \frac{(x+\delta)e^{-x/a}}{a(a+\delta)}$$

and

$$f_p = \frac{1+a\gamma\chi\frac{\delta}{a+\delta}}{(1+a\gamma\chi)^2} = \frac{1+(1+a\gamma\chi)d}{(1+a\gamma\chi)^2(1+d)}, \quad d=\delta/a.$$

Bishop [4] has pointed out that the tailing of exponential $\phi(z)$ curves at great depth is an unrealistic feature which tends to displace the position of the average depth of x-ray generation. In practice, this defect is of little consequence when the absorption is high. However, the model II can be further modified by displacing the base line for the curve:

$$\begin{aligned} \phi(x) &= \frac{(x+\delta)e^{-x/a} - (x_r+\delta)e^{-x_r/a}}{a(a+\delta) - [a^2 + (a+x_r)(x_r+\delta)]e^{-x_r/a}} = \\ &= \frac{(y+d)e^{-y} - (r+d)e^{-r}}{d+1 - [1+(1+r)(r+d)]e^{-r}} a^{-1} \\ f_p &= \frac{1+wd - \frac{w^2}{w-1}(r+d)e^{-r} - [1-(r+d)\frac{w}{w-1}]e^{-rw}}{w^2 \left\{ 1+d - [1+(1+r)(r+d)]e^{-r} \right\}} \end{aligned}$$

where $w=1+a\gamma\chi$, x_r =range of x-ray emission on the same scale as x , $r=x_r/a$, $y=x/a$. The numerical values of the above parameters, and the results obtained, will be discussed.

References

- [1] Castaing, R. and Hénoc, J., Proceeding of the 4th International Congress on X-ray Optics and Microanalysis, University of Tokyo Press, Japan, p. 163 (1972).
- [2] Heinrich, K. F. J., Anal. Chem. 47, 2408 (1975).
- [3] Philibert, J., Proceedings of the 3rd International Symposium on X-ray Optics and X-ray Microanalysis, Stanford, Academic Press, New York, p. 379 (1962).
- [4] Bishop, H. E., The Prospects for an Improved Absorption Correction in Electron Probe Microanalysis, United Kingdom Atomic Energy Authority, Harwell, United Kingdom, Report AERE-R7688 (1974).

An Overview of the Glass Standards Program
for Microanalysis at the National Bureau of Standards

C. E. Fiori, K. F. J. Heinrich, R. B. Marinenko
M. M. Darr, D. H. Blackburn, D. E. Newbury and J. A. Small
Institute for Materials Research
National Bureau of Standards
Washington, D. C. 20234

Abstract

The quantitative procedures developed for flat, thick specimens cannot be easily adapted to the shapes of small particles. Therefore, alternative methods of analysis have been, and are being, developed [1,2]. These methods need to be critically tested. The experimental determination of both characteristic and continuous radiation from a wide range of small targets of well-known concentration and shape must be performed. For this purpose, it has been necessary to prepare suitable experimental samples. For elemental targets, metal wires and spheres have been found useful [3]. For the study of multi-element targets, we have been preparing and testing a set of glasses of widely varying composition which are available in both fiber and bulk form. Work is in progress to spheridize a number of these glasses while not altering their elemental composition.

Table 1 lists those glasses which are presently available in both bulk and fiber form. The values given are nominal compositions as determined from the weights of the oxides used in the manufacture of the glass. These nominal compositions have been found to agree well with subsequent chemical analysis. The bulk glasses are homogeneous and should prove useful as standards in microanalysis. Furthermore, it is possible to add a great number of elements to glass. Consequently, they can be used as standards for those elements which are not stable in their pure form, such as rare earths.

Table 1. Glasses Available

Oxide	<u>K227</u>	<u>K229</u>	<u>K230</u>	<u>K249</u>	<u>K251</u>	<u>K252</u>	<u>K253</u>	<u>K240</u>	<u>K309</u>	<u>K326</u>	<u>K375</u>	<u>K376</u>	<u>K377</u>	<u>K378</u>	<u>K373</u>
Li ₂ O										30.0					
B ₂ O ₃															
Na ₂ O										2.0	14.05	13.99	13.91	13.74	14.06
MgO								5.0		30.1					
Al ₂ O ₃			5.0	5.0	2.5				15.0						
SiO ₂	20.0	30.0	30.0	30.0	30.0	40.0	40.0	40.0	40.0	29.9	68.09	67.72	67.28	66.42	68.13
P ₂ O ₅															
CaO									15.0	8.0					
TiO ₂								10.0							
MnO ₂						5.0	10.0								
FeO															
Fe ₂ O ₃									15.0						
CoO						5.0	2.5								
CuO						5.0	2.5								
ZnO			5.0			10.0	10.0	5.0			6.15	6.12	6.08	6.02	6.15
GeO ₂															
ZrO ₂								10.0							
BaO			10.0	10.0	10.0	35.0	35.0	30.0	15.0		11.58	11.54	11.47	11.34	11.59
CeO ₂															
Ta ₂ O ₅			5.0	10.0	5.0										
PbO	80.0	70.0	45.0	42.5	47.5										
Bi ₂ O ₃				2.5	5.0										
U ₃ O ₈											0.13	0.63	1.26	2.48	0.063

Table 1. Continued

Oxide	K409*	K411*	K412*	K456	K493	K453	K491	K458	K489	K495	K490	K496	K497
Li ₂ O					0.001		0.001		0.002	5.0	4.67		0.001
B ₂ O ₃					.14		.11		.20	75.0	70.0		.15
Na ₂ O	9.68												
MgO	<.1	14.64	19.33									9.03	8.64
Al ₂ O ₃	14.74	<.1	9.26		0.20		0.16		0.29	20.0	18.68	11.43	10.92
SiO ₂	54.28	54.24	45.38	28.77	27.89		.19	49.38	46.76		.42		.27
P ₂ O ₅												79.54	76.03
CaO	0.19	15.53	15.29										
TiO ₂					0.32		0.26		0.46		0.55		0.35
MnO ₂													
FeO	6.43	4.39	2.77										
Fe ₂ O ₃	14.15	11.23	8.15		0.32		0.26		0.46		0.55		0.35
CoO													
CuO													
ZnO								3.82	3.72				
GeO ₂						41.28	37.98						
ZrO ₂					0.49		0.40		0.70		0.85		0.54
BaO								46.8	43.88				
CeO ₂					0.68		0.56		0.98		1.19		0.76
Ta ₂ O ₅					0.88		0.72		1.26		1.53		0.98
PbO				71.23	69.08	58.72	59.35		1.28		1.55		0.99
Bi ₂ O ₃													
U ₃ O ₈													

27C

*An asterisk indicates chemical analysis. Glass fibers available for all except 409, 411, 412. Results are given as weight percent of oxide present.

References

1. Yakowitz, H., Newbury, D. E. and Myklebust, R. L., Approaches to Particulate Analysis in the SEM with the Aid of a Monte Carlo Program, SEM/1975 (Part 1), Proc. of the Annual SEM Symposium, Chicago, Ill. (1975).
2. Armstrong, J. T. and Buseck, P. R., Quantitative Chemical Analysis of Individual Microparticles using the Electron Microprobe: Theoretical, Anal. Chem. 47, 13, 2178-2192 (1975).
3. Hoffman, H. J., Weihrauch, J. H. and Fechtig, H. F., An Empirical Method for the Quantitative Chemical Analysis of Microparticles with the Electron Probe, Proc. Vth International Congress on X-ray Optics and Microanalysis, Möllenstedt and Gaukler, eds., Tübingen, West Germany (in German) (1968).

EVALUATION OF FORMULAS FOR IONIZATION CROSS SECTION IN ELECTRON PROBE MICROANALYSIS

David F. Kyser

IBM Research Laboratory
San Jose, California 95193

One of the fundamental concepts and formulas which enter into any quantitative theory of electron probe analysis is the energy-dependent cross-section for ionization $Q(E)$. In the conventional method of chemical analysis with elemental standards, the absolute magnitude of the cross-section is not important since it cancels out experimentally in forming the k-value, but the energy-dependence of Q is critically important. This is because the incident electron can ionize a particular atomic level in the atom whenever the electron has a kinetic energy greater than the threshold energy E_c for ionization. In those methods which have been proposed for standardless quantitative analysis, the absolute magnitude of the cross-section must also be known before any serious calculations can be made.

A recent survey of cross-section data has been published by Powell [1], and values were proposed for the "effective" Bethe parameters in the linearized Bethe formula to describe the energy-dependence and magnitude of the cross-section. The parameters were fitted over the range $4 \leq U_0 \leq 30$ where $U_0 = E_0/E_c$ and E_0 is the incident electron energy. This is unfortunate because much of the work done in quantitative analysis is in the region $U_0 \leq 4$. Powell has also evaluated other expressions proposed for $Q(E)$ and compared them with the linearized Bethe formula [2].

We have utilized a different method to evaluate several expressions proposed for the cross-section $Q(E)$. The method utilizes a Monte Carlo calculation [3] of electron scattering and energy loss within the target, coupled with an expression for $Q(E)$, to generate the depth-distribution of ionization $\phi(\rho z)$ for a particular electron shell in a solid target. The integral of $\phi(\rho z)$ is also calculated easily, as well as the Laplace transform of $\phi(\rho z)$ which yields the absorption correction $f(x)$. The integral of $\phi(\rho z)$, which is proportional to the total emission intensity I_T generated in the target, is then compared with experimental data of Green [4] for various values of E_0 . While this method is an indirect test of the expression used for $Q(E)$ due to the fact that $Q(E)$ is "integrated"

over the range $E_c \leq E \leq E_0$, it can still be a sensitive test for the proper energy-dependence of $Q(E)$. Green showed that after an experimental correction was made for self-absorption, the generated intensity I_T was experimentally determined to be proportional to $(U_0 - 1)^n$ where $n = 1.63$ for a variety of K and L lines. A theoretical value of $n = 1.67$ had been proposed previously by Green and Cosslett [5] for K-lines.

The Monte Carlo model utilized in the present work for electron scattering and energy loss is the same as that used previously by Kyser and Murata [3] for quantitative analysis of thin films on substrates. The model utilizes screened Rutherford scattering and the continuous energy loss equation of Bethe to calculate the energy loss between angular scattering points. The electron trajectories calculated are independent of the expression for $Q(E)$ used subsequently to calculate the number of ionizations within each step length of the electron trajectory. For each target and value of E_0 , 1000 electron trajectories were simulated to calculate I_T . All of the Monte Carlo calculations were "correlated" because the same list of random numbers were used in each simulation. This results in the maximum precision when comparing results from different cases [6].

Five different formulas for $Q(E)$ were used to calculate I_T versus E_0 in thick targets of Al($AlK\alpha$), Cu($CuK\alpha$) and Au($AuL\alpha$). The five formulas for $Q(E)$ are:

Q_{W-T} : reference [7], section 2.3

Q_G : reference [8], eq. 22

Q_R : reference [9], eq. 15

Q_B : reference [5], eq. 8

Q_{B-p} : reference [2], eq. 2 with $c = 0.65$.

Only the energy-dependence was retained in these formulas, and all other constants which describe the absolute value of $Q(E)$ were deleted in the Monte Carlo calculations of I_T . The expression for Q_B is originally due to Bethe, and is discussed in references [2] and [5]. The expression for Q_{B-p} is the Bethe expression with the particular constants suggested by Powell for $4 \leq U_0 \leq 30$ and the K shell.

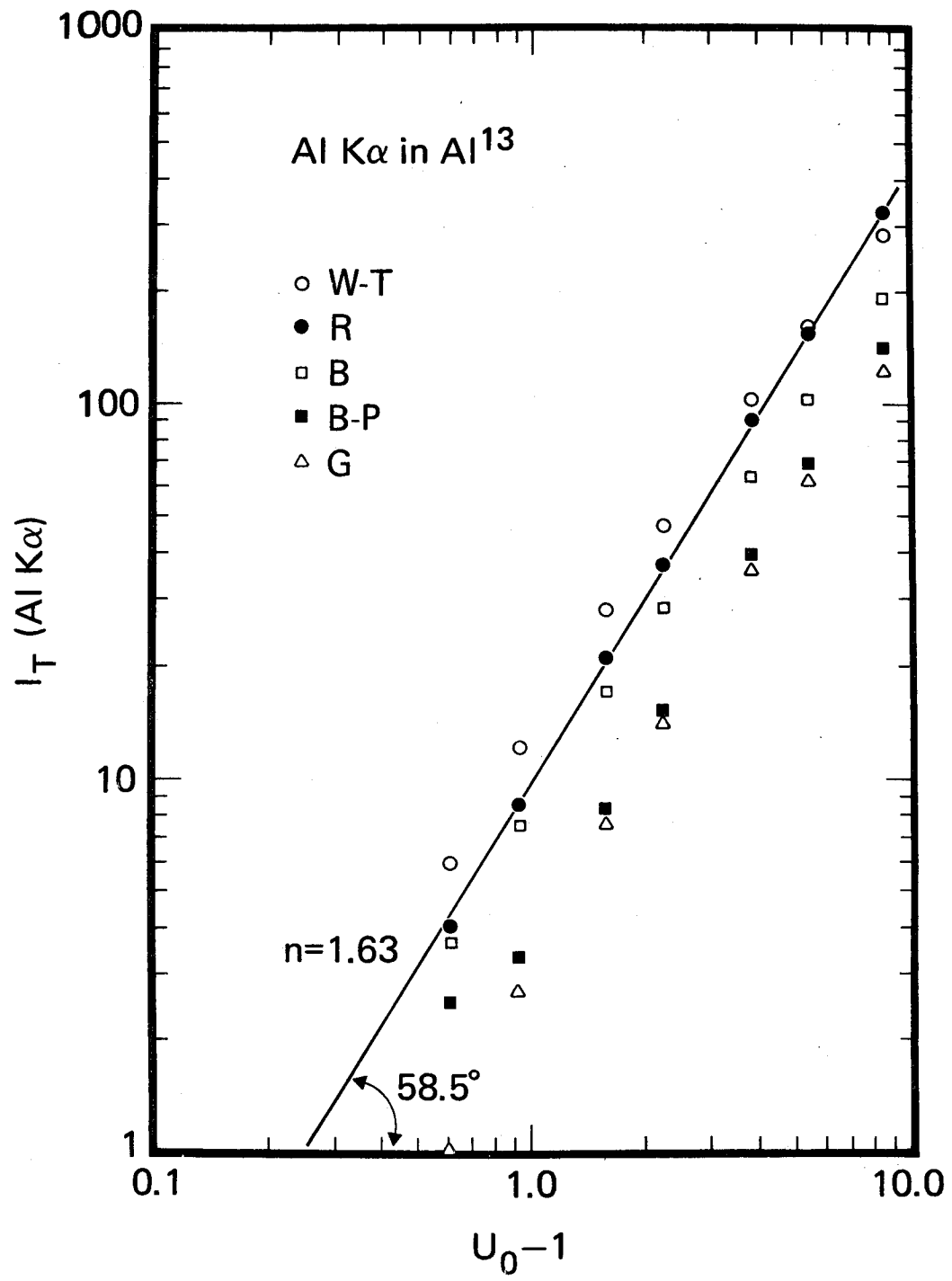
An example of the results obtained with these expressions for $Q(E)$ in a Monte Carlo calculation of I_T is shown in Figure 1 for Al($AlK\alpha$). When $\log I_T$ is plotted versus $\log (U_0 - 1)$, the slope of the curve is n if $I_T \propto (U_0 - 1)^n$. Only the use of Q_R results in a straight line, and hence a unique value of n , over the whole range of $(U_0 - 1)$ investigated. This range of $(U_0 - 1)$ is the

same as that investigated by Green experimentally [4]. The value $n = 1.63$ is also the same as that found by Green. Similar behavior for the five expressions evaluated was observed in $\text{Cu}(\text{CuK}\alpha)$ and $\text{Au}(\text{AuL}\alpha)$ targets. Recently Quarles [10] has suggested that Q_B be corrected with a relativistic term originally proposed by Gryzinski [11]. The addition of this correction to Q_B only slightly improves the non-linearity of I_T .

Based on these results, it appears that the form of $Q(E)$ proposed by Reuter [9] is more accurate than the other forms over large ranges of $(U_0 - 1)$. Of course, this conclusion is based on the accuracy of the Monte Carlo model which simulates electron scattering and energy loss. The Monte Carlo model also has an advantage in that it can easily incorporate any expression for $Q(E)$ to calculate I_T , whereas other analytic models must be able to perform exact integration of $Q(E)$ within an integrand to calculate I_T .

References

- [1] C. J. Powell, Rev. Modern Physics 48, 33 (1976).
- [2] C. J. Powell, Proc. NBS Symp. on Monte Carlo Calculations (Nat. Bur. Stds., 1975), to be published.
- [3] D. F. Kyser and K. Murata, IBM J. Res. Dev., 18, 352 (1974).
- [4] M. Green, Proc. 3rd Int. Symp. X-Ray Optics and Microanalysis (Academic Press, N.Y., 1962), p. 185.
- [5] M. Green and V. E. Cosslett, Proc. Phys. Soc. 78, 1206 (1961).
- [6] J. M. Hammersley and D. C. Handscomb, Monte Carlo Methods (Methuen, London, 1964), Ch. 4.4.
- [7] C. R. Worthington and S. G. Tomlin, Proc. Phys. Soc. 69A, 401 (1956).
- [8] M. Gryzinski, Phys. Rev. 138, A336 (1965).
- [9] W. Reuter, Proc. 6th Int. Symp. X-Ray Optics and Microanalysis (Univ. of Tokyo Press, 1971), p. 121.
- [10] C. A. Quarles, Phys. Rev. 13A, 1278 (1976).
- [11] M. Gryzinski, Phys. Rev. 138, A322 (1965).



Progress in the Measurement of Relative
X-ray Line Intensities

K. F. J. Heinrich, C. E. Fiori and R. L. Myklebust
Analytical Chemistry Division
National Bureau of Standards
Washington, D. C. 20234

Abstract

The relative intensities, or "weights" of lines, (i.e., probabilities of production of photons) of x-ray line generation from the same excited shell of an element are important to x-ray spectrometric analysis. Accurate knowledge of these intensities is required for the estimation of fluorescent x-ray emission [1]. The relative intensities are also used in procedures for the treatment of line interference presently under development in our laboratory [2]. Values reported in the literature differ by large amounts. The development of the solid-state detector and of reliable corrections for absorption of primary x-rays excited by electrons permit an accurate measurement of the intensities. Such measurements were recently performed for K-lines of elements of atomic number from 20 to 30 by Smith et al. [3].

Our measurements are made with a lithium-drifted silicon detector on electron-excited spectra. The background correction applied has been reported previously [4]. The absorption correction is that recently published by Heinrich and Yakowitz [5]. Where lines overlap partially, they are separated by fit to a Gaussian distribution. Corrections are also applied for incomplete charge collection and for the silicon escape peak. In the energy region investigated by Smith et al., our results are in good agreement with those of these authors. Measurements extending over a wider range of atomic numbers and on the x-ray lines of the L- and M-series are in progress.

References

1. Heinrich, K. F. J., Anal. Chem. 44, 350 (1972).
2. Fiori, C. E., Myklebust, R. L., and Heinrich, K. F. J., these proceedings.
3. Smith, D. G. W., Reed, S. J. B., and Ware, N. G., X-ray Spectrometry 3, 149 (1974).
4. Fiori, C. E., Myklebust, R. L., Heinrich, K. F. J., and Yakowitz, H., Anal. Chem. 48, 172 (1976).
5. Heinrich, K. F. J. and Yakowitz, H., Anal. Chem. 47, 2408 (1975).

SECONDARY ELECTRON EMISSION

BY

T. E. Everhart

University of California
 Department of Electrical Engineering
 and
 Computer Sciences
 Berkeley, California

Secondary electron emission results when energetic electrons bombard solid targets, exciting electrons within the target that subsequently escape. Primary electrons that suffer large-angle deflections in the target may also be re-emitted, and may excite additional target electrons in this process. Thus, secondary electrons consist of 3 classes:

- (1) target electrons excited by entering primaries $\Delta_p I_p$,
- (2) re-emitted primary electrons that, in general, suffer some loss of energy, ηI_p (backscattered electrons), and (3) target electrons excited by backscattered electrons, $\Delta_B \eta I_p$.

This paper attempts to provide a physical understanding of the excitation interaction between energetic primary or backscattered electrons and the target electrons, as well as the escape mechanism for excited electrons. The areas from which backscattered and excited electrons escape influence resolution of scanning electron microscopes. The magnitude of the secondary electron emission coefficient, which is

dependent upon geometry, as well as the material constitution of the target, influences the contrast in SEM's. The energy distribution of the secondary electrons is sometimes broadened for nearly-free electron metals such as aluminum, leading to the suggestion that plasmon decay is a mechanism of secondary electron excitation. Slight departures from a pure metal surface can change the observed energy distribution.

Experiments as well as analysis bearing on these matters will be discussed.

APPLICATIONS OF PHOTOELECTRON MICROSCOPY

William J. Baxter

Research Laboratories, General Motors Corporation, Warren, MI
48090

In this form of electron microscopy, photoelectrons emitted from a metal by ultraviolet radiation are accelerated and imaged onto a fluorescent screen by conventional electron optics.^{1,2} Image contrast is determined by spatial variations in the intensity of the photoemission. The dominant source of contrast is due to changes in the photoelectric work function, between surfaces of different crystalline orientation, or different chemical composition. Topographical variations produce a relatively weak contrast due to shadowing and edge effects.

Since the photoelectrons originate from the surface layers (e.g. ~5-10 nm for metals), photoelectron microscopy is surface sensitive. Thus to see the microstructure of a metal the thin layer (~3 nm) of surface oxide must be removed, either by ion bombardment or by thermal decomposition in the vacuum of the microscope. The contrast is then due to the crystalline anisotropy of the work function (Fig. 1). On the other hand this surface sensitivity provides unique observations of the mechanical behavior of the natural oxide during plastic deformation of the underlying metal.³ The white lines of strong photoemission in Fig. 2 (so-called photostimulated exoelectron emission), show where the surface oxide on a steel sample has ruptured along the

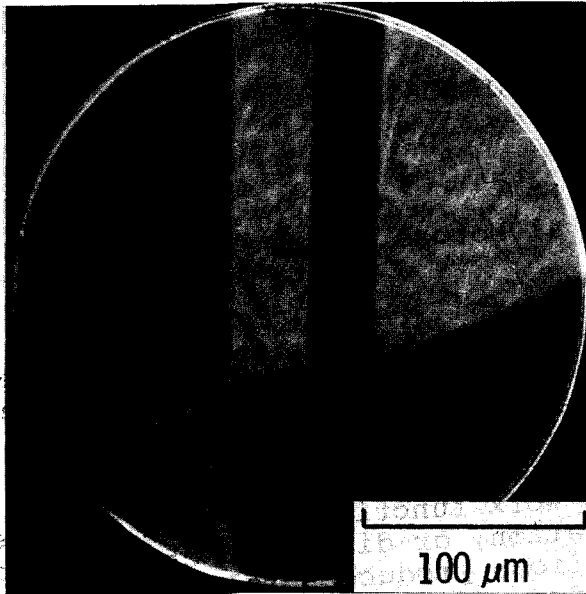


FIG. 1. Photoelectron micrograph of nickel after removal of surface oxide (Ref. 2).

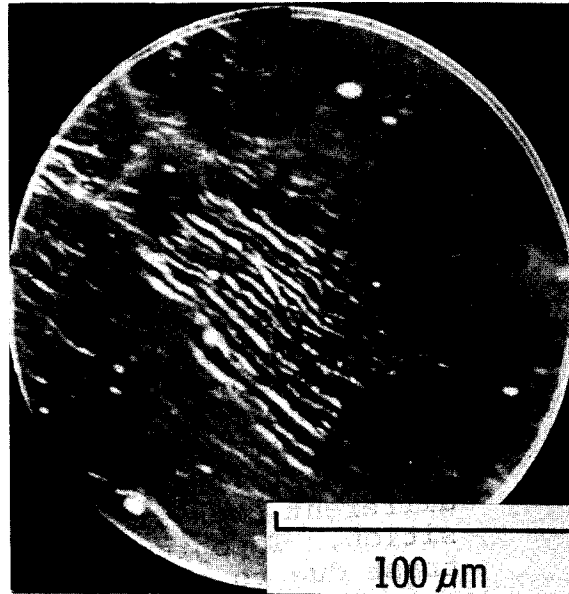


FIG. 2. Slip lines on 1018 steel after ~4% tensile deformation. Strong photoemission from steps where surface oxide has ruptured (Ref. 3).

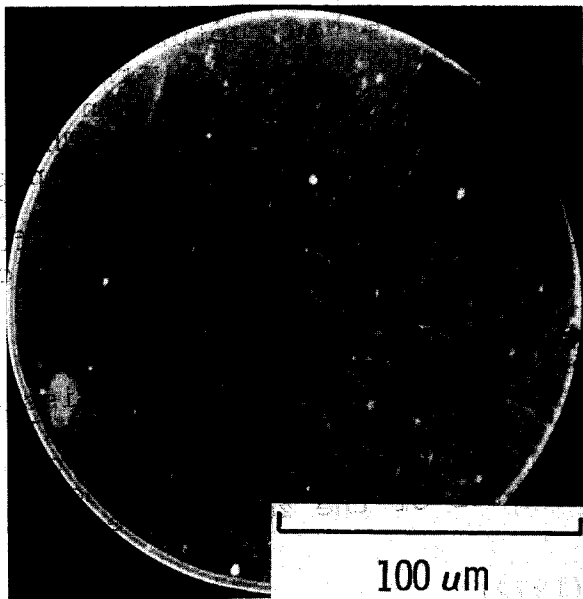


FIG. 3. Topographical contrast of surface scratch and slip lines on 1018 steel after oxide has reformed (Ref. 3).

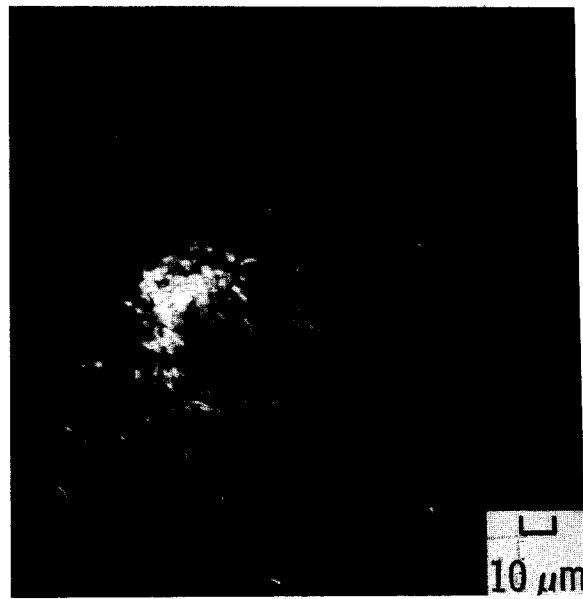


FIG. 4. Photoelectron micrograph of the plastic zone at the tip of a fatigue crack in 1065 steel (Ref. 4).

CONSIDERATIONS IN MAKING STEREO MICROGRAPHS WITH THE SCANNING ELECTRON MICROSCOPE - POSITIONING THE STEREO WINDOW

Earl R. Walter

Research and Development Department, Chemicals and Plastics
Union Carbide Corporation, South Charleston, West Virginia 25303

A variety of factors must be controlled in order to obtain stereo micrograph pairs with the SEM which provide maximum effectiveness along with ease of viewing. These include the following:

1. Where possible, micrographs should be sharp from edge to edge. This may require the use of an Autofocus attachment although somewhat the same effect can be obtained by maintaining the point of sharpest focus near opposite edges of the two micrographs forming the stereo pair.
2. The difference in tilt angle between the two micrographs of the pair should be kept in the 4 to 6° range to provide a normal perspective.¹
3. Micrographs forming a stereo pair should be made at relatively low tilt angles to prevent large differences in the field of view of the two micrographs and to minimize the left to right magnification variations. The minimum tilt angle consistent with adequate signal level and contrast is usually recommended.
4. The tilt axis of the microscope stage should coincide as nearly as possible with the plane and field of the micrographs.
5. The plane of the specimen shown in the micrographs and preferably the complete field of the specimen in the micrographs should appear to be slightly behind the stereo window. The apparent tilt axis will then appear to be outside the particular edge of the micrographs from which the plane of the specimen is tilted. See Figures 1 and 3. Under these conditions, the right eye micrograph will show a greater area of the specimen at the left side than the left eye micrograph and the left eye micrograph will show a greater area at the right side. In effect, the right eye will appear to see behind the stereo window on the left and the left eye will appear to see behind the stereo window on the right. This is accomplished by the way the fields of the two micrographs forming the stereo pair are positioned on the record scope of the SEM.

In practice the stereo window is positioned by shifting the field of the second micrograph of a stereo pair by a discrete amount relative to that of the first. This is done as follows: After the first micrograph of a pair is made, the tilt of the specimen is increased 4 to 6° and the scope is refocussed. The position of the image is realigned with its original position along the bottom edge of the micrograph area on the display scope. The image is then shifted an additional small amount toward the bottom of the screen as indicated in Figure 2. This will reduce the area seen on the bottom edge of the high tilt micrograph and provide the parallax required to maintain the image behind the stereo window when the micrographs are viewed. See Figure 1 for the geometry involved. If the SEM has been set up with the tilt axis vertical rather than horizontal, it will be necessary to shift the image of the second micrograph horizontally rather than vertically. It is obvious that in either case, the micrographs must be viewed with the tilt axis aligned vertically.

1. E. R. Walter, Proc 31st Ann. Mtg. EMSA 1973, p. 234

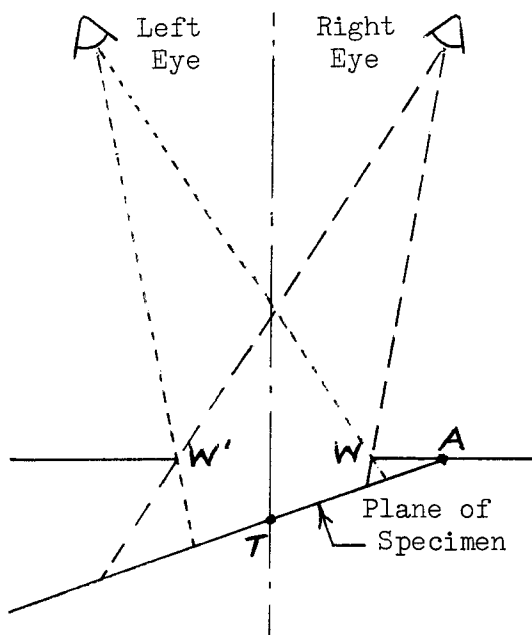


FIG. 1. Geometry of stereo image formation with SEM (exaggerated). WW'- Stereo window and actual size of micrographs. The dashed lines show the limits of the fields in the left and right eye micrographs of the stereo pair. T- Actual tilt axis. A- Apparent tilt axis.

FIG. 2. MoO₃ crystals at 100X. Limits of fields for stereo micrograph pair in Fig. 3 are indicated by dashed lines for left eye image and solid lines for right eye image.

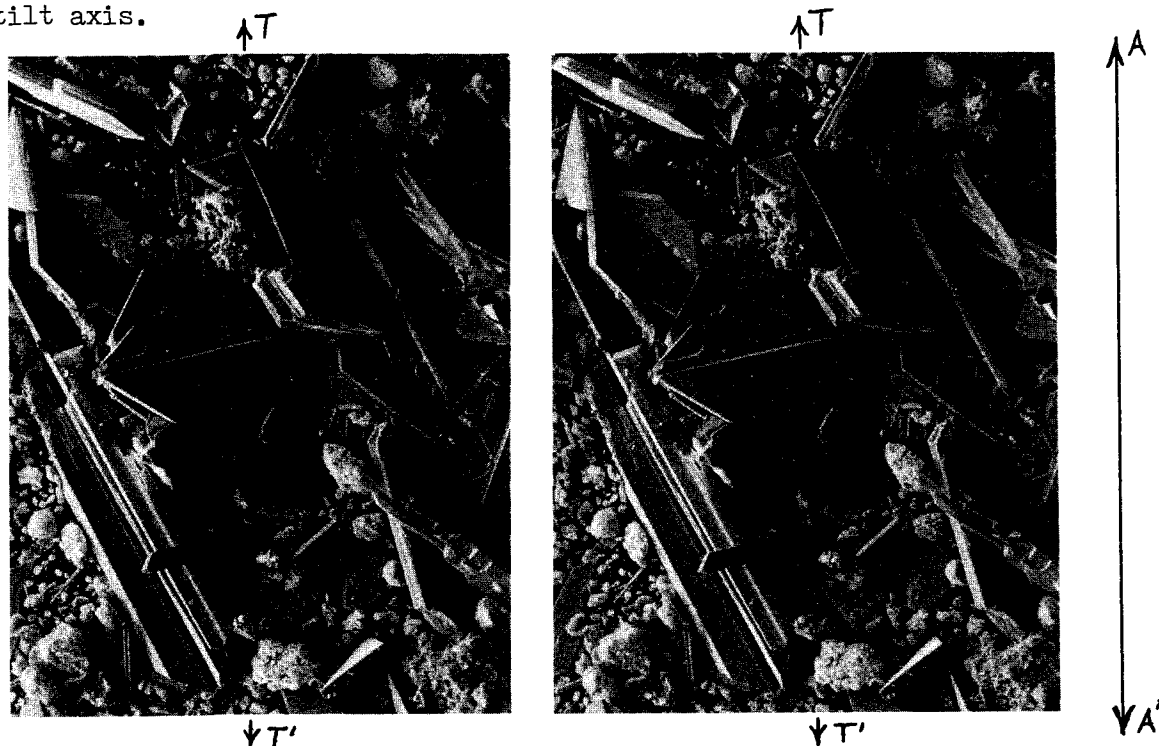


FIG. 3. Stereo micrograph pair with image maintained behind the stereo window by proper specimen field positioning. TT'- Actual tilt axis. AA' Apparent tilt axis.

RESOLUTION TEST FOR THE SEM

R.A. Ploc

Atomic Energy of Canada Limited, Chalk River Nuclear Laboratories
Chalk River, Ontario, Canada K0J 1J0

Many experiments have been proposed for testing resolution in the scanning electron microscope but no standard has been universally accepted. Many investigators have used the smallest separation between two arms of a 50-50% Al-W alloy dendrite as being a measure of resolution but, like other tests, criticism has persisted due to the difference in vertical height between the arms. During the course of our investigations of anodically formed oxides on Zircaloy-2 (a dilute Zr alloy containing 0.05% Ni, 0.1% Fe, 0.1% Cr and 1.5% Sn) a rapid measure of instrument performance was found. The SEM results presented here were obtained on a Coates and Welter CUIKSCAN Model 106A.

The outer surface of two separate oxides labelled A and B were examined while situated on the metal substrate in the scanning electron microscope. The conditions of oxide formation were:

A	B
Zircaloy-2	Zircaloy-2
Constant Current Anodization	Constant Current Anodization
Current Density of 2 mA/cm ²	Current Density of 1 mA/cm ²
Final Cell Voltage of 25 Volts	Final Cell Voltage of 25 Volts
85% Phosphoric Acid Electrolyte	1N Nitric Acid Electrolyte

Figures 1 and 2 show oxide A in the scanning and transmission electron microscopes. The latter instrument has shown that there are approximately 10^{11} surface pores per cm² with an average diameter of 20 nm though considerably smaller pores can be present. The pores resulted from oxide dissolution in the electrolyte and hence, they are rounded at their entrances, making a stringent test of the SEM resolving capabilities.

Figure 3 is of oxide B. The cracked surface is a thin cubic (or tetragonal) ZrO₂ layer situated on a thicker α ZrO₂ base. Care must be exercised in handling this sample as the cubic oxide is easily removed by touch. The crack network is planar and does not suffer from the previously mentioned height criticism. Oxide cracks giving images as small as 5 nm across can be seen while the greater majority are between 6.5 and 20 nm across. Cracks such as in Figure 3 cannot be seen in the TEM or easily revealed by replicas since the latter also removes the oxide as flakes. Only "in situ" studies at high resolution remove the ambiguities of interpretation.

The oxides were coated with a thin layer of gold but comparisons with uncoated samples did not reveal artifacts introduced by gold deposition. SEM magnification was calibrated using ruled gratings.

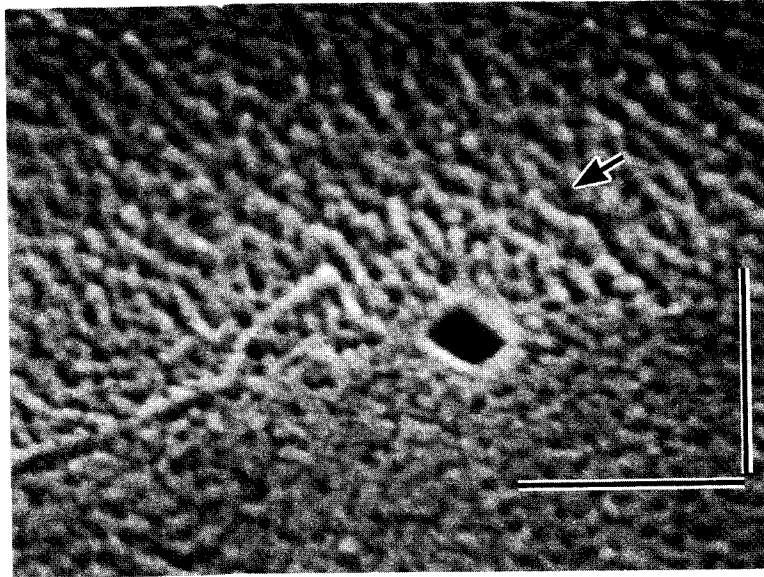


Figure 1

Oxide A taken with an accelerating voltage of 18 keV. Arrow indicates pores seen in Figure 2. Marker represents 500 nm.

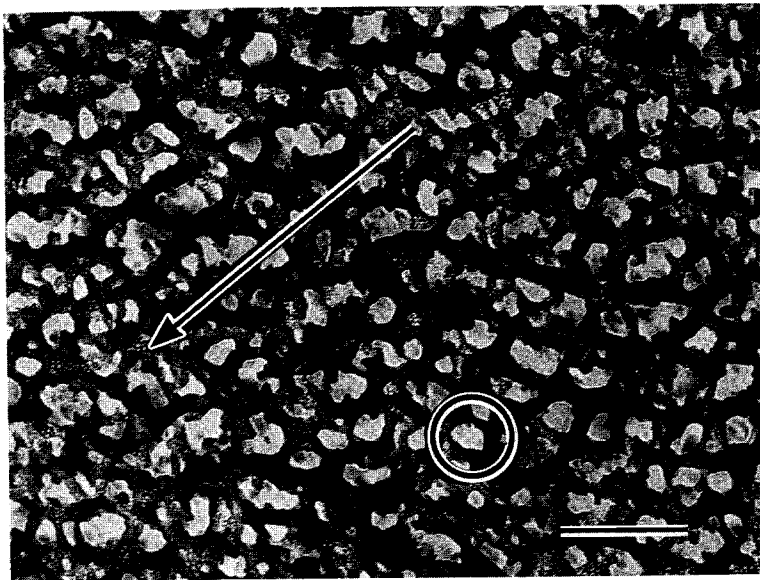


Figure 2

Oxide A in transmission. The 3.5 diameter pores (arrow) are distributed throughout the oxide. The circled area shows a 20 nm diameter surface pore (see Figure 1). Marker represents 100 nm.

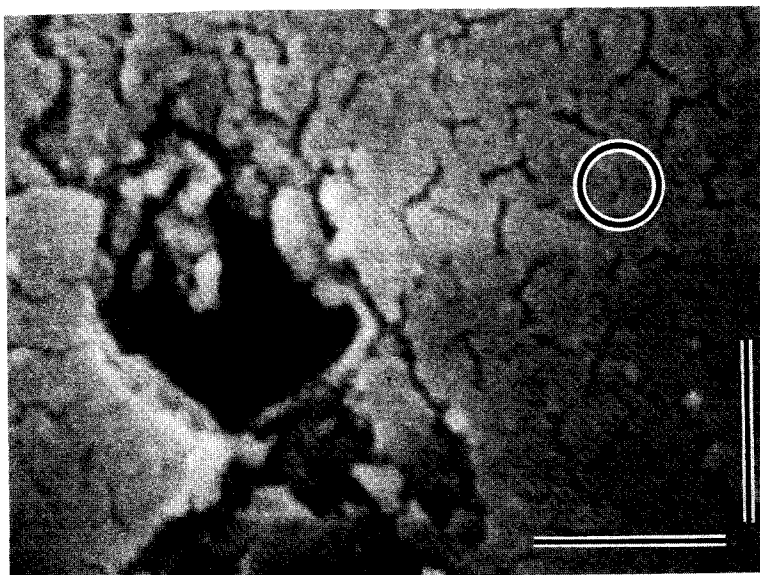


Figure 3

Oxide B taken at an accelerating voltage of 18 keV. Circled area shows a 7 nm wide crack. Marker represents 500 nm.

ACCURATE MICROCRYSTALLOGRAPHY IN THE S.E.M. USING ELECTRON BACK-SCATTERING PATTERNS

J. A. Venables, C. J. Harland and R. bin-Jaya

University of Sussex, School of Mathematical and Physical Sciences, Falmer, Brighton BN1 9QH, England.

We have previously shown that electron back-scattering patterns (EBSP) can be observed on a fluorescent screen placed in the specimen chamber of an S.E.M. with the microscope in the spot mode and the angle of incidence $\approx 60^\circ$. (1, 2). Here we describe methods of determining crystal orientation with 0.5° accuracy using these patterns, and indicate the potential of EBSP's as crystallographic detectors for microscopy at better than 50 nm resolution.

The accuracy of orientation determination using an EBSP is limited by the accuracy with which the position of the emitting point on the specimen is known relative to the screen. By casting geometrical shadows of objects onto the screen this position can be determined. Two types of objects have been investigated, a circular mask and three steel balls. The geometry of the mask arrangement is shown in fig. 1, and an EBSP taken using it is shown in fig. 2; an example using the three ball method is shown in fig. 4. During setting up, these patterns were viewed by closed-circuit TV, and then recorded direct onto 35 mm film. The pattern quality is typical, rather than the best we have obtained.

The output of a simple computer programme (PDP-8E (Basic)) corresponding to fig. 2 is shown in fig. 3. The required input data are (i) the dimensions d, ℓ of the mask (ii) the (x, y) positions of the centre of the mask shadow and its diameter on the screen (iii) the (x, y) screen coordinates of a pole $[uvw]$ and the angle ψ that a plane (hkl) containing $[uvw]$ makes to the y -axis and (iv) the stage tilt angle.

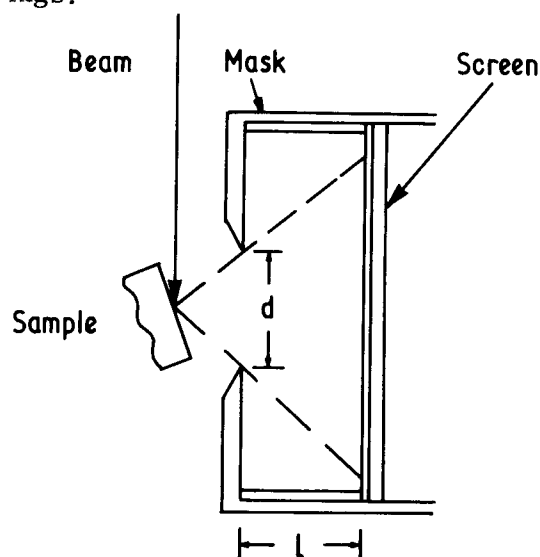
Evaluation of a set of EBSP's from near $-(001)$ GaAs similar to fig. 2 showed that use of different poles and planes on the same print reproduced the same crystallographic orientation within $\pm 0.5^\circ$; use of different prints where the electron beam had been moved but the sample remained at the same tilt angle were reproducible within $\pm 0.5^\circ$ also. Thus, to determine absolute orientations to better than $\pm 1^\circ$, it is necessary to ensure that the stage controls are reproducible to better than this accuracy, which is not normally the case. Relative measurements can always be performed with $\pm 0.5^\circ$ accuracy. A further programme, using least squares fits to the (x, y) coordinates of the shadows of the mask or the balls has also been developed. The programme enables the errors or orientation to be determined by the programme itself and confirms the 0.5° accuracy claimed here (2).

The fact that relatively strong contrast is present in an EBSP within $\sim 2\theta_B$ of planes and zone axes, means that enhanced crystallographic contrast can be obtained in an SEM picture if a detector is used which subtends $< 2\theta_B$ at the sample. Such a detector has been constructed using a fibre optic cable of 0.5 mm diam. coated with P47 phosphor and has been shown to give a large enhancement of grain contrast in polycrystalline samples, with currents of $\sim 1.10^{-8}\text{A}$ (2). These currents limit resolution to $0.2\mu\text{m}$ using W filament guns. With a LaB_6 gun $\sim 50\text{ nm}$ might be achieved. Experiments are underway in our FEG-SEM (3) to obtain EBSP's and crystallographic images with $\sim 10\text{-}20\text{ nm}$ resolution at currents of $1\text{-}2 \times 10^{-8}\text{A}$ (cf. ref 3, fig. 2).

We have no doubt that EBSP's are far superior to the more widely used ECP's for microcrystallography below $1\mu\text{m}$ diam., because there is no need either to rock the beam about a spot or to limit its angular divergence.

It is a pleasure to thank D. J. Dingley for preprints and discussions on the three-ball method. We thank B.A. Joyce for the GaAs samples, and for access to the digital plotter.

1. Venables, J. A., and C. J. Harland; Phil. Mag. 27 1193 (1973); see also SEM 73 (I.o.P.) 294 and Rev. Physique Appliquee 9, 419 (1974).
2. Venables J. A., C. J. Harland and R. bin-Jaya, in Developments in Electron Microscopy and Analysis (ed. J. A. Venables), Academic Press (1976), 101 and to be published.
3. Venables, J.A., A. P. Janssen, C. J. Harland and B.A. Joyce, this proceedings.



```

ELECTRON BACKSCATTERING PATTERN ANALYSIS
MASK CENTRE=-.35 -.2.3 MM
RADIUS= 13.7 MM SCREEN MAGN= 1
SCREEN DIST= 12.412 PATTERN CENTRE= .1332253 .9754933 MM

JVM= 1 1 1
X,Y= .25 -.9.3 MM
AKL=-2 2 0
PSI= 179.5 DEG

P.M. DIRM X .1622695 .188311 .9733333
SPEC RAS Y .6913935 -.7225139 .21906637
BEAM DIRM Z .7843139 .6672935 -.2421999
STAGE TILT= 75 DEG
SPEC NORMAL -.22555839 1.943993E-3 .9996715
DEG 33.53529 99.33337 1.468677

```

Fig. 3. Analysis of fig. 2, using the (x,y) position of the $[111]$ pole and the orientation (PSI) of the $(\bar{2}20)$ plane to the y axis.

Fig. 1. Schematic diagram of the mask method.

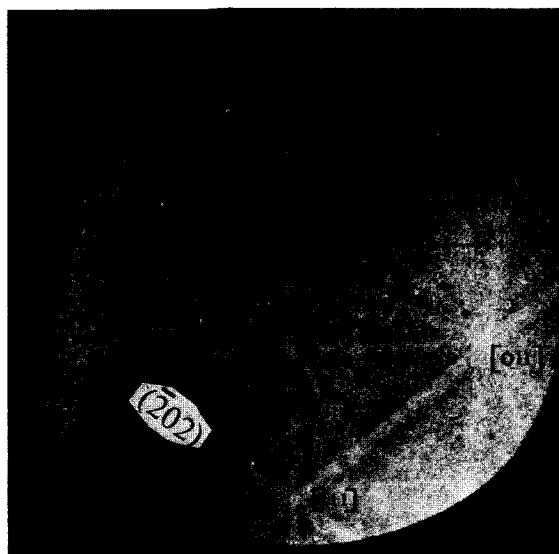


Fig. 2. EBSP from near $-(001)$ GaAs, with some poles and planes labelled. The circular mask shadow is at the top of the pattern.

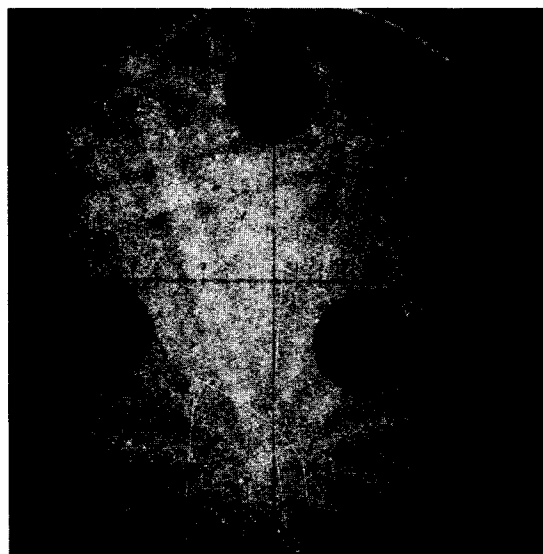


Fig. 4. EBSP from evaporated Au illustrating the 3-ball method. Conditions for figures 2 and 4: 30kV, 2×10^{-7} A, 8s exposure from P20 phosphor.

PROPOSED SCHEME FOR A DIRECTIONAL LOW-LOSS DETECTOR

Oliver C. Wells

IBM Thomas J. Watson Research Center, P.O. Box 218, Yorktown Heights, N.Y. 10598

The conventional low-loss electron detector (1,2) is shown in Fig. 1. The electron beam strikes the specimen with a glancing angle of typically between 30° and 45° . The input grid G_1 is held at +200V. The filter grid G_2 is held at +200V to collect secondary electrons or at -19.8kV for low-loss work with an incident beam energy of 20keV. The scintillator is held at +10kV for secondary electron detection or at -10kV for low-loss work. Comparison pairs of micrographs are obtained by recording one image in each mode. The signal-to-noise ratio is approximately the same in each case.

We are proposing to replace the single scintillator/light-pipe/photomultiplier system with a pair of such assemblies separated by a partition, such that an input electron will reach one or other of the scintillators, depending on which part of the input aperture it enters. The video waveform will be obtained using a sum-or-difference unit connected to the two photomultipliers. This detector will be constructed so that the two light pipes can either be placed side-by-side with a vertical partition between them or one above the other separated by a horizontal partition. Ideally, the photomultiplier voltages should be independently variable.

We are expecting that this detector will have the following advantages:

- (1) As at present, we should be able to obtain the conventional secondary electron and low-loss images. (This will be done by adding the signals from the two photomultipliers.)
- (2) When detecting secondary electrons, the difference mode should provide an enhancement of Type-1 magnetic contrast (such as was done by Cort and Steeds (3) using a pair of metal plates to collect the secondary electron signals).
- (3) In the low-loss difference mode, and with the partition vertical, it is expected to enhance side-by-side topographic contrasts (such as was done by Kimoto and Hashimoto (4) using a pair of solid-state backscattered electron detectors or by Griffiths, Pollard and Venables (5) using a subdivided channel plate detector system).
- (4) In the low-loss addition mode, and with the partition horizontal, the sensitivity of the upper scintillator could be increased to make the apparent illumination more uniform. This would then be similar to the "portrait illumination" technique using multiple solid-state backscattered electron detectors, as described by Ong (6).
- (5) In the low-loss difference mode, and with the partition vertical, it is expected to be able to obtain a form of magnetic contrast similar to Type-2, but with the difference that it should be sensitive to magnetic fields perpendicular to the specimen surface.

It is hoped to have some experimental results in time for the meeting. In all of the above cases, it is expected that the energy filtering capability, together with the low noise characteristic of the scintillator/light-pipe/photomultiplier system, will give an improved signal-to-noise ratio.

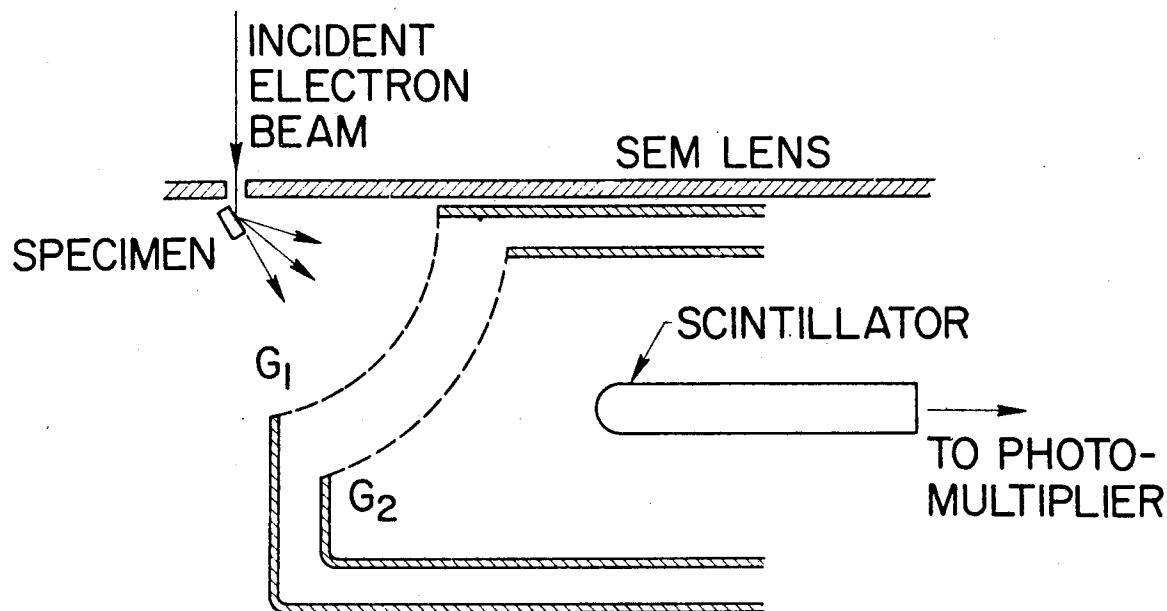


Fig. 1. Low-loss electron collector (from ref. 1).

References

1. O.C. Wells, Appl. Phys. Lett., 19, 232-235 (1971).
2. O.C. Wells, "Scanning Electron Microscopy", McGraw Hill (1974).
3. D.M. Cort and J.W. Steeds, 376-377, Proc. Fifth Eur. Cong. El. Microsc., Manchester (1972).
4. S. Kimoto and H. Hashimoto, 480-489, The Electron Microprobe, Proc. Symp., Washington, T. D. McKinley, et al. Eds., John Wiley (1966).
5. B. W. Griffiths, P. Pollard and J. A. Venables, 176-177, Proc. Fifth Eur. Cong. El. Microsc., Manchester (1972).
6. P. S. Ong, 392-393, Proc. 28 EMSA Meeting, Houston, Claitor's Publishing Division (1970). The "portrait illumination" technique is mentioned by Dr. Ong in this reference but has not been formally published. The effective illumination in the backscattered electron image was improved by using four solid-state detectors in different directions from the specimen, and by then adjusting the relative gains to improve the micrograph.

Quantitative microanalysis by electron energy-loss spectrometry

*R.F. Egerton, C.J. Rossouw[†] and M.J. Whelan[†]

*Department of Physics, University of Alberta, Edmonton, Canada, T6G 2J1.

†Department of Metallurgy, University of Oxford, Parks Rd., Oxford, England.

For elements in the first and second rows of the periodic table, microanalysis based on K-shell energy-loss spectra has two major advantages over x-ray emission methods: (1) The K-loss signal remains high, whereas the x-ray production efficiency is less than 10%. (2) The collection efficiency can be better than 30%, since most of the inelastically scattered electrons lie within 5° of the forward direction.

The practical problems are concerned not so much with the relatively low intensity of K-shell losses as with the background contribution to the spectrum due to valence-electron excitation¹. The latter can be corrected for by extrapolation of the spectrum preceding the K-edge^{1,2} but this procedure becomes inaccurate in the case of a low signal-to-noise ratio or a large range of extrapolation. Therefore it is desirable to measure the loss electrons over as small an energy window as possible, consistent with an adequate K-loss signal/noise ratio.

Figure 1 shows experimental signal/noise ratios for three first-row elements as a function of the acceptance semi-angle α of the electron spectrometer. Whereas signal/background ratio increases monotonically with decreasing α , s/n is an optimum around 10-20 mrad. Similar measurements (fig. 2) as a function of the energy window ΔE of the detector show that ΔE should typically be at least 20eV for adequate s/n ratio.

By sampling over an energy window ΔE either side of the excitation edge, the valence-electron background may be subtracted electronically³, leaving a signal $I_K(\alpha, \Delta E)$ due only to K-shell excitation (see fig. 3). The required number N of light atoms per unit area of the specimen is given by:

$$N = I_K(\alpha, \Delta E) / I_0(\alpha, \Delta E) \cdot \sigma_K(\alpha) \cdot r(\Delta E)$$

where I_0 is the signal recorded in the low-energy region of the loss spectrum (fig.3) and $\sigma_K(\alpha)$ is the cross-section for K-shell scattering through angles up to α , which can be determined experimentally or calculated from Bethe theory. The factor r represents the fraction of K-loss electrons which lie within the energy window ΔE ; experimentally this is found to be a function of ΔE but not of α (see fig. 4).

Using an energy-selecting CTEM⁴, we have applied the above method to microanalysis of nitrogen in AlN precipitates within a steel foil. Nitrogen K-loss spectra of three different areas of foil are shown in fig. 5. Using an energy window ΔE of 50eV and $\alpha = 11$ mrad, we estimate the amount of nitrogen in particle A to be 1.5×10^{-16} gm. The experimental detection limit, represented by particle B, is about 10^{-17} gm of nitrogen. With improved instrumental design, this limit could be reduced by at least an order of magnitude.

1. R.F. Egerton, *Phil. Mag.* **31**, 199 (1975).
2. M. Isaacson and D. Johnson, *Ultramicroscopy* **1**, 33 (1975).
3. R.F. Egerton and C.E. Lyman, *Proc. EMAG 75*, Bristol, England; (Institute of Physics 1975).
4. R.F. Egerton, J.G. Philip, P.S. Turner and M.J. Whelan, *J. Phys. E*, **8** 1033 (1975).

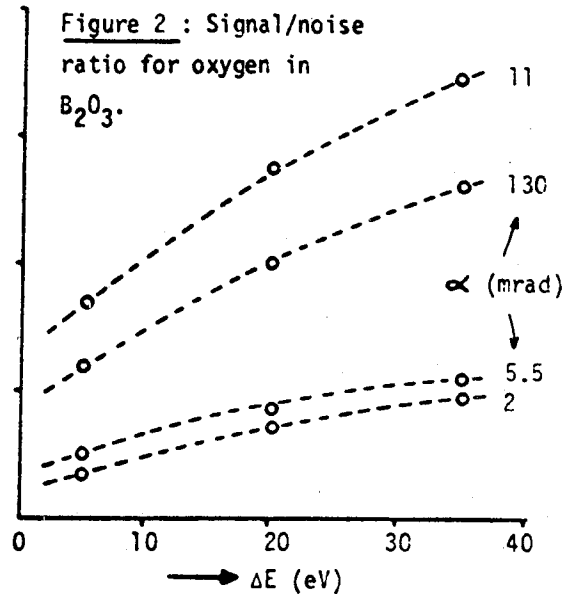
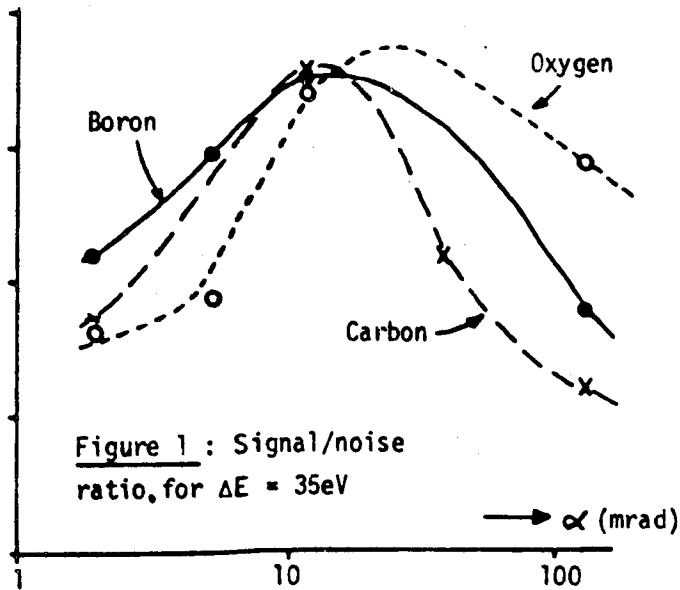
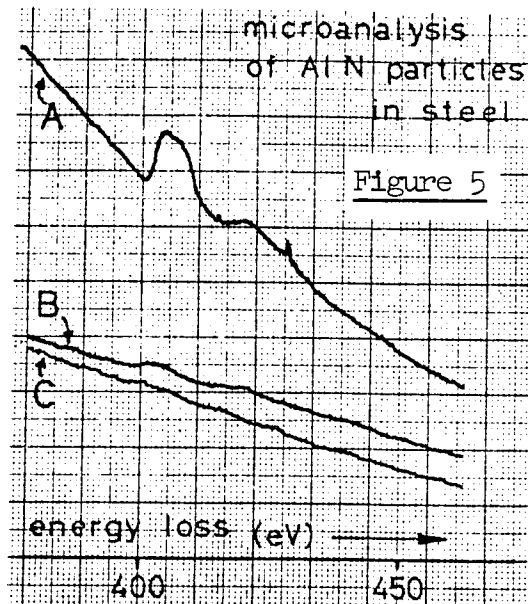
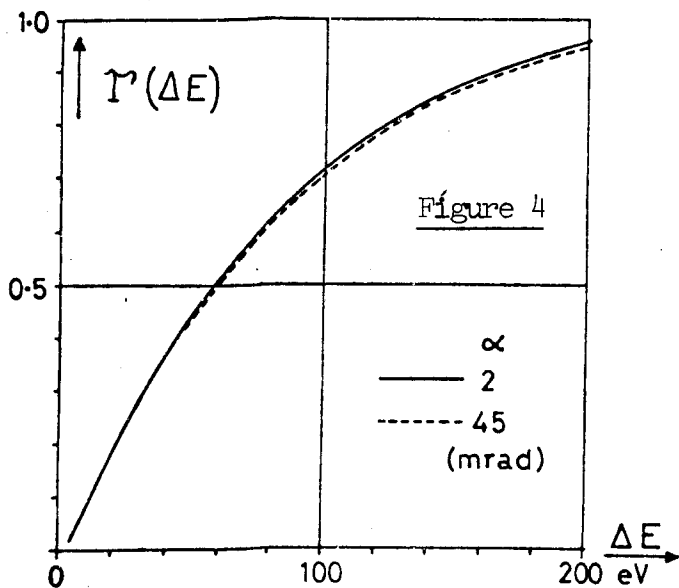
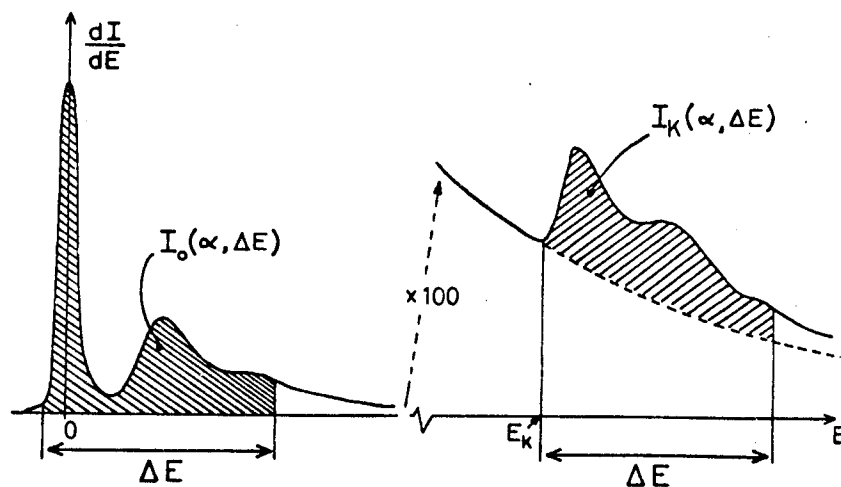


Figure 3.
Procedure for the microanalysis of light elements.



Observations of Direct Non-Vertical Interband Transitions in Al and Si by Electron Energy-Loss Spectroscopy.

C. H. Chen and J. Silcox

School of Applied and Engineering Physics, Cornell University,
Ithaca, New York 14853

Electron energy-loss spectra (at 75keV) of single crystal aluminum and silicon foils of [001] orientation were obtained by using an electron microscope (Hitachi HU-11A)-electron spectrometer (Wien filter) system. The operation of this apparatus has been described previously¹. In the present experiment, the microscope was operated in the selected-area-diffraction mode and the energy-loss spectra were recorded on photographic plates and subsequently obtained data by microdensitometry.

Figure 1 shows the loss spectrum in aluminum with momentum transfer \vec{q} in the $\langle 100 \rangle$ direction. In addition to the usual bulk plasmons at 15eV and surface plasmons at 6.7eV, two dispersive peaks below the bulk plasmon peak are also observed. The first peak which is relatively sharp starts linearly from 1.5eV at $q \sim 0^{2,3}$ and levels off around 9eV at the zone boundary ($q = 1.55\text{\AA}^{-1}$). This peak is due to the excitation of direct non-vertical interband transitions along the X-W-X direction of energy bands in Al⁴. The second peak, broad and diffuse with energy higher than the first one, has approximately linear dispersion which extends beyond 12eV and shows no sign of leveling off at large q . This peak is assigned to direct non-vertical intraband transitions along X- Γ -X of the energy bands. Observations for \vec{q} in the $\langle 110 \rangle$ direction, on the other hand, show two broad and diffuse peaks (Fig. 2). Intraband transitions are dominant in the direction.

Silicon is a semiconductor and only interband transitions can occur. Figure 3 shows the loss spectrum in silicon with \vec{q} in $\langle 100 \rangle$ direction. Again, dispersive peaks were observed below the bulk plasmon peak at 16.6eV. The first peak starts from 4.4eV at small q to 6.5eV at $q \sim 0.6\text{\AA}^{-1}$. The second one varies from 5.5eV at small q to 10eV at $q \sim 0.9\text{\AA}^{-1}$. The third one changes from 7.8eV to 12.5eV at the zone boundary ($q = 1.16\text{\AA}^{-1}$). These peaks are rather weak but relatively sharp and ride on a high rising background. Besides these three peaks, we also observed a threshold-type peak at lower energies, which starts from 3.5eV at small q and energy decreases slightly with increasing q . Correlations of these peaks with features of band structures of silicon^{5,6} along X- Γ -X and X-W-X directions can be found. In comparison, the loss spectrum for q in the $\langle 110 \rangle$ direction is also shown in Figure 4. The most pronounced feature is the peak which increases from 4.4eV at small q and reaches a maximum at 6.8eV and then decreases with increasing q .

This work was supported by the National Science Foundation through the Cornell Material Science Center.

1. G. H. Curtis and J. Silcox, Rev. Sci. Instrum. 42, 630 (1971).
2. H. Ehrenreich, H. R. Phillip and B. Segall, Phys. Rev. 132, 1918 (1963).
3. N. W. Aschcroft and K. Sturm, Phys. Rev. B 3, 1898 (1971).
4. R. Petri and A. Otto, Phys. Rev. Lett. 34, 1283 (1975).
5. D. Brust, Phys. Rev. B 4, A1337 (1964).
6. J. P. Walter and M. L. Cohen, Phys. Rev. B 5, 3101 (1972).

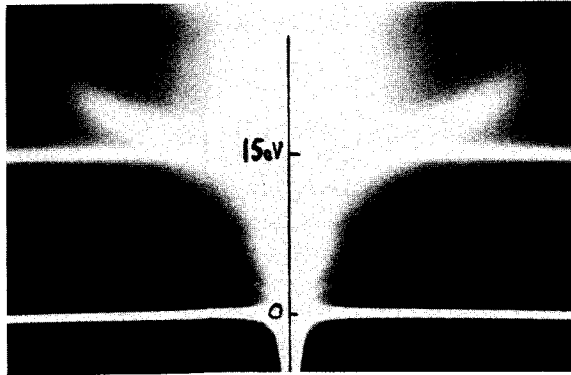


Fig. 1 Electron energy-loss spectrum of single crystal aluminum with momentum transfer \vec{q} in the direction of $\langle 100 \rangle$

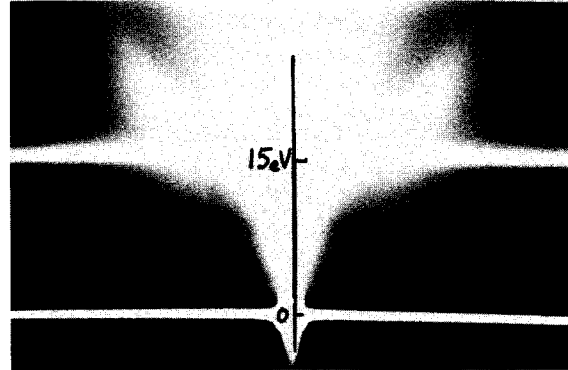


Fig. 2 Electron energy-loss spectrum of single crystal aluminum with momentum transfer \vec{q} in the direction of $\langle 110 \rangle$

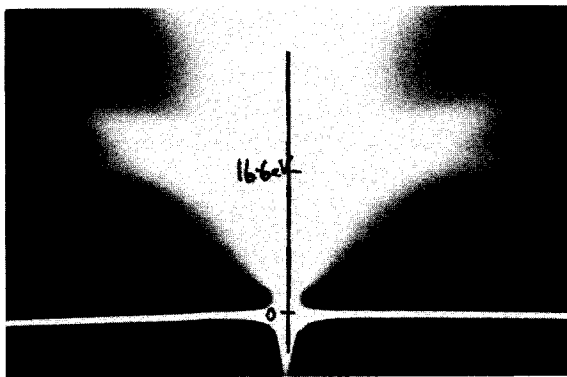


Fig. 3 Electron energy-loss spectrum of single crystal silicon with momentum transfer \vec{q} in the direction of $\langle 100 \rangle$

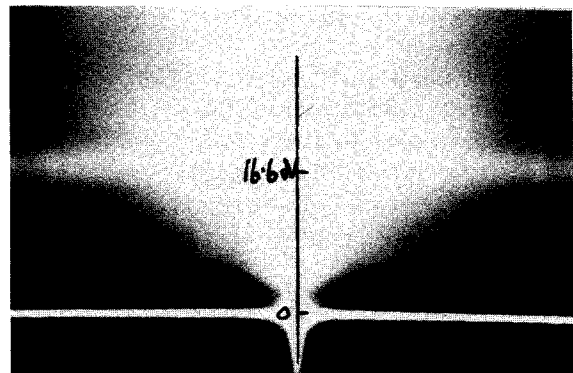


Fig. 4 Electron energy-loss spectrum of single crystal silicon with momentum transfer \vec{q} in the direction of $\langle 110 \rangle$

OPERATIONAL AND INSTRUMENTAL CONSIDERATIONS FOR THE
DEVELOPMENT OF A PLANETARY SEM-EDA

A. L. Albee, J. R. Anderson, and A. A. Chodos

Division of Geological and Planetary Sciences
California Institute of Technology*
Pasadena, California 91125

Introduction--A primary objective of a space mission to a planetary body, asteroid, or comet is to obtain information that bears upon interpretation of the genesis and evolution of that body and of the solar system as a whole. A lander mission must carry those instruments that will provide the maximum amount of information about the material that makes up the surface of such a body. Among the instruments that must be considered are: x-ray diffractometer, x-ray fluorescent analyzer, differential thermal analyzer, optical microscope, magnetic separator, etc. Of the various instruments currently available the scanning electron microscope with an energy-dispersive analyzer (SEM-EDA) is by far the most powerful tool for studying the morphologic, chemical, and mineralogic characteristics of complex, particulate material such as that which constitutes a planetary regolith. A simple SEM-EDA adapted for unmanned missions might provide information otherwise obtainable only by a sample-return mission, which would involve far greater complexity and expense.

This paper considers the type of information that would be desired in the study of a regolith and some resultant operational and developmental considerations for a flight SEM-EDA.

Scientific Considerations--The mineralogy, chemical composition, morphology, and surface characteristics of particles in a planetary regolith can provide substantial evidence that bears on the origin of a planetary body, how it evolved to its present state, and its surface and near-surface processes. Bulk chemical composition of regolith material can provide significant constraints on the above, but the identification of particular mineral phases and assemblages of phases provide much more stringent constraints on the nature of the source rock,

* Contribution No. 2726

the P and T of origin, the fugacity of volatile species, the likely minor element content, the mineral density, the state of hydration and oxidation, etc. The identification of a single grain of a low abundance phase may have great genetic significance. Grain size distribution, shape, and surface features provide information on planetary surface processes, including impact phenomena and mechanical or chemical interaction with an atmosphere.

Using the extensive studies on the lunar regolith as a guide we can outline the major types of information that we need to obtain from such a particulate sample.

- 1) Identification, and abundance, of fragments of various rock types by texture, grain size, and mineral content.
- 2) Identification and abundance of both major and minor particulate mineral species.
- 3) Average and range of chemical composition of the various particle species.
- 4) Bulk chemical composition of the entire sample calculated from 2) and 3).
- 5) Identification and chemical composition of individual particulate grains of genetic significance.
- 6) Distribution of size and shape of particles in a sample as a whole and among the various particulate species.
- 7) Study of special features such as coatings, glass splashes, micro-craters, fracture surfaces, growth surfaces, micro-organisms, etc.

Bulk properties of particulate samples have generally been obtained by such methods as sieving, optical microscopy, bulk chemical analysis, bulk density, etc. However, such bulk properties can also be obtained by measurement of size, shape, chemical composition, etc., on a statistical selection of grains using computerized image analysis. The laboratory SEM-EDA has demonstrated that it is capable of obtaining all these types of information and no other instrument possesses this versatility.

Scientific Requirements--In setting science requirements it should be realized that important scientific information would be obtained about Mars, for example, from the study of a single sample of uncoated and poorly-dispersed grains with an SEM resolution of only several microns and with an EDA having only a small number of pre-selected energy windows. Such an instrument would provide many of the types

of information outlined above. However, a SEM resolution of about 200 Å, obtainable on present table-top instruments, and an EDA resolution of about 160 ev, obtainable on present Si(Li) detectors would provide very complete information on a regolith and would appear to be reasonable design goals. Similarly, although the study of a single, uncoated sample would be of some use, the ability to change samples and to disperse, coat with a conductive film, and manipulate particles are also reasonable design goals and would greatly increase the resolution and precision of the data. Consideration should also be given to the secondary goals of analyzing trace elements by adding x-ray excitation and of analyzing light elements by adding Auger electron detection. Both of these are secondary goals since many minor elements are concentrated in particular minor phases and can be identified and analyzed with the SEM-EDA.

Operational Considerations--In recent years the development of both SEM and EDA has been remarkably rapid, directed both toward high-resolution, more complex instruments and toward moderate-resolution, simple instruments, which are intended for table-top use by non-experts. These latter instruments are logical prototypes for a flight instrument and with a few exceptions current development is sufficient to build a flight instrument.

There are a number of basic operational requirements for an unattended SEM-EDA on a space vehicle. Clearly, it must be small, lightweight, and integrated with other systems in terms of power, data transmission requirements, etc. Thus in a final design spatial resolution may be compromised to weight limitations (for example, a single lens instrument) and energy and spatial resolution may be compromised to data transmission limitations.

Many components and requirements of a SEM-EDA are shared by other instruments on or proposed for other flight missions and development is actively proceeding on them. These include high voltage power supply, vacuum requirements, passive coolers for detectors, transmission of extensive scanning information, multichannel analyzers, etc. However, it would be very difficult to provide continuous pre-flight and in-flight cooling for a Si(Li) detector and it seems very doubtful that one could withstand the sterilization required for a Mars mission. Development of an intrinsic Si detector (or some other detector that does not require continuous cooling) with adequate resolution is the most important developmental problem.

The choice of electron source (W, LaB_6 , or field emission) must be balanced against vacuum requirements, number of lenses, brightness, stability, and life. At the present stage of development the most likely cathode choice would seem to be that which can be changed with the fewest alignment problems. The vacuum requirement is clearly not difficult on planets with no atmosphere, but on others, such as Mars or a comet, the sample could contain volatile ices making it difficult to attain a high vacuum.

Sample handling and collection procedures are engineering problems which must largely be solved in the context of the requirements of a particular mission. Sample handling involves the following considerations:

- 1) Sample splitting and sorting by size.
- 2) Removal of adhering dust from larger particles.
- 3) Dispersal and fixing of the particles to a substrate.
- 4) Coating with a conductive film.
- 5) Interchange of samples for multiple sample capability.
- 6) Manipulation of sample substrate.

Experience with lunar samples indicate that items 2) and 4) are necessary to obtain good quality data. The desirability of multiple sample capability and the type of samples to be analyzed may differ on different missions. For a stationary lander a single set of particulate grains may be studied in very great detail, whereas for a planetary rover it might be desirable to study only the larger fragments from a large number of samples. Flexibility of the instrument is very important and specialized design for a particular mission should be avoided in the early development.

Summary--As indicated current technology is sufficient, with a few exceptions, to build a prototype flight instrument. Suitable cooling systems for the detector are currently being developed for use with intrinsic Ge detectors on orbital flights. However, continued development of the intrinsic Si detector is important. Most of the other requirements are essentially engineering problems and are solvable.

The design requirements for a flight SEM-EDA are for a simple, compact and rugged instrument which does not have the highest spatial resolution currently feasible. Such an instrument could be useful in a variety of terrestrial applications, such as the on-site study of well cuttings, prospecting for placer

deposits, and various geologic and oceanographic studies. At this time there are no lander missions in an advanced stage of planning although many have been or are being considered. At this time it makes little sense to build a prototype instrument since the rapid rate of instrument development by SEM manufacturers indicates that a prototype would be obsolete before a mission was funded.

Clearly a flight SEM-EDA could perform many important data gathering functions in studying the surface of a planetary body, asteroid, or comet. The high magnification imaging, chemical microanalysis, and overall versatility cannot be matched by any other instrument. If the operational and design characteristics desired are considered during future SEM-EDA development, the construction of a prototype will be straightforward when a mission is planned.

Acknowledgement: Study supported by NASA grant NSG-7125.

THE USE OF AUGER ELECTRON SPECTROSCOPY TO STUDY IMPURITY-INDUCED INTERGRANULAR FRACTURE IN STEELS

C. J. McMahon, Jr., and H. C. Feng

Department of Metallurgy and Materials Science, University of Pennsylvania, Philadelphia, Pennsylvania 19174

The introduction of Auger electron spectroscopy (1) has had a major impact on the problem of intergranular fracture of steels (2,3). Recent systematic research (4-7) on impurity-induced embrittlement of NiCr steels has led to a fairly clear understanding of the mechanisms involved. It has been found that the ductile-brittle transition temperature is proportional to the concentration of any given impurity from Groups IV B to VI B. The constant of proportionality (i.e., the potency of the embrittling element) appears to increase with both Group and Period number, suggesting that both electron density and atomic volume effects are important in determining embrittling potency. It has also been found that, for a given impurity concentration the transition temperature increases with hardness and grain size, but the behavior is non-linear.

Elements from Groups VI B are so highly surface active and so potent as embrittling elements that they can embrittle Fe in concentrations of <100 ppm by wt (8). They tend to be precipitated by some of the common alloy elements in steels, however, and are therefore not of primary concern in alloy steels. The Groups IV B and V B elements are attracted somewhat less strongly to certain alloy elements, such as Ni, Mn, and Cr, but this attraction constitutes the driving force for cosegregation of alloy and impurity atoms to the grain boundaries and thereby produces embrittlement. AES measurement on specimens fractured in UHV have shown that there is a unique correlation between the grain boundary concentrations of Ni and Sb, Ni and Sn, and Ni and P in NiCr steels doped with these impurities (4,5,6). In this work calibration curves obtained from series of binary Fe-based alloys have been used to convert Auger peak heights to intergranular concentrations.

Most of our results to date have been obtained with a cylindrical mirror analyser with a relatively unfocused beam (spot size ≈ 0.5 mm). This has been found to give satisfactory results on specimens which exhibit at least 50 pct intergranular fracture. The Auger peak heights are weighted by the simple rule of mixtures method (4), using scanning electron micrographs taken after the Auger analysis, so that the results are indicative of the intergranular composition. Since the degree of impurity segregation appears to be a function of grain boundary orientation (9) (i.e., structure), the intergranular composition can vary from one intergranular facet to another. Hence, the use of a large spot size is an advantage in that the measured concentration is the average over a number of grains.

In cases where the pct intergranular fracture is below 50; it is desirable to do selected area Auger analysis. For this purpose one needs a beam focused to a few micron spot size with which a scanning electron image of the area to be analysed can be obtained. An example of a recent application of such an instrument in our laboratory is the analysis of a commercially pro-

duced pressure vessel steel (A533B) in which intergranular cracking has been found in a simulated post-weld stress relief treatment. The steel was austenitized at 1200°C for 1h and tempered at 625°C for 1h, then fractured at -60°C in a PHI Scanning Auger Microprobe at $\sim 10^{-10}$ torr. Figure 1 gives three spectra: one from an intergranular region (shown in Fig. 2), one from this same region after extensive Ar⁺ sputtering, and one from an adjacent region of transgranular fracture. It is clear that there is segregated P, S, N, Sn, Sb, Mn, Ni, Cu, and As on the grain boundaries. All but the Ni and Mn should contribute directly to the intergranular weakness, and the Ni and Mn are presumably instrumental in producing the segregation. The sputtering profile showing the solute distribution near the intergranular surface is shown in Fig. 3. This particular heat was extraordinarily susceptible to stress relief cracking because it contained inordinately large concentrations of metalloid impurities.

The authors acknowledge the support of the Electric Power Research Institute, the National Science Foundation, and the American Iron and Steel Institute.

1. L. A. Harris, J. Appl. Phys. 1968, Vol. 39, p. 1419.
2. P. W. Palmberg and H. L. Marcus, Trans ASM, 1969, Vol. 62, p. 1016.
3. D. F. Stein, A. Joshi, and R. P. Laforce, Trans ASM, 1969, Vol. 62, p. 776.
4. H. Ohtani, H. C. Feng, C. J. McMahon, Jr., and R. A. Mulford Met Trans. A, 1976, Vol. 7A, p. 87.
5. R. A. Mulford, C. J. McMahon, Jr., D. P. Pope, and H. C. Feng, Met Trans. A, 1976, Vol. 7A, in press.
6. A. K. Cianelli, H. C. Feng, C. J. McMahon, Jr., and A. H. Ucisik, to be published.
7. C. J. McMahon, Jr., E. Furubayashi, H. Ohtani, and H. C. Feng, Acta Met., in press.
8. C. Pichard, J. Rieu, and C. Goux, Mem. Sci. Rev. Met., 1973, Vol. 70, p. 13.
9. T. Ogura, H. C. Feng, and C. J. McMahon, Jr., to be publ.

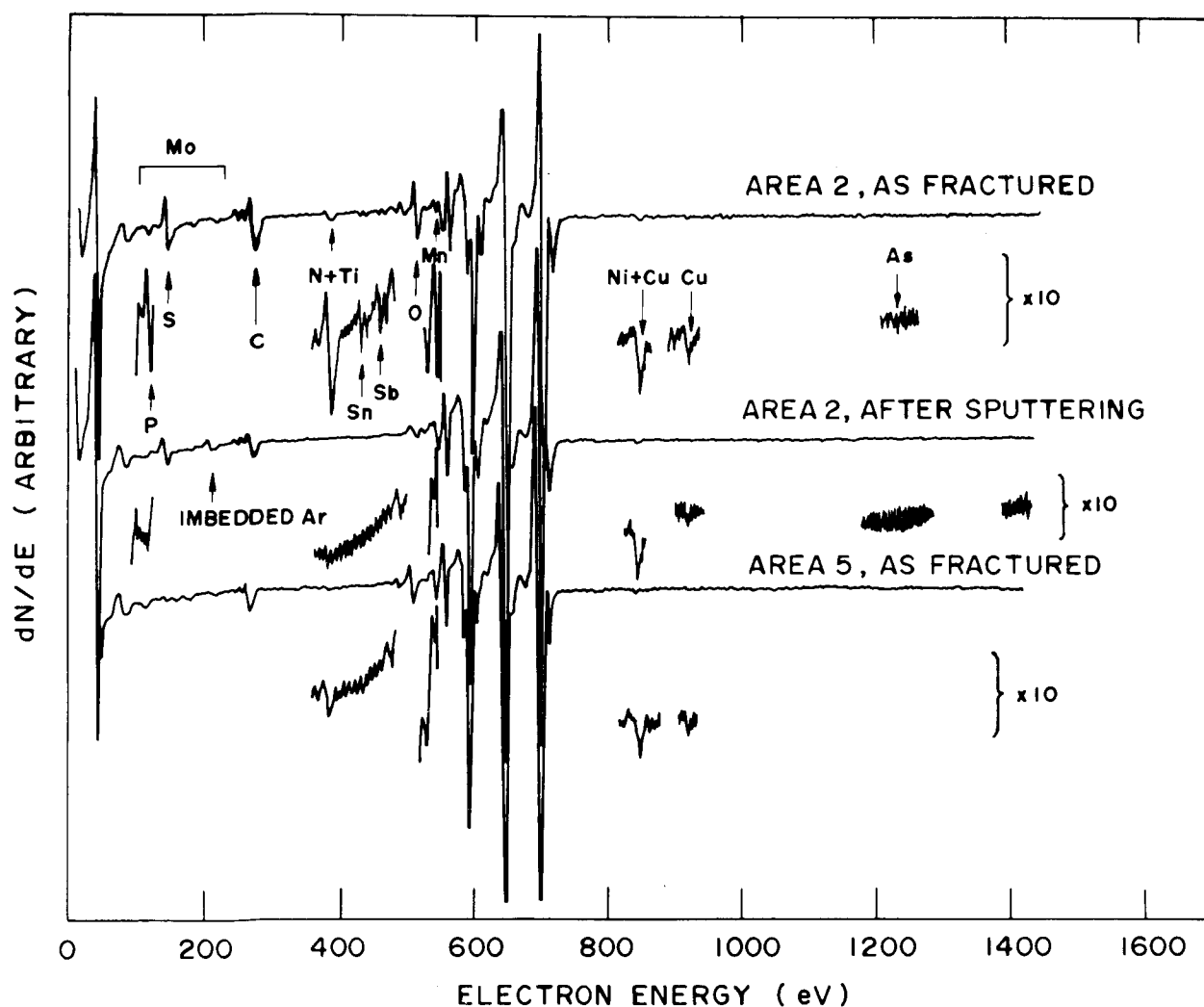


Fig. 1. Auger spectra from fracture surface produced in UHV in A533B steel.

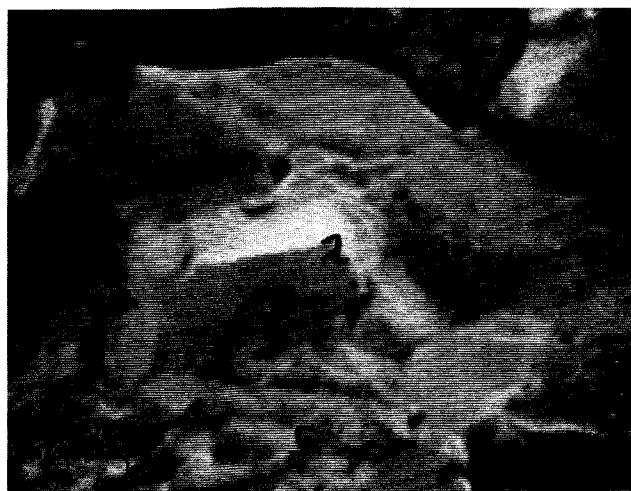


Fig. 2. Scanning electron image showing location of areas analysed.

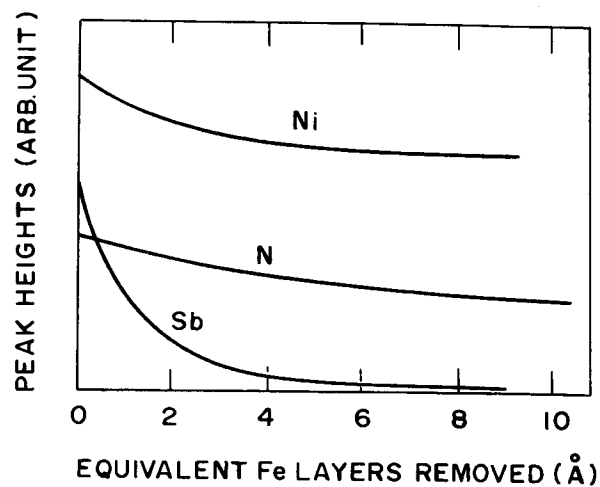


Fig. 3. Sputtering profile of Ni, N, and Sb concentrations on an intergranular fracture facet.

REVISED CALCULATION OF OXYGEN CONCENTRATION IN THE LTE MODEL

By J.D. Brown

Metaalinstituut TNO and The University of Western Ontario, London, Canada

and A.P. von Rosenstiel

Metaalinstituut TNO, Apeldoorn, The Netherlands

In secondary ion mass spectrometry, the problem of quantitative analysis is to calculate the total concentration of a specific mass species in the region immediately above the specimen surface since this concentration is directly related to concentration in the solid.

The total concentration of mass species M can be written

$$N_M = N_{M^+} + N_{M^-} + N_{M^0} + N_{MOL} ,$$

where N is the number of atoms, molecules or ions per meter³ and +, -, 0 and MOL refer to positive ions, negative ions, neutral atoms and molecular species respectively.

A local thermodynamic equilibrium (LTE) model has been proposed by Andersen and Hinthorne (1) to calculate the total concentrations for quantitative analysis. Although the model should apply for any primary bombarding ion, the widest application is for oxygen as the primary ion beam or where oxygen is present because of specimen concentration or flooding of the specimen surface with oxygen since data required for the LTE model is most abundantly available for oxides. In the LTE model, it is assumed that in a plasma at or near the specimen surface, an equilibrium exists which can be described for an oxygen primary beam by equations and equilibrium constants, K such as

$$M^0 \rightleftharpoons M^+ + e \quad \text{and} \quad K_{M^+} = \frac{N_{M^+} \cdot N_e}{N_{M^0}}$$

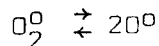
for ionic species and

$$MO^0 \rightleftharpoons M^0 + O^0 \quad \text{and} \quad K_{MO^0} = \frac{N_{M^0} \cdot N_{O^0}}{N_{MO^0}}$$

for molecular species. Data is available for the equilibrium constants as a function of temperature based on the Saha-Eggert (2) ionization equation for ions and the Guldberg-Waage (3) equation for molecules. These equations require knowledge of the variation of partition functions with temperature. Many of these are available in the literature.

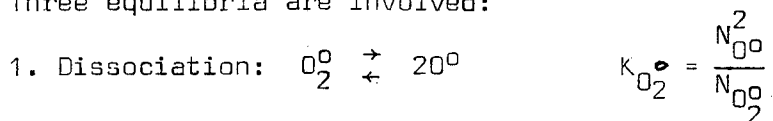
To use the LTE model, three parameters which appear in the equilibrium constants must be established; the concentration of electrons, N_e , the concentration of neutral oxygen atoms, N_{O^0} and the temperature T of the plasma. If these are known then the total concentrations for all mass species in the plasma can be calculated and quantitative analysis performed.

Andersen and Hinthorne have proposed a number of methods to determine N_e , N_o and T based on internal standards and ratios of measured ionic species such as M^{++}/M^+ , O_2^+/O^+ , etc. However their method to calculate N_{Oo} is not ideal since it is based on calculating $N_{Oo}/N_{O_2^+}$ from the measured $N_{O^+}/N_{O_2^+}$ and the equilibrium constant for the reaction²

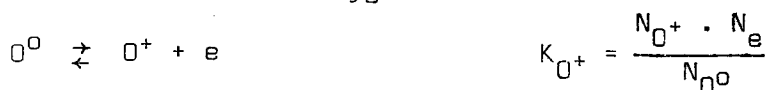


using the Guldberg-Waage equation and Herzberg's (4) approximation to the partition function for neutral diatomic molecules.

Recent data of Shipley (5) permits a more direct approach to calculate N_{Oo} . Three equilibria are involved:



2. Ionization of atomic oxygen:



3. Ionization of molecular oxygen:



Combining these equilibrium constants, then

$$N_{Oo} = \frac{N_{O_2^+}}{N_{O^+}} \cdot \frac{K_{O_2^0} \cdot K_{O^+}}{K_{O_2^+}}$$

Thus N_{Oo} can be calculated directly from the measured secondary ion ratio and the three equilibrium constants. On substituting for these constants using the Saha-Eggert and Guldberg-Waage equations.

$$N_{Oo} = \frac{N_{O_2^+}}{N_{O^+}} \cdot 4.250 \times 10^{11} \cdot T^{3/2} \cdot \frac{B_{O_2^0} \cdot B_{O^+}}{B_{O_2^+}} e^{-6.669/kT}$$

where B's are partition functions and k is Boltzmann's constant in electron volts. $k = 8.6169 \times 10^{-5} \text{ eV/K}$

This method has been used in the LTE model to calculate N_{Oo} and generally yields higher O^0 concentrations than the Andersen and Hinthorne approach. Since the LTE model predicted concentrations for elements with stable oxides which were too low, the increase in O^0 concentrations should yield improved analytical results.

REFERENCES

1. Andersen, C.A. and Hinthorne, J.R. Anal. Chem. 45, 1421 (1973)
2. Saha, M.N. Phil. Mag. 40, 472 (1920), Eggert, J. Z. Phys. 20, 570 (1919)
3. Glasstone, S.M. "Physical Chemistry", D. van Nostrand, Princeton N.J. 1946
p. 817
4. Herzberg, G. "Spectra of Diatomic Molecules" D. van Nostrand,
Princeton N.J. 1950
5. Shipley, K.L. J. Appl. Phys. 40, 3037 (1969).

SECONDARY ION YIELDS OF METALS AND OXIDES OF TI THROUGH ZN

Ian M. Steele*

Ian D. Hutcheon[†]

Todd N. Solberg*

Robert N. Clayton^{*†} and

Joseph V. Smith*

*Department of the Geophysical Sciences

[†]Enrico Fermi Institute

University of Chicago, Chicago, Illinois 60637

Although considerable progress has been made in relating secondary ion (SI) spectra to target composition in ion sputtering experiments (for example, refs.^{1,2}), the theoretical and instrumental factors affecting sputtered ion yields must still be considered rather uncertain. We present here initial data obtained with an AEI IM20 ion probe³ from high-purity metals and oxides of the first transition series (Ti-Zn). These data are compared with published data from other ion microprobes enabling evaluation of the particular operating parameters of our instrument and extension of knowledge of ion emission from metals and their oxides.

All our data were obtained with a 20keV $^{16}\text{O}^-$ mass-analyzed primary beam with a current density of $\sim 1\text{mA}/\text{cm}^2$. The source pressure was maintained between 2 and 5×10^{-8} torr and the sample region was cooled to liquid N_2 temperature. The geometry of the ion extraction system is outlined in Fig. 1. The repeller is typically maintained ~ 700 -1000 volts above the sample potential and is used to maximize the secondary ion signal by "energy-tuning" the extraction system. The function of the repeller and its effect on SI intensity will be discussed later. The aperture einzel lens serves to focus the SI beam onto the source slit. Relative SI intensities are not affected by the voltage on this lens. Total transmitted SI intensity is, however, strongly modulated by this lens. The tubular (first) einzel lens was grounded during this experiment. The mass spectrometer was tuned for low resolution ($\Delta M/M \sim 300$) and the secondary ions were detected with an electron multiplier and dc electrometer.

Initially we determined SI spectra from randomly-oriented, polished metal surfaces mounted in epoxy discs and carbon-coated. Each sample was analyzed under identical conditions, and only the repeller potential was adjusted to maximize the SI signal. Fig. 2a compares the relative yield of the M^+ species ($M = \text{Ti-Zn}$) with published data obtained on ARL⁴ and Cameca⁵ ion probes. (Note that the analytical conditions were not stated in ref. 5). The overall similarity is striking and suggests that to within a factor of about 1.5, all three machines

record nearly equal SI intensities relative to Ti. The agreement in sputtered ion yields for the transition metals is especially interesting in view of the substantial disagreement in ion yields between the ARL and Cameca or AEI instruments for a plagioclase mineral target⁷. The disparity between these two results is a subject of continuing investigation.

From the variation in SI intensity observed in subsequent analyses we estimate the error in any particular measurement as $\pm 20\%$. Crystal orientation did not appear to affect measured SI intensities as several samples gave the same answer for any one metal. We observe two major differences in our data relative to the ARL and Cameca data: (1) the ion yield of Mn is nearly a factor of 3 higher in our results, (2) our instrument appears to have a greater sensitivity for the heavy transition metals Ni, Cu and Zn. The underlying causes of this behavior are not understood at this time.

The experiment described above was next repeated using oxide targets of the transition series metals (MnO and CuO were not available). Once again the basic trend of decreasing ion yield with increasing atomic number is reproduced with only a slight deviation in the Ni-Zn region (Fig. 2b). It is apparent that the added oxygen present in these samples has little or no effect on the relative SI intensities when bombarding with an O^- primary beam. This behavior is not altogether unexpected since the build-up of a thin oxide layer on a pure metal surface is observed to have a pronounced effect on the ion yield under O^- bombardment⁹.

The similarity of ion yields from metal and oxide targets was confirmed in a comparison of the SI intensities of oxide species using photoplate detection. The intensities of the MO^+ , MO_2^+ , M_2O^+ , and $M_2O_2^+$ species relative to M^+ from both metals and oxides were equivalent to within a factor of two (visual photoplate estimate).

To investigate the extent to which the relative SI yields from pure metals collected above could be used as a basis for determining the composition of an unknown, we have measured SI spectra from the Coahuila iron (hexahedrite) meteorite. In an iron meteorite we can first investigate the transition series ions, now not as pure metals but as dilute solutions in a homogeneous, well-characterized Fe matrix, and then hopefully expand upon this foundation to study the behavior of other trace elements. In Fig. 2c we show the intensities of Cr, Co, Ni and Cu normalized to Fe and corrected for actual abundances. It is evident that there is a substantial reduction in the spread of SI yields relative to the pure metals. The Cr/Ni ratio in Coahuila is only 6.5 while for pure metals, Cr/Ni = 30. A similar trend has been observed by Bakale *et al.*⁶ for transition metals in a glass matrix and is attributed to the highly oxidized state of the matrix.

As discussed earlier in this report we found it necessary to adjust the repeller potential with each sample to obtain the maximum SI signal.

Bradley et al.⁷ have emphasized that this maximum intensity corresponds to the maximum in the initial energy distribution of the particular SI that is used for tuning the extraction system. Figure 3 shows typical plots of repeller voltage versus SI intensities for V, Cu and Ni ions. We are impressed by the similarity between the general shapes of these curves and published distributions of ion yield as a function of energy⁸. Tuning the instrument with the repeller presumably affects the relative ion yields by discriminating against certain ion initial energies.

In summary, we recognize 3 basic results from this preliminary ion probe study:

- 1) the trend of decreasing ion yield with increasing atomic number among the metals of the first transition series holds for the AET instrument with its particular operating parameters.
- 2) ion emission is generally similar for pure metals and their oxides, at least for Ti-Zn.
- 3) the variations in ion yields for dilute ions in a matrix are reduced relative to the pure metals. As a result the relative SI intensities obtained from pure metals do not form a good basis for extending ion probe analysis to more complex systems unless suitable corrections are made.

We gratefully acknowledge NSF DES 72-01596 A02 Res and NASA NGL 14-001-169 Res and -171 Res. We thank Joe Goldstein for supplying the meteorite sample.

References

- ¹Andersen, C. A. and J. R. Hinthorne (1973) Thermodynamic approach to the quantitative interpretation of sputtered ion mass spectra. Anal. Chem. 45, p.1421-1438.
- ²Meyer, C., D. H. Anderson and J. G. Bradley (1974) Ion microprobe mass analysis of plagioclase from "non-mare" lunar samples. Proc. Fifth Lunar Sci. Conf. 1, p.685-706.
- ³Banner, A. E. and B. P. Stimpson (1975) A combined ion probe/spark source analysis system. Vacuum 24, p.511-517.
- ⁴Andersen, C. A. (1970) Analytic methods for the ion microprobe mass analyzer. Part II. Int. J. Mass Spect. Ion Phys., 3, p.413-428.
- ⁵Gittins, R. P., D. V. Morgan and G. Dearnaley (1972) The application of the ion microprobe analyser to the measurement of the distribution of boron ions implanted into silicon crystals. J. Phys. D, 5, p.1654-1663.
- ⁶Bakale, D. K., B. N. Colby and C. A. Evans (1975) High mass resolution ion microprobe mass spectrometry of complex matrices. Anal. Chem. 47, p.1532-1537.
- ⁷Bradley, J. G., D. Y. Jerome and C. A. Evans (1975) A comparison of mass spectra from three ion probes. NBS Special Publication 427, p.69-78.

⁸Jurela, Z. (1975) Average energy of sputtered ions from fifteen polycrystalline targets. *Int. J. Mass Spect. Ion Phys.* **18**, p.101-110.

⁹Andersen, C. A. (1969) Progress in analytical methods for the ion microprobe mass analyzer. *Int. J. Mass Spect. Ion Phys.* **2**, p.61-74.

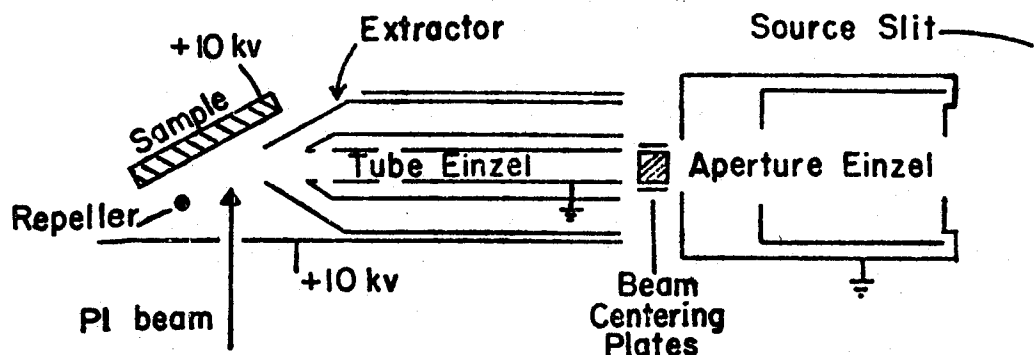


Figure 1. Secondary ion extraction system of the Chicago AEI ion probe. The function of the lenses is discussed in the text.

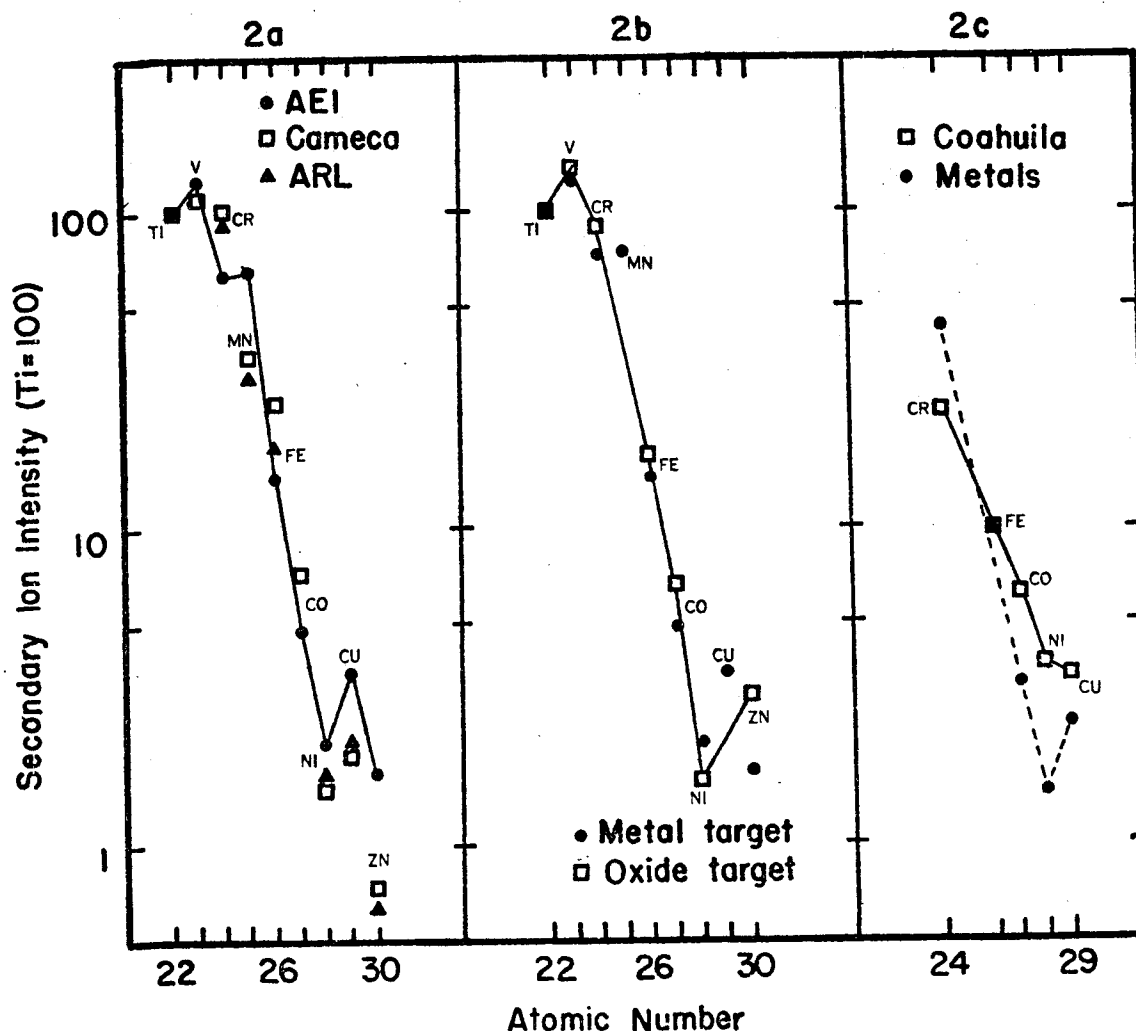


Figure 2. (a) Relative secondary ion intensities for pure metal targets of the first transition series. 20keV $^{16}\text{O}^-$ primary beam. The data are corrected for natural isotopic abundances. Also shown are data from ARL and Cameca ion probes. All SI intensities normalized to Ti = 100.

(b) Relative secondary ion yields for pure metal (solid circles) and metal oxide (open circles) targets of the first transition series. 20keV $^{16}\text{O}^-$ primary beam.

(c) Relative secondary ion intensities recorded from O^- bombardment of the Coahuila iron meteorite. Data are corrected for actual abundances and normalized to Fe = 1. For comparison data from pure metals (Fig. 2) are also shown, now normalized to Fe.

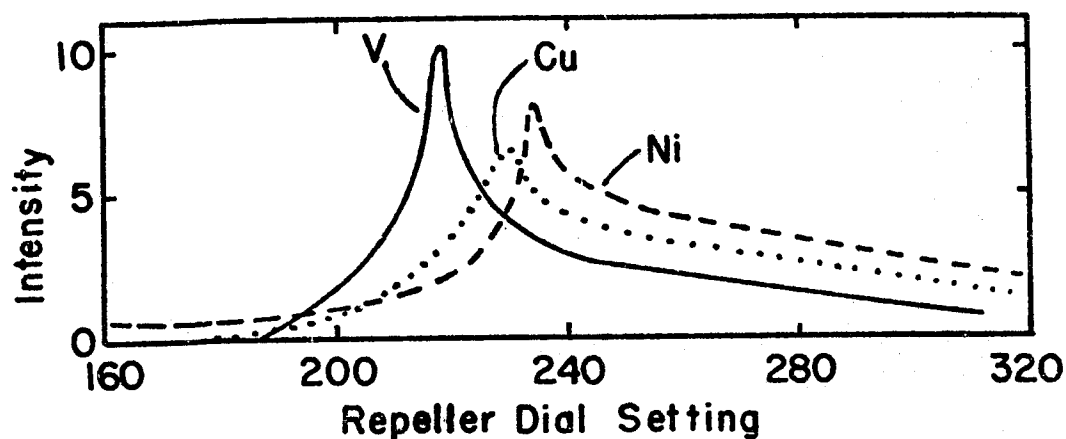


Figure 3. Variation of the SI intensity for V, Cu and Ni as a function of repeller potential. The range in repeller shown corresponds to a variation in applied voltage of 500 to 1000 volts above the sample potential.

Local Thermal Equilibrium Analysis of Secondary Ion Mass
Spectra from Multi-Element Glasses

Dale E. Newbury, Robert L. Myklebust
and Kurt F. J. Heinrich
Analytical Chemistry Division
National Bureau of Standards
Washington, D. C. 20234

Abstract

Of the several approaches to quantitative analysis with secondary ion mass spectrometry [1-3], the local thermal equilibrium (LTE) model [4-6] has been developed to the point of applicability to diverse samples. Because of the difficulty in obtaining close standards for many samples or in transferring sensitivity factors from one specimen to another or, indeed, from one instrument to another, LTE analysis is frequently the only alternative. To assess the accuracy which can be expected from this approach, the LTE model was applied to the analysis of a series of well-characterized multi-element glasses.

The LTE approach [4-6] makes the assumption that the interaction volume of the primary ions with the specimen is a dense plasma in thermal equilibrium. The ratio of ions to neutral atoms in this plasma can then be described by the Saha-Eggert ionization equation in terms of the temperature, electron density, ionization potential, and partition functions. In a particular analysis situation, characterization of the plasma requires determination of the temperature, T , and the electron density, N_e , the other parameters being obtained from other sources. If the concentrations of at least two elements in the sample are known (the internal standards), the ratios of the measured secondary ions to the number of neutral atoms can be used to derive T and N_e from the Saha-Eggert equation. The T and N_e values thus determined are used to determine the ionization ratio and, therefore, the concentration for the other elements in the sample. In addition, a correction

for the formation of oxide species can be carried out, usually by measuring the ion signals for an element and its oxide (such as O/O_2 or Si/SiO); this ratio is then used to estimate the oxide components for other elements.

In the present work, the LTE-model program CARISMA, developed by Andersen and co-workers [4,5], and a simple LTE-model program developed by Simons [6], were used to quantitatively analyze multi-component glasses. These glasses provided excellent test specimens for LTE analysis because (1) the glasses contain at least five cations plus oxygen, allowing various combinations of internal standards to be tested; (2) the glasses have been shown to be homogeneous on a micrometer scale by electron probe microanalysis; (3) since the glasses are amorphous, ion channeling effects are eliminated; and (4) mixtures of many elements can be obtained in a single phase.

The SIMS spectra of the glasses were obtained with an ARL IMMA under standardized operating conditions: (1) Specimen preparation - The specimens were polished with standard metallographic procedures and carbon coated. Prior to data collection, an area of approximately $75\text{ }\mu\text{m}$ square was cleaned by ion erosion to a depth of about 50 nm. (2) Primary beam - A focused beam of $^{16}O^-$ ions at 21.5 keV relative to the specimen was scanned over an area $75\text{ }\mu\text{m}$ square. (3) Secondary ions - The secondary ion transmission was peaked with the sample voltage for the silicon peak, if available. Otherwise, a matrix peak was used. A secondary spectrometer slit of $250\text{ }\mu\text{m}$ or $500\text{ }\mu\text{m}$ was used, as appropriate. (4) The residual pressure was 10^{-4} pa and consisted mainly of oxygen, nitrogen and argon.

In determining the accuracy of the analysis, an error factor, F , was defined as

$$F = C(\text{true})/C(\text{LTE})$$

where C is the atomic concentration.

Table 1 contains a quantitative reduction of a spectrum for NBS glass K-326 with various combinations of internal standards and oxide ratios (analyses 1 to 4). In general, the error factors are small, lying in the range 0.77 to 1.14. Note, however, that the temperature varies from 6640 to 16120 K and the electron density varies from 1×10^{15} to 1.8×10^{20} . The "best fit" values of T and N_e depend strongly on the choice of internal standards; to speak of a "CARISMA temperature" as if it were unique seems to be quite dangerous [7]. Analysis 5 in Table 1 was made with the simple LTE model; error factors similar to those of CARISMA are found.

For comparison, the analysis of glass K-253 is given in Table 2. In this case, the error factors are much higher, ranging from 0.58 to 10.5. Note, however, that in this case the values of T and N_e are relatively insensitive to the choice of internal standards, with T ranging from 14,000 to 16,900 K, and N_e ranging from 3×10^{19} to 3×10^{20} e^-/cm^3 .

Twenty-six elements present in various matrices at a level of 0.02 a/o to 10 a/o were studied. The error factors F or $1/F$ for 311 elemental determinations with CARISMA are plotted in the form of a histogram in Figure 1. The general observation is that 50 percent of the analyses lie within a factor of two of the known concentration, and 80 percent within a factor of five. Of the 20 percent of the determinations outside a factor of five, the majority have $F > 5$, which indicates that the LTE model underestimates the concentration. Moreover, certain elements, particularly zinc, lead, tantalum and phosphorus, consistently give large error factors. Unfortunately, the error factors are not constant, but range widely. Histograms for approximately 100 elemental determinations with O/O_2 (figure 2), Si/SiO (figure 3), and no oxide ratio (figure 4) show similar distributions. The reasonable fit without an

Table 1. LTE Model Analysis of SIMS Spectrum from NBS Glass K-326. Analyses 1-4 were made with the CARISMA Program [4,5]. Analysis 5 was made with the Simple LTE Model [6].

NBS Glass K326

Element	atom %	1	F	2	F	3	F	4	F	5	F
B	15.6	15.6 ⁺	1	15.5 ⁺	1	14.7	1.06	15.1	1.03	15.6	1
Mg	13.5	12.7	1.06	12.8	1.05	13.5 ⁺	1	13.5 ⁺	1	12.5 ⁺	1.08
Na	1.18	1.18	1	1.1	1.07	1.14	1.04	1.0	1.14	0.99	1.19
Ca	2.6	3.3	0.77	3.1	0.84	2.6 ⁺	0.99	2.6 ⁺	0.99	2.7 ⁺	0.96
Si	9.0	9.0 ⁺	1	9.3 ⁺	0.97	9.9	0.91	9.6	0.94	10.1	0.89
T, K°		6640		9400		16120		14620		12035	
n _e		1 15		1.6 17		1.8 20		5.1 19		5.1 18	
oxide		O ₂		SiO		O ₂		SiO		none	

+ Internal Standard

5 LTE (Simons)

Table 2. LTE Model Analysis of SIMS Spectrum from NBS Glass K-253. Analyses 1-5 were made with CARISMA.

NBS Glass K253

Element	atom %	1	F	2	F	3	F	4	F	5	F
Si	20.9	26.7 ⁺	0.78	20.9 ⁺	1	20.9 ⁺	1	20.9 ⁺	1	26.7	0.78
Ba	7.3	7.3 ⁺	1	12.5	0.58	12.5	0.58	12.5	0.58	7.3 ⁺	1
Zn	2.9	0.38	10.3	0.38 ⁺	10.3	0.37	10.5	0.38	10.3	0.38	10.3
Co	1.0	0.48	2.2	0.49	2.1	0.49 ⁺	2.1	0.47	2.2	0.48	2.2
Cu	0.99	0.42	2.4	0.41	2.4	0.39	2.5	0.42	2.4	0.42	2.4
Mn	3.7	2.5	1.5	3.0	1.2	2.9	1.2	3.0 ⁺	1.2	2.5 ⁺	1.5
T, K°		14000		16600		16000		16900		14000	
n _e		3.1 19		1 20		5.7 19		1.4 20		3 20	

Ba/BaO

+ Internal Standard

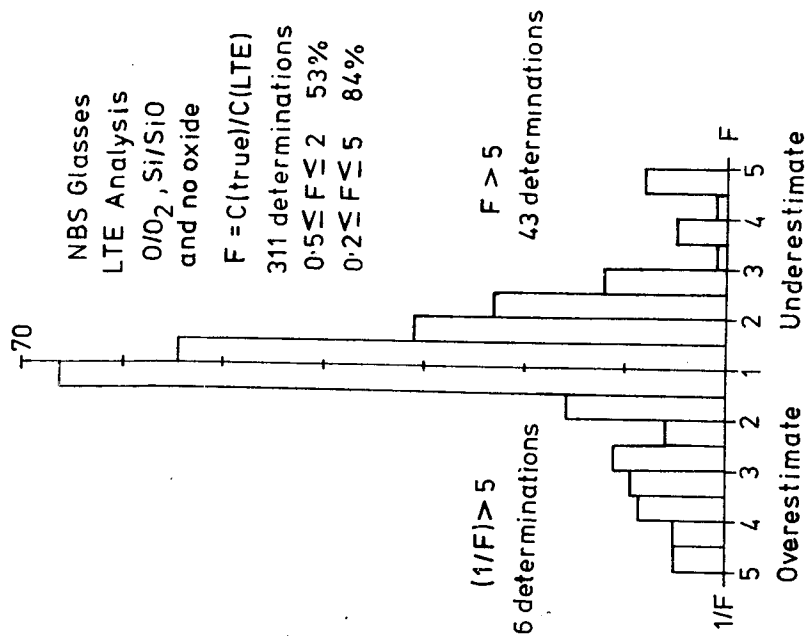


Figure 1. Error factor histogram of 311 elemental determinations with the LTE model CARISMA. The analyses were made with O₂ and Si/SiO₂, and with no oxide ratio supplied.

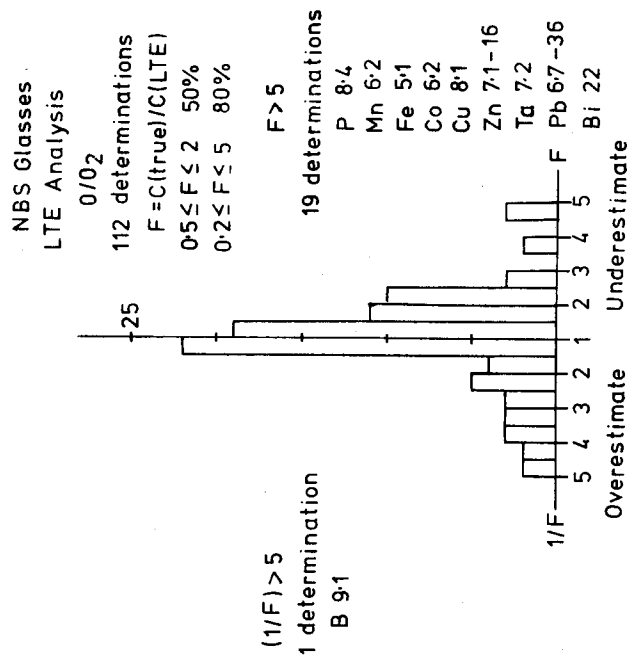


Figure 2. Error factor histogram of 112 elemental determinations with the LTE model CARISMA. O₂ was used as the oxide ratio.

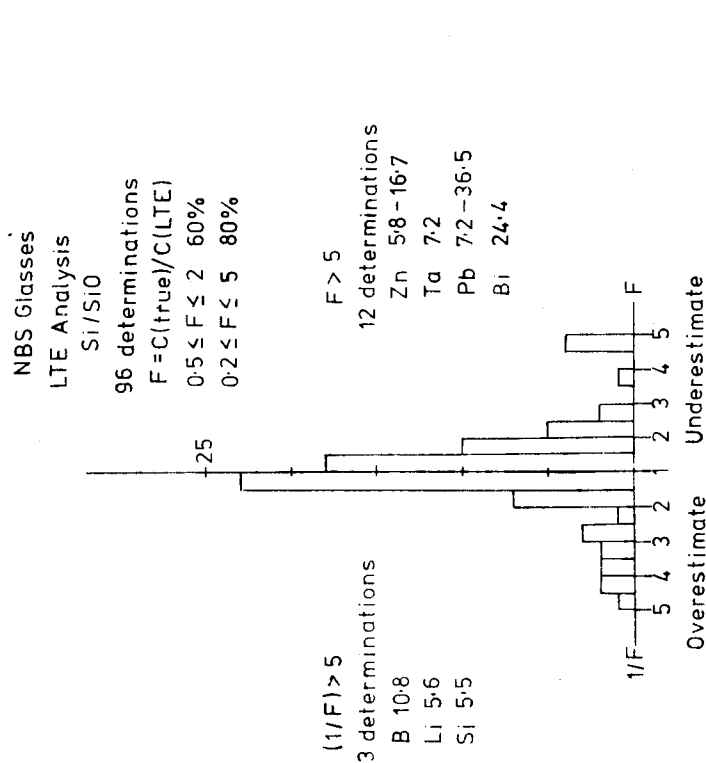


Figure 3. Error factor histogram of 96 elemental determinations with the LTE model CARISMA. Si/SiO was used as the oxide ratio.

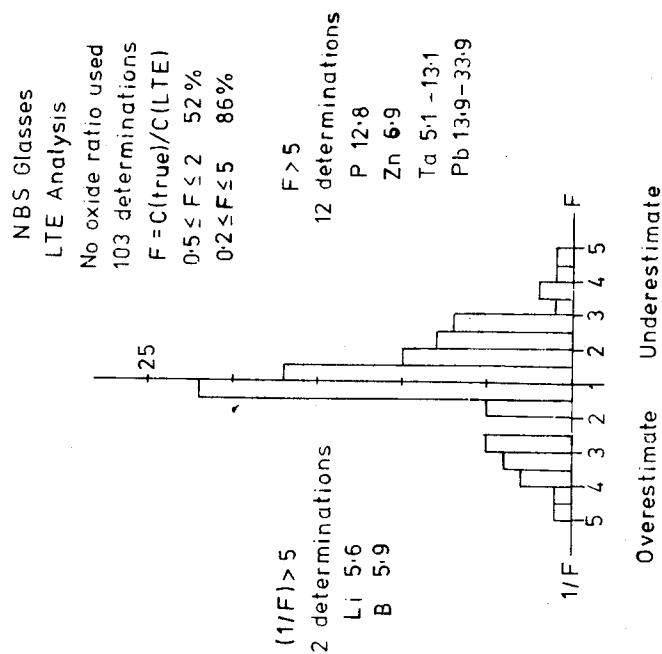


Figure 4. Error factor histogram of 103 elemental determinations with the LTE model CARISMA. No oxide ratio was used.

oxide correction may indicate that such corrections are not particularly valuable.

Further work is being carried out on glasses with up to ten elements in a matrix of two oxides.

References

1. Schroeer, J. M. in Secondary Ion Mass Spectrometry, NBS Special Publication 427, Heinrich, K. F. J. and Newbury, D. E., eds. (U.S. Dept. of Commerce, Washington, D. C.) p. 121 (1975).
2. McHugh J. A. in Secondary Ion Mass Spectrometry, *ibid.*, p. 129 (1975).
3. Jurela, Z., *Int. J. Mass Spectr. and Ion Phys.* 12, 33 (1973).
4. Andersen, C. A. and Hinthorne, J. R., *Anal. Chem.* 45, 1421 (1973).
5. Andersen, C. A. in Microprobe Analysis, Andersen, C. A., ed. (Wiley, New York) p. 531 (1973).
6. Simons, D., presented at the United States-Japan Joint Seminar on Quantitative Techniques in Secondary Ion Mass Spectrometry, Oct. 13-17, 1975, Honolulu, Hawaii.
7. Andersen, C. A. in Secondary Ion Mass Spectrometry, NBS Special Publication 427, Heinrich, K. F. J. and Newbury, D. E., eds. (U.S. Dept. of Commerce, Washington, D. C.) p. 79 (1975).

PHASE ANALYSIS IN STEEL BY SECONDARY ION MASS SPECTROMETRY

by Ph. MAITREPIERRE, R. NAMDAR-IRANI, J. ROFES-VERNIS,
B. THOMAS and G. HENRY (*)

Analysis of materials by secondary ion mass spectrometry (SIMS) has become an increasingly widespread method over the past few years. Besides use in surface or thin film analysis, SIMS has been applied to a number of analytical problems, particularly in the area of trace elements analysis.

Whereas a complete understanding of the precise laws governing secondary ion emission is still lacking ⁽¹⁾, a number of semi-empirical models ^(2, 3) for quantitative analysis have been put forward. The physical basis of such models is, however, still a matter of discussions. In spite of this situation, there is now a general agreement about the basic parameters which influence secondary ion emission. Among the most conspicuous ones, the effects of chemical bonding have been recognized for some time ⁽¹⁾.

In the analysis of metallurgical samples by SIMS, the general trend ^(4, 5) has been to use appropriate calibration curves deduced from experiments on standards. In most cases, a residual oxygen gas pressure was used to suppress chemical effects. In another respect, attention has been drawn by various authors ^(6, 7) towards the information contained in the polyatomic ions part of the secondary spectra.

We will report here on a preliminary set of data obtained on austenitic steels containing carbide-forming Nb. In contrast to classical elementary analysis, the approach used here stems from the idea that secondary ion emission can be made sensitive to phase transformations (precipitation or redissolution of carbides) by monitoring the intensity of selected monoatomic or polyatomic species.

Experimental procedure.

Two austenitic steels, with compositions (wt %) as follows, were studied :

(*) - All authors are associated with the Institut de Recherches de la Sidérurgie Française (IRSID) - B.P. n° 129 - 78104 ST GERMAIN EN LAYE CEDEX - FRANCE.

Table I

	Ni	Cr	Nb	C	N	B
Fe-Ni ₃₇ steel	36.9	/	0.46	0.036	n.d.	/
18-10 stainless steel	9.4	18.7	0.31	0.03	0.07	0.004

The Nb, C and N contents of these two steels are such that all of the Nb can precipitate (with proper heat treatment) as Nb (C, N) carbide.

Secondary ion emission studies were performed with a CAMECA - IMS 300 ion probe. Primary ions were O_2^+ (10 keV) with a 400 μm in diameter beam, of approximately 5 μA . Vacuum was kept at about 1.5×10^{-7} Torr in the system throughout the experiments.

Intensity of secondary positive ion signals were monitored. Relative intensities with respect to $^{56}Fe^+$ signal were used to minimize effects of primary beam intensity fluctuations and lattice effects. All measurements were made in steady state conditions, after 1 minute sputtering.

Experimental results.

Preliminary experiments having indicated that the presence of Nb as carbide or in solid solution would have an effect on secondary ionic yield of this element, data were systematically obtained on both steels in various heat treatment conditions.

a) Fe-Ni₃₇ steel.

A preliminary heat treatment (1300°C - 30 mn + water quenching + 850°C - 48 hours) was used to assure complete precipitation of Nb as NbC. Samples were then re-treated 1 hour at temperatures ranging from 900°C to 1350°C to study the re-dissolution of NbC carbide (known to occur in that temperature range). The normalized secondary $^{93}Nb^+ / ^{56}Fe^+$ and $^{105}(NbC)^+ / ^{56}Fe^+$ ionic intensities were determined on that series of samples. $^{93}Nb^+$ was chosen as possibly indicative of an influence of the chemical state of Nb on secondary emission, whereas $^{105}NbC^+$ was looked for as a direct "witness" of the presence of NbC carbide.

The results obtained are presented in Fig. 1. It can be observed that both Nb/Fe and NbC/Fe signals vary strongly and continuously with the heat-treatment conditions. Moreover, the $^{105}\text{NbC}^+$ signal goes to zero at approximately 1300°C, temperature which should be that of complete NbC redissolution in the system considered here ⁽⁸⁾.

b) 18-10 stainless steel.

Both re-dissolution, in the 1000-1300°C temperature range, and isothermal precipitation of Nb (C, N) at 900°C were studied in this steel ^(*). Additional X-ray diffraction experiments were also conducted on the same samples which were ion-analyzed, in order to obtain additional information on the volume fraction of Nb (C, N) present in each case.

Both sets of results pertaining to the isothermal precipitation at 900°C (after soaking at 1250°C - 1 hour) are presented in Figure 2. Nb/Fe intensity is shown to be approximately constant up to 1 hour and then increases by a factor 3 to saturate for about 24 hours holding time. Austenite lattice parameter (which decreases with increasing volume fraction of Nb (C, N)), reaches also constant levels for the same holding times. It appears therefore that both ion emission and X-ray diffraction yield analogous information on the precipitation of Nb (C, N) in the conditions considered. To check further this point, a correlation is sought (Fig. 3) between the ion emission data and the lattice parameter measurements. All the data presented refer to the same steel, in various heat treatment conditions. A satisfactory linear correlation between both sets of data appears in Figure 3.

Discussion and conclusions.

The two sets of results presented here, both relative to precipitation or re-dissolution of Nb (C, N) carbide in austenite, emphasize the following points.

- It appears that the secondary $^{93}\text{Nb}^+$ intensity (normalized to $^{56}\text{Fe}^+$) is strongly dependant on whether Nb is in solid solution or bound in an Nb (C, N) carbide.

(*) - In stainless steels, these precipitates contain some Cr substituted for Nb ⁽⁹⁾. The possible influence of that substitution is currently being investigated.

- The polyatomic ion $^{105}\text{NbC}^+$ is also a marker of the presence of Nb (C, N) and its intensity goes to zero for complete solution.

It is well known that chemical effects, in general, can have a strong influence on secondary ion yield : the case of ionic compounds such as oxides and halides is well documented (1, 10). The high ionization efficiency observed for M^+ ions is then directly linked to the ionic state of bonding of these elements in these compounds.

Nb (C, N) carbide has an NaCl-type crystallographic structure and directional bonding between metal and non-metal atoms (11). In such a case, one could expect some effect of this on secondary ion emission when compared to emission from an FCC solid solution. The secondary ion yield for $^{93}\text{Nb}^+$ would vary with the amount of Nb bound to carbon (and nitrogen) in a system where Nb could be distributed (according to heat treatments) between solid solution and Nb (C, N) precipitates.

Whether chemical bonding alone is responsible for the observed effects, it remains that the polyatomic $^{105}\text{NbC}^+$ mass yields an analogous information on the precipitation of Nb (C, N). It has been recognized for a long time (6, 7), that polyatomic masses could be taken, in some cases, as markers of specific phases. It appears here that $^{105}(\text{NbC})^+$ is such a marker ion. Unfortunately, its intensity is much smaller than that of $^{93}\text{Nb}^+$, which makes it less attractive for a systematic investigation on a large series of samples.

In conclusion, the results presented here indicate that, at worst, a semi-quantitative and, at best, a fully quantitative information on the amount of Nb precipitated as carbides can be obtained by secondary ion emission. Preliminary results indicate also that Ti and V (11) precipitated as carbides would also be revealed by secondary ion emission.

This technique appears therefore as a new tool in the array of methods used for phase analysis. Its specific characteristics (mostly its sensitivity to trace amounts) might make it indispensable in a number of cases, like phase analysis of microalloyed steels.

Acknowledgements.

We thank M. MABILLE for his contribution to the experiments and Dr. PHILIBERT for stimulating discussions.

References.

- (1) - G. SLODZIAN. - Surf. Sc. 48, 161 (1975).
- (2) - C.A. ANDERSEN and J.R. HINTHORNE. - Science 175, 853 (1973).
- (3) - R. SHIMIZU, T. ISHITANI and Y. VESHIMA. - Jap. J. Appl. Phys. 13, 249 (1974).
- (4) - V. LEROY, J.P. SERVAIS and L. HABRAKEN. - Bull. du C.R.M. n° 35 (jun. 1973), p. 69.
- (5) - V. LEROY, J.P. SERVAIS and L. HABRAKEN. - Report EUR 5329 F. Commission of European Communities (1975).
- (6) - H.W. WERNER, H.A.M. DE GREFFE and J. VAN DEN BERG, in Advances in Mass Spectrometry, Vol. 6, p. 673 (Applied Science Publishers Ltd. - England).
- (7) - R. LAURENT. - Thèse 3ème cycle - Orsay (1973).
- (8) - S.R. KEOWN and F.B. PICKERING, in "Creep strength in steel and high temperature alloys". Metals Society, London (1974), p. 134.
- (9) - J. BOURGEOT, J. CHARBONNIER, G. HENRY, B. MICHAUT and B. THOMAS, final report on DGRST contract 73-7-1594 (1975).
- (10) - M. BERNHEIM, in "Second Colloque International de Physique et Chimie des Surfaces" - Brest (1975), p. 28 (Ed. by Société Française du Vide).
- (11) - H.J. GOLDSCHMIDT. - Interstitial alloys. Ed. by BUTTERWORTHS - London (1967).
- (12) - T. TSUNOYAMA, Y. OHASHI, T. SUZUKI and K. TSURUOKA. - Jap. J. Appl. Phys. 13, 1039 (1974).

*

*

*

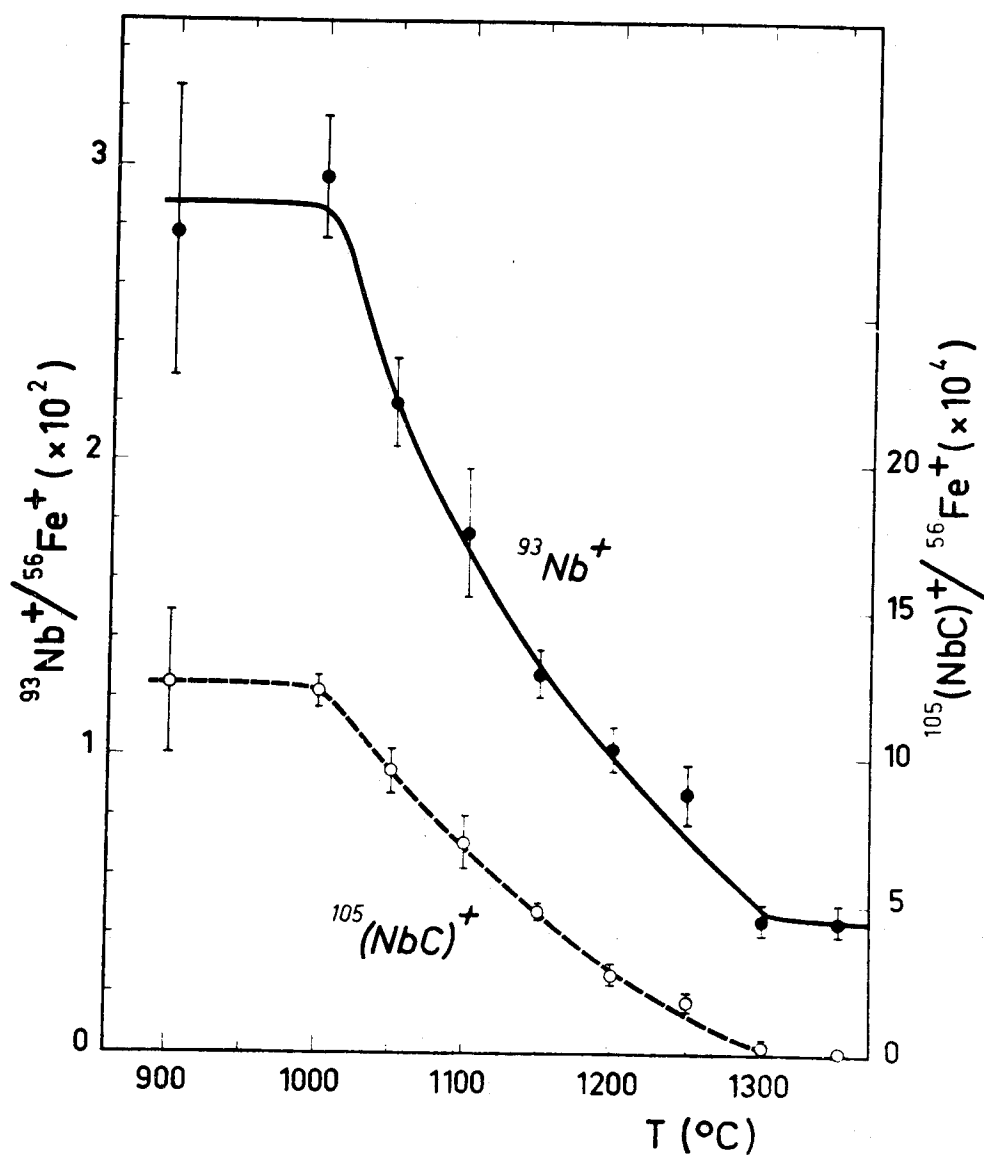


Fig. 1 - Fe-Ni₃₇ Steel : Evolution of normalized $^{93}\text{Nb}^+ / ^{56}\text{Fe}^+$ and $^{105}(\text{NbC})^+ / ^{56}\text{Fe}^+$ signals as a function of redissolution temperature (O_2^+ primary - energy window 0-7 volts, residual pressure $\approx 1.5 \times 10^{-7}$ Torr).

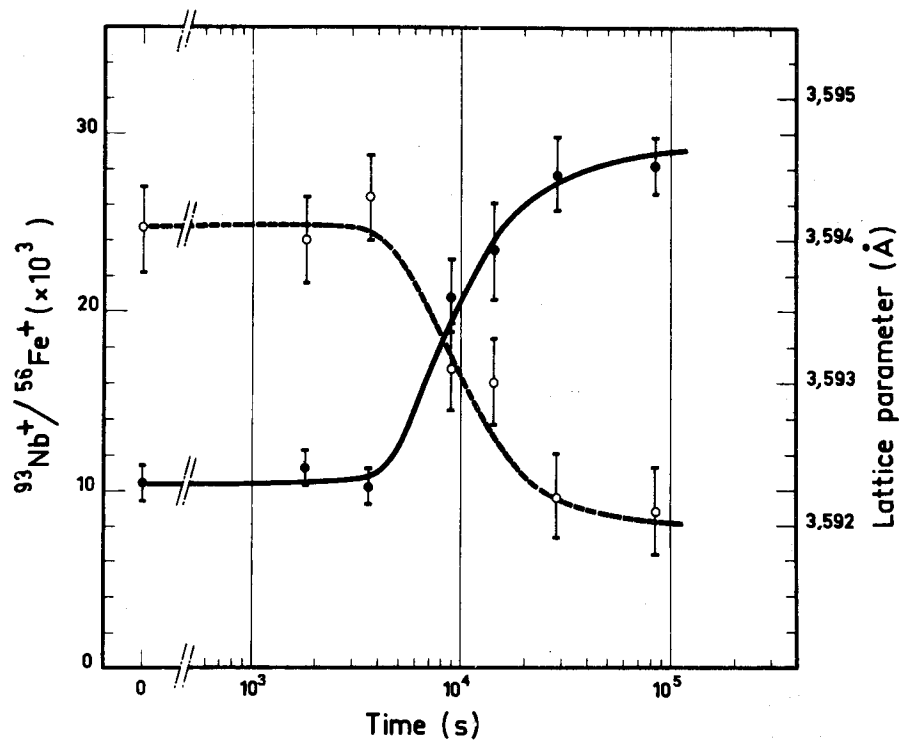


Fig. 2 - 18-10 stainless steel : Isothermal precipitation of Nb(C,N) at 900°C.

- open symbols and dotted line : evolution of austenite lattice parameter.
- full symbols and solid line : evolution of $^{93}\text{Nb}^+ / ^{56}\text{Fe}^+$ signal.

(O_2^+ primary - Energy window 0-15 volts - Residual pressure 1.5×10^{-7} Torr).

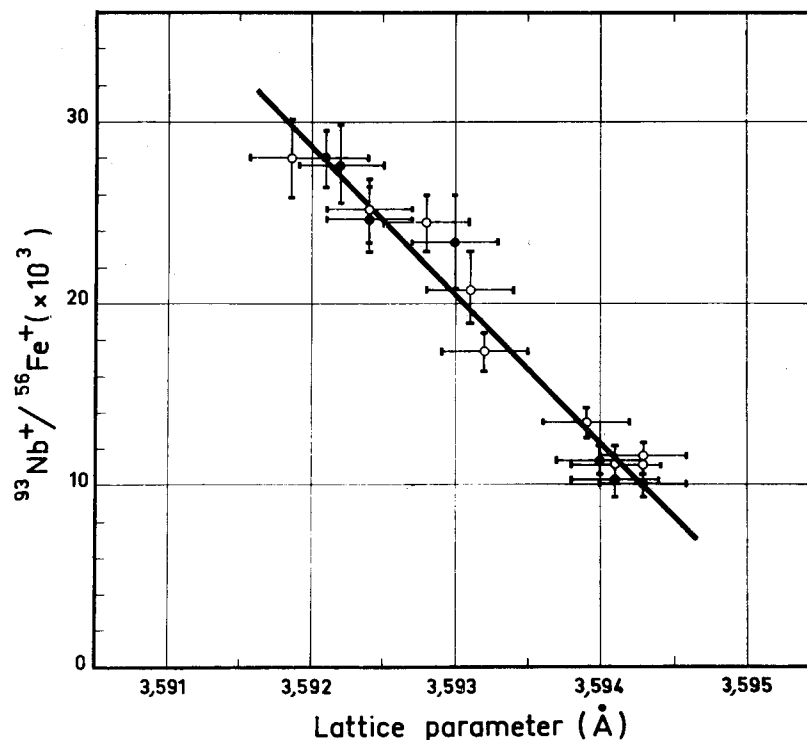


Fig. 3 - 18-10 stainless steel : Correlation between austenite lattice parameter and secondary Nb/Fe signal for precipitation () and redissolution () treatments (same experimental conditions as in Fig. 2).

Sensitivity Effects in the Analysis of Ni-Cr-Fe Alloys by IMMA

by

J.D. Brown, Metaalinstituut TNO and The University of Western Ontario,
London, Canada

D.J. Gras, Metaalinstituut TNO, Apeldoorn, The Netherlands

A.P. von Rosenstiel, Metaalinstituut TNO, Apeldoorn, The Netherlands.

B.H. Kolster, Metaalinstituut TNO, Apeldoorn, The Netherlands.

A series of Ni-Cr-Fe alloys (Table 1) of varying compositions were analysed using an IMMA to establish the diffusion of Co and Mn from the surface as a result of heat treatment. The alloys were prepared from research grade metals by vacuum melting and homogenization.

The scanning micrographs of Fig. 1 show the increased concentrations of Ni, Mn and Co at the surface as well as an enhanced Cr and Mn concentration at the grain boundaries of the heat treated specimen of Alloy 5, nominally pure iron. It was required to establish the Co and Mn depth profiles from the surface and to compare these profiles from one base composition to another.

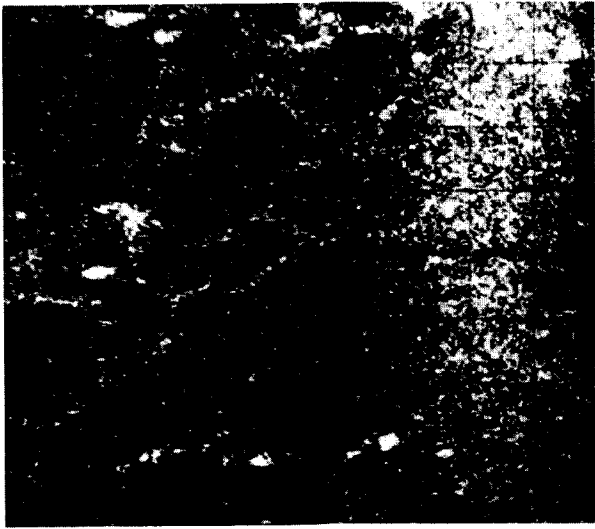
Typical depth profiles showed increases in surface Mn and Co ion intensities by one or even two orders of magnitude over that of the bulk material, with the zone of enhanced concentration extending into the material for up to 5000 Å.

The depth of sputtering was measured from the final crater depth by an interference microscopy technique, assuming that the sputtering rate was constant. Interpretation of a single intensity profile in terms of relative concentration changes was straightforward since the matrix composition was essentially constant and secondary ion intensity then directly related to concentration. However two severe problems are encountered in comparing one depth profile with another where the matrix composition is significantly different. First the relative intensities from the same alloy change dramatically with primary ion beam density requiring careful standardization of analysis conditions. Second the total ion yield from the Ni alloy 1 is depressed by an order of magnitude compared to other alloys of lower nickel content such as alloy 2 or 3. Along with the depressed total ion yield is a similar decrease in the ion intensity for Co and Mn. The question of whether these decreased intensities reflect lower actual concentrations of Co and Mn was answered using the LTE model for quantitative analysis.

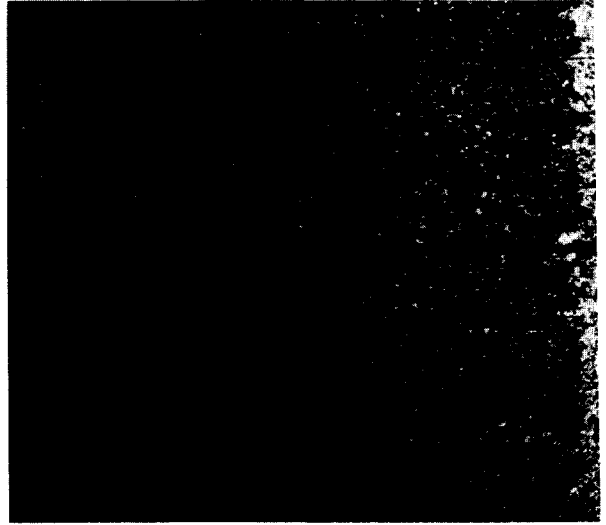
Table 1
Nominal Compositions of alloys

<u>Alloy</u>	<u>Composition</u>
1	Ni
2	20 Fe - 80 Ni
3	50 Fe - 50 Ni
4	80 Fe - 20 Ni
5	Fe
6	80 Fe - 20 Cr
7	50 Fe - 50 Cr
8	20 Fe - 80 Cr
9	Cr

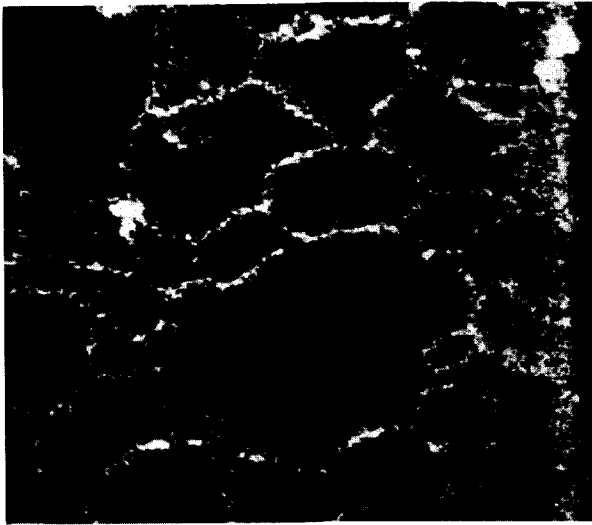
44B



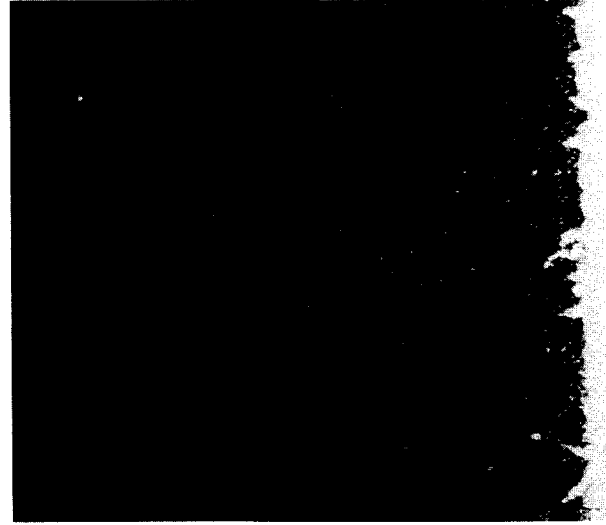
Mn



Co



Cr



Ni

30μm

Fig. 1
Scanning ion micrographs of Alloy 5

ION-MICROSCOPE CHARACTERIZATION OF CARBURIZED
THORIATED-TUNGSTEN WIRE CATHODES

B. F. PHILLIPS AND J. A. AMY
ELECTRON OPTICS LABORATORY (CODE 30333)
NAVAL WEAPONS SUPPORT CENTER
CRANE, INDIANA 47522

Specimens for examination were obtained from highly carburized thoriated-tungsten wire-mesh cathodes of commercial power tetrode tubes as follows:

1. From the centers of cathodes which had been operated for approximately 10 hr (FT4-807 (Center) and B4C (3-4)).
2. From the center of a cathode which had an operating life of approximately 3500 hr (LV29572 (3-4)).
3. From one end of the cathode with 3500-hr life, adjacent to a nickel support disc which acted as a heat sink and reduced the temperature of the wire locally (LV29572 (1)).

Figures 1 and 2 show typical fracture surfaces of these wires: a central core of metallic tungsten is surrounded by a layer of carburized tungsten. Details of the microstructure are reported elsewhere (1).

Metallographically-prepared transverse sections of these specimens were examined using an automated CAMECA Direct-Imaging Mass Analyzer (2, 3). High-sensitivity mass scans were performed for all elements (both positive and negative ions) to determine elements present in the wire, after which images of portions of the surfaces were obtained with ions of all elements detected in each wire (Figure 3). It is useful to discuss these ion micrographs on an element-by-element basis.

Tungsten

The layer of radial columnar crystals is much thinner and may be more equiaxed in the 3500-hr specimens than in the 10-hr specimens; this may well be related to differences in fabrication, however, rather than to differences in operating life. The coarser texture of the metallic W at the center of the 3500-hr cathode than at the end suggests that the tube operates with the central portion just above the recrystallization temperature and the ends just below it.

Carbon

In the 10-hr cathodes C is associated with W in the radial columnar crystals at the surfaces of the wires. In the center of the 3500-hr cathode, however, the C layer lies a few micrometers below the surface, as expected because of the slow decarburization which occurs during tube operation. There is less C in this specimen, and it is less uniformly distributed; i.e., there are fewer carbide grains.

Thorium and Thoria

In the 10-hr specimens, both the size and frequency of ThO_2 particles in the carburized layers seem to be less than in the metallic core, perhaps due to reduction of ThO_2 to Th by C and H during cathode processing, followed by evaporation of the Th. In the 3500-hr cathode, however, the ThO_2 dispersion seems fairly even across the wire, especially in the cooler end specimen.

Silicon

Silicon is present in all wire specimens examined. It appears to be closely related to the C layers, and in the center of the 3500-hr cathode it too lies in a band a few micrometers below the surface.

Barium

Barium is present in all wire specimens examined. Its concentration is much higher and its inclusion size is much smaller in the 10-hr cathodes than in the 3500-hr one.

Sodium and Potassium

These elements are dispersed throughout all the wires as inclusions, mostly less than 1 micrometer in diameter, which are more numerous in the 10-hr wires than in the 3500-hr wire.

Conclusion

Commercial thoriated tungsten wire contains a number of elements which may affect the emitting life of cathodes for electron tubes. While K is beneficial at low concentrations in lamp-filament wire, being added together with Si and Al to control the microstructure (4), there is no reason to believe that such deliberate doping was performed in these wires. Also, the presence of trace amounts of Ba in the thoriated tungsten wire may affect the emission characteristics. Further work is needed to clarify the roles of the elements found in the cathodes.

REFERENCES

1. J. A. Amy, R. A. Alcorn, B. F. Phillips, "Scanning Electron Microscopy of Carburized Thoriated Tungsten Direct Emitting Cathodes," EMSA Proceedings (1976).
2. B. F. Phillips, "Secondary-ion mass analysis: Instrumentation, data interpretation, and applications," Journal of Vacuum Science and Technology, Vol. 11, No. 6, Nov/Dec 1974 pp 1093-1099.
3. L. E. Plew, "Automation of an Ion Microscope," Quantitative Techniques in Secondary Ion Mass Spectrometry," U. S. National Science Foundation, University of Hawaii, October 12-17, 1975.
4. C. J. Smithells, Tungsten, Chapman and Hall, 1952.

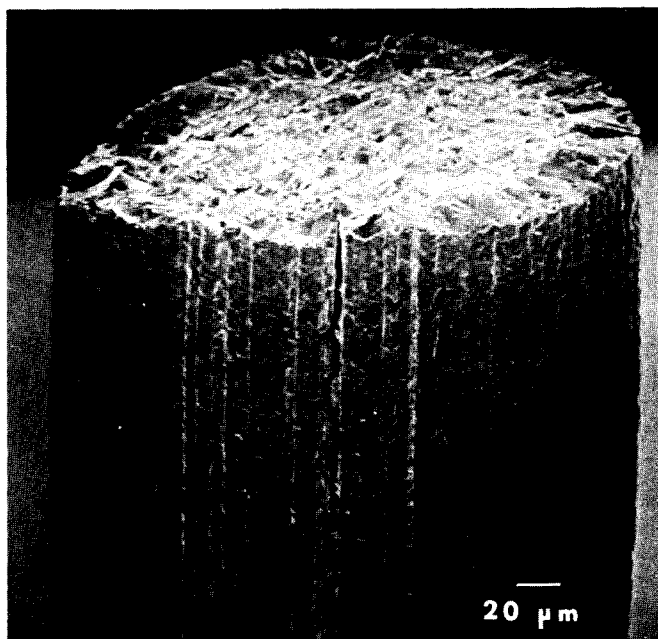


Figure 1. Typical scanning electron micrograph of fracture surface of carburized W-ThO₂ wire, here from the center of a cathode with 10-hr life (FT4-807 (center)). Note the clear distinction between carburized layer and metallic core. (NWSC-EOL-75-195)

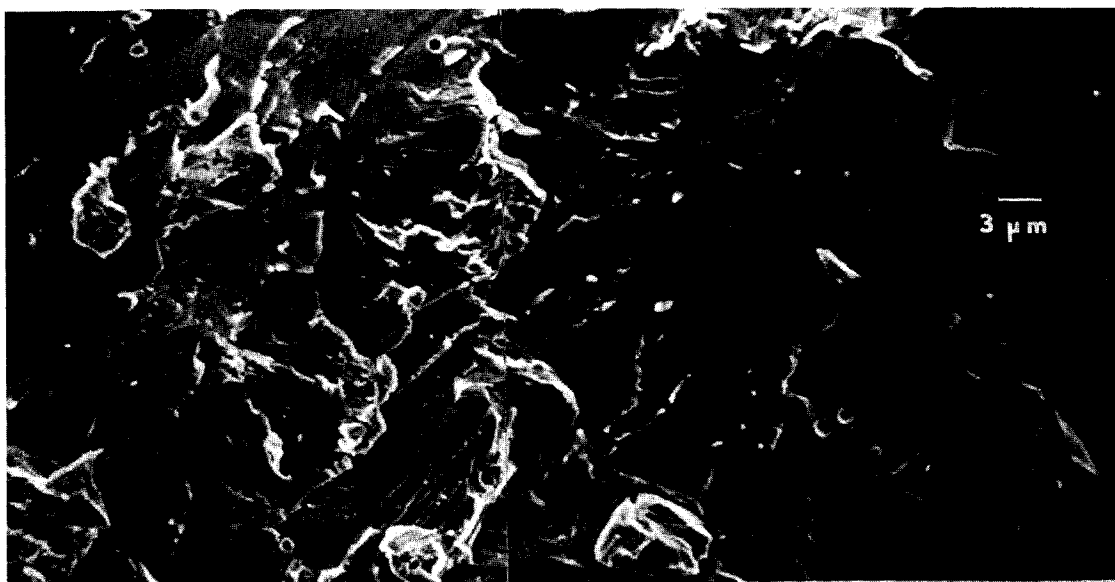


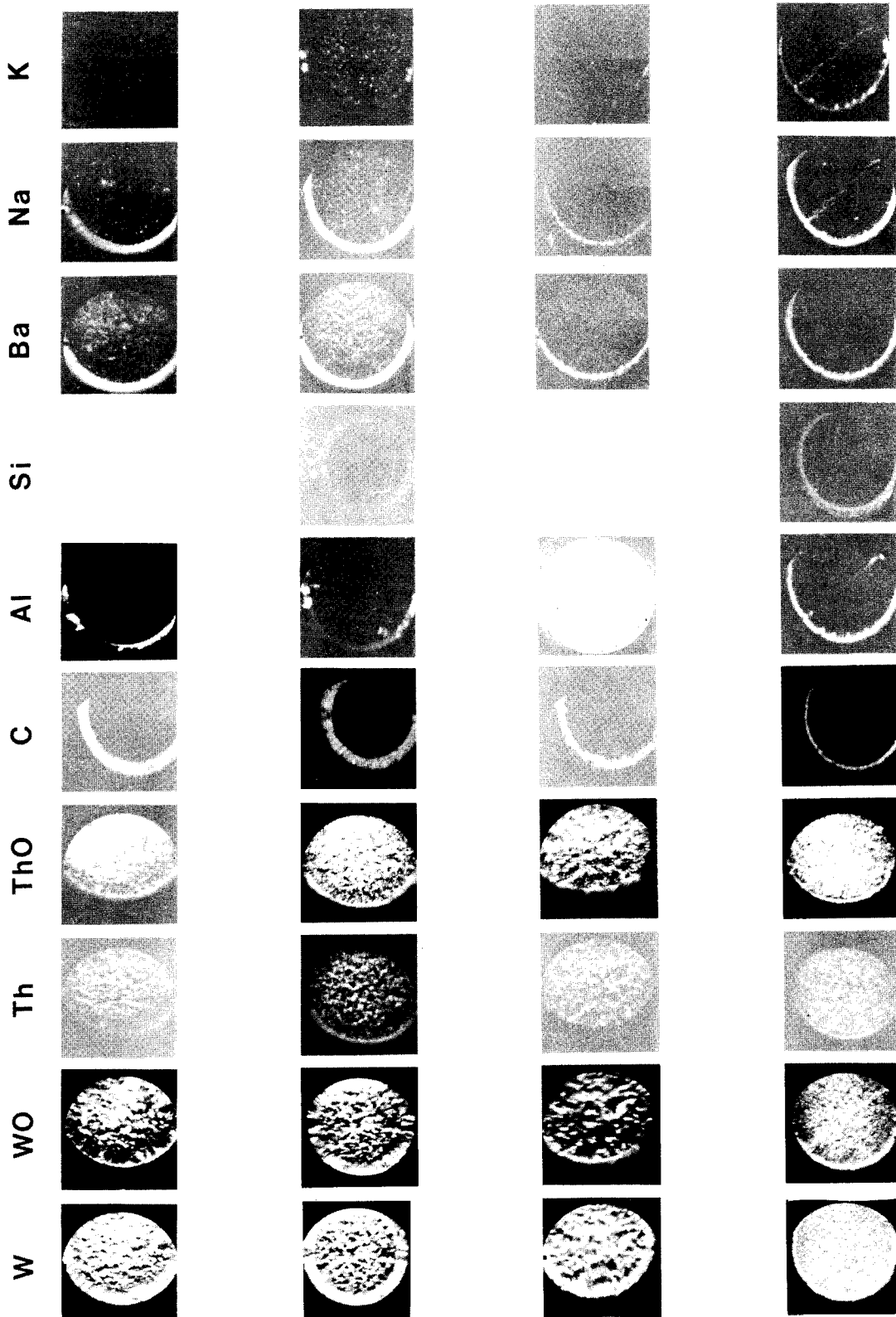
Figure 2. Typical scanning electron micrograph of fracture surface of carburized W-ThO₂ wire, here from the center of a cathode with 3500-hr life (LV29572 (3-4)). The distinction between carburized layer and metallic core is less evident at this magnification. (NWSC-EOL-75-228/230)

Figure 3. DIMA STUDY OF CATHODE WIRES

0.1 mm

Tube

Chemical Species



45D

HIGH MASS-RESOLUTION ION MICROPROBE ANALYSIS

S.J.B.Reed, J.V.P.Long, J.N.Coles & D.M.Astill

N.E.R.C. Ion Probe Unit, Dept. of Mineralogy & Petrology, University of Cambridge,
Madingley Rise, Cambridge CB3 0EZ, England.

Molecular interferences

The molecular peaks in ion microprobe mass spectra often interfere with the monatomic peaks used for analysis. The difference in mass between peaks occurring at the same mass number determines the mass resolution required to separate the peaks, and the way in which mass defect (δm) depends on mass number (m) allows prediction of the resolution required ($\text{res.} = m/(\delta m_1 - \delta m_2)$). From mass 20 to 64, which includes many of the commonest elements, δm decreases linearly (fig.1). Generally monoxides are the most intense molecular peaks. For $m < 64$ the resolving power required to separate monoxide and monatomic peaks ranges up to 3300. This also applies to other binary molecules (except hydrides - see below) since they lie approximately on the same line on the δm plot. However, beyond mass 64 the slope decreases and the monatomic and binary lines cross at about mass 90. In this region it is therefore difficult to resolve binary molecule interferences. Beyond 90 the lines diverge and it again becomes relatively easy to resolve monatomic and binary molecule peaks.

Similar considerations apply to ternary molecules: ternaries composed of species lying on the straight section at the low-mass end of the δm plot lie on a parallel straight line to the right of the binary line, and a line still further to the right may be drawn to represent quaternaries (fig.1).

The ternary and monatomic lines cross at 108, while the quaternary crosses at 122. Beyond the crossover points molecular and monatomic peaks become increasingly easy to resolve: for example ^{156}Gd and $^{56}\text{Fe}^{28}\text{Si}_3^{16}\text{O}$ require a resolution of only 2500. Molecular interferences are likely to be difficult to resolve at high mass numbers only when other heavy atoms are present in significant amounts (e.g. a resolution of 8700 is required to separate ^{174}Yb and $^{158}\text{Gd}^{16}\text{O}$).

Hydride peaks are typically 1/100 to 1/10000 of the intensity of the parent (1). The mass defect of ^1H is +8 m.m.u., therefore the negative slope of the δm plot for $m < 90$ helps to keep hydride and monatomic peaks apart. For example the resolution required to separate ^{40}Ca from $^{39}\text{K}^1\text{H}$ is 4500. Beyond mass 90 hydrides become increasingly difficult to resolve, especially above mass 140 where the slope becomes positive (e.g. ^{153}Eu and $^{152}\text{Sm}^1\text{H}$ need a resolution of 24000).

Resolution/intensity relationship

In most ion microprobes resolving power is sacrificed in order to maximise secondary ion transmission. With low mass resolution (<500) practically no molecular peaks can be resolved, and subtractive corrections have to be applied where possible. It is preferable to have an instrument capable of high mass resolution but intensity is inevitably sacrificed owing to the necessity of reducing the width of the mass spectrometer entrance slit, and for trace element analysis especially intensity is crucial. In the AEI IM-20 instrument (2) resolution of several thousand (10% valley definition) is obtainable, but at maximum resolution the loss of intensity is severe (fig.2). At around 3000 resolution the intensity is reduced by a factor of about 10, and in many cases trace element analysis is feasible. The preceding discussion shows that such resolution is sufficient to separate many interfering molecular peaks, though there are still examples which it is impracticable to resolve.

Analysis of diopside glass for Cr

As a test case for the use of the high mass resolution available with the AEI IM-20 instrument we analysed synthetic diopside glasses ($\text{CaMgSi}_2\text{O}_6$) containing from 10 to 3000 ppm Cr (by weight). The samples were mounted together in a block of epoxy resin, polished, and coated with a thin evaporated carbon film. The primary beam consisted of $^{16}\text{O}^-$ ions accelerated to 35 keV relative to the sample, with a current of 4 nA and a beam diameter of about 10 μm . A cold finger near the sample was used to minimise hydrocarbon contamination.

The principal isotope of Cr at mass 52 coincides with the $^{26}\text{Mg}_2$ peak. The difference in masses is 25 m.m.u., and with 3000 resolution the peaks are well separated (fig.3), the loss of intensity compared with low resolution being about a factor of 10. The beam was left for 30s on each analysed point on the sample to allow secondary ion emission to stabilise, after which ^{52}Cr ions were counted for 20s. The six specimens were analysed in rapid succession several times and the results averaged. Fig.4 shows the mean count-rate plotted against Cr concentration. The detection limit is estimated to be below 1 ppm. In this case the 'working curve' approach is evidently applicable, though it might not work so well for crystalline samples, due to the possible effect of crystal orientation on secondary ion emission. If low mass resolution were used errors due to interference from $^{26}\text{Mg}_2$ would occur, especially at low Cr concentrations.

References

1. Colby, B.N. & Evans, C.A., Appl. Spectrosc., 24, 274 (1974).
2. Banner, A.E. & Stimpson, B.P., Vacuum, 24, 511 (1974).

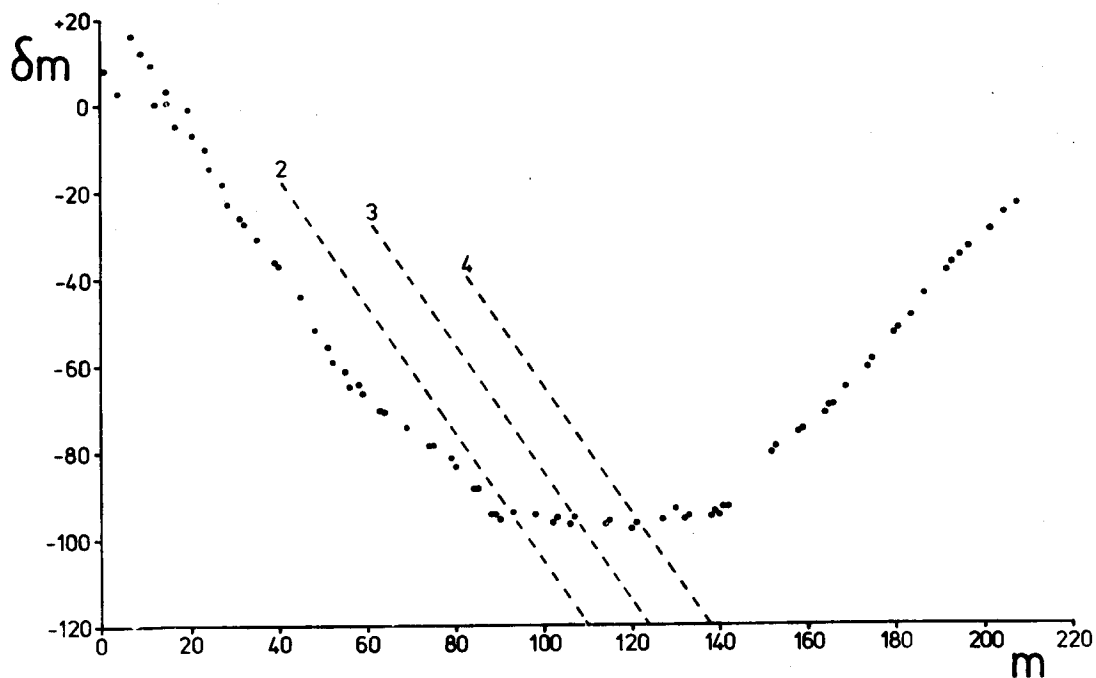


Fig.1. Mass defect (δm) in milli-mass units as a function of atomic mass (m) for the most abundant stable isotope of each element (other stable isotopes lie on the same curve). Dashed lines represent δm for binary (2), ternary (3), and quaternary (4) molecules made up of atoms of mass < 60 .

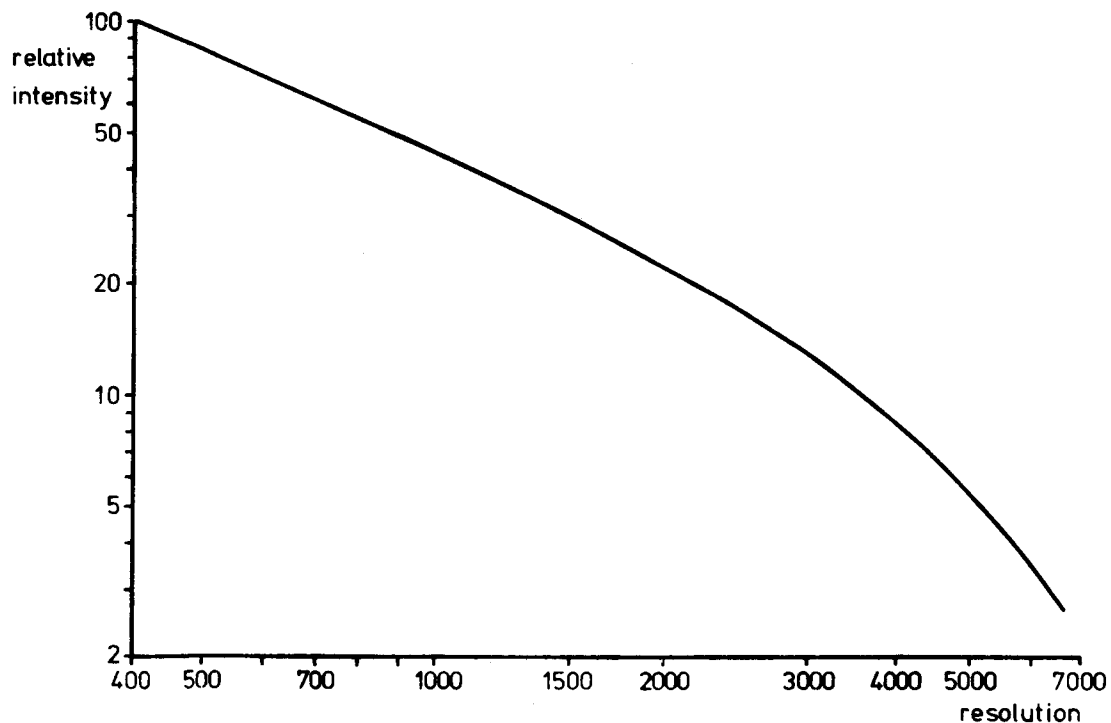


Fig.2. Relative secondary ion intensity as a function of mass resolution (10% valley definition) for AEI IM-20 ion microprobe.

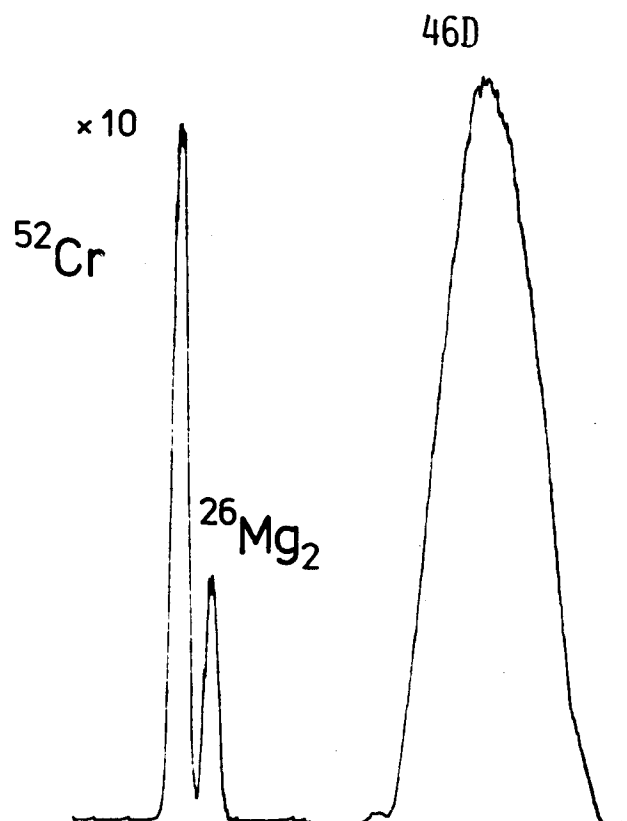


Fig.3. Mass 52 peak from diopside glass with 1000 ppm Cr (by wt.): low resolution peak on right; resolved doublet on left (resolution ~ 3000).

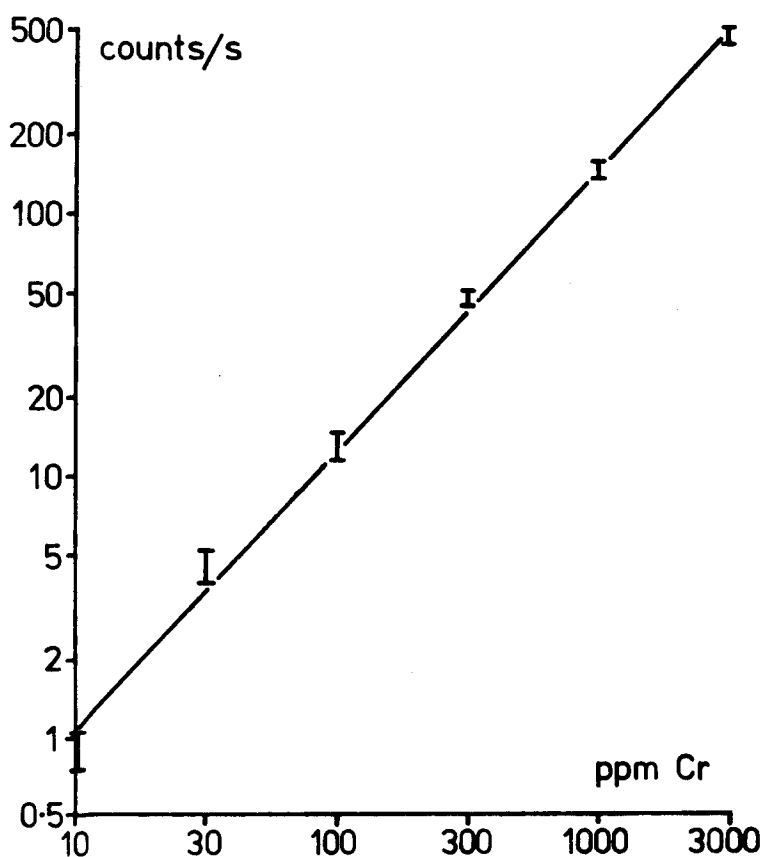


Fig.4. Intensity of ^{52}Cr against ppm Cr (by wt.) in diopside glass.

SCANNING AUGER MICROANALYSIS OF PARTICLES

by

N. C. MacDonald and R. L. Gerlach

Physical Electronics Industries, Inc.
6509 Flying Club Drive
Eden Prairie, Minnesota 55343

Scanning auger microprobe analyses were performed on on graphite particles in cast iron. Both metallurgically polished samples in samples fractured in situ at a pressure of 5×10^{-10} torr were analyzed. On both the polished and fractured samples, scanning auger images and line scans provide a semi-quantitative analysis of carbon, both on the graphite particle and in the adjacent ferrite region. Secondary electron images indicate the perlitic regions of the sample and auger analysis confirms the increased carbon content in the cementite (Fe_3C) regions. It is shown that auger line scans are possible even on the rough fracture surface; the influence of topography is determined by taking a line scan with the spectrometer set at an energy off the selected auger peak. The SAM results are compared with electron microprobe results obtained on similar cast iron samples by other investigators.

THIN FILM STUDIES WITH THE QMAS METALLURGICAL AND ELECTRONIC APPLICATIONS

T. A. Whatley and R. D. Fralick

APPLIED RESEARCH LABORATORIES

Sunland, Calif. 91040

The QMAS (Quadrupole Mass Analyzer for Solids) is a surface and thin film analyzer operating on the principal of mass spectral analysis of material eroded from solid samples by ion sputtering. Since its description by Roden and Fralick (1) it has been applied to a variety of analytical problems. Some of them are discussed below.

Arsenic Implants in Silicon

Typical of applications of the QMAS to semiconductor electronics is the determination of the distribution gradient of arsenic implanted into silicon. This is a difficult problem because of the low ionization yield of arsenic and, more importantly, because of mass interferences from silicon-oxygen compound peaks. At mass 75, the interfering peak is from $^{29}\text{Si}^{30}\text{Si}^{16}\text{O}$, where the oxygen content arises principally from the oxygen primary ion beam. Hydrides of lower mass peaks are not significant in the QMAS when operating with the cold plate cooled with liquid nitrogen. The lack of hydride interference can be readily confirmed by measuring the 75/74 ratio from pure silicon; this should be 0.051 in the absence of hydrides.

Experimental data from a wafer implanted at 1 MeV to a fluence of 1×10^{15} atoms/cm² are shown in Figure 1. The depth scale shown was determined by interferometric measurement of the final crater depth, assuming a constant sputter rate. The concentration scale was determined by reference to a bulk arsenic standard that contained 7.9×10^{19} atoms/cc, confirmed by electron microprobe measurements. Using tabular LSS data from Mayer et. al. (2) we calculate the implant maximum to be 1.5×10^{19} atoms/cc at a depth of 6,630 Å. By calibration we find experimentally a maximum of 1.5×10^{19} at a depth of $7,000 \pm 250$ Å.

Experimental conditions used were oxygen primary beam (positive), 10 KeV, 6×10^{-7} amperes in a 100 μm beam rastered over a rectangular area 550 μm wide. This gave a sputter rate of about 2 Å/sec. Under these conditions, for 25 second measuring intervals, the arsenic detectability is about 1×10^{18} atoms/cc (one sigma, 25 seconds).

Thin Films

By reducing sputtering voltage and sputter rate QMAS data can be optimized to yield a greater amount of information regarding initial sample surface and the composition of very thin surface layers. This is apparent in the data of Figure 2, which is a depth profile of 180 Å of copper over a nickel substrate. A beam of 3 keV (positive) oxygen was used rastered over 650 μm, to give a sputter rate of 0.3 Å/sec in the copper. This allows ample time to obtain spectra of surface constituents, for instance. At this low kV, depth resolution is substantially better than 50 Å.

Oxide/Metal Interfaces

A distinct problem area in SIMS analyses concerns transitions that take place at conductor/insulator interfaces due to charge-up at the insulator surface causing defocusing problems. This problem is overcome in the QMAS design by bombarding such samples with a negative ion beam so that charging is nearly non-existent.

The profile data of Figure 3 illustrates the behavior of a multilayer metal/insulator sample when subjected to QMAS analysis. The sample consisted of an SiO_2 substrate covered with 1100 Å of copper, covered in turn with 1100 Å of gold. (The gold was not monitored in this run). The primary beam was 3 keV negative oxygen ions.

The gold-copper interface presents no problems. At the copper-silica interface there is a rise in count rate for all of the monitored ions. This is a natural consequence of the change of matrix, from a metal to an insulator. The Local Thermodynamic Equilibrium (LTE) model (3) predicts that copper, for instance, will be sputter ionized to about 5% in a typical metal, but the ionization will increase to 22% in a silicate. This increase in sensitivity factor along with a change atom sputter rate, accounts for the temporary increase in ion intensity at the interface. Stable conditions are indicated by the plateau in the silicon signal, while the metals exhibit typical exponential knock-on trailing.

Note that the chromium peak does not show as much enhancement at the interface. This is also consistent with the LTE model, which predicts that the relative insulator/metal sensitivity increase will be a factor of 4.8 for copper, but only 2.4 for chromium; this is just about what is observed.

Throughout the whole profile no adjustments were made to sample biasing, nor were any other conditions changed. The sensitivity variation observed are entirely consistent with LTE predictions of matrix effects. It is clear that in this application negative ion bombardment largely controls the metal-insulator transition problem.

References

1. H. J. Roden and R. D. Fralick, "The QMAS - A Quadrupole Mass Analyzer for Solids." Paper No. 70, 26th Pittsburgh Conf. 1975.
2. Mayer, Eriksson, and Davies, Tabular data from Ion Implantation in Semiconductors, Academic Press, 1970.
3. C. A. Andersen and J. R. Hinthorne, Anal. Chem. 45, 1421 (1973).

48 C

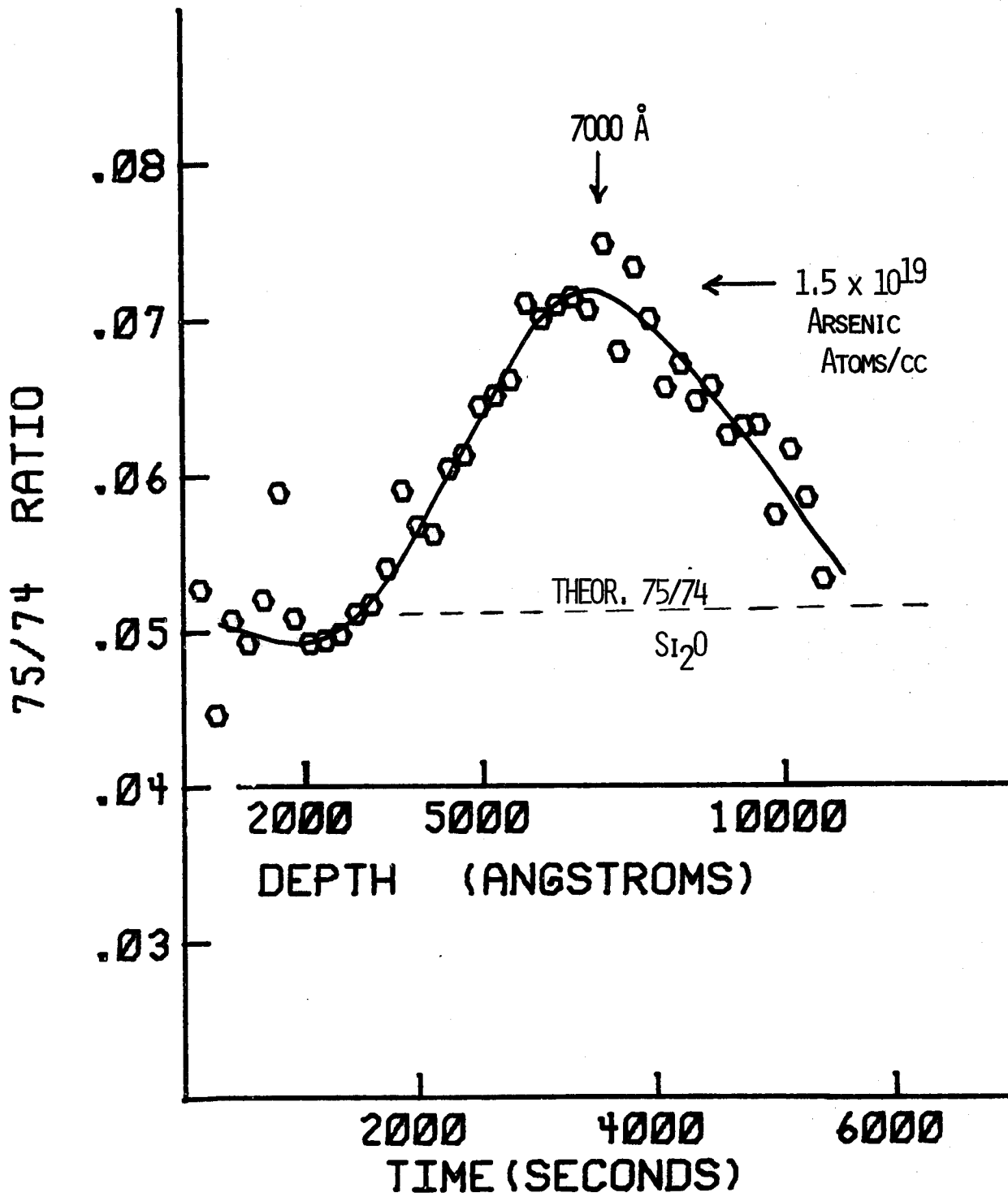


Fig. 1- Depth profile of arsenic- implanted silicon. Implanted at 1 MeV with a fluence of 1×10^{15} atoms/cm².

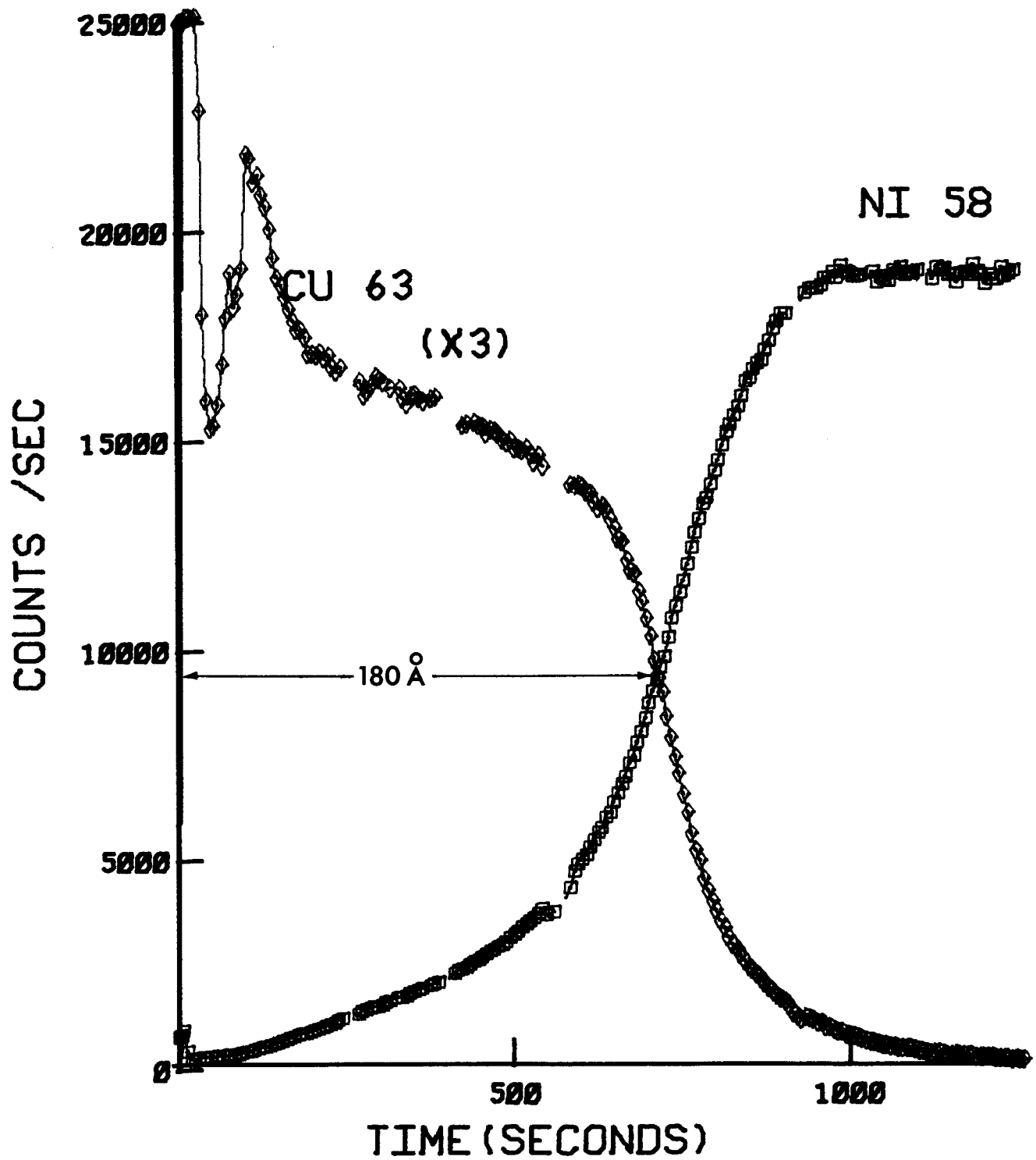


Fig. 2- Depth profile of a thin (180 Å) copper film deposited on a nickel substrate.

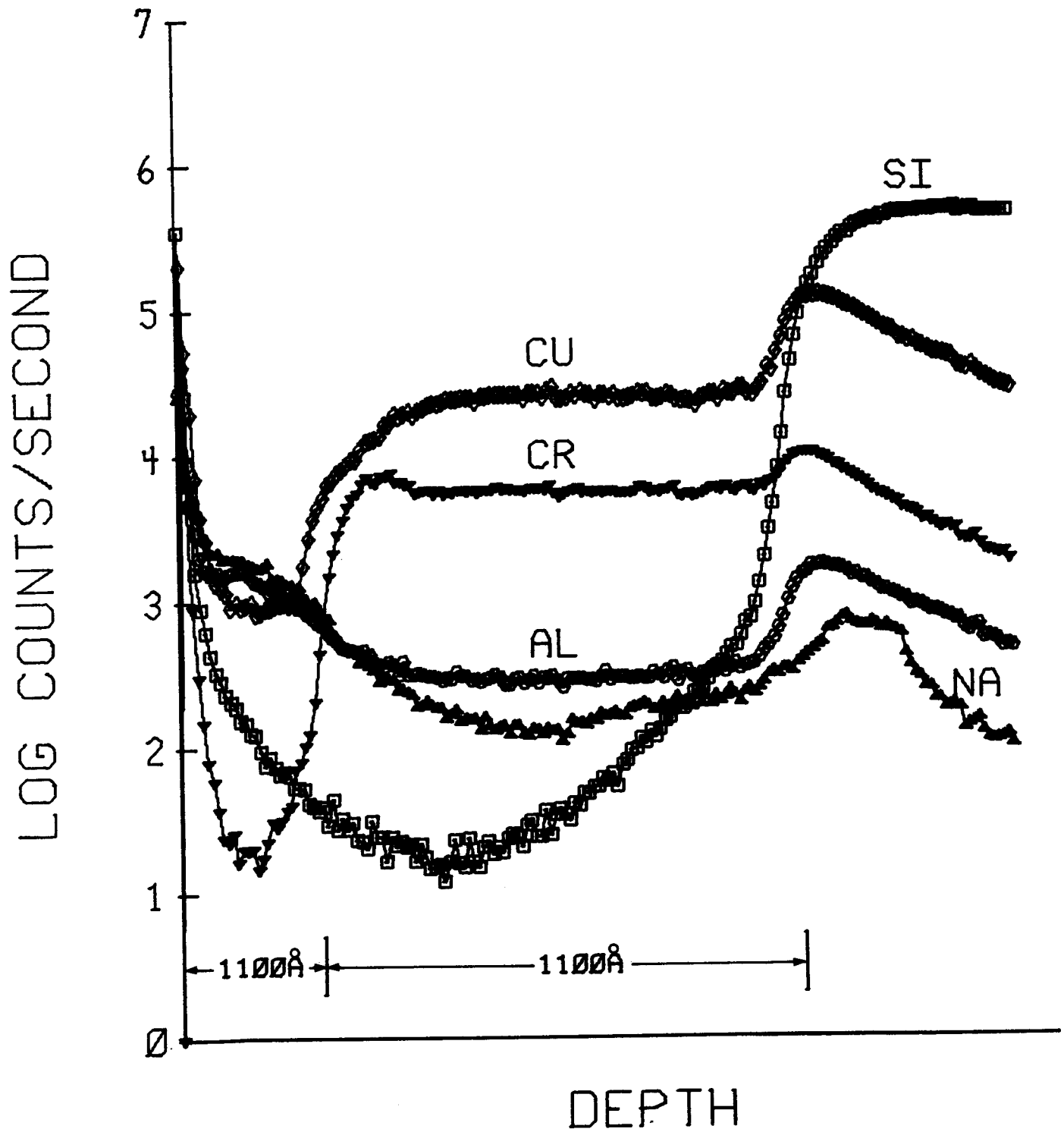


Fig. 3.- Profile through a metal-insulator interface using a beam of negative oxygen ions.

SURFACE ANALYSIS OF INSULATORS BY SIMS

J. A. Leys 3M Central Research Lab., P.O. Box 33221, St. Paul,
Minn. 55133

G. R. Sparrow 3M Analytical Systems, 3M Center, St. Paul, Minn. 55133

Irradiation of an electrically insulating surface with a positive ion beam gives rise to the emission of secondary electrons from the surface. The resulting positive charge accumulation on the specimen causes erratic secondary ion emission. While it is generally possible to perform some type of qualitative SIMS analysis under these conditions, there are several factors which make the results questionable. For example, it is known that this charge buildup can cause migration of certain elements, alkali ions in particular, from the surface into the bulk of the sample. Erratic deflection of the ion beam on the surface caused by charge buildup causes uncertainties in small area and depth profiling analyses. In addition, the resulting energy spread of the secondary ions is characterized by a large proportion of high energy ions which cannot be mass filtered efficiently with a quadrupole. Consequently, the resolution and signal to noise ratio are poor. If only the low energy secondary ions are selected for quadrupole analysis, it has been observed that the signal originates predominately from the outer periphery of the crater formed by the ion beam. Anderson, Roden and Robinson^① have demonstrated successfully the use of a negative primary beam of a reactive gas, generally oxygen, to alleviate the charge-up problem. The ion source used in their case was a duoplasmatron with a hollow cathode instead of a filament which would otherwise deteriorate from reaction with the active gas. Goff^② and others have demonstrated that the charge buildup from positive ion beam bombardment can effectively be neutralized by flooding the surface with low energy electrons from a simple electrically heated tungsten filament. This allows the use of positive noble gas ions as a primary ion source and permits the use of a relatively simple low cost electron bombardment type ion gun.

The SIMS apparatus used has previously been described^③. It is attached to a conventional diffusion pumped scanning electron microscope. A schematic is shown in Figure 1. The flood gun filament operates typically at about 1 ampere and 3 volts. Low energy electrons are attracted to the specimen surface at the point of impact with the positive ion beam. High energy electrons from the SEM column have not generally been found to be effective for charge neutralization. Perhaps emission of secondary electrons from the sample caused by the electron beam

itself compounds the charging problem. The apparent "self-focusing" action of low energy electrons seems to be required. A reactive gas, usually oxygen is introduced to the specimen surface through the capillary jet shown. This maintains the high secondary ion yields characteristic of electro-negative gases as well as displacing diffusion pump oil vapors from the vicinity of the specimen surface.

Several examples of surface and bulk analyses of insulators will be discussed. Additional data concerning the interaction of electron and ion beams will be presented.

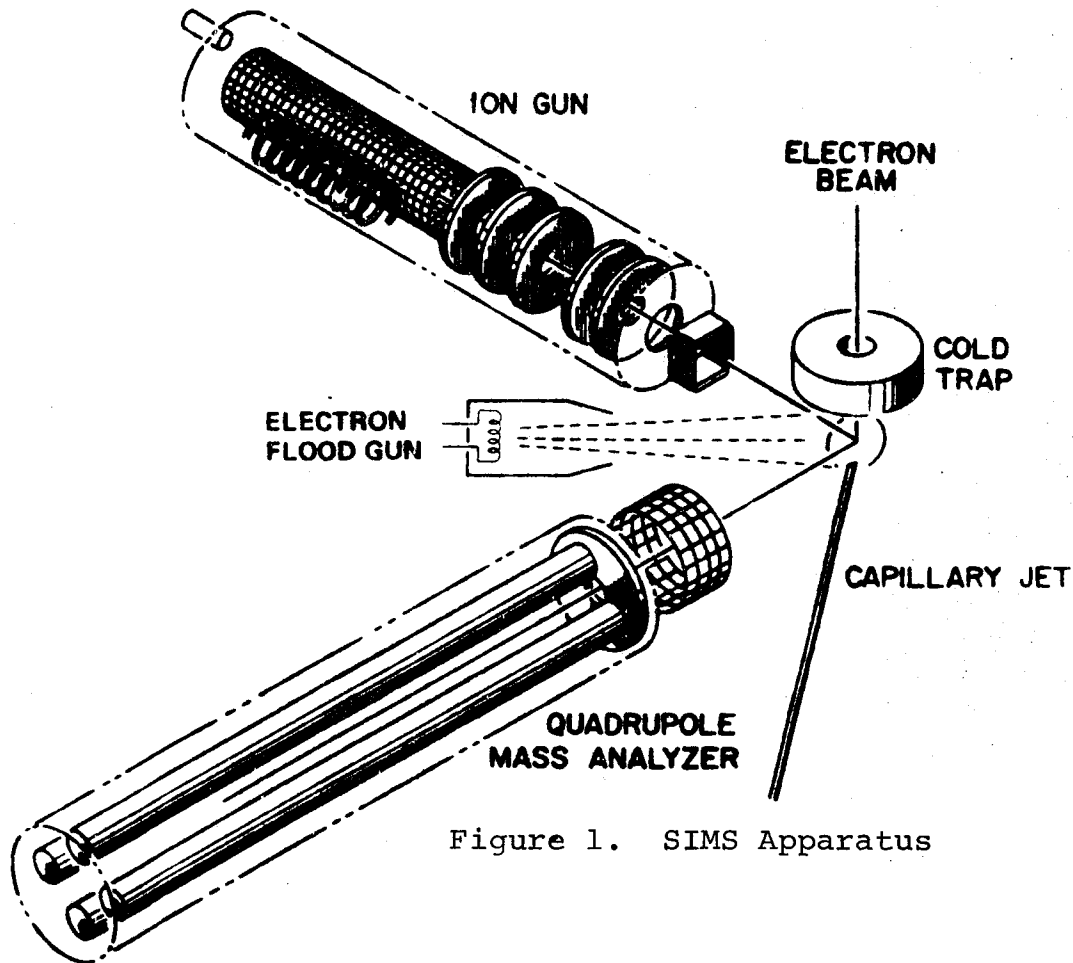


Figure 1. SIMS Apparatus

References

- ① Andersen, C.A.; Roden, H.J. and Robinson, C.F.; J. Appl. Phys. 40 3419-20 (1969).
- ② Goff, R.J. Vac. Sci. Technol. 10 355-358, 1973.
- ③ J.A. Leys, J.T. McKinney, SEM+SIMS: A Unique Combination for Surface Characterization, Proc. 10th Ann. Conf. of Microbeam Analysis Society, Las Vegas, Aug. 11-15, 1975.

"USE OF SCANNING ELECTRON MICROSCOPY
IN APPLIED MATERIALS STUDIES"

Om Johari, Metals Division
IIT Research Institute
10 West 35th Street
Chicago, Illinois 60616

Tremendous growth is taking place in the applications of Scanning Electron Microscope (SEM) to studies of a wide range of materials. The variety of signals generated by the interaction of the incident electron probe with the specimen can provide more information about its basic nature than any single analytical or microscopic technique (1,2). For several of these characterization studies, special suitable attachments may be required, which are not available on every SEM. The purpose of this paper is to briefly review, based on experiences in our laboratory, some techniques which are particularly applicable in materials analysis which do not require extensive SEM modifications or accessories. The emphasis is on examination of microstructure in materials.

The secondary electron imaging-mode commonly used in the SEM is most sensitive to topographic changes on the sample surface. For the examination of smooth surfaces commonly encountered in microstructural studies via metallography, disappointing results are generally obtained (specially at low magnifications) when secondary electron imaging is used. Due to shadowing effects, as well as the availability of atomic number and crystallographic contrasts, we use either backscattering mode (using the standard SEM detector) or use a very large diameter beam (by decreasing the condensor lens current). With this procedure images comparable to optical images have been obtained at low magnifications. As the magnification is increased, the condensor lens current is also increased, so that best resolution at each magnification is obtained. As necessary, we go from the backscattered mode to the secondary mode at higher magnifications. Absorbed current imaging can be also used similar to backscattered imaging (3).

We have encountered frequent problems due to charging of the specimen due to the mounting medium. This is easily recognized if brightness from one side to the other on

the viewing CRT is different, or frequent adjustment of image parameters (contrast and brightness) or astigmatism are required. The best procedure for avoiding problems due to charging is to examine conductive specimens after removing the non-conductive mounting material. In many cases this may not be desirable or practical. A conductive paint-line of silver or graphite works except in those cases where areas at or near the specimen edges are to be examined. Further, presence of silver near the sample may cause problems in analysis i.e., elements whose peaks are in the same region as silver (or other conductive paint) cannot be detected with certainty, particularly when they are present in small amounts. Copper filled mounting material works best in almost all cases, but again problems of analysing copper or elements with peaks near copper peaks cannot be overlooked. In some situations, e.g. in aluminum alloys, copper caused problems due to reaction with the sample, particularly during etching. It is always possible to coat the sample with a conductive layer (evaporative or sputter coating) of carbon or another element consistent with analytical requirements. However, unless a heavier coating is applied some charging related effects may still be observed.

Many mounting materials contain clay or other type of particles which get into areas close to the specimen edges. In one case, while analysing a metallographically prepared failed steel piece we detected some silicates near the crack opening. The result was very misleading, and only discarded later, when an accidental analysis of areas away from the sample showed similar elements.

Generally, etching of samples is desirable, especially when one is first comparing SEM results with optical micrographs. For SEM examination, a slightly heavier etch is recommended. In a few cases etching procedures removed the very phases we were interested in analysing; repolishing and etching with different etchants had to be used to establish the most desirable etching procedure. A very common problem due to etching, not readily recognized in optical metallography, is that etchants often produce debris which may either mask or interfere with examination of the structure of interest. The sample must be first examined as etched. If etching debris is observed, the

sample should be cleaned by replication method, and re-examined. The replica should be allowed to dry (we typically let it stand for 15 minutes) before being peeled off & discarded. Replica can be left on longer to preserve the specimen surface. For some materials, examination immediately after etching is strongly recommended, e.g., in a study of crystalline glasses we found that all glasses (subjected to different heat treatments) were showing same structure in the range of 3000-10000 magnifications. The problem was traced to reaction of the etched glass surface with environment and when the samples were examined immediately after etching, excellent understanding of nucleation and growth processes was obtained.

When the sample is not etched, structure due to crystallographic or atomic number contrast will be observed depending on the observation conditions (usually as already mentioned, at low magnifications, higher beam currents are required). Unetched samples are preferred when phases with different chemistries are to be identified so that preferential attack due to etching is avoided.

The polishing of the samples for SEM metallography is not as critical as for conventional metallography. Due to large depth of focus polishing scratches are easily recognized and normally do not interfere with observation of structure of interest. The polishing compounds used as well as prior condition of polishing equipment often cause problems in analysis and cannot be overlooked. Replica cleaning method discussed above will take off any remaining polishing material also, particularly from interfaces or porosities in the samples. Small particles of polishing material also tend to charge up and affects the appearance of an otherwise good micrograph by appearing very bright.

The method we have used successfully often is to carefully generate fracture faces and examine them for understanding the microstructure. Often the microstructural studies are to relate to mechanical behavior of materials, and a fracture face reflects that well, since a crack goes through the weakest path. Carefully generated fracture faces retain most of the second phase particles for determination of their size and chemistry. In several studies, we have found fractures useful for studying interfaces also.

In conclusion, with proper techniques, SEM provides an excellent tool for the study of microstructures. The major advantages over optical microscopy are (1) structures are examined at better resolutions without additional preparation, (2) chemistry and crystallography can be determined, (3) sample preparation does not have to be as critical, (4) structures on rough surfaces can be also determined, and (5) effects of etching are better understood. The major disadvantages are (1) some modes unique to optical microscopy (color, polarization etc) are not readily available (unless one has an optical microscope as an accessory, as on some electron microprobes) and (2) considerable correlation work needs to be done (i.e. no handbooks of SEM microstructures and methods are available yet as for optical microscopy). In some studies, use of fracture faces to study many important aspects of microstructure should be tried.

I am grateful to my colleagues at IITRI who enable me to understand several of the approaches described above.

REFERENCES

- (1) O. Johari, Characterizing Materials with the SEM To-day. Res./Dev., Aug, 1974, Vol. 25, No. 8, P. 16 to 23.
- (2) O. Johari, Total Material Characterization with the SEM ibid, July, 1971, Vol.22 No. 7, P. 12-20
- (3) D.E. Newbery, "The Utility of Specimen Current Imaging in the SEM", in Scanning Electron Microscopy/1976, Vol. I IIT Research Institute, Chicago, P. 111-119

ENERGY DISPERSIVE X-RAY IDENTIFICATION
OF ROCK FORMING ALUMINOSILICATES

Arthur B. Merkle
Department of Geology
The University of Nebraska-Lincoln
Lincoln, Nebraska 68508

Introduction

Identification of the rock forming aluminosilicate mineral constituents is requisite to any mineralogical, petrological, or geochemical study of rock suites. Usually identification is accomplished by optical mineralogical techniques. A second method of identification is microprobe analysis utilizing wave length dispersed x-rays (WDX) or energy dispersed x-rays (EDX).

Depending on sample type; the preparation, data acquisition, and reduction techniques for WDX analysis may prove exceedingly tedious. In comparison, sample preparation and data acquisition for EDX analysis is relatively simple. However, the EDX analysis of aluminosilicates presents its own special set of problems. One of the main analytical problems is the close proximity of $AlK\alpha$ energy (1.49 kev) and $SiK\alpha$ energy (1.74 kev). The 0.250 kev separation of these peaks result in considerable Al-Si peak overlap in all but the most sophisticated EDX systems. The Al-Si $K\alpha$ peak overlap complicates quantitative EDX aluminosilicate analysis negating the relative ease of sample preparation and data acquisition.

This paper describes a method developed for rock forming aluminosilicate mineral identification taking advantage of the incomplete separation of Al and Si energy peaks.

Analytical Procedure

Analysis is accomplished utilizing a Jeolco JSM-2 SEM in combination with an EDX system comprised of an Ortec solid state detector and power supply, Northern Scientific NS-600 multichannel analyzer (MCA), and Beckman 10" recorder. Resolution of the system is 250 ev FWHM at 5.9 kev. Basic probe conditions of analysis are 15 kv accelerating potential with an auxillary lens setting to yield a sample current of 1×10^{-9} Amps on brass. Other sample and instrumental variables: sample coating, specimen stage tilt, counting interval, etc. are maintained constant. An energy spectrum for each sample accumulates in the MCA for 60 seconds and is traced by the recorder.

Results

The recorded spectrum for each aluminosilicate mineral standard contains an unresolved Al-Si energy peak. The measured distance between the Al-Si energy curve and the position of zero energy at a value of 25% the Al-Si peak height is designated I_e and correlates with a specific energy value and Al content.

Table 1 presents a listing of the mineral standards analyzed, and their chemical composition, Al%, and I_e value.

Figure 1 plots the relationship between I_e and Al% for each mineral standard analyzed. As indicated by Figure 1 a linear relationship exists between I_e and Al%. Linearity of the I_e plot allows a characterization of the Al content of the rock forming aluminosilicates. Determination of the major cation associated with the aluminum further identifies the mineral as a specific feldspar, feldspathoid or related framework silicate.

Conclusions

Determination of the I_e value and the major mono or divalent cation in association with aluminum aids petrographic investigations by providing a rapid identification of rock forming aluminosilicates by energy dispersive x-ray analysis. These minerals may be analyzed as they occur in natural rock surfaces, as inconsolidated mineral fragments, or in thin and/or polished sections.

The technique, as described, may be expanded to other aluminosilicate mineral groups. Similar techniques may be developed to analyze other mineral groups. Because of the component variabilities in EDX systems and their combination with a multitude of different EPMA and SEM systems, individual curves utilizing mineral standards must be developed for each instrumental system.

Acknowledgement

I would like to thank the Department of Geology at Louisiana State University, Baton Rouge for the use of their SEM-EDX analyzing system and for access to their reference collection of minerals.

Table 1. Aluminosilicate Mineral Standards

Mineral	Composition	Al%	Ie
Quartz	SiO_2	-	8.1
Orthoclase	KAlSi_3O_8	9.7	7.5
Microcline	KAlSi_3O_8	9.7	7.5
Leucite	KAlSi_2O_6	12.4	7.3
Pyrophyllite	$\text{Al}_2\text{Si}_4\text{O}_{10}(\text{OH})_2$	15.0	7.2
Nepheline	$\text{NaAlSi}_3\text{O}_8$	19.0	7.0
Kaolinite	$\text{Al}_2\text{Si}_2\text{O}_5(\text{OH})_4$	20.9	6.8
Corundum	Al_2O_3	52.9	6.5

Plagioclase feldspars

	1	2		
Albite	$\text{Ab}_{100}\text{An}_0$	$-\text{Ab}_{90}\text{An}_{10}$	10.3-11.2	7.6
Oligoclase	$\text{Ab}_{90}\text{An}_{10}$	$-\text{Ab}_{70}\text{An}_{30}$	11.2-13.0	7.3
Andesine	$\text{Ab}_{70}\text{An}_{30}$	$-\text{Ab}_{50}\text{An}_{50}$	13.0-14.8	7.2
Laboradorite	$\text{Ab}_{50}\text{An}_{50}$	$-\text{Ab}_{30}\text{An}_{70}$	14.8-16.7	7.1
Bytownite	$\text{Ab}_{30}\text{An}_{70}$	$-\text{Ab}_{10}\text{An}_{90}$	16.7-18.5	6.9
Anorthite	$\text{Ab}_{10}\text{An}_{90}$	$-\text{Ab}_0\text{An}_{100}$	18.5-19.4	6.9

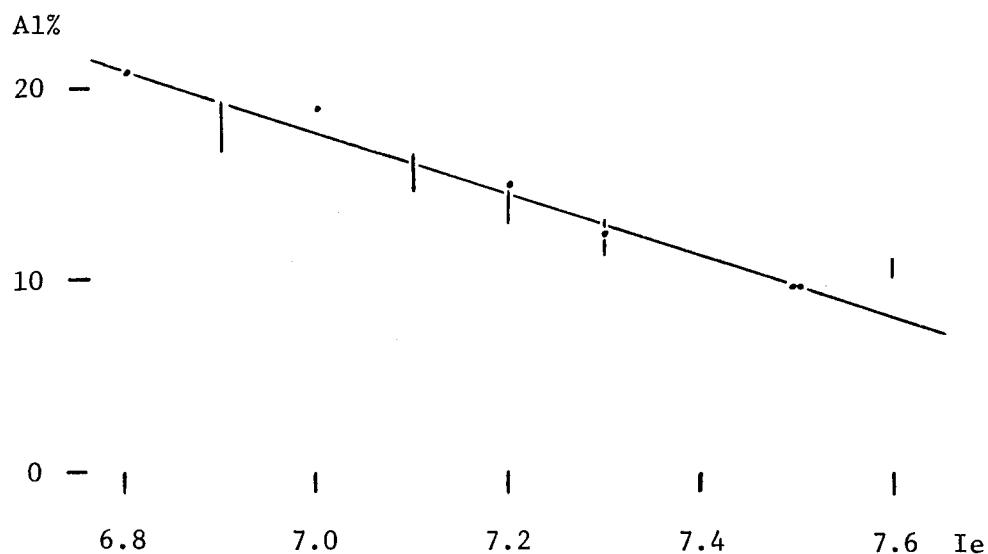
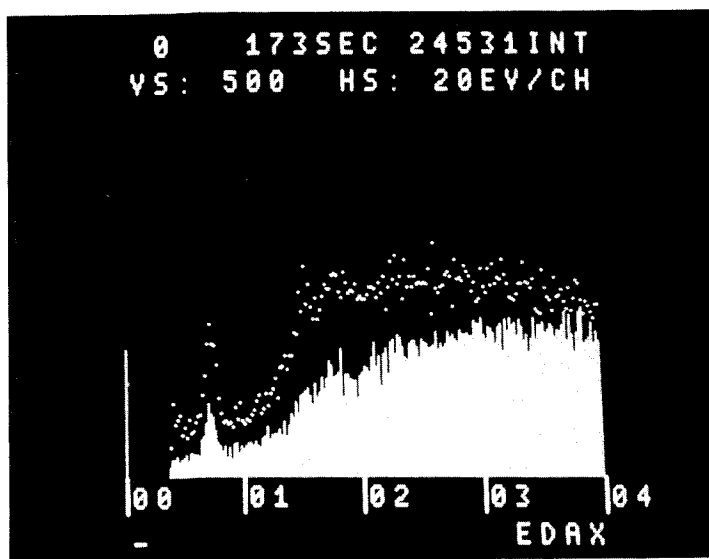
1 Ab = $\text{NaAlSi}_3\text{O}_8$ 2 An = $\text{CaAl}_2\text{Si}_2\text{O}_8$ 

Figure 1. Plot of Ie vs Al% for the rock forming aluminosilicates. Plagioclase minerals are indicated by compositional ranges.

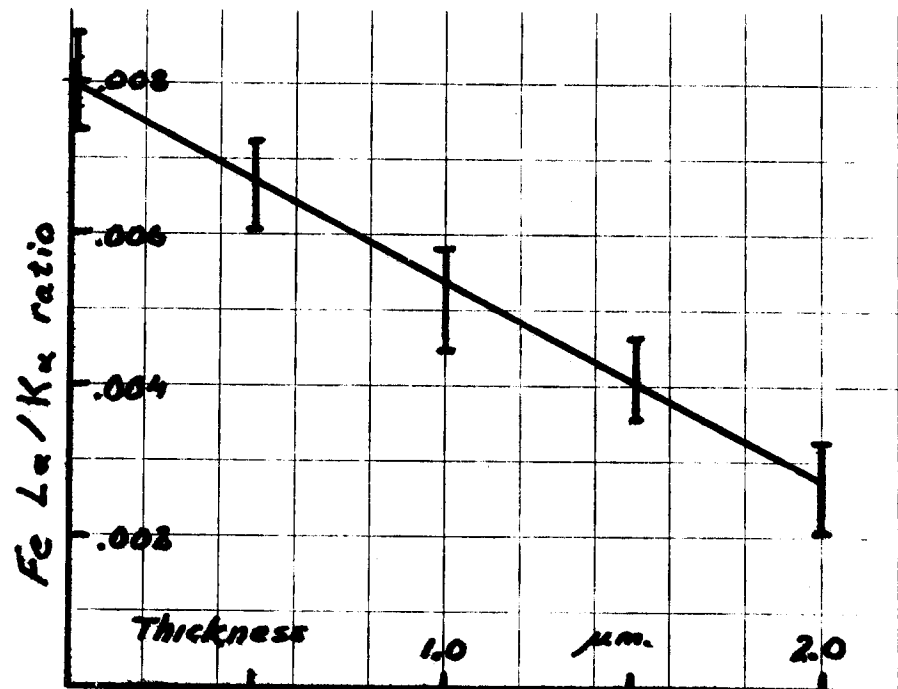
ORGANIC COATING THICKNESS MEASUREMENT

John C. Russ
EDAX Laboratories
Prairie View, IL 60069

Measurement of thickness variations in an experimental sprayed-on organic coating on the inside of steel beverage cans has been carried out by SEM/Energy Dispersive X-ray analysis. Examined at 12kV accelerating voltage, there was sufficiently little surface charging that no conductive coating was required. The absence of any analyzable X-rays from the coating made it necessary to instead use the absorption of substrate iron X-rays to measure thickness. Since the maximum coating thickness of interest in this experimental coating was only 2 μm , negligible absorption of the Fe $K\alpha$ line (6.4 KeV) was present. The Fe $L\alpha$ line (0.7 KeV) was used instead. In order to normalize variations in beam current from sample to sample, and to partially compensate for variations in specimen position, the ratio of the Fe $L\alpha$ to Fe $K\alpha$ was used. This was simply accomplished by counting to a preset Fe $K\alpha$ intensity of 100,000 counts. This required times typically of the order of 3 minutes per point. The specimen surface was normal to the beam, and the X-ray takeoff angle used was approximately 45° . Typical spectra illustrating the change in $L\alpha$ intensity with coating thickness, and the calibration curve prepared from standards, are illustrated below.



Absorption of Fe L line
Dots: no coating
Solid: 2 μm coating



INTERACTION OF A GLASS-BASED
NUCLEAR WASTE SIMULANT AND NATURAL ROCK*

P. F. Hlava
W. F. Chambers

Sandia Laboratories
Albuquerque, New Mexico 87115

An experiment was conducted to determine the interaction between a glass containing simulated radioactive waste from a nuclear reactor and natural rock.¹ This experiment was part of a study to examine the feasibility of disposing of high level radioactive wastes in solid rock bore holes in which radioactive heat would generate a molten zone at depth. As the molten zone cooled by dilution and natural aging of the radioisotopes, the zone would solidify to form a silicate mass which would hopefully retain the waste elements for a long period of time relative to their half-lives.

The basic experiment consisted of inserting a simulant glass containing stable isotopes in a hole bored into a 0.9 m x 0.9 m x 1.4 m block of microgabbro. The waste was maintained in a molten state for approximately 1 month by resistive heating. After cooling, the block was sectioned and samples were examined for relative elemental composition by x-ray fluorescence.

Visual inspection revealed distinctly colored zones within the glass. Of particular interest was a narrow white band which was thought to represent a convection flow boundary. Since knowledge of the compositions within and on either side of this boundary could provide an insight into the convection behavior and cooling sequence as well as the glass-rock interactions, detailed electron microprobe analyses of selected specimens were performed. This paper summarizes the results of the investigation. A full discussion of the results is published in reference 2.

The samples were mounted in epoxy, polished according to standard metallurgical procedures, and coated with carbon for conduction. In order to quantify the glass-rock interactions, a focused electron beam which was operated at 15 kV and about 25 nA was scanned over a sample area of $\sim 40 \times 50 \mu\text{m}$. This procedure was used to determine bulk compositions for the samples and to decrease volatilization of alkalis. By mechanically traversing the specimen under the beam, it was then possible to detect

*This work was supported by the Energy and Research Development Administration.

differences in the glass composition from zone to zone. In order to determine the chemical differences across the colored zones, samples were traversed from the rock across the zones into the black glass representative of the central core. When analyzing crystallites, a stationary point beam was used. In all cases, the analyses were for 17 elements which were assumed to be present as stoichiometric oxides, and B_2O_3 was calculated by difference. The elements analyzed included all of those from the simulated waste glass (Na, Si, K, Cr, Fe, Co, Ni, Sr, Y, Zr, Mo, Ba, Ce, U) and some important elements from the rock (Mg, Al, Ca). During data collection, the electron microprobe was operated under computer control by a program developed at Sandia for the quantitative analysis of oxide-based materials.³

Electron microprobe analysis provided significant information about the convection behavior and waste-rock interactions that transpired during the experiment. The regions of interest are shown schematically in Fig. 1. Within the melted region, a convection cell was created which kept the central part of the cell well mixed and homogeneous. An amount of rock equal to approximately one-half that of the original waste simulant was melted and incorporated into the convecting glass. A stagnant zone of molten glass was present at the sides and below the bottom of the convection cell. This zone was usually very narrow at the sides but enlarged a few centimeters from the bottom of the cell. At this point, it was composed of a complex series of colored bands. The boundary between stagnant and convected glass is marked by a white band. In general, the stagnant zone was the site of rapid compositional changes such as the logarithmic decrease of rock components from rock to convection cell and corresponding increase in waste components. The white band itself is thought to be the result of the diffusion of light by myriads of small pyroxene crystals. These pyroxenes grew in the stagnant zone and the white band rather than in the convection cell because of slight differences in CaO and MgO concentrations.

Four types of crystalline phases have grown from the melt: two oxides, a borate, and a silicate.* The oxides include spinels of four major oxides [MgO , NiO , Cr_2O_3 , and FeO (Fe_2O_3)] and a non-naturally occurring metal oxide solid solution.

Dispersed throughout the melted regions are small spinel crystals (Fig. 2) consisting of MgO , NiO , Cr_2O_3 and FeO (Fe_2O_3). The oscillatory zoning of these crystals and their skeletal morphology (Fig. 3) record variations in growth conditions during transportation in the convection cell. Where the spinels were not carried by the cell they are simpler. At the bottom of the melt zone which contains essentially no rock components, the spinels lack MgO and are completely homogeneous. A cluster of $(Fe,Cr)_2O_3$ crystallites is also observed in this region.

In the central part of the convection cell, clusters of skeletal Mg-Fe-borate crystallites (Fig. 2) are found. Since these crystallites are randomly oriented, they must have been formed about the time that convection ceased.

*Similar observations were reported by K. Keil, Un of NM, in an independent study on other samples from this experiment.⁴

A silicate similar to Fe-rich diopside ($\text{CaMgSi}_2\text{O}_6$) (Fig. 4) with unusual amounts of Ce_2O_3 and other heavy metal oxides formed as larger crystallites in the stagnant melt at the side of the convection cell and as many very small crystallites in the white band, but are lacking in the convection cell. The presence and size of this phase may be controlled by the availability of Ca and Mg in various parts of the melt.

References:

1. R. D. Klett, "High Level Waste Melting Experiment," Proc. of the Symposium on Waste Management '75, pp 127-137.
2. P. F. Hlava and W. F. Chambers, "Electron Microprobe Analyses of Selected Samples from Deep Rock Disposal Experiment #1," SAND76-0153, Sandia Laboratories, April 1976.
3. W. F. Chambers, "GEOPAC - A Set of Programs for On-line Quantitative Microprobe Analysis of Oxide-based Specimens," SAND76-0154, Sandia Laboratories, April 1976.
4. R. D. Klett, Personal communication.

Acknowledgements:

The authors wish to thank R. D. Klett and B. T. Kenna for helpful discussions and B. T. Kenna and M. R. Gutierrez for the sample preparation.

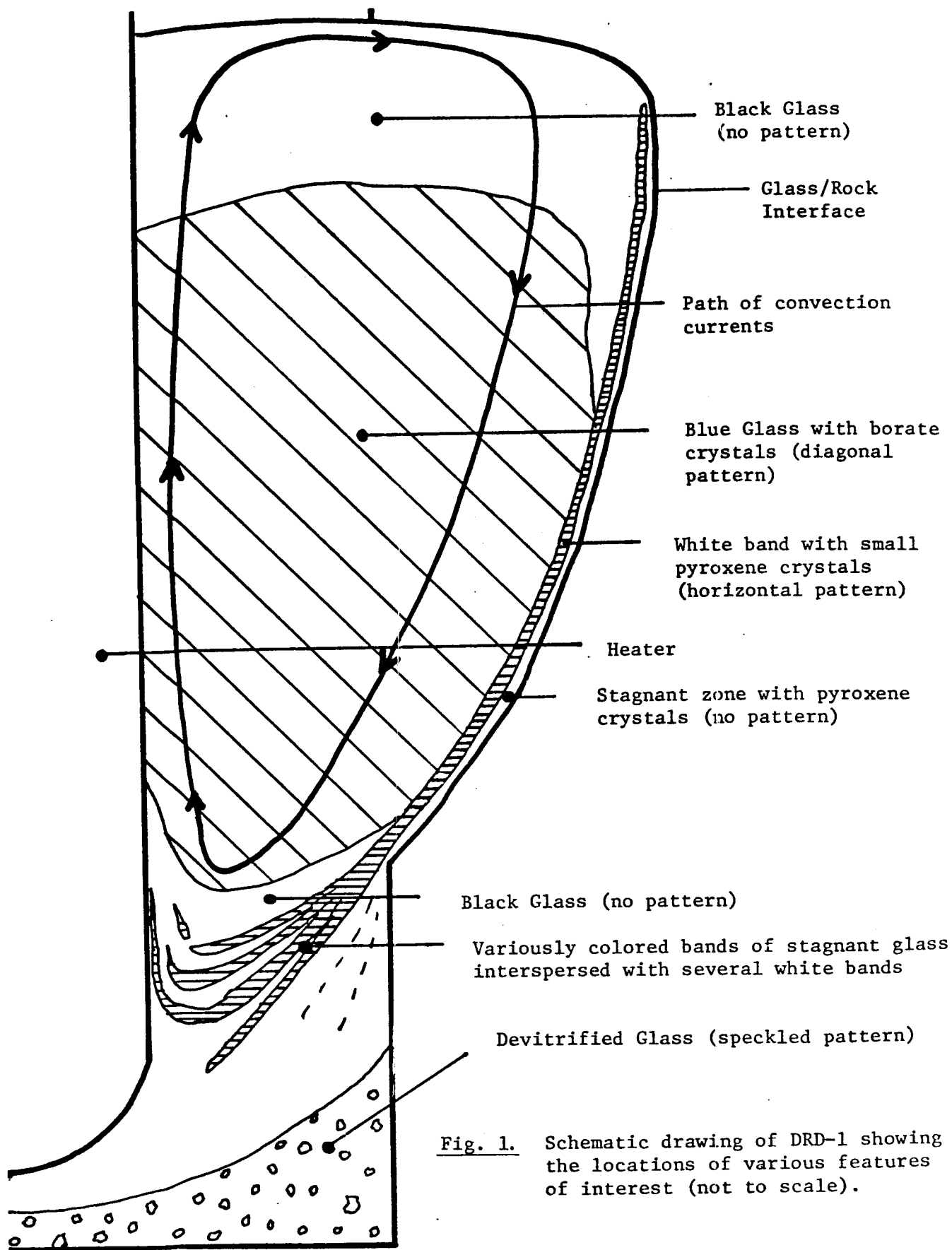


Fig. 1. Schematic drawing of DRD-1 showing the locations of various features of interest (not to scale).

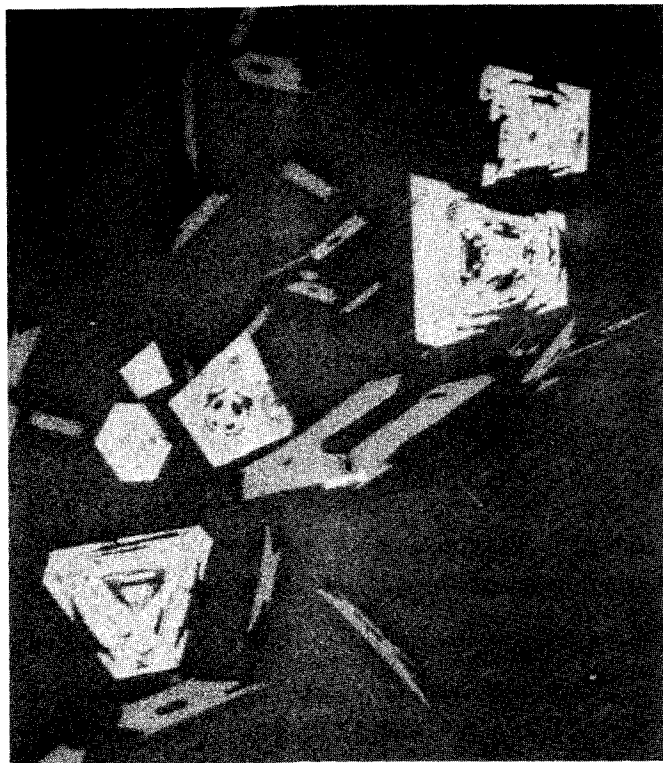


Fig. 2. Optical photomicrograph of skeletal, zoned spinel and skeletal Mg-Fe-borate crystallites. (650X)

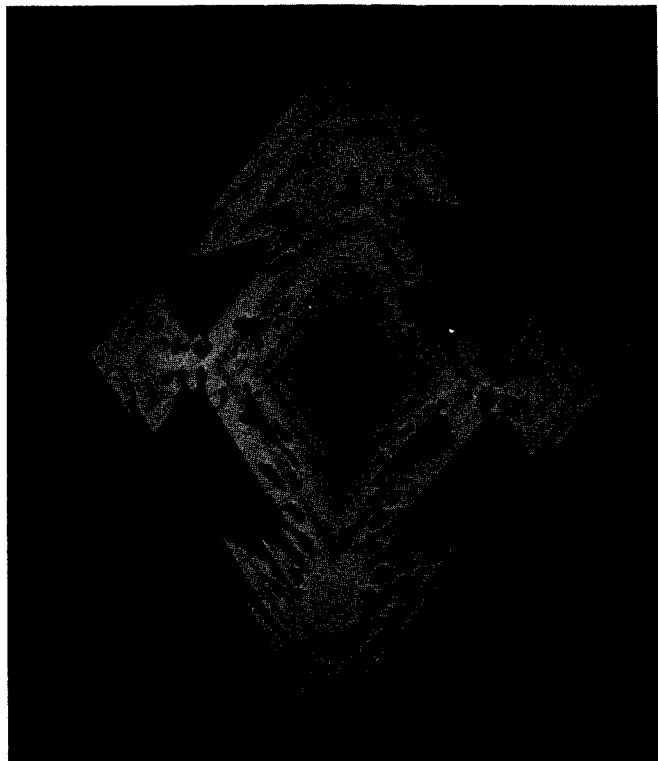


Fig. 3. Optical photomicrograph showing details of the skeletal morphology and zoning of a spinel crystallite. (1000X)

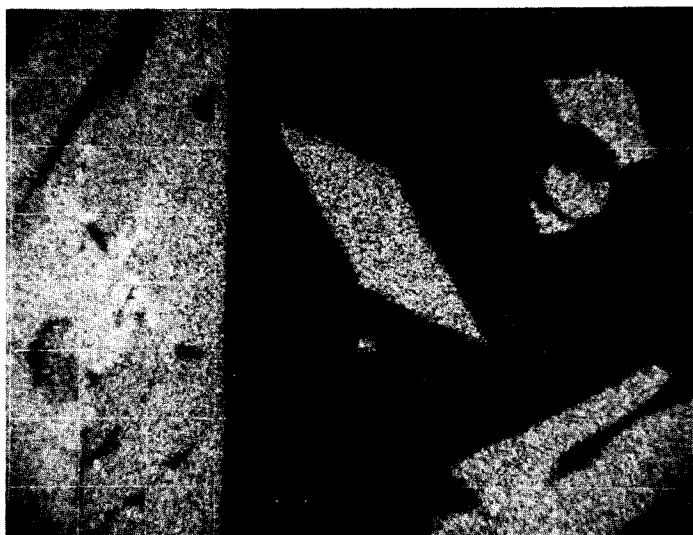


Fig. 4. Elemental distribution photomicrograph (for MgK α) showing size and morphology of pyroxene crystallites in glass. Left one-third of photomicrograph is unmelted well rock. (500X)

ELECTRON MICROPROBE STUDIES OF METAL-CERAMIC BRAZE JOINTS*

W. F. Chambers
P. F. Hlava

Sandia Laboratories
Albuquerque, New Mexico 87115

Cracking in the metallized portion of metal-ceramic braze joints has been attributed to stresses generated during the brazing operation. The work reported here was part of a study undertaken to develop an improved capability for stress analysis of these joints. The joints of interest were assembled from Kovar,[†] oxygen-free high conductivity copper and metallized WESGO Al500^{††} alumina ceramic, as shown schematically in Fig. 1. The composition and, therefore, the mechanical properties of each constituent are altered to some degree during joint fabrication. In order to determine

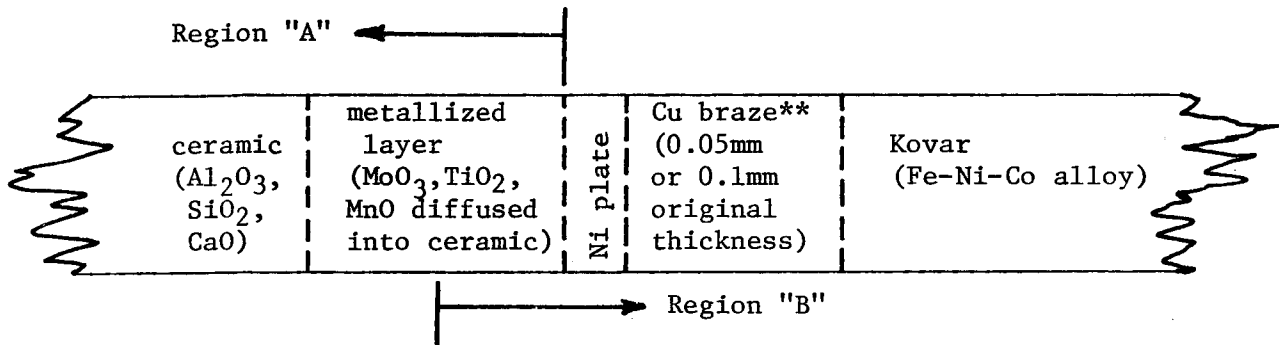


Fig. 1. Schematic illustration of braze configuration.

material properties for accurate stress predictions, it was necessary to obtain quantitative composition data at all positions across test joints, including the interaction regions between each component; however, only the ceramic and metallized layers (Region A of Fig. 1) are discussed here.

The analytical work on the ceramic portion of the joints was conducted to measure the resultant composition of the glassy phases in the ceramic and to determine the volume fractions of glass, Al₂O₃ crystals, and pores as functions of distance from the ceramic/nickel interface of the metallized

*This work was supported by the Energy Research and Development Administration.

[†]Westinghouse Electric Co.

^{††}Western Gold and Platinum Co.

**Two different braze thicknesses were used in this study.

ceramic. Cross sections of the joints were ceramographically polished by vibration in a 15 μm diamond slurry for 6 weeks and were coated with ~ 20 nm of carbon to provide a conductive surface.

A sequence of identical area secondary electron and elemental distribution photomicrographs (EDPMs) was obtained within region "A," the region affected by metallization and into the bulk ceramic. The EDPMs showed that changes in component composition due to metallizing were restricted to the glassy phases and provided a basis for determining the volume fractions of glass and void. Image analyses of the EDPMs yielded average volume fractions of 0.123 glass, 0.081 void, and balance crystalline Al_2O_3 .

The WESGO Al500 ceramic used in this study was specified by the manufacturer to be 94 w/o Al_2O_3 with a composite density of 3.67 gm/cm^3 . Assuming the density of sapphire (3.99) for the Al_2O_3 grains and a density of 2.7 for the glassy phase,¹ one can predict volume fractions of 0.865 Al_2O_3 , 0.082 glass, and 0.054 void. Assuming that polishing pull-out accounts for the difference between the 0.204 measured glass plus void and the 0.135 predicted from published and assumed information, the volume fraction results can be normalized to a 0.135 average as shown in Table I. Note that the volume fraction of glassy phases increases slightly and that of the void decreases slightly near the metallized region.

Table I. Distribution of glass and voids in metallized ceramic

Distance from Interface, mm	Volume Percent				
	Measured		Normalized		Total
	Glass	Void	Glass	Void	
0.0-0.1	15	5	10	3	13
0.1-0.2	13	5	9	3	12
0.2-0.3	17	7	11	5	16
0.3-0.4	11	7	7	5	12
0.4-0.5	10	11	7	7	14
0.5-0.6	10	9	7	6	13
0.6-0.7	11	10	7	7	14
0.7-0.8	11	9	7	6	13
0.8-0.9	14	8	9	5	14
0.9-1.0	13	9	9	6	15
1.0-1.1	11	8	7	5	12
1.1-1.2	13	9	9	6	15
Average	12.4	8.1	8.3	5.3	13.5

For quantitative analysis of the glassy phase, the electron microprobe was operated under computer control² with a point beam at 15 kV and 26 nA. The elements Na, Mg, Al, Si, Ca, Ti, Mn, Fe, and Mo were analyzed for and assumed to be present as their respective stoichiometric oxides. (Energy dispersion analyses indicated that the Cu and Ni had not penetrated into the glassy phase.) On-line reduction of the probe data was made via a

Bence-Albee technique^{3,4} using the GEOPAC⁵ program. The glassy phases are typically 2-10 μm in cross-sectioned diameter and extend an unknown distance beneath the polished specimen surface. Because of the small size of the glassy grains and the finite penetration of the electron beam, spot analyses at the centers of the grains were not always valid. This problem was overcome by selecting larger grains and taking series of analyses across these individual grains in spatial increments of 0.6-1.5 μm . For some grains the individual analyses had totals which were as low as 80 w/o or as high as 120 w/o. The results were affected by the extreme absorption and fluorescence characteristics of the material as compounded by an abundance of voids and submicron heterogeneity. Since the glassy phase was imbedded in a crystalline Al_2O_3 matrix, the best analysis for a particular grain was assumed to be that analysis for which Al_2O_3 was the lowest. The compositional totals are very near 100% except within 5 μm of the interface where the grains are very small. Table II shows a typical analysis for one grain. The relative position data indicate that the beam was on the grain from about 1.5 μm to about 5.5 μm . The apparent compositional variations are probably due partially to the effects of glass devitrification during processing and partially to the finite size of the electron beam.

Table II. Analysis set across a glassy grain approximately 4 μm in diameter located 150 μm from nickel interface. The analysis at relative 3.6 μm was taken as representative of this pocket glassy phase.

Oxide	Relative Distance (μm)						
	0.0	1.2	2.4	3.6	4.8	6.0	7.2
Na_2O	0.4	0.13	0.42	0.41	0.25	0.16	0.02
MgO	0.51	0.78	3.38	5.06	3.58	0.54	0.18
Al_2O_3	76.81	92.53	61.65	36.78	50.03	82.76	97.35
SiO_2	3.52	7.04	27.39	31.77	18.89	8.59	1.04
CaO	2.04	3.36	6.56	4.87	3.43	1.31	0.14
TiO_2	0.11	0.88	3.02	18.26	22.58	4.90	0.33
MnO	0.23	0.58	3.29	4.44	4.11	1.32	0.19
FeO	0.05	0.04	0.39	0.62	0.38	0.07	0.01
MoO_3	0.00	0.00	0.00	0.26	0.60	0.17	0.00
	103.99	105.34	106.09	102.46	103.86	99.82	99.28

The data on composition versus distance from the nickel interface in region "A" are compiled in Table III. SiO_2 was found to be the major component of the glasses, as expected. CaO is often the third most abundant compound; however, it is substantially depleted at the metallize interface. The TiO_2 content fluctuates greatly but decreases beyond 300 μm from the interface. MnO is still present in significant concentrations at 500 μm , but neither MoO_3 nor FeO penetrated detectably into the ceramic. These data are supplemented by Table IV which shows the composition ranges for each compound.

Table III. Best analyses for metallized WESGO Al500 Ceramics-Glass Phase

Oxide	Distance from Interface (μm)								
	0	5	20	50	100	150	200	300	500
Na ₂ O	0.38	0.33	0.67	0.24	0.78	0.93	0.85	1.18	0.63
MgO	1.19	0.19	2.20	8.19	1.72	0.61	1.18	0.86	2.76
Al ₂ O ₃	32.94	44.63	29.66	28.69	23.88	34.77	33.87	35.92	33.80
SiO ₂	45.47	36.66	36.12	44.37	45.92	47.10	41.37	45.94	49.73
CaO	0.40	3.12	7.86	1.25	9.51	13.96	9.31	13.82	5.47
TiO ₂	1.74	2.81	17.41	3.44	8.58	1.25	9.17	2.64	0.86
MnO	2.52	1.90	5.02	9.43	4.25	1.68	2.17	1.27	2.66
FeO	0.10	0.12	0.44	0.85	0.18	0.03	0.15	0.18	0.25
MoO ₃	0.00	0.02	0.04	0.10	0.00	0.03	0.04	0.01	0.00
Total	84.74	89.78	99.42	96.56	94.80	100.36	98.11	101.82	96.16

Table IV. Composition range for glassy phase components, WESGO Al500 (metallized)

Oxide	w/o	
	Min.	Max.
Na ₂ O	0.08	1.18
MgO	0.19	9.83
Al ₂ O ₃	23.86	49.12
SiO ₂	31.77	48.02
CaO	0.23	13.96
TiO ₂	0.73	37.76
MnO	0.63	11.19
FeO	0.02	0.85
MoO ₃	0.00	0.26

In all areas examined, the Al₂O₃ level in the glass phases is lower than the 47 w/o reported by Reed, et al.¹ as representative of these phases in metallized 94% alumina ceramics. The Al₂O₃ concentrations are similar to those found in the glass region of the glass-sapphire reaction couples examined by Reed et al.

These analyses have been used to establish a range of compositions of glasses for physical property determinations. Specifically, glasses corresponding to the seven compositions given in Table III for the 20-500 μm locations were fabricated in the Sandia Laboratories Glass Shop. Through mixture theory, using measured and tabulated properties plus relative amounts of each phase, mechanical and physical properties of the metallized region of the alumina ceramic have been determined and will be published elsewhere.⁶

Acknowledgements:

The authors want to thank J. Swearengen for his helpful discussions, K. Lawson for the quantitative metallography, and E. Hawn for fabricating the braze joints.

References:

1. L. Reed et al., "Metallurgical Research and Development for Ceramic Electron Device," Final Report, Contr. No. DA-36-039-SC-90903, U.S. Army Electronics Command, Ft. Monmouth, N. J., Jan. 1966, OAD-636950.
2. W. F. Chambers, "Sandia FOCAL-76," SAND76-0044, Sandia Laboratories, March 1976.
3. A. E. Bence and A. L. Albee, "Empirical Correction Factors for the Electron Microanalysis of Silicate and Oxides," J. Geol., 76, 382-403, (1968).
4. A. L. Albee and L. Roy, "Correction Factors for Electron Probe Microanalysis of Silicates, Oxides, Carbonates, Phosphates, and Sulfates, Anal. Chem., 42, 1408-14, (1970).
5. W. Chambers, "GEOPAC - A Set of Programs for On-line Quantitative Microprobe Analysis of Oxide-based Specimens," SAND76-0154, Sandia Laboratories, April 1976.
6. J. C. Swearingen and W. F. Chambers. To be published.

A Preliminary Investigation of the Fouling of Catalyst
Pellets by Residual Oils and Tars

R.H. Packwood † M. Ternan* and B.I. Parsons*

CANMET - EMR, 555 Booth St., Ottawa, Canada Δ

Introduction

In stark contrast to earlier estimates, Canadian reserves of readily accessible crude oil are strictly limited. Considerable foresight was shown some years ago when investigations were undertaken into the possibility of using the Alberta Tar Sands (ATS) as a potential source for part of future Canadian fuel requirements⁽¹⁾. The ATS are estimated to contain some 10^{11} - 10^{12} bbls of bitumen. Both conversion processes presently contemplated are of the 'coking' type and yield ~70% fluid fuel. The remaining product, coke, is high in sulphur and metals and at present is of no use as a fuel. One company alone is producing several hundred tons of coke per day, a problem in itself.

CANMET is presently developing a catalytic hydrocracking process⁽²⁾ which will give more usable fuel and will not result in piles of coke. There are problems with catalytic hydrocracking, chiefly fouling of the pellets by carbon, etc., and suspected poisoning by metals. These effects reduce the catalyst life to the extent that catalytic hydrocracking is not a commercially viable process at current prices.

Experiment

This work is concerned with the nature and distribution of the poisons and fouling agents.

The catalyst in question is cobalt molybdate formed in-situ on a gamma-alumina substrate that has been pelletised in the form of small cylinders approximating 3.0 mm dia x 2.75 mm long. The initial study involved two exposure times, 20 hr and 120 hr, and compared the state of the catalyst when used with bitumen feedstock derived from ATS and a conventional source.

The exposure closely duplicated commercial temperatures pressures and flow rates. The pellets subjected to long exposures have been regenerated, i.e., decarburized by heating in air. The other pellets still contained oil which was removed by an overnight soak in acetone.

† Physical Metallurgy Research Laboratories

* Energy Research Laboratory

Δ Canadian Centre for Mineral and Energy Technology,
Department of Energy, Mines and Resources

Sample pellets were broken in two, for microprobe examination and the exposed faces prepared in the conventional fashion, finishing with a 200Å carbon coat for conduction purposes. A typical pellet is shown in radial cross-section in Figure 1a, and again after exposure to ATS for 120 hours in Figure 1b. Here the outer layers of the pellet have undergone some change in structure as witnessed by the altered polishing rate and smoother appearance. The principal catalyst poisons were thought to be V, Ni and Fe, consequently line traces were made for these elements on the four categories of sample. Figures 2a and 2b show typical results; however note that

- i) the 120 hr: V trace had to be reduced by 3.3x to be shown on the graph and
- ii) the Fe is overestimated because it is essentially on the outer-surface of the pellet, and the counting rate is accentuated by the increased take-off angle at the edge. The traces were run at 20 $\mu\text{m}/\text{min}$ with a 10 μm dia beam to reduce sample heating and also to smooth out the effects of cracks and holes.

Conclusions

Clearly, the ATS crude has a much greater concentration of the elements investigated, and therefore, the catalyst is fouled, and probably poisoned, much sooner. V and Ni show a long, near exponential decrease into the bulk of the pellet, whereas Fe is stopped at the outer surface. Our ORTEC Si(Li) detector showed that the exterior of the 120 hr ATS pellet contained a large quantity of S (~6 wt%) together with smaller quantities of Si, Ca and Ti, in addition to other elements known to be present (see Figure 3a). For comparison an analysis of elements in the exterior of the pellet used with conventional crude is shown in Figure 3b. For the ATS sample, additional traces were run in particular for S, Mo-L β and Ca (Figure 2c); these show clearly the correspondence between the S concentration and the morphologically altered layer. The Mo-L β traces served to illuminate the degree to which the S readings are affected by the Mo-L α line. Ca, on the other hand, appears to have penetrated cracks and holes near the surface and further inside. Ti and Si were found to be in the outer part of the layer. X-ray powder diffraction photographs were able to show the presence of $\text{Al}_2(\text{SO}_4)_3$ and possibly CaSO_4 in the layer material and, judging by the yellow colour of the abraided sample, there may well be other compounds of sulphur present as well. This work is continuing.

Acknowledgements

Our thanks to Mrs. V.E. Moore for assistance with the microprobe work and Mr. E. Cousineau for the powder diffraction work.

References

- 1) A.R. Aitken, et al, Can. J. Chem. Eng. 42, 234 (1964).
- 2) E.C. McColgan, et al, "The Hydrocracking of Residual Oils and Tars". Pts 1-6, Mines Branch Research Reports (1971-73).

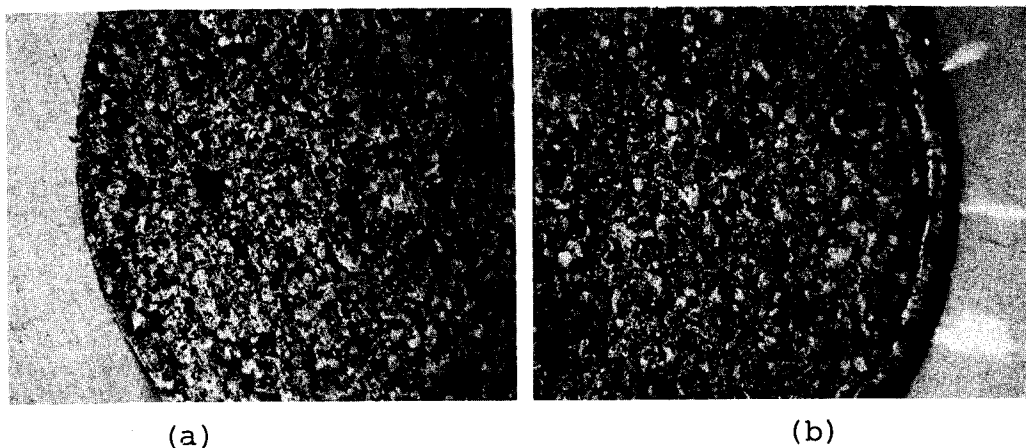
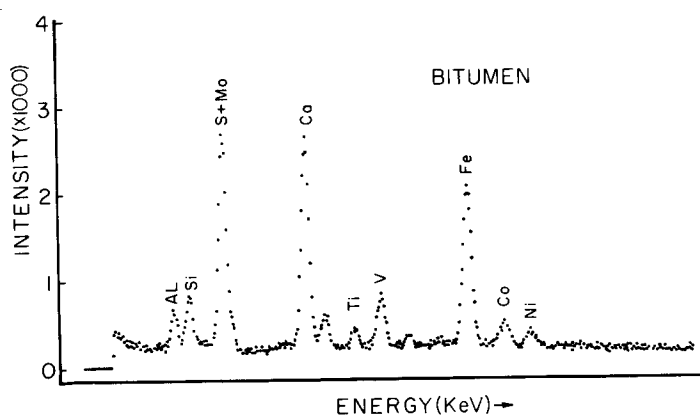
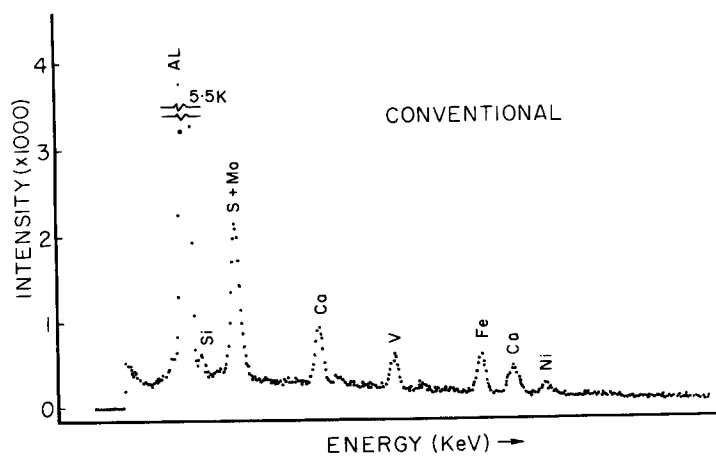


Figure 1. Catalyst pellets a) before, b) after exposure to ATS bitumen for 120 hr. (X30)



(a)



(b)

Figure 3. EDS of exterior of catalyst pellets exposed 120 hr a) to ATS bitumen, b) conventional crude.

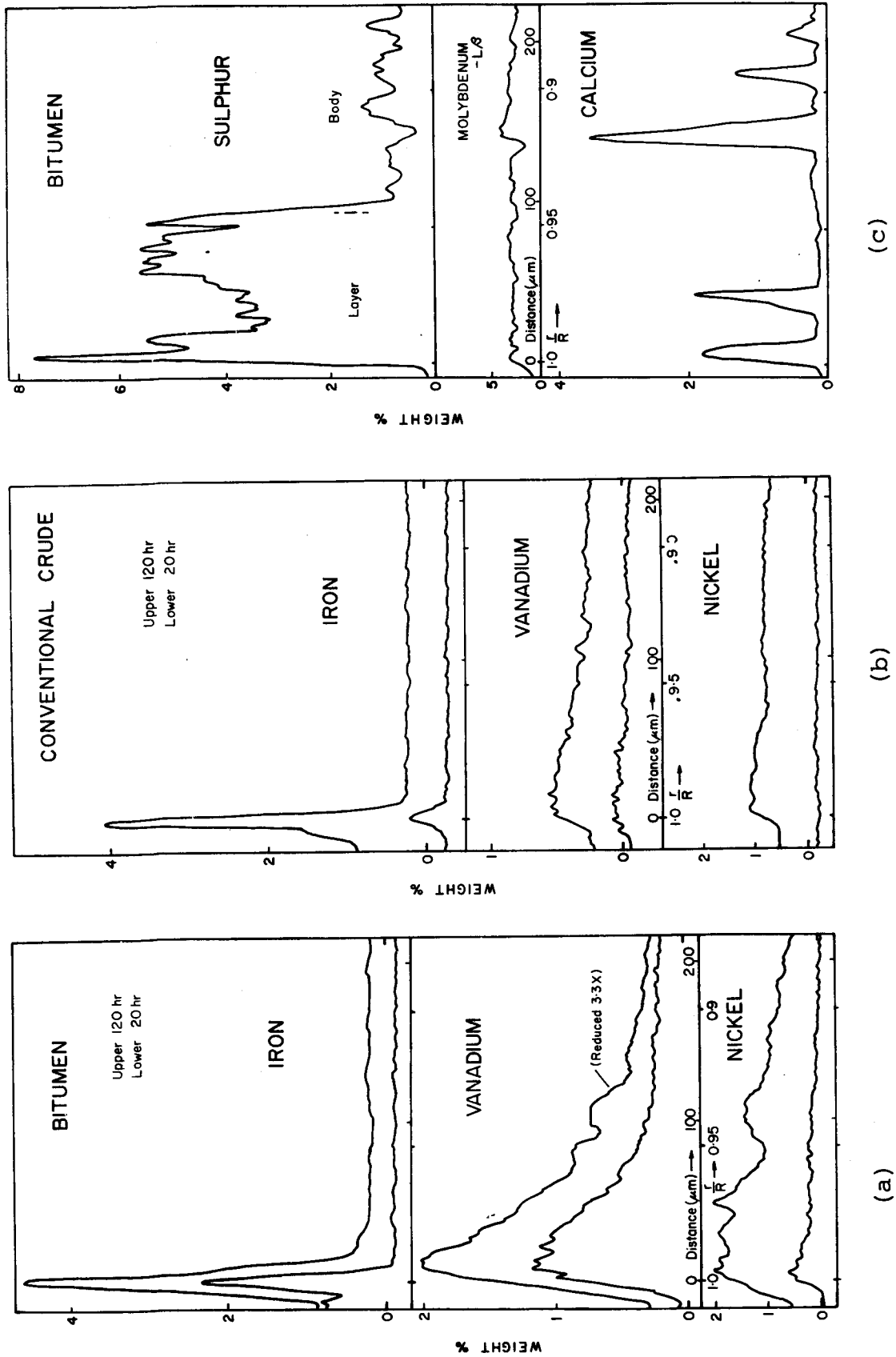


Figure 2. Line traces across catalyst pellets.

LIMITATIONS OF MICROPROBE ANALYSIS
OF ANGLE-LAPPED MULTILAYERED SPECIMENS

M. J. Mitchell and J. N. Ramsey
IBM System Products Division--East Fishkill
Hopewell Junction, New York 12533

Angle-lapped samples are commonly used in optical microscopy because they provide an optical exaggeration of the thickness of a layer (Fig. 1). It can be seen that the thickness of a layer is seemingly increased by $1/\sin \alpha$. Such mounting techniques are especially widely used in semiconductor and integrated-circuit studies because the vertical structures are often made up of layers below optical resolution on 90° sections. Such samples are often submitted for electron microprobe analysis for characterization of unusual particles, debris, or reaction zones, and much valuable qualitative analysis is done. There is a natural tendency, however, to attempt to extend such analysis on angle-lapped specimens to the quantitative level.¹ Often there has been little or no comment as to the possible errors encountered in this procedure, especially the confusion of data (the "smearing") from different layers due to different irradiating volumes, enhancements (backscatter and fluorescence), and absorptions, especially when traverses are run. Similarly, the usual

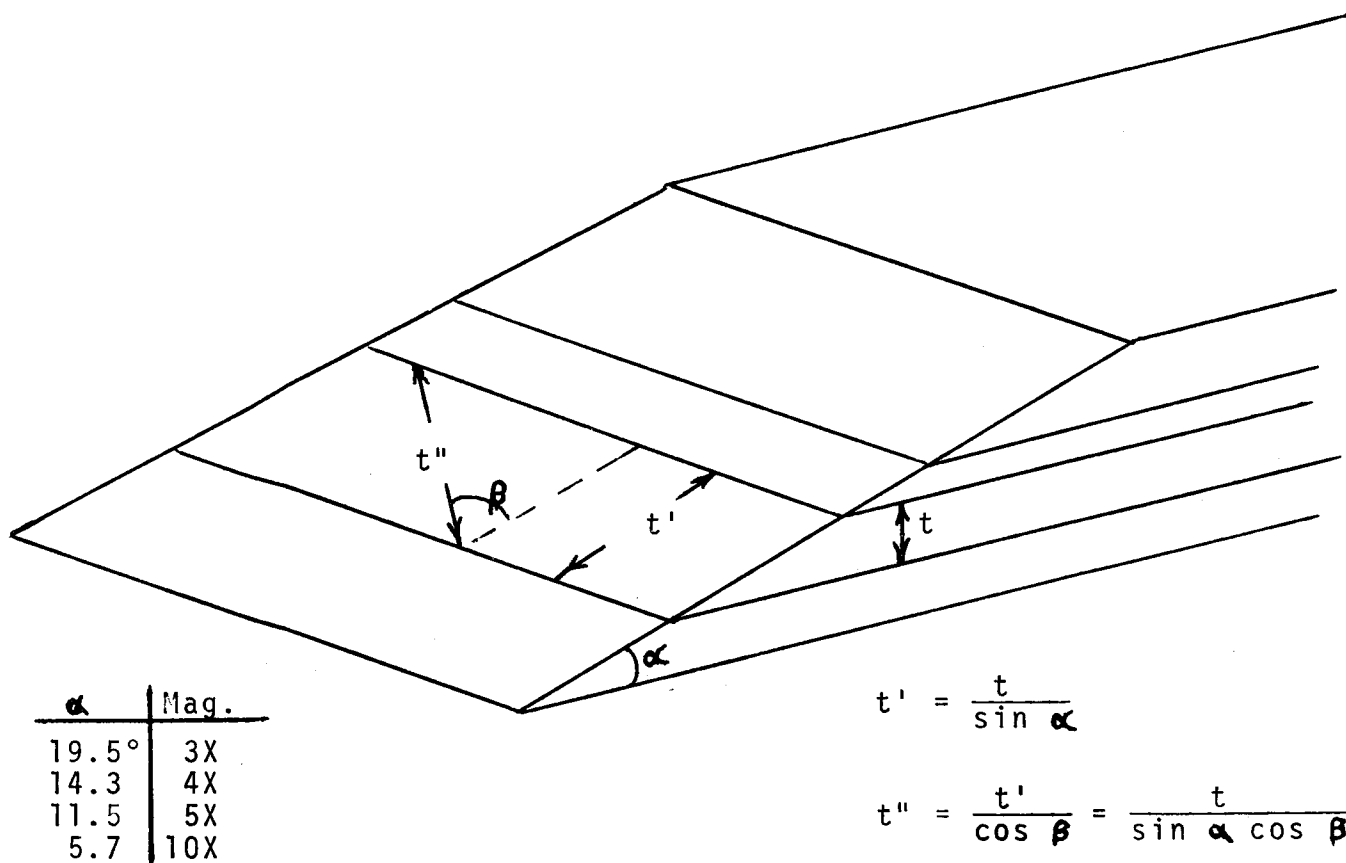


Fig. 1. Taper, bevel, or angle sections.

loss of small beam size on commercial equipment, as the kV is reduced (for shallower penetration), has been largely ignored.²

It would seem wise to explore more fully the limitations of the microprobe analysis of angle-lapped sections, and to make a risk assessment of the techniques used. To this end, samples with high atomic number differences (Pt-Al and Pt-Si) and with small atomic number differences (Cu-Cr) were chosen for these experiments. The cold-substrate evaporated film structures were found to be uniform laterally, from point to point, and no interactions were discernible by secondary ion mass analysis. The samples were mounted and sectioned at angles that gave optical exaggerations of 3X and 10X. The samples were also mounted at each angle with the surfaces reversed in the mount, so that a given metal would appear on the top and bottom of a metal sequence (i.e., high Z over low Z, as well as low Z over high Z). Electron microprobe analyses were made on the specimens, and the limitations will be discussed.

The great usefulness of angle-lapped sections in a light microscope occurs largely because light has extremely shallow penetration and does not "smear" the data. Auger Electron Spectroscopy (AES) is also an extremely-shallow-penetration technique because of its shallow escape depth. Fine beam size AES, which lends itself to the resolution of planar interfaces,³ was also applied to these specimens.

REFERENCES

1. G. DiGiacomo, "Microprobe Techniques for Determining the Thickness of Ag₂S Films as a Function of Sulfur Vapor," Tenth Annual Conference, Microbeam Analysis Society, Las Vegas, Nevada, August 1975.
2. J. N. Ramsey and P. Weinstein, "Electron Microprobe Applications to Advanced Electronic Components," in The Electron Microprobe, Theodore David McKinley, Editor, p. 715, John Wiley & Sons, Inc., New York (1966). There is a brief discussion of these pitfalls on p. 721. The necessity of small beam size is emphasized on pp. 733-737.
3. E. K. Brandis, "High Spatial Resolution Auger Electron Spectroscopy in an "Ordinary" Diffusion Pumped SEM," Eighth Annual Conference, IITRI-SEM, St. Louis, Missouri, April 1975.

REAL-TIME CATHODOLUMINESCENCE SPECTROSCOPY

A. Sicignano
Philips Laboratories
Briarcliff Manor, N.Y. 10510 U.S.A.

ABSTRACT

Philips Laboratories has designed a system for real-time cathodoluminescence (CL) spectroscopy using a scanning electron microscope (SEM) and a slitless-spectrometer.

The generated CL in the SEM is used routinely to characterize semiconductor materials and device structures. For example, CL is used to study the composition uniformity of GaAl As lasers and to characterize defects in GaAs and GaP. Defect and compositional information are obtained from areas as small as 1 μm in diameter. If a mechanically-scanned-1/4 meter-Ebert-grating-spectrometer is used, it is sometimes impossible to take spectra under dynamic conditions when sample parameters, such as temperature, bias, and position are varied. Under static conditions it is time-consuming (up to 5 hours) to make compositional or defect maps of a crystal.

In adding a slitless-spectrometer on the SEM, we were able to take CL spectra in real time. This allows them to take a compositional map in only 30 minutes without sacrificing spectral (5 Å) and spatial (1 μm) resolution. The sensitivity of the real-time spectrometer (5×10^{-11} Watts at the detector) is one order of magnitude higher than that of a grating spectrometer.

The specifications developed for the slitless-spectrometer are as follows:

Spectral range:	0.38 to 1.10 μm ; 0.5 to 1.0 displayed
Entrance slit (slitless):	object a self-luminous 1 μm spot
Collimator:	F 5.6; focal length 300 mm
Dispersing element:	signal element EDF glass having a 90% efficiency
Camera optics:	F 2.8; focal length 135 mm
Detector:	Philips MP-type camera using a 16 mm SIT Vidicon with red sensitive S-20 photocathode

The CL signal is obtained from the area of the sample excited by the electron beam of the SEM. The beam scans a selected area or remains stationary at one point. The CL signal from a line scan on the crystal is viewed by the use of a standard TV monitor. Then, a spatial-versus-spectral display appears. A single horizontal line from the TV monitor can be displayed on an oscilloscope to show the spectrum for a fixed point on the crystal. Figure 1, a composite view of the slitless-spectrometer on the SEM, shows the relationship of sample, prism, and camera. Figure 2 is the CL spectra obtained from the separate layers of a $\text{GaAl}_x\text{As}_{1-x}$ laser which were excited alternately with the SEM's electron beam. This demonstrated the better-than-1 μm spatial resolution. Figure 3 shows the optical elements of the slitless-spectrometer.

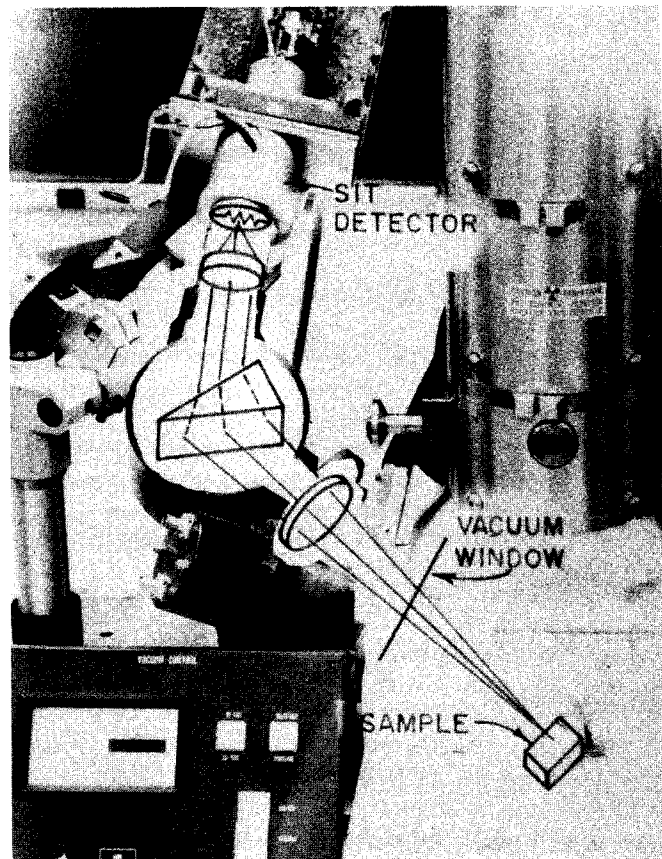


FIG. 1

POSITION OF ELECTRON BEAM ON SAMPLE

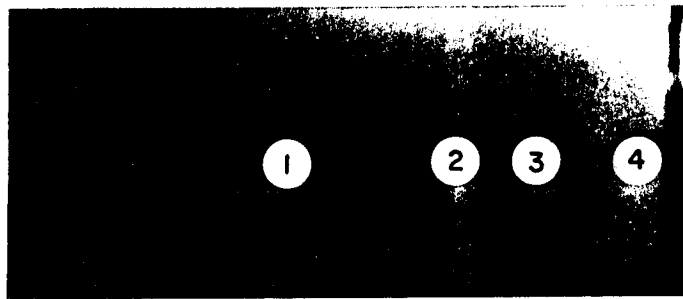
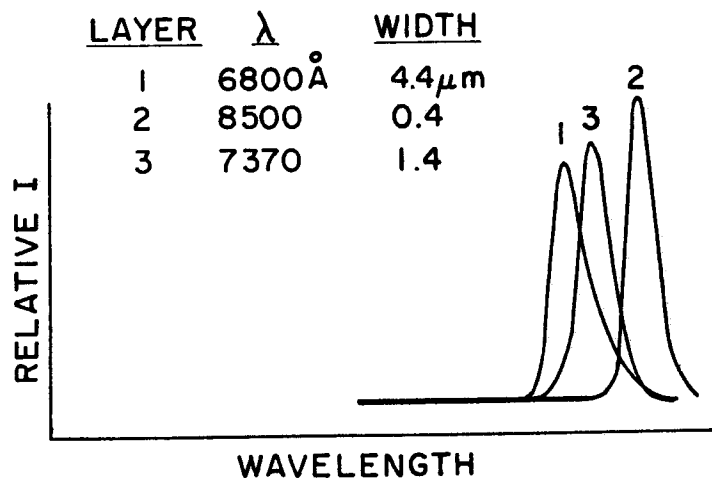
 $\text{H} \quad 0.4 \mu\text{m}$ 

FIG. 2

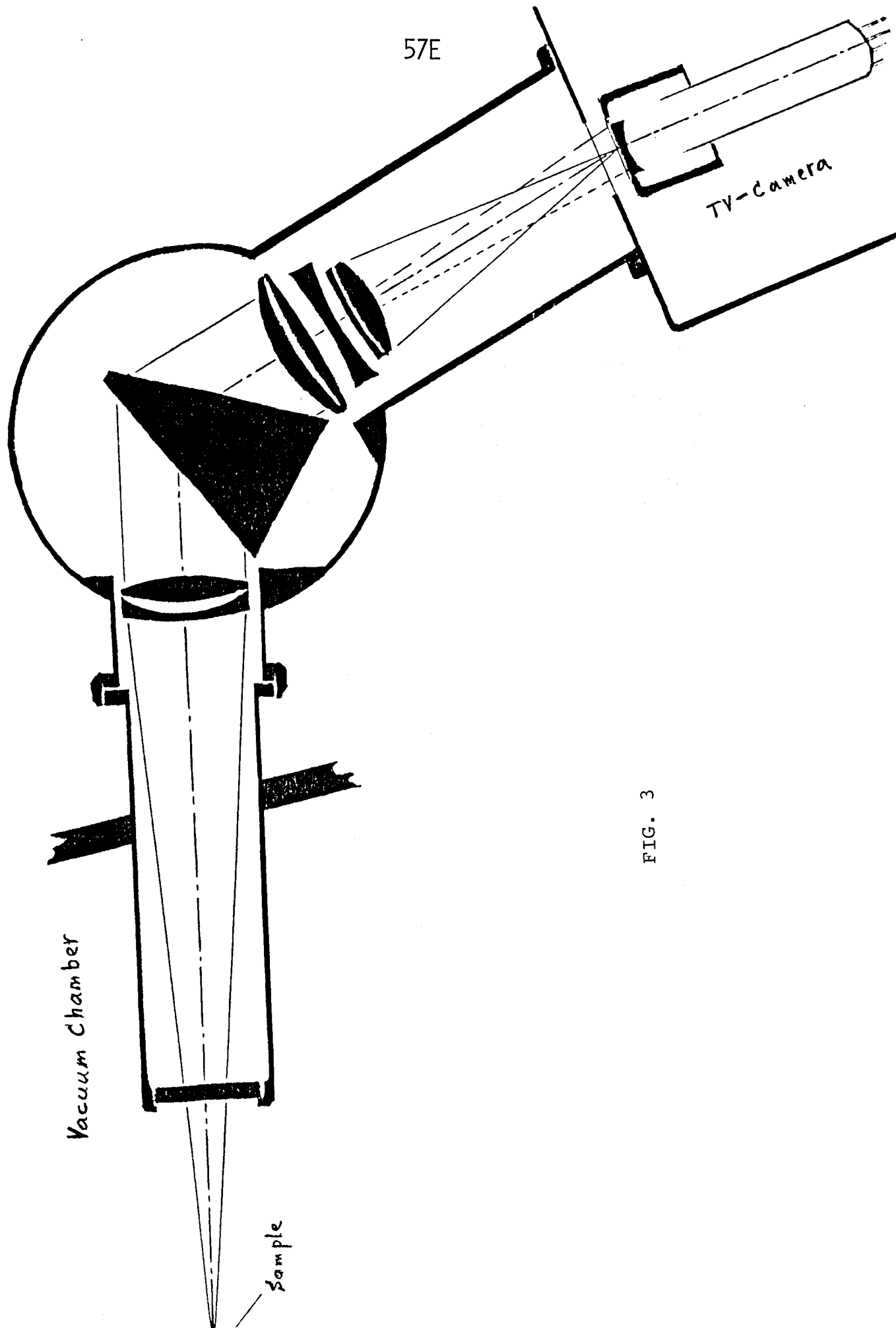


FIG. 3

ELECTRON PROBE STUDIES OF CALCIUM TRANSPORT

by

James R. Coleman

Department of Radiation Biology and Biophysics
University of Rochester School of Medicine and Dentistry
Rochester, New York 14642

Calcium is an essential element for most living things; and this is simply a reflection of the fact that calcium is involved in so many vital processes. Indeed, calcium is not merely involved in a passive fashion, but serves a regulatory role. Muscle contraction, cyclic AMP levels, enzyme reaction rates, and oxidative phosphorylation, to name but a few, are extremely sensitive to the concentration of calcium. A large body of evidence has established the biological activities of calcium, but a central question about calcium remains: how is calcium, the regulator, regulated? Many investigators have toiled to answer this question and to discover which cell organelles and which metabolic processes exercise control over the concentration of cell calcium.

The work in this laboratory has been concerned with one aspect of the problem of calcium regulation: how is the concentration of calcium controlled in cells which move large amounts of calcium through their cytoplasmic spaces? The problem we addressed may be stated simply: how does calcium move through a calcium transporting cell without adversely affecting the many calcium sensitive processes that are vital to the transporting cell?

Answering this question is made difficult because of the organization and occurrence of calcium transporting cells. Such cells occur in complex tissues and organs so that it is not easy to distinguish the activity of a single cell or group of cells; and yet, because the cells may not operate simultaneously or synchronously, it is necessary to resolve the actions of a few or single cells. In some cases it is possible to employ tissue fractionation techniques and isolate homogeneous

populations of identical cells, and this permits study of one type of cell, even if all do not operate simultaneously. But more frequently only partial purification is achieved, and even this sort of study is not possible. Electron probe microanalysis offers distinct advantages for such studies because it is capable of mapping and measuring the amount of calcium within single cells; thus it can be used to determine where calcium pools exist within cells and what changes occur in these pools as the cells carry out their various functions.

Our interests were focussed on the movement of calcium through cells that are organized into epithelia, and our investigations centered on two organs, the embryonic chick chorioallantoic membrane and the small intestine of young rat and chick. The ectoderm of the chick chorioallantoic membrane, and the mucosa of small intestine are the tissues in which the calcium transporting activity is located. These tissues are composed of more than one cell type, and the cells in the ectoderm of the chick chorioallantoic membrane do not resemble those of the small intestine mucosa. Therefore our first goal was to identify which cells in each tissue were responsible for active transport. We reasoned that the cells which actually carried out the active transport would show an increased calcium content when they were actively transporting at a maximum rate. It was known that active transport reached a maximum at 1 millimolar calcium in the chorioallantoic membrane (2,3) and at 2 millimolar calcium in the rat and chick small intestine (15).

However, before these tissues could be analyzed it was necessary to section them so that individual cells could be identified. We began by fixing the tissues with glutaraldehyde to preserve cell structure. We included oxalate in the fixative to form an insoluble precipitate with calcium and prevent its loss during subsequent dehydration, embedding and sectioning. This procedure has been used extensively with muscle, (5,9). It retained about 85% of the tissue calcium, did not permit selective loss of calcium from any specific calcium pool, and produced no redistribution of calcium that was detectable with the electron probe (2). With this preparative procedure we found that only the capillary covering cells, of the chick chorioallantoic membrane, and the

absorptive cells of the small intestine increased their calcium content under conditions that promoted maximum active transport (3,15). This was taken as evidence that these cells were the ones actually carrying out the process of active calcium transport.

Furthermore, since only some cells of the large number present were actually involved in the transport process at any one time, each transporting cell moved more calcium than had been thought when the total amount moved was averaged over all the cells present. Additionally it was found that the goblet cells of intestine contained much more calcium than expected (15) and this is the subject of a paper in this session by Dr. Halloran.

We also found that the calcium which entered the transporting cells did not spread throughout the entire cell, but was sequestered in one or a few sites within the cell.

These two pieces of information were important for they permitted us to choose between two types of mechanisms that had been proposed for the transport process (12).

The first class of mechanisms depended on transported calcium entering the transporting cells, diffusing throughout the cytoplasm, and then being actively transported across the cell membrane to the intercellular (extracellular) space. This type of model required that the concentration of calcium in the cytoplasm rise only slightly during transport, for otherwise the many calcium sensitive processes might escape from normal control mechanisms. The second class of models described calcium as entering the cells by a variety of mechanisms, but not diffusing through the cytoplasmic space. Instead, some cell organelle or some material with a high affinity for calcium binds the calcium while it is in transit through the cell, and in doing so, prevents this calcium from affecting the calcium sensitive processes in the cell. Since electron probe microanalysis showed that the calcium in transit through the cells was restricted in location and did not diffuse throughout the cytoplasm, the second class of models was more likely correct.

When a transmitted electron detector was developed it became possible to use the electron probe to analyze thin sections that had been examined with a conventional transmission electron microscope (4). This effectively

increased the spatial resolution of the images to which the X-ray maps were referred, and so permitted more precise identification of cell sites rich in calcium.

At this point we encountered a limitation of the oxalate technique in the chorioallantoic membrane. The intercellular (extracellular) spaces in the ectoderm are narrow, about 0.025 to 0.1 μ across, and they cannot be resolved in conventional electron probe images, although they are readily resolved in the transmission electron microscope. Examination of thin sections of chorioallantoic membrane fixed with glutaraldehyde and oxalate showed that dense deposits occurred in the extracellular spaces between cells, and in some cases these deposits could be several hundred angstroms in size. Electron probe analysis showed that these deposits were calcium. It seems unlikely that these deposits were the result of high local concentrations of calcium in the extracellular space that existed in vivo. It seemed far more likely that they had developed at the site by depleting the surrounding region of calcium. Thus, at the level of resolution available with this technique they could not be considered to reflect the true distribution of calcium that obtained in vivo. Consequently, in order to carry out investigations that permit highest resolution, an alternative method is required.

We have investigated several cryogenic methods, the rationale being that very rapid freezing would immobilize calcium, as well as other soluble elements, in a rigid ice matrix. Then the ice could be removed by freeze-substitution (10) or by freeze-drying (7). The first method has produced variable results, and unacceptable losses elements. Freeze-drying was tried in two ways: frozen-sectioning followed by drying of the section; and freeze-drying of the tissue followed by embedding in epoxy, and subsequent sectioning. Frozen sectioning was technically difficult and unacceptably inefficient in producing sections that could be analyzed with confidence that both morphology and calcium distribution had been preserved. Freeze-drying has offered more promise. However, the limit to the method appears to be the rapidity with which the tissue can be frozen. The method we have developed has been described in detail in Dr. Halloran's thesis (6) but is outlined here briefly. Tissue is frozen

by rapidly bringing it into contact with a copper block cooled by liquid nitrogen with the device described by Christensen (1). The freeze-dryer is an adaptation of that described by Terracio (13), and the tissue is dried under a vacuum of 5×10^{-4} mm Hg by raising the temperature of the tissue 10-15 °C per hour (13). The dried tissue is exposed to OsO₄ vapor in a closed chamber at atmospheric pressure for 1 - 24 hours. The osmium acts as a contrasting agent for electron images and may serve as a fixative to stabilize the tissue. The tissue is embedded in Spurr's epoxy monomer (11), which is polymerized and sectioned. An example of chick chorioallantoic membrane prepared this way is seen in Figure 1. Although not evident in low resolution images such as produced in the electron probe, it can be seen in electron microscope images that ice crystal formation is the major problem with this technique. It is known that ice crystal formation can lead to redistribution of even large particles (16), thus the size of such crystals must be kept to a minimum by freezing as rapidly as possible. However, when rapid freezing occurs not only is morphology preserved but so are the normal distributions of such mobile elements as sodium and potassium.

The normal intercellular concentrations of sodium and potassium are not well established for chick, but have been reliably established for rat small intestine by Nellans and Schultz (8). We therefore prepared rat small intestine by this method and measured the intracellular concentrations of sodium and potassium with the electron probe using the BASIC procedure (14) to correct X-ray intensities. The values determined by bulk analysis (8) are compared to those obtained by electron probe analysis in Table 1. This close correspondence between the two methods strengthens our confidence in the electron probe analysis of tissue freeze-dried by this method and we intend to continue its use in the study of calcium transport and homeostasis.

References

- 1) Christensen, A. K., J. Cell Biol. 51:772 (1971)
- 2) Coleman, J. R. and Terepka, A. R., J. Histochem. Cytochem. 20:401 (1972)
- 3) Coleman, J. R. and Terepka, A. R., J. Histochem. Cytochem. 20:414 (1972)

- 4) Coleman, J. R., Davis, S., Halloran, B. P., and Moran, P.,
Proc. Tenth Natl. Conf. Microprobe Analytical Society
Las Vegas, 45 (1975)
- 5) Diculescu, I., Popescu, L. M. and Ionescu, N., Exptl. Cell Res.
68:210 (1971)
- 6) Halloran, B. P. 1976
Ph.D. Thesis, University of Rochester
- 7) Ingram, F. D., Ingram, M. T. and Hoghen, C. A. M.
In, Microprobe Analysis Applied to Cells and Tissues.
(T. Hall, P. Echlin and R. Kaufmann, eds.) New York
Academic Press, 119 (1974)
- 8) Nellans, H. and Schultz, S., Personal Communication 1976
- 9) Podolsky, R. J., Hall, T. and Hatchett, S. L.,
J. Cell Biol. 44:669 (1970)
- 10) Rebhun, L. I. in Principles and Techniques of Electron
Microscopy (M. A. Hayat, ed.) New York, Van Nostrand Reinhold
Vol. III p. 1 (1972)
- 11) Spurr, A. R., J. Ultrastr. Res., 26:31 (1969)
- 12) Terepka, A. R., Coleman, J. R., Armbrrecht, H. J. and Gunter, T. E.,
Symp. Soc. Exptl. Biol. 30:117 (1976)
- 13) Terracio, L. and Coulter, D., Proceedings of the Thirty Third
Annual EMSA Meeting Las Vegas, p. 614 (1975)
- 14) Warner, R. R. and Coleman, J. R. in Electron Probe Analysis as
Applied to Cells (T. Hall, P. Echlin and R. Kaufmann, eds.)
New York, Academic Press p. 249 (1974)
- 15) Warner, R. R. and Coleman, J. R., J. Cell Biol. 64:54 (1975)
- 16) Zingsheim, H. P., Biochem. Biophys. Acta 265:339 (1972)

Acknowledgements

This paper is based on work performed under contract with the U. S. Energy Research and Development Administration at the University of Rochester Biomedical and Environmental Research Project and has been assigned Report No. UR-3490-944.

Figure 1: Transmission electron micrograph of thin section from chick chorioallantoic membrane frozen and dried as described in text. The upper surface of the tissue was that which contacted the cold copper block first. A nucleated red blood cell in a capillary is prominent. The cytoplasm contains very well preserved regions which appear homogeneous, as well as regions which show evidence of ice crystal formation. Within the red blood cell the largest ice crystals are 200-300 A. Nuclei and mitochondria are well preserved in other cells, but there is obvious evidence of ice crystal formation. There is a gradient in the size of ice crystals: the smallest formed in the regions closest to the cold copper block, and larger ones appearing in cells deeper in the tissue. Generally, these ice crystals as deep as 10 μ into the tissue are not larger than 0.1 μ .

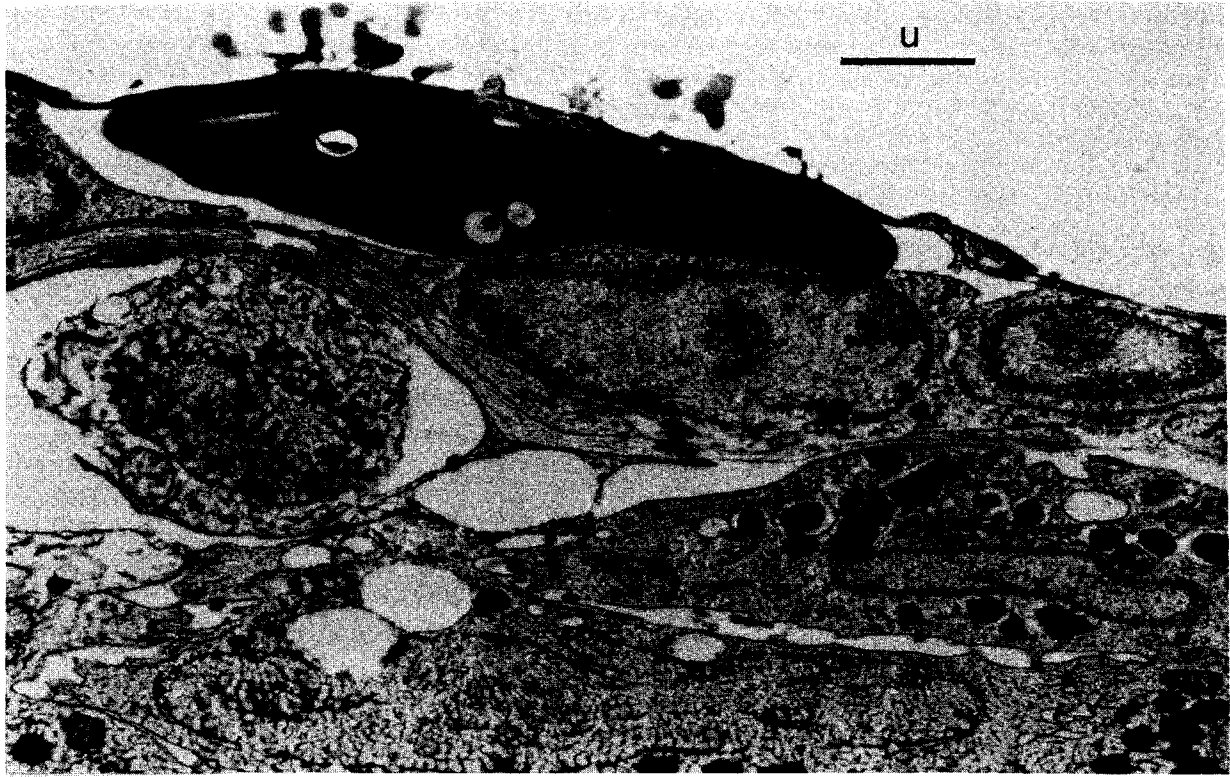
Table 1

Concentration in millimoles/liter

Electron Probe	K	Na
Cell #1	143.4	47.9
#2	134.0	47.9
#3	157.5	67.8
#4	<u>129.3</u>	<u>47.9</u>
	$141.0^{+9.6}(\text{S.D.})$	$52.9^{+7.7}(\text{S.D.})$
Nellans and Schultz	130.0^{+5}	60.0^{+1}

Data from reference 6

58H



ELECTRON PROBE ANALYSIS OF LIMITING TRANSEPITHELIAL INORGANIC ION
CONCENTRATION DIFFERENCES ACROSS THE RAT PROXIMAL TUBULE

by

R. R. Warner and C. P. Lechene

Biotechnology Resource in Electron Probe Microanalysis
Harvard Medical School
Boston, Massachusetts

This laboratory has demonstrated the efficacy of using electron probe analysis (EPA) of droplets to determine concentrations, in moles per liter, of all major elements in biological fluid samples (1, 2). Advantages of this technique are: that it can simply and routinely be used to determine concentrations of elements measured only with difficulty using other techniques (3); that the ability to determine all elements of interest in single samples allows one to easily perform inter-element correlative studies (4); and that determinations can be made on fluid samples so small that analysis using other techniques would not be feasible (5). In this report we describe a study of inorganic ion reabsorption along the length of rat kidney convoluted proximal tubule. Our study requires the determination of all major physiological inorganic elements in fluid samples never greater than 200 pL, which can only be done with the liquid droplet technique (1, 2).

Although the proximal convoluted tubule is regarded as a functional unit, studies have revealed morphological and electrophysiological differences along its length. Similarly, transport differences between early and late portions of this tubule have been observed for amino acid (6, 7) and phosphate transport (8, 9) but not for Na transport (10). The paucity of these latter studies reflects the difficulties encountered in analyzing the required small volumes. The entire proximal convoluted tubule has a luminal volume of 1.5 nL. Since not all this volume is accessible to micropuncture, and since a simple division into early and late portions divides even the remaining volume in half, one must analyze a sample of less than 500 pL.

With ultra-micro techniques other than EPA of liquid droplets, it is difficult or even impossible to analyze for more than one or two elements using such small volumes. Moreover, even smaller volumes are desirable in order to more adequately resolve transport differences with position along the tubule.

Our studies utilize Wistar rats anesthetized with Inactin, prepared for micropuncture following standard procedures (11) and infused with isotonic saline at 5.3ml/hr. Using the "standing droplet" technique (12) under stereomicroscopic control and with a micromanipulator, a column of oil is injected into a tubule lumen and split by 200 pL of a solution containing the poorly permeant solute raffinose (see composition in Table 1). Movement of ions and water occurs in this droplet until a limiting concentration difference between droplet and the peritubular blood across the nephron epithelial tissue is obtained. The droplet is then withdrawn for analysis and a blood sample taken. The tubular location is determined by latex injection and tubular micro-dissection. Following the liquid droplet technique (1, 2) pipettes calibrated between 15 and 20 pL are used to manipulate aliquots of samples as well as graded standard salt solutions. The calibrated aliquots are placed on a beryllium block under saturated oil; the oil is removed with a xylene wash, and the block is frozen in pre-cooled isopentane and freeze-dried overnight. Samples are analyzed with a Cameca MS46 microprobe at 11 KV, 200 nA, and a beam diameter approximately 60 μ . Na and Mg are analyzed with a KAP crystal; P, S, Cl, K and Ca with a PET crystal. Concentrations are determined by direct comparison with the standard solutions. Control of the probe and data reduction are performed with the automated system developed in this laboratory (13).

Table 1 shows the limiting inorganic ion concentrations obtained in droplets using two different injection solutions. In spite of the drastic differences in composition between the two injected solutions, the composition of the withdrawn droplets is equivalent; all values but P are

statistically identical. Considering the short contact time, this illustrates the high permeability of this epithelium. In spite of this high permeability, the tubule is able to maintain significant concentration differences between luminal droplet fluid and peritubular capillary blood due to the strength of its reabsorptive mechanisms. The limiting gradients (droplet fluid to blood ultrafiltrate) are also shown in Table 1. Limiting gradients for Na, K and Cl agree with literature values (14, 15). Values have not previously been reported for the remaining ions under our conditions. Differences found in the limiting P values between the two withdrawn solutions is under investigation.

One problem we encountered in this study is that droplets, frequently less than 100 pL, lose water even when handled under water-saturated paraffin oil. Presently, collected samples are isolated by columns of water-saturated oil within their collection micropipettes and stored at -80°C . Prior to analysis they are thawed, transferred to a concavity slide under a minute amount of saturated oil in hydrated containers, and aliquots taken for analysis. Control studies were done following this same technique; 80 pL droplets containing tritiated inulin were placed on a concavity slide under saturated oil, picked up in micropipettes and stored at -80°C for various times before liquid scintillation counting. As seen in Table 2, droplets lose no more than 16% of their water using these techniques. Samples at day zero were not frozen and were under water-saturated oil at room temperature for less than 30 minutes. The results show that droplets had already concentrated by 10% before freezing, and that there was no water loss as a function of time when frozen. We conclude that droplets can be stored at -80°C without concentrating; water loss occurs in the transfer process at room temperature.

This is the first step of a study on inorganic ion transport by a mammalian epithelium. It is possible only by use of EPA of picoliter droplets.

REFERENCES

1. Lechene, C. P. Proc. Fifth Nat. Conf. on Electron Probe Analysis, New York (1970) 32A-32C.
2. Lechene, C. P. Microprobe Analysis as Applied to Cells and Tissues (Eds. T. Hall, P. Echlin, R. Kaufman) Academic Press, New York (1974) 351-367.
3. Knox, F. G. and C. P. Lechene. Am. J. Physiol. 229 (1975) 1556-1560.
4. Abraham, E. H., R. R. Warner and C. P. Lechene. Proc. 10th Nat. Conf. MAS, Las Vegas, Nevada (1975) 47A-47F.
5. Borland, R. M., J. D. Biggers and C. P. Lechene. Submitted, J. Exp. Zool.
6. Seely, J. F. and E. Chirito. Am. J. Physiol. 229 (1975) 72-80.
7. Lingard, J., G. Rumrich and J. A. Young. Pflügers Arch. 342 (1973) 1-27.
8. Brunette, M. G., L. Taleb and S. Carrier. Am. J. Physiol. 225 (1973) 1076-1081.
9. Baumann, K., C. deRouffignac, N. Roinel, G. Rumrich, K. J. Ullrich, and P. Malorey. Pflügers Arch. 356 (1975) 287-297.
10. Györy, A. Z., J. M. Lingard and J. A. Young. Pflügers Arch. 348 (1974) 205-210.
11. Lechene, C. P., F. Morel, M. Guinnebault and C. deRouffignac. Nephron 6 (1969) 553-570.
12. Shipp, J. C., I. R. Hanenson, E. E. Windhager, H. J. Schatzmann, G. Whitttembury, H. Yoshimura and A. K. Solomon. Am. J. Physiol. 195 (1958) 563-569.
13. Moher, T. and C. P. Lechene. Biosciences Communication. In Press.
14. Kashgarian M., Y. Warren, H. Levitin. Am. J. Physiol. 209 (1965), 655-658.
15. Malnic, G., R. M. Klose, and G. Giebisch. Am. J. Physiol. 211 (1966) 548-559.

TABLE 1

Comparison of the elemental composition (mM/L) of droplets measured by EPA before and after 45 second contact with proximal tubule epithelium.

	<u>K</u>	<u>Cl</u>	<u>P</u>	<u>Na</u>	<u>S</u>	<u>Ca</u>	<u>Mg</u>
Injected Solution A*	.24	-1.0	.69	1.0	.18	.22	-.12
Withdrawn Droplet (6, 23)**	3.71	138.	1.22	114	1.03	1.23	0.67
Injected Solution B*	4.29	137.	2.12	127.	1.30	1.61	1.51
Withdrawn Droplet (11, 31)**	4.04	136.	2.03	119.	1.29	1.42	0.91
Droplet/Plasma	0.92	1.10	1.35	0.82	1.03	1.98	1.98
Δ Between Droplet and Plasma	NS	P<.01	P<.05	P<.01	NS	P<.01	NS

*Solution A is 300mM raffinose in deionized water.

Solution B was prepared to contain (mM/L): K, 4.0; Cl, 125.; P, 2.0; Na, 125.; S, 1.10; Ca, 1.10; Mg, 1.0

** (Number of rats, number of droplets)

TABLE 2

Conservation of liquid droplets

Day	0	3	5	10	12	14
<u>Droplet CPM*</u>	1.10	1.19	1.15	1.14	1.20	1.14
<u>Source CPM</u>	\pm .03	\pm .04	\pm .04	\pm .05	\pm .03	\pm .05

* Ratio of tritiated inulin concentration (in counts per minute) in picoliter droplets manipulated under oil and stored at -80°C to that of an identical volume of the same solution.

COMPARISON OF SCANNING TRANSMISSION AND BACKSCATTERED ELECTRON
IMAGING IN THE SEM, USING HEAVY METAL STAINED SECTIONS OF BIOLOGICAL TISSUE

Phillip B. DeNee
*Richard G. Frederickson

Appalachian Laboratory for Occupational Safety and Health
National Institute for Occupational Safety and Health
Morgantown, West Virginia

*Department of Anatomy, School of Medicine
West Virginia University Medical Center
Morgantown, West Virginia

The Transmission Electron Microscope (TEM) has been used extensively for the study of biological tissues in thin section (50-100 nm). For sectioned material greater than 100 nm the Scanning Transmission Electron Microscope (STEM) and the High Voltage Electron Microscope (HVEM) have become the only alternatives for the study of these tissues at a resolution better than that obtained with the light microscope. Recently, it has been shown (1) that tissue stained with heavy metal can be studied in the Scanning Electron Microscope (SEM) by Backscattered Electron (BSE) imaging to give results similar to those obtained with the TEM. Because BSE imaging is a method complementary to STEM, it seemed worthwhile to compare the two techniques using the same specimens and beam conditions.

Direct observation of the total specimen is possible with BSE imaging without interference by grid bars. Therefore, an improved perspective of tissue-to-tissue structural relationships can be obtained at a resolution significantly better than that of the light microscope. With the TEM, only a minimal tissue sample can be examined and patterns of tissue organization are difficult to interpret. Morphological studies can be productive with a system of analysis involving a series of microscopic techniques that provide information at different levels of resolution and different levels of cellular and tissue organization. BSE imaging with the SEM provides an extremely significant transition from the poorer resolution of light microscopy to the superior level of detailed visualization of cellular fine structure obtained with the TEM.

For this study we chose embryonic chick tissue already available and previously observed with the 1MeV HVEM. Sections were cut at thicknesses of 60 nm, 100 nm, 200 nm, 400 nm, 600 nm, and 800 nm, and collected on 300 mesh carbon-coated nylon grids. Each section was stained with uranyl acetate for 60 min., and lead citrate for 20 min. The grids were observed and micrographed using a commercially available SEM, with factory equipped solid state backscatter detector and scintillator/photomultiplier transmission electron detector. Working voltage was 20 Kv and beam current was 0.7 na.

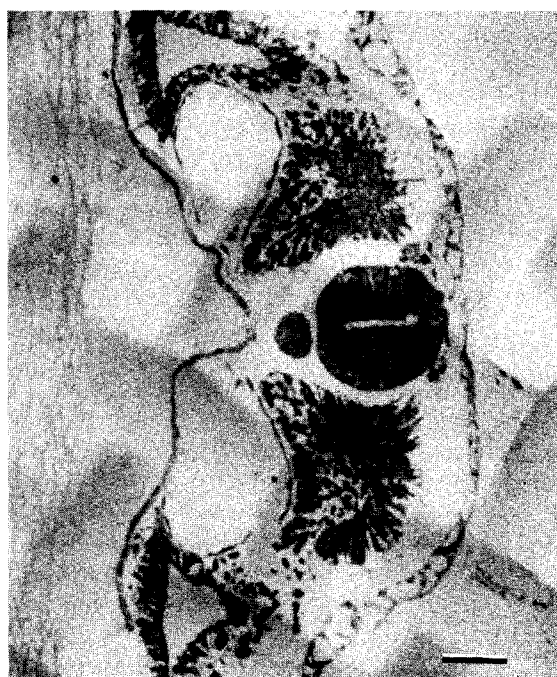
The micrographs were taken from the 200 nm thick section, which was found to be the optimum thickness for both STEM and BSE imaging. Figs. 1a and 1b illustrate a low power comparison of the same section as viewed with STEM and BSE imaging. In Fig. 1a, only about 25% of the tissue section can be seen in the STEM image because of the grid bars. However, the complete tissue section can be seen in the BSE image (Fig. 1b). The latter allows unrestricted obser-

vation of total tissue continuity. Figs. 2a and 2b, show a higher magnification of the tissue illustrating good resolution of cellular detail with both imaging modes. Comparing Figs. 2a and 2b, it can be seen that cellular detail is more distinct in the BSE image (Fig. 2b) while delicate extracellular material (arrow) is more distinct in the STEM image (Fig. 2a). Under the conditions of the experiment it was determined that STEM was marginally adequate for sections of 60 to 100 nm, and optimal at 200 nm. Above 200 nm, resolution deteriorated markedly and was uninformative. Conversely, the BSE' image was extremely poor for sections of 60 to 100 nm, but became optimal for thicknesses of 200 nm and greater.

1) DeNee, P.B. et al. "Histochemical Stains for the SEM -- qualitative and semi-quantitative aspects of specific silver stains". In: Scan.Elect.Microscopy (O.Johari, ed.) IITRI, Chicago, IL. (1974) p.259.



a



b

Fig. 1. Low magnification of 200 nm thick section of chick embryo stained with uranyl acetate and lead citrate. a) STEM image; b) Backscattered electron image with polarity reversed -Note that grid bars do not interfere with the image. Bar = 50 μ m.

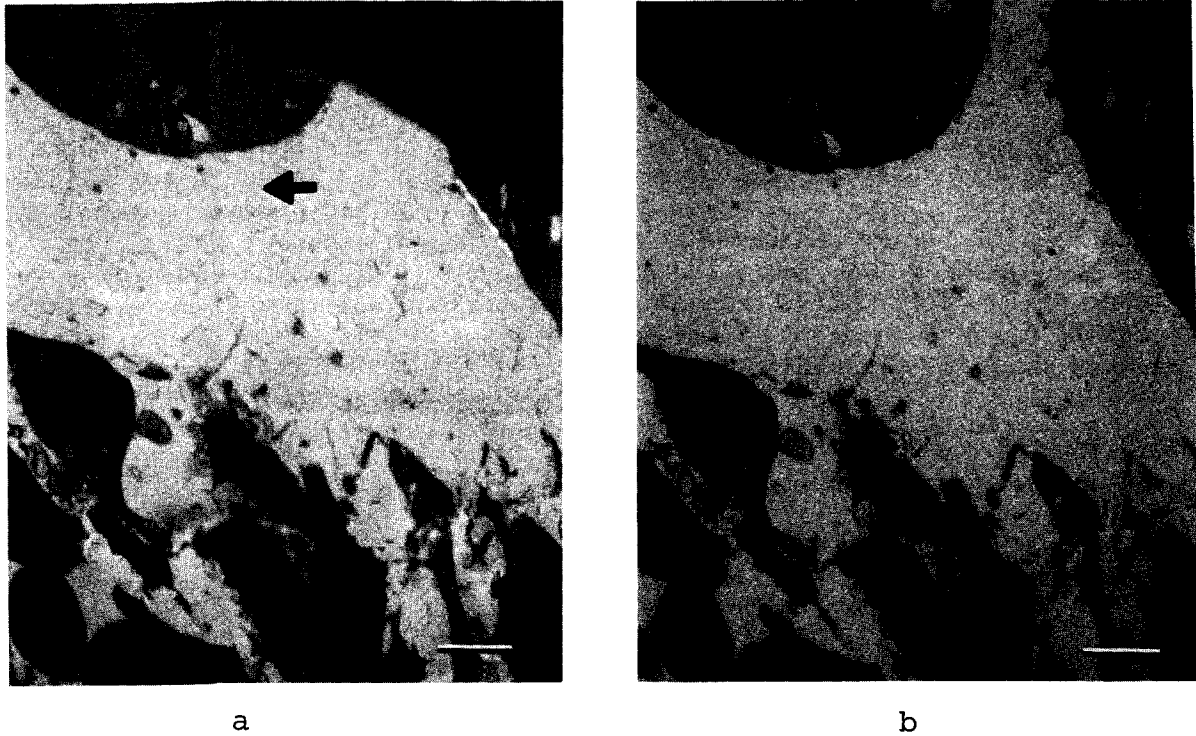


Fig. 2. Higher magnification of same section shown above. a) STEM image;- Note extracellular material (arrow); b) Backscattered electron image with polarity reversed - Note improved cellular details. Bar = 5 μ m.

ELECTRON PROBE STUDY OF THE URINARY CONCENTRATING MECHANISM
ELEMENTAL CORTICO-PAPILLARY GRADIENT IN FROZEN HYDRATED RAT KIDNEY

C. P. Lechene and J. V. Bonventre

Biotechnology Resource in Electron Probe Microanalysis
Harvard Medical School
Boston, Massachusetts

The mammalian kidney is able to produce a urine which is much more concentrated than plasma. When the organism needs to conserve water its kidneys can elaborate a urine 4 times more concentrated than plasma (300 mOs) in man, and up to 20 times plasma in some desert rodents.

The kidney is divided into three zones: cortex, outer medulla, and inner medulla which are clearly definable by the naked eye in a hemisected organ. Each zone has specialized functions unique to it. The osmotic work of the kidney is performed primarily by the specialized structures of the outer and inner medulla which establish an osmotic gradient with the osmotic pressure increasing in all structures of the renal medulla from the cortico-medullary junction to the tip of the papilla. The constituents of this osmotic gradient are primarily sodium, chloride and urea (1). Osmotic work is then performed by osmotic equilibration of the collecting tubule fluid losing solute free water as it transverses the longitudinal gradient (1). The existence of this gradient has been established by analyzing kidney slices taken perpendicular to the axis of the gradient (2, 3). However, the thickness of these slices, generally several millimeters, made it difficult to obtain a precise determination of the gradient profiles and resulted in the inability to recognize abrupt changes in concentration. Electron probe microanalysis of sodium and chlorine (4) has been used to analyze freeze dried tissue slices cut frozen at varying temperatures.

We would like to thank the Cameca Company (92-Courbevoie, France) for making the Camebax Microprobe with its special frozen stage attachment available to us. We would also like to thank C. Conty of Cameca whose experience and help with the equipment was greatly appreciated.

From these tissue slice studies it was concluded that in the water deprived (antidiuretic) mammal the medullary gradient increases gradually and relatively uniformly from cortico-medullary junction to papilla tip. However, recent observations from our laboratory have indicated that an extracellular marker, sodium ferrocyanide, while increasing in concentration throughout the medulla exhibits a marked change in concentration profile at the boundary between outer and inner medulla in antidiuretic kidneys. When animals were given a water load and made water diuretic, the dissipation of this ferrocyanide gradient occurred first at the papilla tip (5, 6). Since the existence of similar gradient profiles for sodium and chlorine would have significant implications in the understanding of the concentrating mechanism, we used EPA to establish the relative Na, Cl, K, and P concentrations along linear scans from cortex to papilla tip. In order to avoid distortion of the profiles due to diffusion, the kidneys were analyzed in the frozen hydrated state below -150°C .

Methods

Wistar rats were made antidiuretic by water deprivation for 48 hours. Other rats were made water diuretic by intragastric infusion to 10% of their body weight of warmed 1/4 saline in two equal doses separated by one hour. The urinary osmotic pressure was determined with a vapor pressure osmometer. The urinary osmotic pressure of water diuretic rats was documented to be below the plasma osmotic pressure for at least 2 hours before removal of the kidneys. After the animals were anesthetized with Inactin (R) (125 mg/Kg), a midline abdominal incision was made and within 5 seconds both kidneys were rapidly removed and quenched in isopentane cooled to -160°C by liquid N_2 .

The whole kidneys were kept 24 hours in liquid nitrogen and transported from Boston to Paris maintained in dry ice (12 hours). In Paris they were transferred back into liquid nitrogen for 2-7 days. Immediately before EPA the frozen kidneys were hemisected. Cutting of the kidney was performed using a small circular saw mounted on a stepping motor and special forceps

to hold the tissue. The saw was immersed in the liquid nitrogen. The stepping motor allowed us to cut at a low rotation velocity (200 to 300 rpm) and a high torque. After the surface to be analyzed had been exposed, the kidney was transferred under liquid nitrogen into the air lock of the special frozen stage of a Camebax microprobe. The air lock was then vacuum pumped and the frozen kidney was introduced into the cooled holder within the microprobe column. Practically no rewarming was observed when the tissue was in the holder which was maintained at -156°C during the entire experiment. The sample was observed and oriented by microscopic observation of the frozen surface ($\times 400$). A linear scan was affected by moving the sample along one dimension using a motor. The coordinates of the cortex, outer medulla, inner medulla, cortico-medullary junction and border between outer and inner medulla were recorded from microscopic observation. During all these observations the electron beam was turned off. Linear scans of the elemental profiles were then recorded using the previous coordinates to establish the precise localization. Accelerating voltage was 10 or 20 KV. The beam current was 50 to 90 nA. The beam was either kept stationary, focused or defocused to 20μ or was scanned over an area of $50\mu^2$. In one case the sample was reanalyzed after carbon coating with a special coater adapted to the interlock of the probe. Na $K\alpha$ was analyzed with a TAP crystal; K, P and Cl $K\alpha$ were analyzed with a PET crystal.

Results and Discussion

Five antidiuretic and one water diuretic kidneys were analyzed. The same results were observed for all the antidiuretic kidneys, independent of probing conditions or coating. In antidiuresis (Fig. 1 and 2) the characteristic intensity lines for Na (and for Cl) increase suddenly at the boundary between outer and inner medulla. The X-ray intensity lines for potassium and phosphorus along the same linear scan remained relatively flat.

In the water diuretic kidney, the overall medullary gradient for Na was abolished and the sodium concentration decreased from the outer-inner

medullary junction to the tip of the papilla (Fig. 3). The same profile was observed for chlorine. Potassium and phosphorus remained flat.

The oscillations observed along the linear scan are most likely due to the change in characteristic line signal locally as the beam passes from cellular to extracellular compartments of different compositions. The characteristic X-ray signals have been expressed without background subtraction. It was assumed that the mean atomic number of the biological matrix does not appreciably vary from the cortex to the papilla. This assumption was supported by potassium and phosphorus flat profiles.

These results indicate that a brisk increase in elemental concentration of Na (and Cl) occurs at the boundary between outer and inner medulla of antidiuretic rats and that in water diuresis the concentration of Na (and Cl) is dissipated from the papilla tip. This sharp rise in concentration at the boundary between outer and inner medulla in antidiuresis together with the washout of the medullary gradient from the papilla tip in water diuresis is consistent with our results using ferrocyanide. We believe that these results support our view that the pelvic urine which bathes the entire inner medulla, together with the marked change in vascularization at the outer-inner medulla boundary (5, 6, 7, 8), plays an important role in the mechanism of concentration in the kidney.

In this study electron probe microanalysis was used to study the elemental profiles in a soft biological tissue by treating it as if it was a piece of rock using liquid nitrogen for preparation and keeping the sample frozen and hydrated below -150°C during the analysis. The lack of adequate tools to work under liquid nitrogen made the preparation difficult. However, necessary hardware to prepare hardened soft tissues under these conditions will be relatively easy to develop. In addition, it should be mentioned that while no trouble was encountered with frost during preliminary cutting assays under liquid nitrogen in Boston where the air was very dry (winter), frost was a significant problem in Paris where the air was

very humid. Liquid nitrogen trapped water from the atmosphere in the form of small ice crystals. These ice crystals not only obscured viewing in the liquid nitrogen bath but tended to deposit onto the surface of the sample in the bath. Such difficulty could be avoided by working in the liquid nitrogen bath under positive pressure of nitrogen gas.

Preparation under liquid nitrogen and analysis of frozen hydrated tissues will permit the biologist working with soft biological tissue to apply the well developed electron probe analytical techniques used by the metallurgist and geologist on their hard samples. This preparation most likely prevents translocation of the diffusible elemental components of biological tissue.

In conclusion, electron probe microanalysis along a linear scan of frozen hydrated kidneys has provided new information which is serving to help us understand more completely how the kidney performs one of its most important functions - the conservation of water.

REFERENCES

1. Wirz, H. and R. Dirix. Urinary concentration and dilution. In: Handbook of Physiology, Am. Physiological Soc. Section 8, Renal Physiology, Chapt. 13, Pg. 415-430, Washington, D. C. 1973.
2. Wirz, H. Der osmotische Druck des Blutes in der Nierenpapille. *Helv. Physiol. Pharmacol. Acta* 11: 20-29, 1953.
3. Ullrich, K. J., F. O. Drenckhahn, and K. H. Jarausch. Untersuchungen zum Problem der Harnkonzentrierung und -verdünnung. Ueber das osmotische Verhalten von Nierenzellen und die begleitende Electrolytanhäufung im Nierengewebe bei verschiedenen Diuresezuständen. *Arch. Ges. Physiol.* 261: 62-77, 1955.
4. Koepsell, H., W. A. Nicholson, W. Kriz and H. J. Höhling. Measurements of exponential gradients of sodium and chlorine in the rat kidney medulla using the electron microprobe. *Pflügers Arch.* 350: 167-184, 1974.

REFERENCES, CONT.

5. Lechene, C. P., J. Fusco, J. V. Bonventre and B. Schmidt-Nielsen. Contact between pelvic urine and renal inner medulla as part of the concentrating mechanism. Abstract, VI International Congress of Nephrology, A153, 1975.
6. J. V. Bonventre and C. P. Lechene. Renal-medullary concentration gradient due to urine-to-papilla urea cycling. *Kidney Int.* 8, No. 6, p. 469 (Abstract). 1975
7. Bonventre, J. V. and C. P. Lechene. Effect of pelvic urine on renal concentrating ability. Abstract, No. 917. *Fed. Proc.* 35: 372, 1976.
8. C. P. Lechene, J. V. Bonventre and M. J. Karnovsky. Permeability of the renal papillary epithelium and urinary concentrating ability. Abstract, Am. Fed. Clin. Research. National Meeting, May, 1976.

Fig.1

ANTIDIURESIS IN THE RAT (3130mOs)

-156°C 20KV FOCUSED

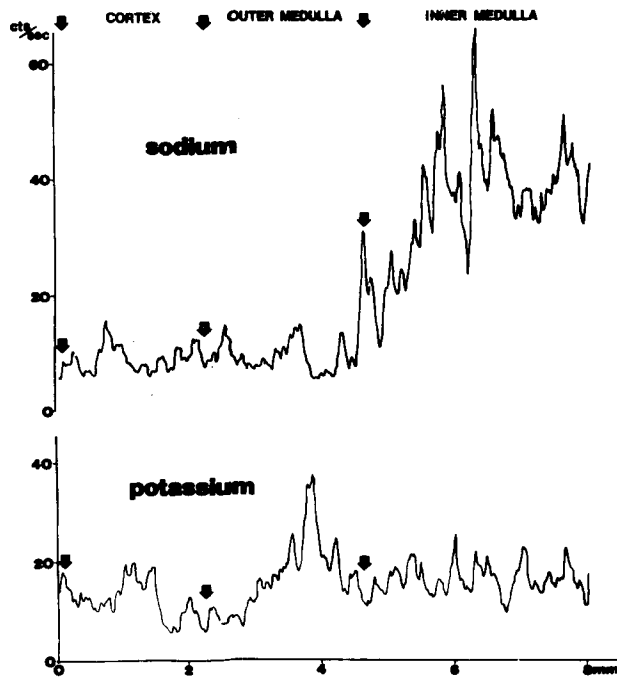


Fig.3

WATER DIURESIS IN THE RAT (95mOs)

-156°C 10KV 70nA 60μ scan

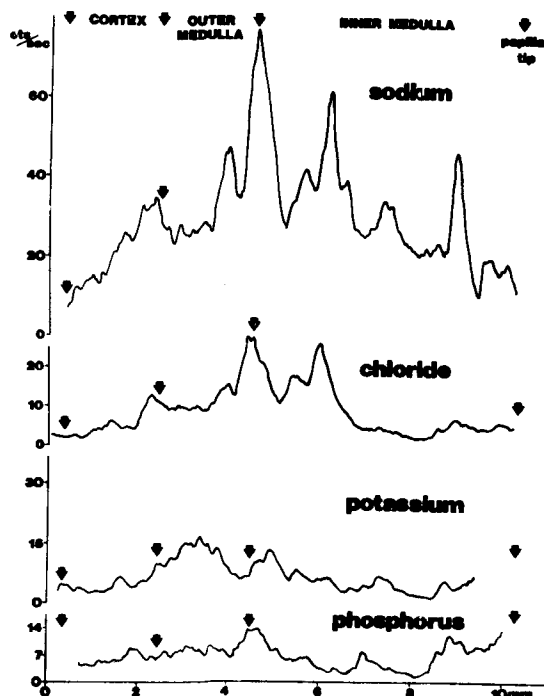


Fig.2

ANTIDIURESIS IN THE RAT (2828mOs)

-156°C 10KV 90nA 60μ scan

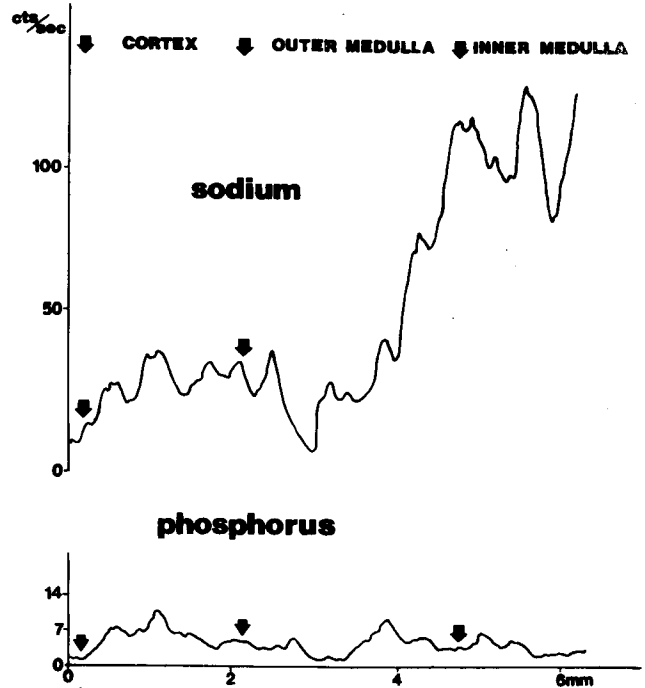


Fig. 1 EPMA*of the longitudinal concentration profile for Na and K in a frozen hydrated kidney from an antidiuretic rat.

Fig. 2 EPMA*of the longitudinal concentration profile for Na and P in a frozen hydrated kidney from an antidiuretic rat.

Fig. 3 EPMA*of the longitudinal concentration profile for N, Cl, K and P in a frozen hydrated kidney from a water diuretic rat.

*EPMA = Electron Probe Micro Analysis.

CALCIUM IN GOBLET CELLS OF THE SMALL INTESTINE

Bernard P. Halloran and James R. Coleman

Department of Radiation Biology and Biophysics

University of Rochester School of Medicine and Dentistry

Rochester, New York 14642

Intestinal absorption and secretion of calcium is an extremely complex process. The absorptive and goblet cells which make up the intestinal epithelium are in turn responsible for these transport processes. Calcium balance studies have shown that calcium absorption and secretion depend primarily on dietary calcium uptake and vitamin D status of the animal (1,2). A normal man absorbs approximately 50% of his total ingested calcium per day (500-900 mg/day), the remainder being lost to the feces (2). In addition, a certain amount of fecal calcium (20-30% of the total) is the result of endogenous secretion by the intestine. The actual amount of calcium secreted may be larger since some secreted calcium may be subsequently reabsorbed.

On a cellular level the absorptive and secretory processes appear to be both active and passive (3,4). A recent investigation of the cellular distribution of calcium in calcium absorbing cells from vitamin D-depleted and -repleted intestine indicated that calcium is somehow sequestered at the brush border and then transported across the absorptive cell in a packaged or localized form (5). Although goblet cells are generally thought only to produce a mucus which protects and lubricates the intestinal surface (6,7), it was shown that they were also involved in the total calcium absorption mechanism. Calcium binding protein, a protein implicated in vitamin D mediated transport, is produced by goblet cells (8) and goblet cells contain high concentrations of calcium as discrete localizations apparently associated with mucin droplets. In order to elucidate the role of goblet cells in overall calcium metabolism it was necessary to examine the association of calcium and goblet cell mucin more closely, since the previous studies were limited to spatial resolution of morphological features of about $1/2 \mu$ or larger.

Using a previously described transmitted electron detector (9) and coordinated electron probe and transmission electron microscope studies we were able to overcome this spatial resolution limitation and define the spatital relationship of calcium localizations and mucus.

Tissue was prepared following the procedure of Warner and Coleman (5). Thin sections (1000-1500 Å) were cut on water or on an ammonium oxalate saturated water bath (in an attempt to minimize calcium redistribution). Cutting sections greater than approximately 1000 Å on water instead of ammonium oxalate had little effect on calcium concentration.

Goblet cells of unstained tissue were photographed in a CEM, the sections coated with aluminum and mounted in the probe. Scanning transmission images were used for purposes of identification and a series of 2-minute point counts were taken across the cells in a matrix fashion. Analysis was carried out at 22 KV with a beam current of 5×10^{-8} A and a probe diameter of approximately $1/4$ - $1/2$ μ .

The results of this work (as summarized in Tables I and II) indicate that the goblet cell distribution of calcium is characterized by: 1) electron dense granules of various sizes (probably calcium oxalate precipitates) which appear randomly throughout the mucus, 2) by a relatively homogeneous distribution of calcium throughout the mucus which appears to be slightly more concentrated at sites surrounding and in between mucin droplets, and 3) by elevated concentrations associated with the endoplasmic reticulum (ER).

Preliminary results of point counts taken within the apical portion of absorptive cells indicate a more or less homogeneous distribution with concentrations somewhat less than any of the goblet cell sites investigated. As osmium signal was detected at all probe sites but did not appear to be associated with calcium. The electron dense granules were not enriched in osmium.

These findings suggest that elevated concentrations of calcium are characteristic of both mucin production and storage. The site of calcium accumulation appears to be coincident with the site of protein synthesis (ER), a finding consistent with the high calcium affinity of calcium binding protein (CaBP). The relative concentrations of calcium in newly formed mucus and stored mucus are the same, suggesting that little, if any, additional calcium is added to mucus after its initial synthesis.

The distribution of calcium in mucus-rich areas suggest that at least two separate pools of calcium exist; one more or less homogeneous which may be associated with CaBP and/or act to stabilize mucin droplets in their spherical form, and another granular which does not appear to be associated with any specific structure or area within the mucus and which may represent a secretory product contributing to endogenous fecal calcium.

REFERENCES

1. Omdahl, J.L. and DeLuca, H.F., *Physiol. Rev.* 53, (1973), 327.
2. Bronner, F., in *Mineral Metabolism: An Advanced Treatise*. Fr. Bronner and C. Comar, eds. Academic Press, NY, (1964), 342.
3. Walling, M.W. and Kimberg, D.V., *Am. J. Physiol.* 225, (1973), 415.
4. Papworth, D.G. and Patrick, G., *J. Physiol.* 210, (1970), 999.
5. Warner, R.R. and Coleman, J.R., *J. Cell Biol.* 64, (1975), 54.
6. Schrager, J., *Gut*, 11, (1970), 450.
7. Cheng, H., *Am. J. Anat.* 141, (1974), 481.
8. Taylor, A.N. and Wasserman, R.H., *J. Histochem. Cytochem.*, 18, (1970), 107.
9. Coleman, J.R., Davis, S., Halloran, B. and Moran, P., in *Tenth Annual Proceedings of the Microbeam Analysis Society*, Las Vegas, (1975), paper #45.

Acknowledgements

This paper is based on work performed partially on NIH Grant No. AM14272 and partially under contract with the U.S. Energy Research and Development Administration at the University of Rochester and has been assigned Report No. UR-3490-909.

Figure 1 a,b. Thin (1000-1500 Å) unstained section of intestinal tissue showing a goblet cell before exposure to the probe (a). Figure 1b is the same goblet cell after microprobe analysis. Numbered sites correspond to areas probed (see Table I). Tissue damage is obvious at sites where the electron beam has struck the section and in turn allows one to identify the exact location of the probe.

TABLE I

Calcium concentrations expressed as counts per 2 minutes at various sites in the goblet cell of Figure 1b. (Site numbers in Figure 1 correspond to those listed here.)

<u>Site No.</u>	<u>Tissue Area</u>	<u>Peak</u>	<u>Background</u>
1	absorptive cell	19	12
2	absorptive cell	23	12
3	ER	33	13
4	ER	32	15
5	mucin droplet	29	12
6	mucin droplet	34	17
7	granule	51	15

TABLE II

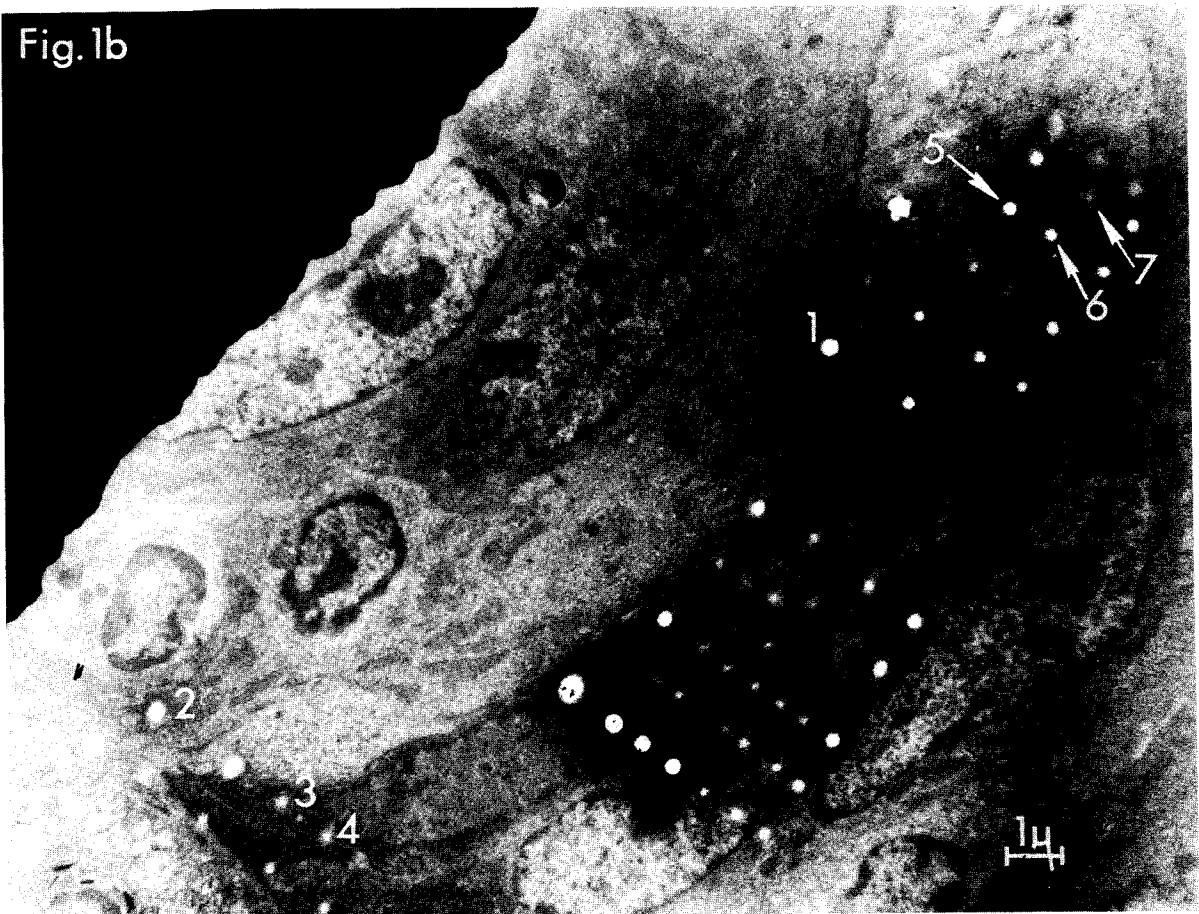
Average calcium concentrations expressed as counts per 2 min. (peak-background \pm 1 SD) from 7 separate cells. Note that variation in thickness, aluminum coat and contamination from the probe result in significant differences in the count rates from similar areas in different sections. The trend in counts indicated by the averages is similar in any one cell but the variation is less than is reflected by the standard deviations presented below. Count rates over granules vary considerably but do so in relation to size.

	<u>Absorptive Cell</u>	<u>ER</u>	<u>Mucin</u>	<u>Intermucin Sites</u>	<u>Granules</u>
<u>Avg. Counts</u> 2 min.	9.0 \pm 2.0	18.4 \pm 6.8	20.6 \pm 6.7	25.0 \pm 13.4	42.2 \pm 12.1
No. Points Counted	38	14	70	6	7

Fig. 1a



Fig. 1b



VOLUME CHANGES IN FREEZE-DRIED TISSUE

F. Duane Ingram, Mary Jo Ingram

Department of Internal Medicine

University of Iowa, Iowa City, Iowa 52242

and

Arthur R. Spurr

Department of Vegetable Crops

University of California

Davies, California 95616

Biological soft tissue is an extremely poor sample material for electron probe microanalysis. An ideal electron probe sample is a high density substance, uniform and homogeneous in composition with good electrical and thermal conductivity. Biological tissue, unfortunately, is deficient in each of these important properties.

As an attempt to improve the qualities of biological tissue, it is common to dehydrate and embed samples in a plastic matrix. The density, uniformity and stability of the sample are improved at the expense of decreasing the atomic concentrations of the elements of interest. The presence of the embedding media can also complicate quantitation of measurements unless appropriate standards are developed.

Albumin solutions containing known quantities of electrolytes have been adopted by some laboratories as standards materials for calibrating the electron probe signal (Ingram et al., 1973). These standards are chemically similar to tissue, and since they are prepared in a parallel fashion with tissue, preparation-induced distortions are likely to be similar.

An alternate method of preparing standards consists of complexing known quantities of Na or K in macrocyclic polyethers (Spurr, 1974). The homogeneity and uniformity of such samples commend their use as organic standards. Since they have not been subjected to the same preparation stresses as the materials for which they are to serve as standards, it is of some interest to compare them with standards materials, such as albumin, which have been prepared in the same fashion as tissue.

Hall, 1968 has demonstrated that selection of a standards material is not particularly critical for thin section analysis. With thick or bulk samples, however, the physical dimensions of the excitation volume are dictated almost solely by the density of the embedding medium for any given accelerating voltage. It is thus important to determine the nature and extent of volume changes that may occur during preparation. Evidence that shrinkage occurs during preparation

of freeze-dried tissue has been reported by Ingram et al., 1974. Additional evidence of similar volume change is presented here.

A series of standards blocks of NaCNS-dicyclohexyl(18)-crown-6 with from 0 to 400 mEq/liter Na were analyzed using the same 10 kV, 50 nA beam conditions as were used for albumin standards data reported earlier, Ingram et al., 1973. With spectrometer parameters that resulted in 7605 ± 29 (S.D.) NaK α cts/sec on NaCl crystals, the NaK α x-ray intensities with albumin standards were 0.376 ± 0.016 (S.D.) cts/sec/mEq/liter, whereas they were 0.327 ± 0.004 (S.D.) cts/sec/mEq/liter with the plastic standards. All samples were bombarded for a period of two minutes before data was collected to "stabilize" the sample. The difference between intensities from the two types of samples could be explained if the albumin standards had shrunk about 15% during preparation. This is compatible with results of the study using ^{22}Na radioactive tracers (Ingram et al., 1974). In that study it was found that the ^{22}Na counting rates per unit volume were a factor of 1.20 ± 0.06 (S.D., $n=16$) higher for embedded samples of albumin than for fresh solution. This effect could result if the samples had shrunk during preparation.

Volume change in animal tissue was also studied (Ingram et al., 1974) but scatter in the data was too large to establish the precise magnitude of shrinkage in the various types of tissue. It is evident from these studies, however, that the analyst should be aware that shrinkage of 15 to 20% is highly likely, and allowance must be made for volume changes if absolute measurements are attempted on dehydrated, plastic embedded tissue samples.

References

Hall, T., 1968. In Quantitative Electron Probe Microanalysis, Proc. Seminar, National Bureau Stds., Gaithersburg, Maryland, Heinrich, K.F.J., Ed., 269-299.

Ingram, F.D., M.J. Ingram, and C.A.M. Hogben, 1973. Proc. Eighth Natl. Conf. on Electron Probe Analysis, 62A-62E.

Ingram, F.D., M.J. Ingram, and C.A.M. Hogben, 1974. In: Microprobe Analysis as Applied to Cells and Tissues, Eds. T. Hall, P. Echlin, and R. Kaufman, Academic Press, New York, 119-146.

Spurr, A.R., 1974. In: Microprobe Analysis as Applied to Cells and Tissues, Eds. T. Hall, P. Echlin, and R. Kaufman, Academic Press, New York, 213-227.

ALUMINIUM, ZINC AND LEAD IN ARTERIAL CALCIFICATIONS
OF HUMAN BRAIN

S. DUCKETT* and P. GALLE**

*Jefferson Medical College - Philadelphia -(U.S.A.) and
 **Département de Biophysique de la Faculté de Médecine
 de Créteil -(France).

In some human diseases, localized arterial calcifications are observed specifically in the pallidum. The lesions are found particularly in Parkinson Disease.

Conventional Histochemical methods had demonstrated before the presence of Calcium deposits (Von Kossa reaction) and Iron deposits (Perls reaction) in these arterial walls.

Brain tissue taken "post mortem" in seven cases of Parkinson diseases have been studied by X-Ray microanalysis.

In all these cases, a high concentration of Phosphorus, Calcium and Iron and a lower concentration of Magnesium have been found ; but besides, the evidence for the presence of other varieties of mineral elements has been proved ; Those data lead us to distinguish two groups of patients. In the first one (4 patients), Zinc and Lead are added to the existing arterial wall deposits (Fig.1). In the second one (3 patients), the element added is Aluminium (Fig.2).

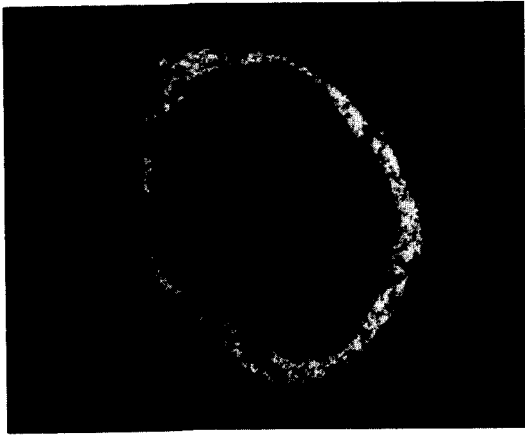
Abnormal deposits of mineral elements such as Aluminium or Iron have recently been demonstrated by X-ray micro-analysis in human brain tissues (DUCKETT and coll.) but the localization of the deposits and the clinical course were different.

Human organism is frequently under contamination by Aluminium, Lead or Zinc through pulmonary or digestive way ; The relation between this contamination and the arterial lesions localized in the palladium may be discussed.

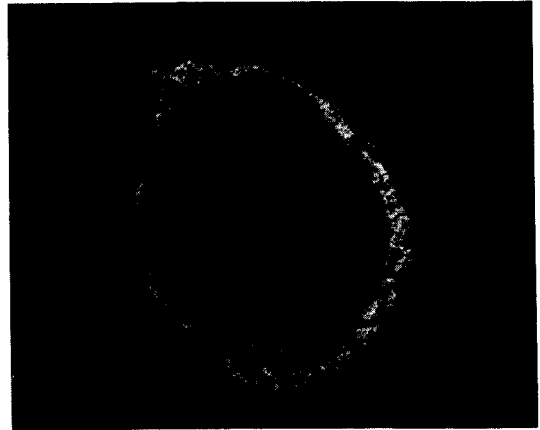
FIGURES LEGENDS

FIGURE I : Phosphorus, Calcium, Iron, Zinc and Lead distribution in the wall of a pallidal artery (Parkinson disease). Magn = x 1 000

FIGURE 2 : Phosphorus, Calcium, Iron and Aluminium distribution in the wall of pallidal artery (Parkinson disease). Magn = x 1 000.



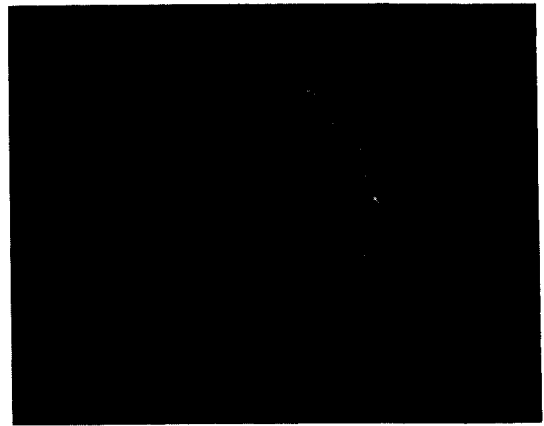
PHOSPHORE



CALCIUM



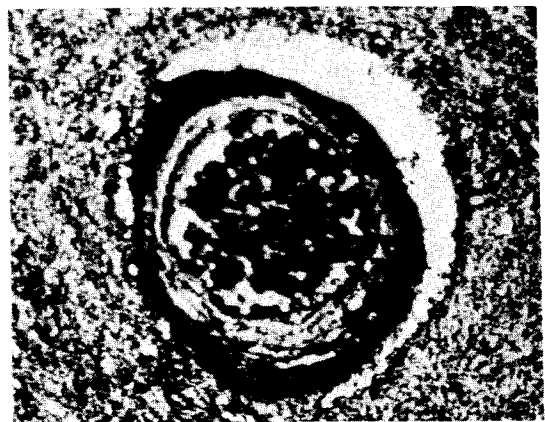
FER



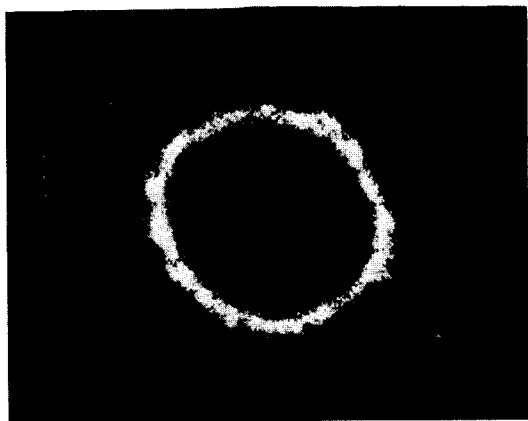
ZINC



PLOMB



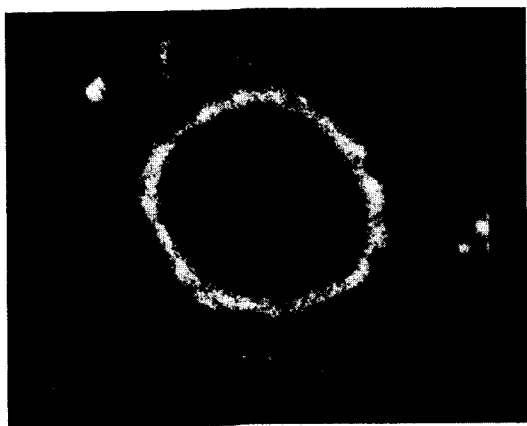
64D



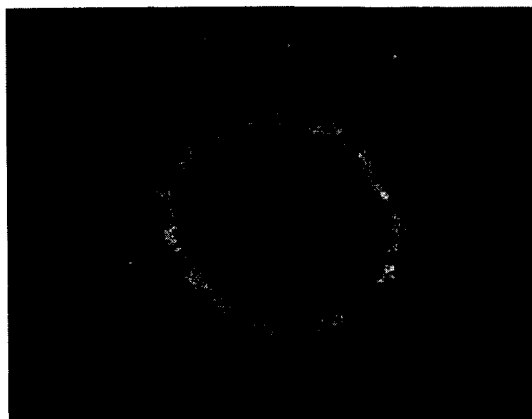
PHOSPHORE



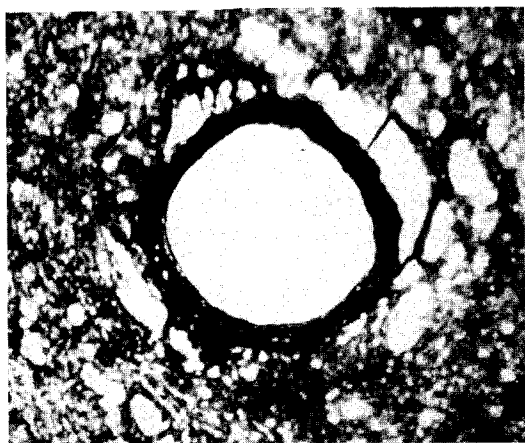
CALCIUM



FER



ALUMINIUM



DYNAMIC EFFECTS ON QUANTITATION IN THE ELECTRON PROBE ANALYSIS OF MINERALIZED TISSUES

by

John W. Edie, Dental Research Laboratory, University of Iowa,
Iowa City, Iowa 52240

and

Paul L. Glick, V.A. Hospital and College of Dentistry, Univer-
sity of Iowa, Iowa City, Iowa 52240

The electron probe analyzer has frequently been used to examine Ca and P concentrations and the Ca/P ratios in mineralized tissues. In what should be a relatively straight forward application in biological applications, there have been difficulties in acquiring accurate quantitative results (1,2).

As an example, the progression of mineralization from the pulp through the enamel has been examined in an ARL EMX-SM electron microprobe using polished transverse sections of developing rat tooth incisor embedded in plastic. Fig. 1 displays the resulting isoconcentration lines for Ca and P using uncorrected data with a fluorapatite (FAP) crystal as the standard. The associated Ca/P level curves are also shown. Since the final mineralization state of enamel approaches that of pure hydroxylapatite, the results for the enamel agree well with those obtained with chemical analyses performed on gross specimens. However, in the dentine, values for Ca and P concentrations are 10-20% higher than believed to exist and these differences cannot be accounted for through ZAF correction procedures.

It would be necessary to know the absolute Ca and P concentrations to within a few percent accuracy in order that the observed differences in mineralization may be deemed to be significant. The interpretational difficulties that exist are apparent and dictate that an understanding of the physical phenomenon involved be acquired before reliable and valid data may be obtained.

A few obvious difficulties for quantitation within dentine would be the increased heterogeneity of the sample due to the organic matrix ($\sim 30\%$ in dentine compared to $\sim 4\%$ in enamel), the decreased density relative to the standard and the apparent volatilization of the sample under the electron beam. A beam-induced loss in organic mass has been previously observed in thin, soft tissue sections and/or resins in which mass is lost at very low electron doses (3,4,5). There is a time dependence in count rate for continuum X-radiation for the duration of this mass loss and the effect is believed to be temperature dependent. To observe this effect, it is necessary to reduce the electron exposure by defocusing the electron beam to a point where an electron dose of $\sim 10^{-16}$ C/ μm^2 is prolonged over several seconds.

The possible influence of this mass loss on characteristic X-ray measurement was observed in a similar manner. An ADP crystal spectrometer was used to monitor the Ca K_{α} count rate as a function of electron dose (estimated from specimen current, beam diameter and time of analysis) for the FAP standard and different regions in the rat tooth. An acceleration voltage of 12 kV, a specimen current of 80 nA (on FAP) and a beam diameter of 100 μm was used. Count rates on FAP, which were constant, were used to predict k-ratios for the teeth runs. Fig. 2 shows the resulting electron exposure dependence of the k-ratios for the different regions in the tooth. Practically identical curves exist for P K_{α} measurements on these specimens. These curves demonstrate that the k-ratios undergo various percentage increases as a result of the electron exposure. Also, a single counting interval for 10^{-8} C/ μm^2 electron dose would yield an average value which was intermediate between the initial count rate and the final, stable count rate.

The influence of specimen preparation procedures on these results was examined by preparing similar teeth by different techniques (see Table 1) and observing the count rate variation under the same operating conditions at analysis points on mature dentine. The percentage variation in k-ratios as a function of electron exposure is displayed in Fig. 3-a. Initial k-ratios, k_0 , are also shown. The count rate dynamics are observed to be dependent upon these procedures, the type of embedding media used and the degree of plastic penetration into the specimen. The final stable k-ratio, k_f , had a spread of $\sim 10\%$ which was beyond the range that might be expected for specimen to specimen variation. Of special interest was the specimen prepared by the hydrazine-deproteination technique (6). Only the crystalline matrix should remain after the extraction process and the observed variation must be due to the embedding media penetration into the tooth.

Fig. 3-b illustrates the effect of accelerating voltage on the counting dynamics in the same tooth. k_f was observed to increase with accelerating voltage, presumably due to greater electron penetration in the reduced density dentine. However, the amount of increase did not become noticeable until an accelerating voltage of 20 kV was reached.

To aid in the interpretation of the above results, different Ca-containing compounds and plastics (see Table 2) of known compositions and densities, some of which had exhibited volatile characteristics, were examined. Fig. 4 shows the resulting dynamic counting exhibited by the volatile specimens. The volatility of the specimen was most closely associated with the H and C compositions of the specimen. Attempts were made to apply ZAF corrections using MAGIC IV (7) to k_0 - and k_f -values. The existence of H, C and O simultaneously in these specimens complicates the correction procedure since only one element is ascertained by difference and it is difficult to acquire reliable data for C and O. For these reasons, a "weighted average" correction was applied using known H, C and O compositions to obtain a final prediction

of Ca concentrations. The results are shown in Table 2. The initial count rates appear to best characterize these specimens with the worst predictions occurring for low Ca content specimens of low density.

The following observations are made regarding quantitation in mineralized tissues:

1. Ca and P determinations are elevated as a result of a changing light element portion of the excitation volume upon exposure to the electron beam. It is tempting to interpret the final stable counting conditions in terms of the inorganic fraction within the original matrix, but the presence of embedding plastic residues and heavier elements within the organic matrix confuse the results.
2. Since Ca and P undergo very similar variations in count rate, the resulting Ca/P ratio is comparatively constant. It should, therefore, be possible to predict Ca/P with $\sim 2-3\%$ accuracies.
3. The method of specimen preparation has a direct influence on quantitation. This fact should be taken into account when probe studies of mineralized tissues are contemplated.
4. When stable counting conditions exist, it is possible to predict Ca and P concentrations with accuracies of a few percent over wide ranges of concentrations and densities.

References

1. C. Andersen, Methods of Biochem. Anal., Vol. 15, D. Glick, Ed., Interscience, N.Y., 1967.
2. J. E. Wergedal and D. J. Baylink, Amer. J. of Physiology 22, No. 2, 1974.
3. T. A. Hall and B. L. Gupta, J. of Microscopy, Vol. 100, Pt. 2, 1974.
4. G. F. Bahr, F. B. Johnson and E. Zeitler, Lab. Invest. 14, 1965.
5. K. Stern and G. F. Bahr, J. Ultrastruct. Res. 31, 1970.
6. J. D. Termine, E. D. Eanes, D. J. Greenfield and M. U. Nylen, Calc. Tiss. Res. 12, 1973.
7. J. W. Colby, Advances in X-ray Analysis, 11, Plenum Press, N.Y., 1968.

TABLE 1

Rat Tooth Specimen and Method of Preparation

Specimen Number	Preparation Technique
1	Alcohol fixed, vacuum dried, embedded in methacrylate
2	Formalin fixed, dried at 100°C, embedded in methacrylate
3	Formalin fixed, dried at 100°C, embedded in methacrylate with rapid polymerization to limit penetration
4	Hydrazine deproteinization, alcohol dehydration, dried at 100°C, embedded in methacrylate
5	Hydrazine deproteinization, alcohol dehydration, dried at 100°C, embedded in Buehler epoxide

TABLE 2

Quantitation of Calcium-containing Compounds and Plastics

Specimen	Specific Gravity	Accepted Ca Wt.%	k _o Prediction of Ca Wt.%		k _f Prediction of Ca Wt.%	
			Uncorr.	Corr.	Uncorr.	Corr.
<u>Ca Standard:</u>						
Fluorapatite (FAP) [Ca ₁₀ (PO ₄) ₆ F ₂]	3.1	39.74	-	-	-	-
<u>Volatile Specimens:</u>						
Ca Acrylate (Ca-A) [(CH ₂ :CHCOO) ₂ Ca]	1.2	22.0	19.4	21.7*	22.5	25.2*
Ca Methacrylate (Ca-M) [(CH ₂ :C(CH ₃)COO) ₂ Ca]	1.1	19.1	18.1	21.3*	23.3	26.6*
Ca Stearate (Ca-S) [Ca(C ₁₈ H ₃₅ O ₂) ₂]	0.9	6.6	6.0	7.4*	7.3	9.0*
<u>Stable Specimens:</u>						
Monetite [CaHPO ₄]	2.8	29.5	28.9	28.8		
Whitlockite [Ca ₃ (PO ₄) ₂]	3.1	38.8	38.7	38.8		

* Uses weighted average correction for known H, C and O compositions.

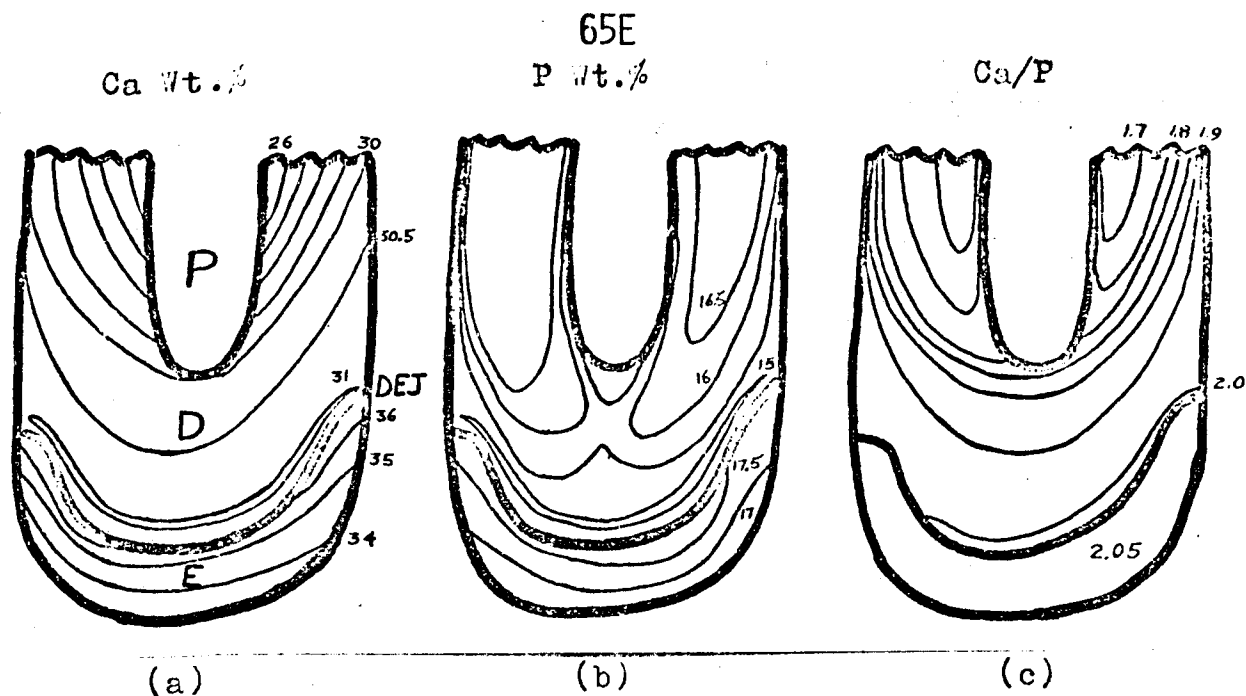


Fig. 1. Cross sections of developing rat incisor with pulp (P), dentine (D), dentinoenamel juncture (DEJ) and enamel (E) regions are shown. The uncorrected isoconcentration contours for (a) Ca weight percent and (b) P weight percent and level curves for (c) Ca/P are shown as determined by electron microprobe analysis.

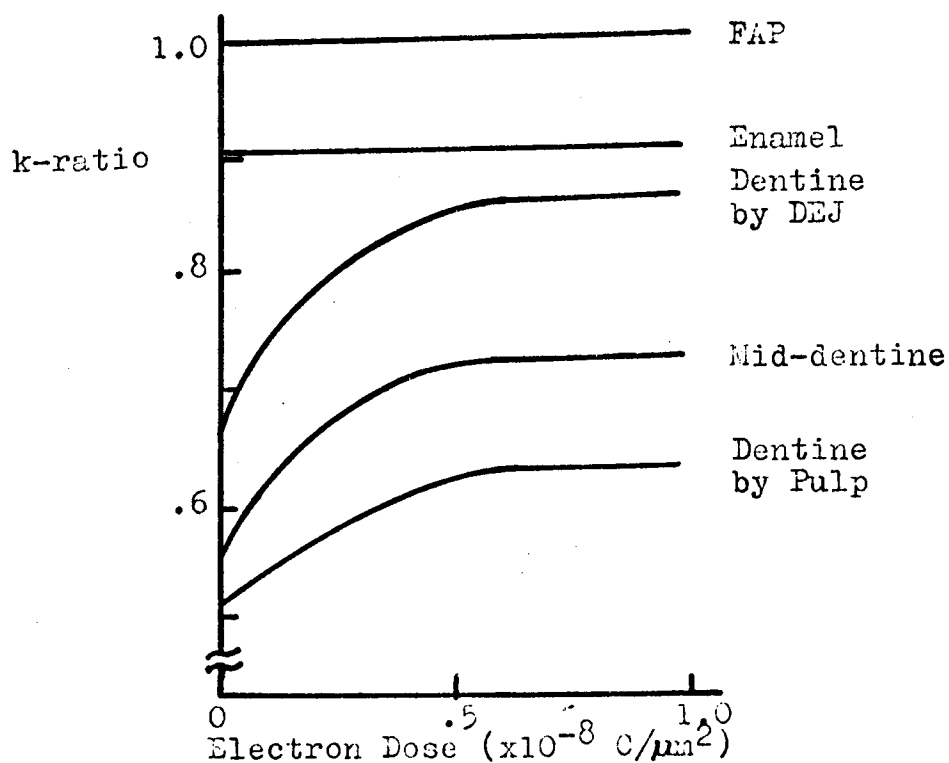


Fig. 2. The Ca k-ratio, using fluorapatite (FAP) as standard, is plotted as a function of electron dose for different regions from the pulp to enamel of a rat incisor.

Specimen

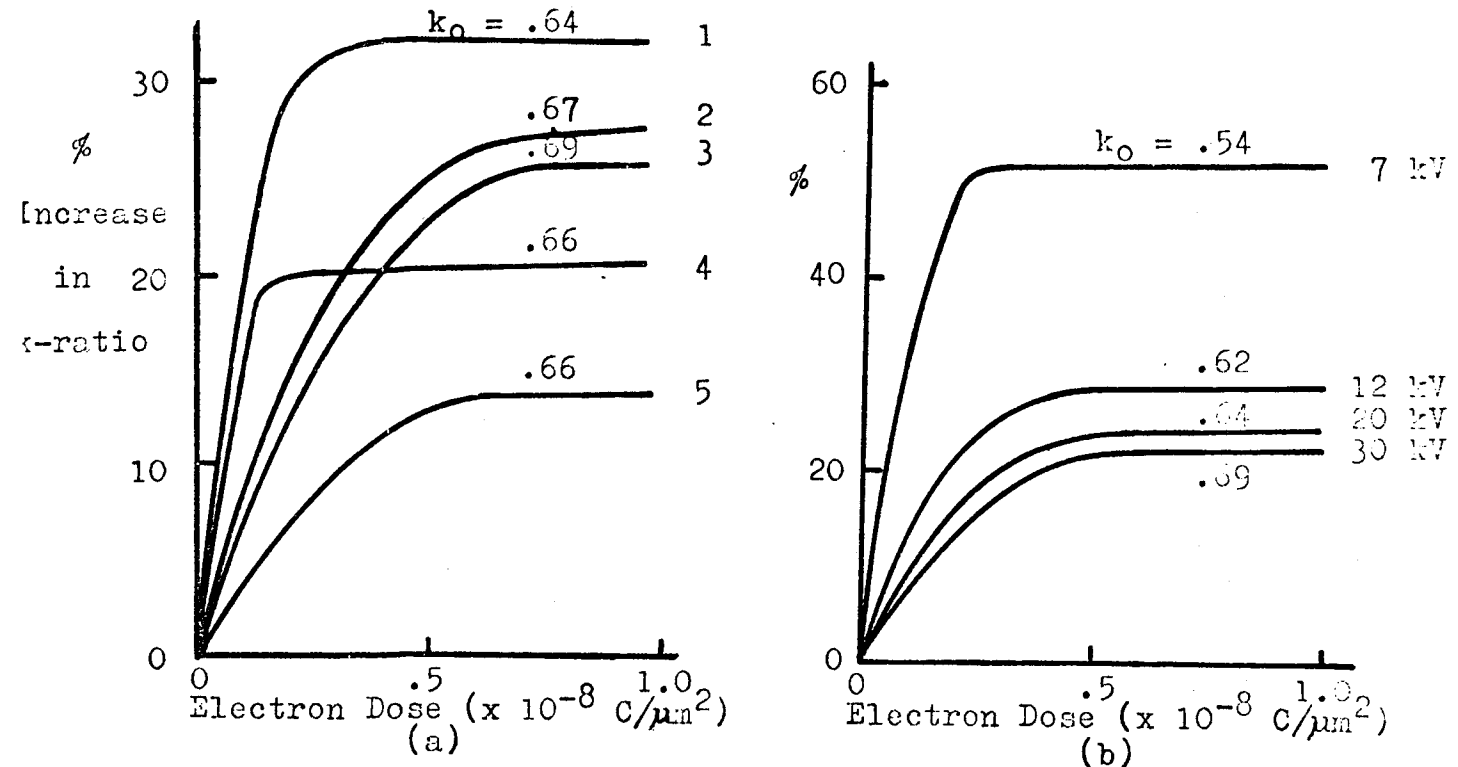


Fig. 3. The percentage increase in Ca k-ratios from initial values, k_0 , is plotted as a function of electron dose for analyses on (a) the same dentine area of rat incisors undergoing different specimen preparations (see Table 1) and (b) the same dentine area of a rat incisor for different accelerating voltages.

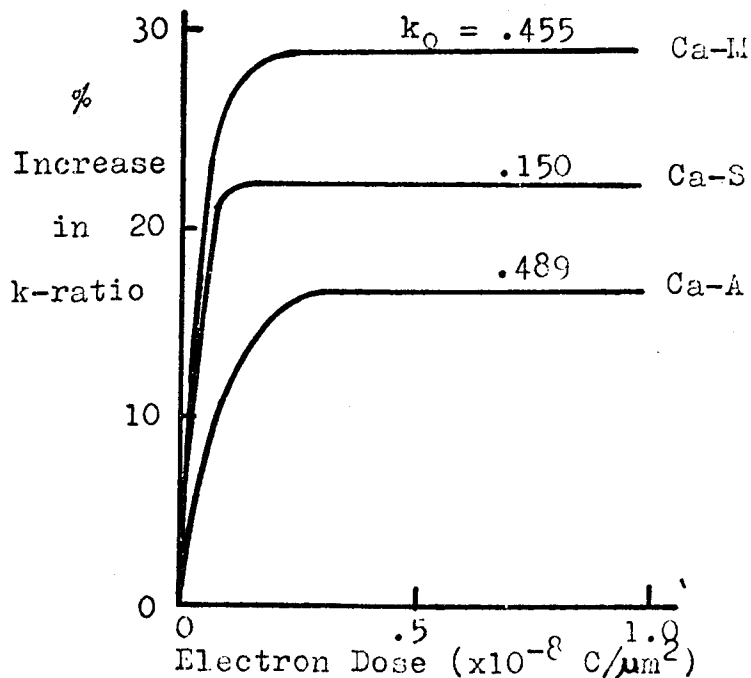


Fig. 4. The percentage increase in Ca k-ratios from initial values, k_0 , is plotted as a function of electron dose for analyses on different Ca-containing compounds and plastics (see Table 2).

AN ULTRA-HIGH VACUUM SEM FOR MICROANALYSIS OF ULTRASTRUCTURE OF THIN SPECIMENS

Lloyd V. Sutfin
Department of Orthopaedic Surgery
Harvard Medical School
Children's Hospital Medical Center
Boston, Massachusetts 02115

Perhaps one of the greatest impediments to the acceptance of the electron probe microanalysis as a tool for biological research was the inability of standard instruments to analyze at the ultrastructural level. That microanalysis of purposely selected individual structures only a few hundred angstroms in dimension is practical was demonstrated several years ago (1). The physical principles involved in making such analyses have also been discussed (2) and instrumentation for performing high spatial resolution microanalysis was described at this meeting in 1973 and earlier (3,4). Currently many options are open to investigators wishing to employ this mode of analysis. These are generally based on transmission microscopes which can be readily converted to scanning electron microscopes or SEMs with transmitted electron detectors, and usually rely on non-dispersive solid state x-ray detectors. Even though equipment is readily available, there are several major hurdles to overcome in applying the technique. Although specimen preparation without chemical change (translocation) and obtaining chemical information from x-ray count spectra are the most demanding and important problems in the long run, the one thing that has stopped all investigators in this field from making point analyses is electron beam induced contamination (3,5,6). The instrument to be described was developed to meet specifications which would minimize and hopefully eliminate this major roadblock to progress.

In order to provide an electron beam instrument which was inherently contamination free, specifications were prepared for a JEOL JSM-50A modified to provide contamination free ultra-high vacuum in the specimen chamber. The essential performance specs were a vacuum of better than 5×10^{-8} torr measured at a point in the specimen chamber which is a greater distance from the pump than the specimen and that a focussed stationary electron beam of 10^{-11} amps could be positioned on a collodian film for a period of 15 minutes without

evidence of contamination.

If there is a moral to this story it is that it is not just what you have but how you use it that determines success in eliminating contamination in a scanning microscope. For the initial result was that in spite of the complete absence of mechanical and diffusion pumps, specimen contamination was no better in this microscope when first assembled than in a microscope with the usual vacuum system. High contamination rates persisted even though a vacuum level of 5×10^{-8} torr in the specimen chamber was attained. This was due to the fact that initial assembly was performed with the following deficiencies which nullified the inherent capabilities of the ultra-high vacuum system:

1. High vacuum techniques for preparing surfaces and handling components were not followed.
2. Improper material had been used in construction.
3. Hydrocarbon base vacuum grease had been used excessively on static seals.

The vacuum system of this microscope utilizes no mechanical pump. Cryosorption pumps perform the roughing of the specimen chamber, gun chamber, and specimen insertion airlock. Two triode Varian VacIon pump modules perform the final evacuation of the gun chamber. The pump for the specimen chamber consists of 4 triode Varian VacIon modules mounted on a cylinder concentric with a cylindrical cryopanel which in turn surrounds a titanium sublimation pump. The inner surface of the cryopanel serves as the active surface of the sublimation pump.

After rebuilding and final assembly the vacuum performance is as follows. Use of the ion pumps and sublimation pump alone produce a vacuum level of 5×10^{-8} torr in the specimen chamber. The addition of cryopumping further reduces the pressure to below 2×10^{-8} torr. To obtain these vacuum levels and reduce the specimen contamination it was not necessary to improve or change in any way the basic vacuum design. It proved to be adequate. But it was necessary to correct the deficiencies listed above. This was accomplished by eliminating all brass, chemically cleaning and polishing all copper surfaces, using single strand wire with teflon insulation where electrical isolation was necessary, replacing the standard polymethyl-methacrylate light pipes with quartz light pipes, baking all phosphor coated surfaces to

eliminate organic carriers, relieving all screw threads and heads with grooves to reduce gas entrapment, cleaning all surfaces with freon degreaser followed by a methanol rinse, vacuum baking all O-rings before assembly and using silicon vacuum grease very sparingly on any sliding seals. Plastic gloves and degreased tools were used whenever internal parts were handled (7).

The assembled electron optical column is shown in Figure 1 and the results of the contamination test are shown in Figure 2. In order to obtain a contamination rate as low as that demonstrated in Figure 2 it was necessary to prepare a clean collodian film and subject this film to low energy electron bombardment for an extended period in the microscope. This procedure probably either volatilized through heating or immobilized through crosslinking contaminants in the specimen. This performance demonstrates that an inherently clean vacuum system is only a partial solution to the specimen contamination problem because contaminants on the surface of the specimen or which may be released by degradation of the specimen also cause a build-up of material at the point where the electron beam strikes. This has been found to be true even at vacuums as good as 10^{-10} torr (8). Even though a clean ultra-high vacuum only eliminates one component of specimen contamination the absence of this component makes the evaluation of specimen handling techniques possible. It makes sense that everything in the ultra-high vacuum chamber must be prepared following high vacuum technique standards including that which is closest to the point of analysis, the specimen itself. Heating within the vacuum chamber (8) and electron bombardment have been shown to improve the cleanliness of the specimen. Perhaps cooling to very low temperatures will immobilize surface contaminants and reduce specimen degradation thus preventing contamination build-up during microanalysis.

Regarding the other aspects of performance, this instrument produces excellent scanning transmission and secondary electron micrographs but achieves only the standard level of resolution. Working time is greatly increased because of the low contamination rate. The selection and microanalysis of ultrastructural features can be performed readily. Even without special handling of the specimen the contamination is much less of a problem in this microscope than in any other the author has observed and is an improvement over gas-jet decontamination used previously (1,2,3). Other advantages of the ultra-high vacuum are negligible contamination of electron optical apertures and greatly extended filament life.

REFERENCES

1. Sutfin, L.V., Holtrop, M.E., and Ogilvie, R.E. Microanalysis of individual mitochondrial granules with diameters less than 1000 Å. Science 174: 947-949, 1971.
2. Sutfin, L. High spatial resolution x-ray microanalysis in the scanning electron microscope. Proc. 5th Ann. Symp. on Scanning Electron Microscope. Chicago: IIT Research Inst., 1972. p 65-72.
3. Sutfin, L.V. Electron probe analysis of subcellular structures in biological tissues. Proc. 8th Natl. Conf. on Electron Probe Analysis, 1973. p 59A-59E.
4. Sutfin, L.V., and Ogilvie, R.E. A comparison of x-ray analytical techniques available for scanning electron microscopes. In: Scanning Electron Microscopy, O. Jahari, Ed. IITRI, Chicago, 1970.
5. Thurston, E.L., and Russ, J.C. Scanning and transmission electron microscopy and microanalysis of structural granules in Fischerella ambigua. In: Scanning Electron Microscopy, O. Jahari, Ed. IITRI, Chicago, 1971. p 511-516.
6. Shuman, H., and Somlyo, A.P. Quantitative electron probe analysis of ultra-thin biological sections. Proc. 10th Ann. Conf. Microbeam Analysis Society, Las Vegas, Nevada, 1975. p 41A-41E.
7. The author wishes to acknowledge the advice and assistance of Dr. W.R. Bottoms, Princeton University, rendered in the analysis and correction of problems encountered after initial assembly. For more information see: Bottoms, W.R. Contamination in the SEM. In: Scanning Electron Microscopy, O. Jahari, Ed. IITRI, Chicago, 1973. p 182-188.
8. Isaacson, M., Langmore, J., Wall, J. The preparation and observation of biological specimens for the high resolution scanning transmission microscope. In: Scanning Electron Microscopy, O. Jahari, Ed. IITRI, Chicago, 1974. p 20-26.
9. The performance of this microscope is a tribute to the plodding doggedness of the management, engineers and technicians of JEOL (USA) and the pig-headedness of the author.

This work was supported by The John A. Hartford Foundation and by the National Institutes of Health Grants AM 15671 and HL14322.

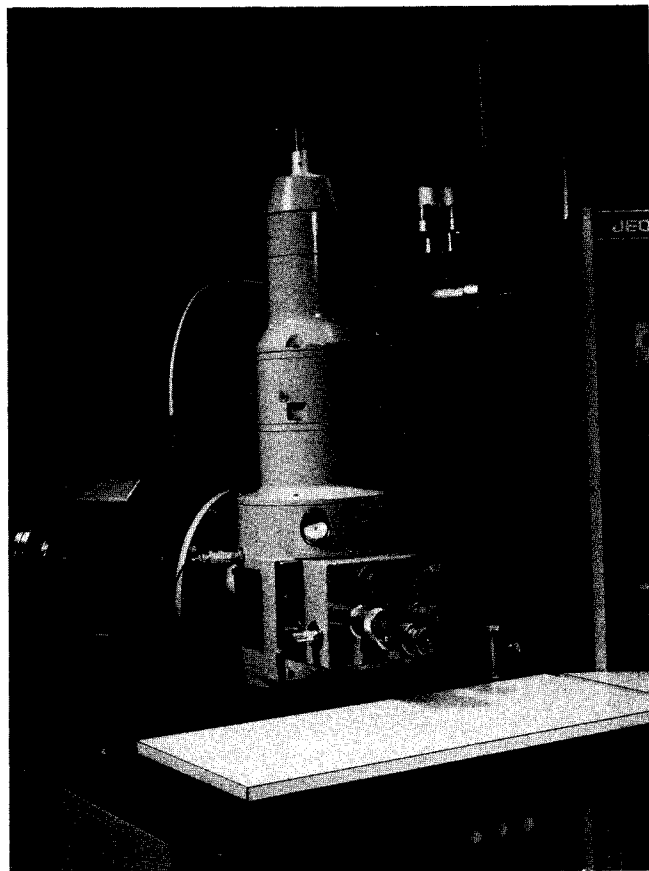


Figure 1. Vacuum pumps mated to electron optical column of JEOL-50A. X-ray detector has been removed.

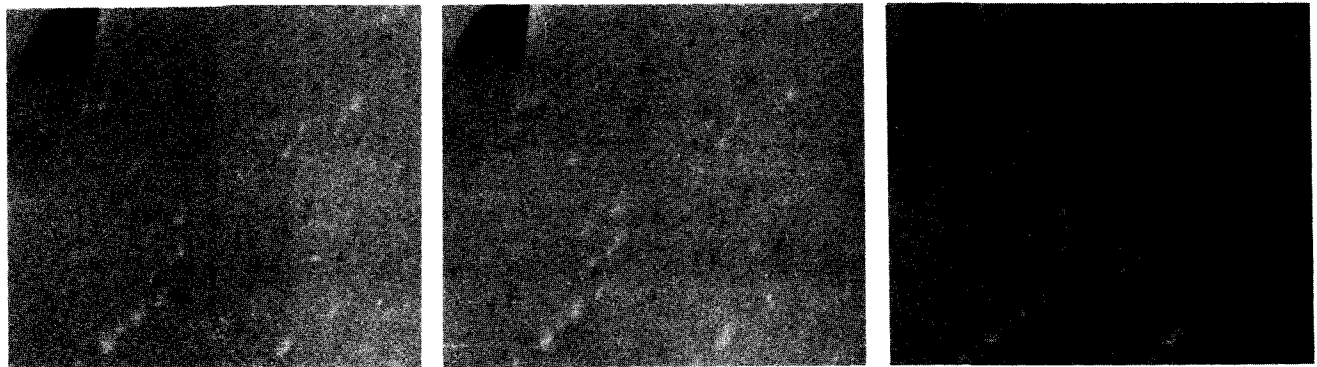


Figure 2. Results of a contamination test. Micrographs were taken in the scanning transmission mode. A stationary electron beam of 10^{-11} amps was focussed on the collodian film and was interrupted at 5 minute intervals to observe contamination. A contamination spot became barely visible at 20 minutes and was distinct but still very small at 25 minutes. The 0, 15, and 25 minute exposures are shown here from right to left respectively. The drift rate (image shift) was 0.5 angstroms/second, observations were made at 30,000 magnifications and the test was conducted at 20 KV. Bar is $\frac{1}{2}$ μ m.

MICROPROBE AUTOMATION
PAST, PRESENT AND FUTURE

W. T. Hatfield

General Electric Company
Corporate Research and Development
P.O. Box 8
Schenectady, New York 12301

By following the evolution of hardware and software for microprobe automation, it is possible to see how advancing technology has brought about the sophisticated systems in use today. Minicomputers now control a wide variety of instrument functions (Table 2) and in some cases control several different instruments on a real-time basis. Development of the microprocessor and other large scale integrated devices are certain to have a dramatic effect on future developments in microprobe automation.

First attempts at microprobe automation reported in 1966 were limited to the use of a hard-wired controller to move the specimen stage and log intensity data on paper tape for later processing on a large computer (Table 1). During the next few years this approach was extended to the development of more sophisticated systems capable of exciting a sequence of commands read from paper tape, such as moving the stage, presetting a timer/scalar, setting of a P.H.A. window, or positioning a crystal. When a number of reliable minicomputers became available in the late 1960's, hard-wired controllers were gradually replaced. Initially they were programmed in assembly language and were usually limited to qualitative analysis or controlled data acquisition for quantitative analysis programs run on larger computers.

A major breakthrough came when Modular hardware using NIM or CAMAC standards became available along with higher level interpretative languages such as BASIC, FOCAL, and CLASS which could be used with minicomputers. These tools made it possible for the noncomputer expert to put a microprobe automation system together and program it to perform a variety of analyses. Systems were

then built which more completely controlled the microprobe and in some cases were used to reduce data by means of chained versions of larger quantitative analysis programs. As more instruments were automated, quantitative analysis programs were re-written to run on minicomputers thus making truly on-line quantitative analysis possible. As systems became more sophisticated compiler level languages such as FORTRAN were used for instrument control as well as data reduction.

In parallel with the efforts towards microprobe automation, there was a great interest in developing programs for quantitative analysis. Beamen evaluated forty such programs written between 1963 and 1970⁽⁴³⁾. Initially programming was done in FORTRAN or ALGOL and later in BASIC and APL. Several of the later programs were written to use less core storage making them useful in minicomputers. Other programs were written after 1970, but of all the programs written, only a few have gained wide acceptance due to their ready availability and ease of use. Some of these are used directly on minicomputers employing FORTRAN compilers or have been re-written in one of the interpretative languages⁽¹⁶⁾.

With the cost of microprocessors coming down at such a rapid rate and hardware and software support increasing at an equally rapid rate, it is inevitable that they will play a major role in microprobe automation. Many of the initial interfacing problems have been solved by the introduction of LSI chips specifically designed to interface microprocessors with the outside world^(44,45). In addition higher level languages have been developed specifically for use with microprocessors and already existing languages such as BASIC, APL and FORTRAN have been adapted for microprocessor use. These tools should make automation systems available at greatly reduced cost. So-called "smart terminals" are already available and are easily interfaced to microprobes.⁽⁴²⁾ It is also quite possible that microprocessors will be incorporated as functional units within microprobes (scanning and display, beam control, lens control, HV and filament current control, etc.) (Table 3).

TABLE 1

- 1966 - Hard-wired controllers used to step specimen stage and log data.⁽¹⁾
- "Control cubicles" used to control specimen stage, PHA window settings, counting time commands read sequentially from paper tape.⁽²⁾
- 1967 - Mini-computers used to control specimen stage, beam position, position crystals and set timer scalar.
- Interfacial with potentiometers, relays, ADC and DAC's.^(3,4)
- 1969 - Mini-computer automation systems coupled to large time-sharing computers for data processing.
- Interpretative languages used to program mini-computers for microprobe automation.^(5,6,7)
- 1970 - Mini-computer systems using modular electronics to interface microprobes. Programming in FOCAL AND CLASS, chained quantitative analysis programs.
- Mini-computer used as MCA for processing of MCA Spectra.^(8,9,10,11,12)
- 1971 - Quantitative analysis programs written for use with mini-computers. Introduction of more sophisticated operating systems and computer level language (FORTRAN) for microprobe control programs.^(13, 14, 15, 17, 18)
- 1973 - Extensive use of higher level operating systems (disk based, time shared).
- 1974 - Use of real-time cooperating system and functional control electronics to control several different instruments simultaneously.
- Extensive use of both interpretative and compiler level languages for both machine control and data reduction^(27,35,38)
- 1976

TABLE 2

Some functions which are presently controlled by various Microprobe Automation Systems.

- | | |
|---|---|
| 1. Stage | - in x, y and z directions |
| 2. Beam Positioning | - in x and y; digital scanning systems |
| 3. Filament Current & H.V. power supplies | - Automatic setting of acc. potential;
Automatic filament saturation |
| 4. Crystal Spectrometers | - Automatic selection and positioning of crystals. |
| 5. Timer/scalars | - Preset time; preset counts; read-out of scalars. |
| 6. Beam Monitor | - Insertion and retraction of monitor/stop; monitor of beam current. |
| 7. Multi-channel Analyzer | - Controlled collection and readout of data; use of computer memory for data acquisition. |

TABLE 3

Functions which might be controlled by a Microprocessor.

- | | |
|------------------------|---|
| Computer and Interface | - Microprocessor control system may be used to interface directly to the microprobe by passing modular type interfacing hardware. |
| Beam Position Control | - Digital scanning and beam position. |
| Beam Current Control | - Realignment of beam using electronic beam shift combined with lens control to maintain constant beam current. |
| Contrast | - Auto adjust of brightness and contrast levels to maintain optimum micrograph. |
| Crystal Spectrometer | - Automatic selection and peaking. |

REFERENCES

1. "An Automated Method for the Collection and Analysis of Microbeam Probe Data," E. Lifshin and R.E. Hanneman, Proc. First National Conference on Electron Probe Microanalysis, College Park, MD (1966).
2. "Progress in Fully Automatic Scanning Electron Probe Microanalysis," A.W. Browning, D.J. Cooknell, K. Heathcote, I.K. Openshaw, J.L. Williams and P.W. Wright, Proc. Second National Conference on Electron Microprobe Analysis, Boston, Mass. (1967)
3. "A Computer-Operated Microprobe," M.A. Bayard, Proc. Fourth National Conference on Electron Microprobe Analysis, Pasadena, Calif., (1969).
4. "A Small Computerized On-Line Data Gathering System for the Electron Microprobe," F.D. Ingram, Proc. Fourth National Conference on Electron Microprobe Analysis, Pasadena, Calif. (1969).
5. "MANIP: A Computer Program for Processing X-ray Intensity Data on Punched Paper Tape From the Electron Probe Microanalyzer," G.L. Fisher and W.G. Wickersty, Jr., Proc. Fourth National Conference on Electron Microprobe Analysis, Pasadena, Calif. (1969).
6. "Automatic Stepping System for Carbon Analysis," J.S. Duerr, J. Adario, R.E. Ogilvie, Proc. Fourth National Conference on Electron Microprobe Analysis, Pasadena, Calif., (1969).
7. "Computer Controlled Scanning Electron Microprobe," D. Yaukovich, R.E. Ogilvie, R.E. Warren, Proc. Fourth National Conference on Electron Microprobe Analysis, Pasadena, Calif. (1969).
8. "Computer Processing of Solid State X-ray Detector Data," E. Lifshin, Proc. Fifth National Conference on Electron Probe Analysis, New York, New York (1970).
9. "Time Sharing Computer Programs for Data Processing and Corrections in Microprobe Analysis," F. Borli, Fifth National Conference on Electron Probe Analysis, New York, New York, (1970).
10. "An Automated Electron Microprobe Analyzer," E. Eichen and F. Kunz, Proc. Fifth National Conference on Electron Probe Analysis, New York, New York (1970).

11. "Computerized Electron Microprobe," R. Wolf and A.J. Saffir, Proc. Fifth National Conference on Electron Probe Analysis, New York, New York (1970).
12. "A Computer Assisted Microprobe Laboratory," W.F. Chambers, Proc. Fifth National Conference on Electron Probe Analysis, New York, New York (1970).
13. "LRL Computer Program: Microanalysis," W.J. Steele, Proc. Sixth National Conference on Electron Probe Analysis, Pittsburgh, Pennsylvania (1971).
14. "Storage and Treatment of Energy-Dispersive X-ray Data by Time Shared Computer," J.M. Short and J.F. Stephany, Proc. Sixth National Conference on Electron Probe Analysis, Pittsburgh, Pennsylvania (1971).
15. "Quantative Microprobe Analysis and Data Reduction Using an On-line Mini-computer," A.A. Chodos and A.L. Albee, Proc. Sixth National Conference on Electron Probe Analysis, Pittsburgh, Pennsylvania (1971).
16. "Magic IV-A New Improved Version of Magic," J.W. Colby, Proc. Sixth National Conference on Electron Probe Analysis, Pittsburgh, Pennsylvania (1971).
17. "Electron Microprobe Automation," F. Kunz, E. Eichen, G. Matthews, S. Piner, Proc. Sixth National Conference on Electron Probe Analysis, Pittsburgh, Pennsylvania (1971).
18. "An Automated Microprobe Under PDP-8 Control Using an IBM 360/65 for Program and Data Storage," T.D. Kirkendall and P.F. Varadi, Proc. Sixth National Conference on Electron Probe Analysis, Pittsburgh, Pennsylvania (1971).
19. "Electron Microprobe Automation: X-ray Peak Location," F. Kunz and E. Eichen, Proc. Seventh National Conference on Electron Probe Analysis, San Francisco, Ca. (1972).
20. "An Automated Electron Microprobe System," F. Kunz, E. Eichen, G. Mathews and J. Francis, Advances in X-ray Analysis, Vol. 15, (1972).
21. "An Automated Crystal Spectrometer System for Qualitative Microprobe Analysis," E. Lifshin, Proc. Seventh National Conference on Electron Probe Analysis, San Francisco, CA (1972).
22. "Expanded Wavelength Coverage With Digitally Controlled X-ray Spectrometers," E. Davidson, A.J. Hartwick, J.M. Taylor, Proc. Fifth National Conference on Electron Probe Analysis, New York, New York (1970).

23. "Microprobe Analysis Integrated Automation Computer System," J.W. Colby, Proc. Seventh National Conference on Electron Probe Analysis, San Francisco (1972).
24. "Computer Automation of an Electron Microprobe," L.W. Finger and C. Haclidiacos, Proc. Seventh National Conference on Electron Probe Analysis, San Francisco, CA (1972).
25. "The Program Cyclops for the Quantitative Analysis of Electron Microprobe X-ray Data," H.R. Thresl and T.E. Keller, Proc. Seventh National Conference on Electron Probe Analysis, San Francisco, CA (1972).
26. "The Sandia Approach to Electron Probe Automation," W.F. Chambers, Proc. Eighth National Conference on Electron Probe Analysis, New Orleans, Louisiana (1973).
27. "Time-Shared Computer Control of Electron Microprobe and X-ray Diffraction Equipment," W. Holzwarth, E. Quigg and C.T. Prewitt, Proc. Eighth National Conference on Electron Probe Analysis, New Orleans, Louisiana (1973).
28. "Practical Aspects of Microprobe Automation," W.B. Estill and D.E. Benthusen, Proc. Eighth National Conference on Electron Probe Analysis, New Orleans, Louisiana (1973).
29. "On-Line Microprobe Analysis With a Hosted IBM System/7 Computer," D.F. Kyser, G.L. Ayers, D.E. Horne, Proc. Eighth National Conference on Electron Probe Analysis, New Orleans, Louisiana (1973).
30. "Optimization of Computer-controlled Quantitative Analysis of Minerals," A.A. Chodos, A.L. Albu, A.J. Gancarz and J. Laird, Proc. Eighth National Conference on Electron Probe Analysis, New Orleans, Louisiana (1973).
31. "A CAMAC Automated Electron Microprobe," W.T. Kane, Proc. Ninth Annual Conference of the Microbeam Analysis Society, Ottawa, Canada (1974).
32. "Applications With a Computer-Controlled Electron Probe Micro-analyzer System," S. Ohudera, H. Ohyi, and Y. Harada, Proc. Ninth Annual Conference of the Microbeam Analysis Society, Ottawa, Canada (1974).

33. "Automation of An Electron Probe for Biological Analysis," T. Moher, C.M. Aden, R. Beeuwkes, A. Sanderson and C. Lechene, Proc. Ninth Annual Conference of the Microbeam Analysis Society Ottawa, Canada (1974).
34. "Data Reduction System for Electron Probe Microanalysis," E.D. Glover, Proc. Ninth Annual Conference of the Microbeam Analysis Society, Ottawa, Canada (1974).
35. "A Real Time Approach to Laboratory Automation," W.T. Hatfield, M.F. Ciccarelli, R.B. Bolon and E. Lifshin, Proc. Ninth Annual Conference of the Microbeam Analysis Society, Ottawa, Canada (1974).
36. "Practical Applications of Automated Microprobe Analysis," W.T. Hatfield, R.B. Bolon and E. Lifshin, Proc. Tenth Annual Conference of the Microbeam Analysis Society, Las Vegas, NA (1975).
37. "Automated Characterization of Particulates and Inclusions by Computer-Controlled SEM/Probe," M.R. Hoover, E.W. White, J. Lebieczik, G.G. Johnson, Proc. Tenth Annual Conference of the Microbeam Analysis Society, Las Vegas, NA (1975).
38. "A Minicomputer Based Multi-Instrument Automation System," E.M. Butler and A.K. Agrawal, Proc. Tenth Annual Conference of the Microbeam Analysis Society, Las Vegas, NA (1975).
39. "Experimental APL Programming for Quantitative Electron Microprobe Analysis," H.R. MacQueen and R. Lasky, Proc. Tenth Annual Conference of the Microbeam Analysis Society, Ottawa, Canada (1975).
40. "FRAME: An On-Line Correction Procedure for Quantitative Electron Probe Microanalysis," H. Yakowitz, R.L. Myklebust and K.F.J. Heinrich, Nat. Bur. Stand. Tech. Note 796, U.S. Government Printing Office (October 1973).
41. "A Rigorous Correction Procedure for Quantitative Electron Probe Microanalysis (COR2)," J. Henoc, K.F.J. Heinrich and R.L. Myklebast, U.S. Nat. Bur. Stand. Tech. Note 769, U.S. Government Printing Office (August 1973).
42. "MAD: A Data System for Instrumental Analysis, Research/Development pp40-44 (March 1976).

43. "Electron Beam Analysis,: D.R. Beaman and J.A. Isasi, ASTM Special Technical Publication 506, American Society for Testing and Materials (1972).
44. "Soft patching: One Future for Analytical Instrument Interfacing," P.R. Rony and D.G. Larsen, Proc. The Twenty-Seventh Pittsburgh Conference on Analytical Chemistry and Applied Spectroscopy, Cleveland, Ohio (1976).
45. "Universal Asynchronous Receiver Transmitter (UART): Operation and Applications in a Laboratory Enviroment," G.L Brezler, Proc. The Twenty-Seventh Pittsburgh Conference on Analytical Chemistry and Applied Spectroscopy, Cleveland, Ohio (1976).

Computer Applications to Multiple User Microprobe Systems

G.G. Yagunoff, T.A. Baillieul, W.A. Ranson, Dept. of Geology and Geography,
University of Massachusetts, Amherst, MA 01002

With the growing interest in the electronmicroprobe as an analytical instrument in geology and crystal chemistry, the need for versatile automation and computer assistance to the user has become obvious. We have determined several criteria in our system of user aids. They must be simple so that only a minimum amount of training is required to allow a scientist to pursue his investigation without undue concern with the technology involved, yet be flexible enough to allow sophisticated corrections and ratios to be determined on line during actual analysis; and finally, it must be capable of rapid changes in standards to provide for oxide, silicate, and even pure element analysis on a given sample with a minimum time expended in changing programs and restandardizing.

The demand for time on the instrument has also warranted a limitation of use to actual analyzing. This consideration has generated a number of peripheral programs to enhance the utility of the microprobe and aid the operator prior to the time actually in contact with the instrument as well as after his analyses are completed.

This abstract will discuss both the philosophy of the programs used to control the microprobe and the actual peripheral programs needed to prepare the operator for using the instrument as well as perform additional post-analytic operations to present the data acquired in the most useful form to the researcher.

Control Programs

The choice of computer language and type of control system is exceptionally important. As supplied by ETEC our system utilized an interactive BASIC compiler which we consider one of the best choices. First, BASIC is an easily understood language and is related to a number of other first generation high level computer languages (e.g. FORTRAN and PL1). Second, an interactive system provides the user with the ability to modify both the program and its parameters during actual operation without an extensive knowledge of computers or programming.

The control program may be further modified to make the actual control functions of the computer transparent to the user so that the BASIC program need only concern itself with calculations and data presentation. A large number of machine language subprograms have been used to implement this philosophy and these have resulted in two major benefits: the user program has been simplified and made more efficient by using the machine code instead of the interactive BASIC statements.

The addition of a fast, random-access, bulk-storage device, such as a disk, provides an additional degree of freedom to the system. We feel that this is a necessary expenditure to assure maximum utility in the system. The disk system provides nearly unlimited storage capability for constants used in the correction routines, accumulated data, and additional data reduction routines. In conjunction with an overlay system, which provides a simplified method for exchanging both the program and the data, the disk oriented system provides extreme flexibility to the instrument.

As an example of this flexibility, we are able to standardize both an oxide analyzing routine and a sulfide routine and interlace analysis with single commands. This gives the investigator the ability to analyze his entire sample in a single day and, thereby, provide conclusive results without long delays.

Peripheral Programs

Many tasks including standard selection and system optimization as well as post analysis data reduction and display can be handled on a separate computer facility. We have found that this type of computer assistance in standard choice and system optimization is a great aid to the users of our facility. The ever growing number of available standards can easily be searched with a simple BASIC program to provide the operators with a small subset of viable standards for their research projects. The program also contains data on spectrometer, crystal, and detector which provides the operator with a selection of spectrometer combinations which are both optimized for collection efficiency and speed during the analysis. The objective of this system is to provide the user with the maximum useful information without overwhelming him with unnecessary data. The system contains two large data files with entries for all the standards in use as the operating parameters of the spectrometers. An easily implemented program first examines the contents of the files and compares the parameters of the standard sought with those of the accessible standards. All entries in the file that meet the parameters requested are printed in a list which includes all the significant data on the particular element and standard. An appropriate standard may then be selected from the list and the search continued. Upon completion

of the search the operator may request a listing of the spectrometer and analyzing crystal data associated with the chosen elements and the preparation of a tape suitable for input to the microprobe computer system.

In devising such a system we considered the essential parameters for categorizing our standards which would be sufficiently concise to fit on one printed line of 72 characters. The following nine categories were chosen as most useful.

1. Standard number. This is either an arbitrary number of a special code number. It is used basically to tie the computer file entry to a complete listing which contains the detailed chemical analysis, source and other pertinent information.
2. Mount type. The type of mount in which the standard is housed (or is designed to fit) can be critical in standard selection. Some standards may require a special mount for placement on the microprobe stage. A simple alphabetical code may be used to designate the type of mount in the file.
3. Element. The most important entry in the file is the element sought. Standard abbreviations are sufficient. Special valencies can be designated by a numeric suffix. (.e.g. ferrous iron = FE, ferric iron = FE3).
4. Weight percent. In the case of oxides, phosphates, carbonates, and silicates, this category represents the analyzed weight percent of the oxide of the element in question. For pure metals and sulfides this entry would take whatever form the analysis was reported in. Two decimal places are sufficient for accuracy.
5. Standard type. This parameter describes the standard's matrix; it can be a silicate (SIL), an oxide (OXI), a sulfide (SUL), carbonate (CAR), or a metal (MET). Standards chosen should closely approximate the type of mineral being analyzed.

6. Beta factor. A self-explanatory item; this number is usually reported to 3 decimal places.
7. Mineral name. To avoid confusion caused by abbreviated code names, the name of the actual mineral species is used.
8. Standard name. This is the simplified code name for the standard that is used by the microprobe operating program.
9. Comments. This miscellaneous category is useful for printing warnings about chemical inhomogeneity, uncertain beta factors, or other complications.

Any of the first eight parameters may be selected either separately or in groups to provide a basis for the file search. As can be seen from the flow-chart (Fig. 1) the search program is conceptually simple. It matches the chosen parameters with the file entries and outputs all matches. It then stores the operator choice if more than one entry per element matches and produces a tape for input to the microprobe system. A similar program is used to select the desired spectrometers.

Since initial results of mineral analyses obtained from the microprobe are often in need of further manipulation, such as ferric iron adjustments, frequently desired in analysis of pyroxenes, amphiboles, garnets, and spinel group minerals, the user may program the microprobe computer to rapidly perform the arithmetic manipulations involved in the process or may choose an additional output which is compatible with direct input into the University time sharing system.

The availability of this additional output has prompted a number of faculty and students to write programs to further manipulate the data. Plotting routines, mineral identification, and hydrous correction routines, are some of the programs which have been developed and are available.

This paper is presented in the hope that it may serve as a guideline for the software requirements for a microprobe system in an academic environment which must service diverse interests and research projects. It presents several basic suggestions and the concepts behind a number of programs in use at the University of Massachusetts.

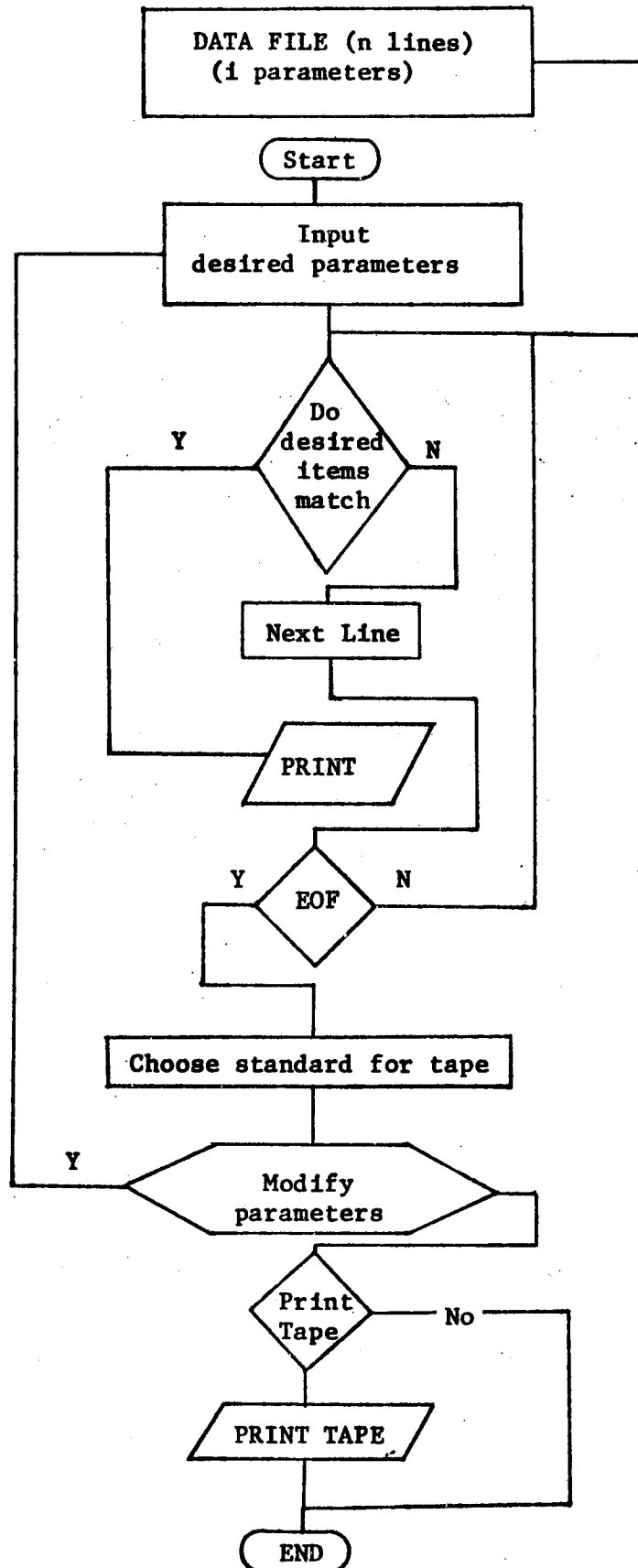


Figure 1. Flow-chart of search program.

A PROGRAMMABLE EPMA CONTROLLER USING A MICRO-PROCESSOR

M. FUJISAWA , K. HIRATA

JEOL LTD.

1418, Nakagami-cho, Akishima, Tokyo, JAPAN

Elemental analysis with an EPMA requires very complicated process and data correction. Thus, analytical accuracy is very much dependent upon the skill of the operator. Even so, the element of human error is always present. The introduction of computer control techniques, while eliminating the human error factor, presents another problem in that the operator must be able to operate the computer competently, a necessity requiring time and effort.



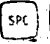
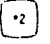
By incorporating a micro-processor (MICRO-PM), however, computer control can be effected very easily. All that is required is the ability to push keys on an operation key board in the same fashion as with an everyday, run-of-the-mill desktop calculator. Fig.1 shows the MICRO-PM (left side cabinet) combined with the JXA-50A electronprobe X-ray microanalyzer.

As shown in Fig.2, the MICRO-PM can control the movement of the specimen stage along the X,Y and Z axes, the crystal position of up to four spectrometers, crystal exchange devices, a timer, up to four counters, up to four PHAs (Pulse Height Analyzer) and an A-D converter for absorbed current measurement.

Fig.3 shows the operation key board. Ten basic functions are provided; viz., crystal position setting (), spectrometer scanning (), automatic peak searching and peak measurement (), automatic background measurement (), crystal exchange (), specimen position setting (), line analysis () , automatic Z-axis focusing () , absorbed current measurement () and X-ray intensity measurement (). An additional five function can be incorporated featuring thru .

These include PHA base line setting, PHA window scanning, high speed qualitative analysis, etc.

The specimen stage and spectrometers are controlled simultaneously in order to save time. However, the salient feature of the MICRO-PM is its programmability. That is to say, the measuring sequence incorporating the above functions can be programmed up to 255 steps simply by pushing keys.

The MICRO-PM has 36 memory sets and each memory set is comprised of three 6-digit memories. These memory sets are used for presetting the spectrometer channel number, crystal position, P-B distance, for example, or for presetting the position of the standard or unknown specimen. Once presetting is complete, the operator can designate the element to be measured with keys  ,  , etc.

The contents of the memory sets and the various step constituting the program can be recorded on and reloaded from a handy sized magnetic card back into the memory sets. The measured data is printed out by a built-in mini-printer, and, if necessary, can be punched out on paper tape in the ASCII code by incorporating a paper tape puncher. The incorporation of a paper tape puncher means that the punched output can be used for off-line data processing in conjunction with another computer.

Fig.4 and 5 show examples of measurement; viz., peak and background intensities for iron and chromium in stainless steel and qualitative analysis by the high speed qualitative analysis function.

The micro-processor used is 8080 (intel) and the memories required are PROMs - 4k and RAMs - 1k.

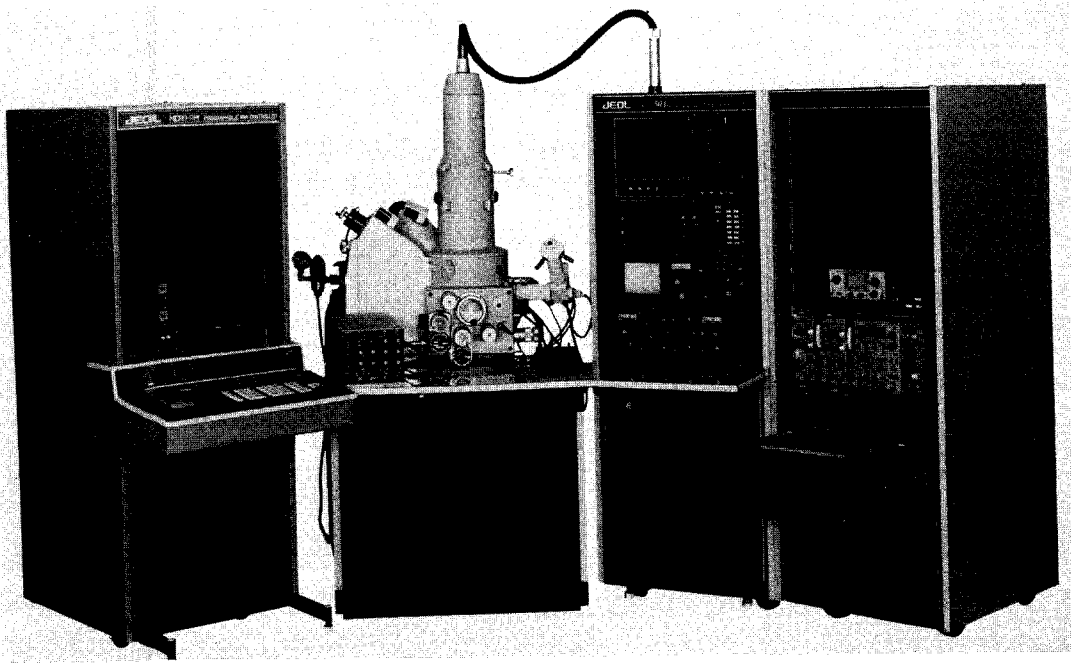


Fig.1 MICRO-PM combined with the JXA-50A

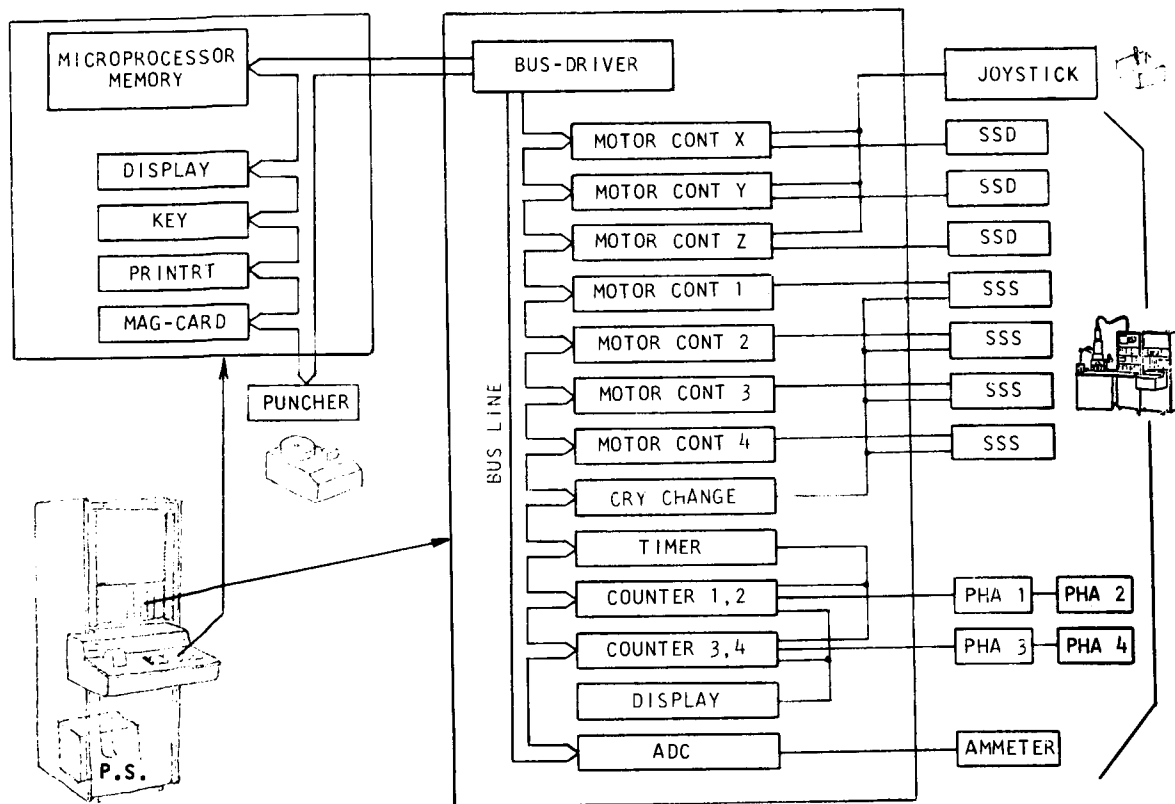


Fig.2 Block diagram of the MICRO-PM

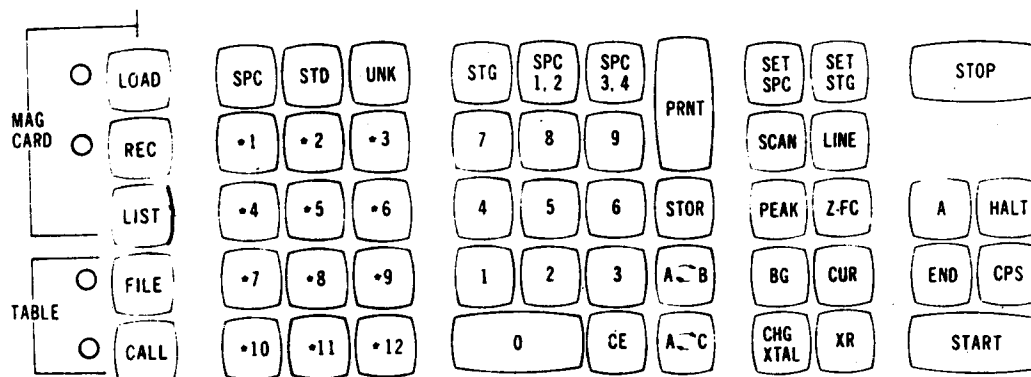


Fig. 3 Operation key board

* INTENSITY (PEAK)

C EL POS INT

2- 195
2 2 13401 65579

* INTENSITY (BG)

(-B)

C EL POS INT

2- 195
2 2 13101 107

(+B)

C EL POS INT

2- 196
2 2 13701 112

* INTENSITY (PEAK)

C EL POS INT

2- 199
2 3 15867 38599

* INTENSITY (BG)

(-B)

C EL POS INT

2- 199
2 3 15567 58

(+B)

C EL POS INT

2- 200
2 3 16167 67

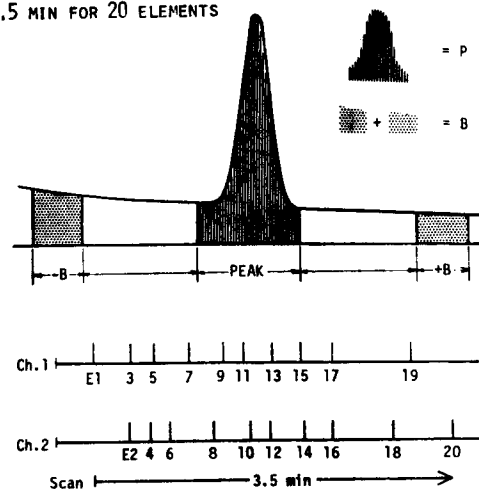
Fig. 4 Peak and background measurement

Fig. 5 Qualitative analysis

OUTPUT

E	P	B
P	1101	1051
AU	31	37
SR	694	370
ZN	39	40
W	210	264
W	31	76
SI	358	202
CU	54	31
AL	106	86
NI	736	28
SE	59	71
CO	48	120
AS	114	48
FE	6063	53
MG	48	46
MN	79	44
NA	21	18
CR	1778	19
F	11	7
TI	23	6

3.5 MIN FOR 20 ELEMENTS



KRISEL CONTROL AUTOMATION PLUS MAC 5 (ETEC)
MICROPROBE USED IN TEACHING AND RESEARCH
IN GEOSCIENCES

HENRY O.A. MEYER
DALE L. HAWKINS

Department of Geosciences
Purdue University
West Lafayette, IN 47907

A particular aspect of the curricula at Purdue University is the emphasis placed on the practical aspects of Geosciences. Accordingly, a formal course in the use of the electron microprobe was instituted for both undergraduate and graduate students in order to emphasize the role of this instrument in pure and applied mineralogy and geochemistry. Initially the course was structured around the use of a non-automated, three spectrometer MAC-5 (ETEC) microprobe. However, during the last year and a half the students have been able to gain further experience by using the same microprobe in both automated and non-automated modes. Use of the probe as a tool in teaching has caused no interference with the routine research problems for which the microprobe was initially installed. In fact the teaching program has enabled several students to become relatively skilled operators and have been usefully employed in the research programs.

The original MAC-5 system consisted of three spectrometers with RAP, PET and LiF analyzing crystals, plus Ortec model 486 PHA's and Datatron digital display with output through a teletype. During the course all students had to correct raw data by hand for drift, deadtime and background. Furthermore, they were expected to complete at least one refinement by hand of ZAF corrections for some unknown mineral they had analyzed. Subsequently, they were allowed to utilize the program ABFAN (1) to correct for absorption, fluorescence and atomic number effects.

To this system was added the Krisel Control automated microprobe control equipment. The basic Krisel system consists of a D.E.C. PDP-11/05 minicomputer with 8k word memory, plus high-speed paper tape reader and teletype. Internally mounted in the PDP-11 is the computer interface with capability for allowing independent control of seven stepping motors, plus related circuitry for controlling various operations of the system.

Digital output of beam and specimen currents are displayed through a microprobe logic control, which also includes a timer and three scaler displays, plus circuitry for manual control of the spectrometers. Another feature includes a beam interceptor device that monitors the electron beam when no counting is underway. This device enables normalization of count rate for changes in beam current during analyses (2).

Three of the seven stepping motors control the independent motion of the spectrometers. Thus while one spectrometer is moving to a new position the other two can be independently counting with no electronic interference in any counting channel. Three other motors control the X, Y and Z-specimen stage motions and all three axes can be programmed to move to pre-set positions determined initially by "joy-stick" control. This enables selection of individual points for analysis, or a line scan or a set of points in some pre-set grid arrangement. The seventh motor is an optional device and is associated with the computer control for periodic resaturation of the filament. No hardware axis positioners are used since all control of spectrometer motion is through software via teletype instructions. The computer control of all spectrometers can be manually overridden if desired.

At the present time several versatile programs are available including standard peak search and stepping routines. Qualitative and semi-quantitative analysis programs enable approximate determinations of elemental abundances.

The currently used major quantitative analysis program is a modified version of the Bence and Albee(3) and Albee and Ray (4) correction procedures plus Ziebold-Ogilvie method (5). On-line MAGIC IV (6) is available; however, this correction scheme requires more core than is present in our system but this program will be incorporated into the system shortly.

The availability of both automated and non-automated microprobe systems in teaching has proven very effective in illustrating the use to students of minicomputers in laboratory automation. This is especially so with a versatile system such as that of Krisel Control which allows the student to use the microprobe in a semi-automated mode, prior to utilization of a completely automated system. As an example, the students after preparing their own polished mineral mounts have to collect peak and background counts on standard and unknown using the microprobe in the manual mode. These data they then correct by hand and subsequently, by use of a ZAF program. Following this exercise the student then repeats the analysis for the same elements using the complete automated system. In this way the student appreciates the complexities of the various correction procedures and understands the nature of the automated control system. Also available is a BASIC interpreter modified for real time extension. With this language the student may write specialized data collection and reduction routines for problems of specific interest.

Reproducibility of analyses obtained using the system is very good and typical analyses obtained by students are shown in table 1, together with other analyses presented for comparison. A distinct advantage of the system is the relative ease with which an untrained person can produce satisfactory analyses. This is particularly useful in research projects or applied problems which require large amounts of data for statistical study.

References

1. Hadidiacos, C. G., Finger, L. W. and Boyd, F. R.: Carnegie Inst. Wash. Yearbook, 69, 294 (1970).
2. Finger, L. W. and Hadidiacos, C. G.: Proc. 7th Nat. Conf. Electron Probe Anal., 68A (1972).
3. Bence, A. E. and Albee, A. L.: Jour. Geology, 76, 382 (1968).
4. Albee, A. L. and Ray, L.: Anal. Chem., 42, 1408 (1970).
5. Ziebold, T. O. and Ogilvie, R. E.: Anal. Chem., 36, 322 (1964).
6. Colby, J. W.: Tutorial Notes from 7th Nat. Conf. Electron Probe Anal., (1972).

TABLE 1. Representative mineral analyses performed by students using automated microprobe system

Oxide	Sapphirine		Plagio- clase	Garnet in Diamond	Pyroxene	Lunar glass	Lunar olivine
	1*	2					
SiO ₂	13.3	13.1	61.7	53.9	42.2	43.0	39.2
TiO ₂	-	-	0.00	0.95	0.03	0.48	0.11
Al ₂ O ₃	61.9	62.1	24.5	0.14	18.5	29.4	0.42
Cr ₂ O ₃	-	-	0.04	0.45	7.64	0.05	0.09
FeO	8.62	8.21	0.07	2.16	6.22	4.45	16.2
MgO	16.2	16.5	0.01	18.0	23.7	5.73	43.1
CaO	0.03	0.03	5.52	24.4	2.25	17.0	0.29
Na ₂ O	-	-	8.30	0.45	0.07	0.01	0.00
K ₂ O	--	-	0.43	0.17	0.00	0.03	0.00
Totals	100.1	99.9	100.6 ¹	100.6 ²	100.6 ³	100.2 ²	99.4 ⁴

*Non-automated analysis for comparison.

Analysts

1. S.R. Brand
2. H.M. Tsai
3. R.D. Lewis
4. R.J. Mlinac

AN ARTEFACT IN X-RAY MICRO-ANALYSIS
SECONDARY X-RAYS EMITTED FROM THE SPECIMEN CHAMBER
A STUDY IN THE CASE OF THIN SPECIMEN ANALYSIS

P.GALLE - CONTY - BOISSEL

Département de Biophysique de la Faculté
de Médecine de Créteil and CAMECA

France

In an X-ray micro-analyzer, the specimen chamber is excited by X - radiation (characteristic and continuum) and scattered electrons both. Consequently, secondary X-rays are emitted from the whole surface of the specimen, even from area located far away from the target. These radiations are not characteristic of the volume to be analyzed and may be detected by spectrometers. These possibilities of artefacts have specially to be taken in consideration in the case of ultra-thin sections of biological tissues, where local concentrations are very low : in this case, intensity of primary X-rays emitted under the probe may be lower than the secondary one.

MORLEVAT [1,2] and NICHOLSON [3] had pointed out this possibility of artefacts and their consequences in quantitative analysis. In the present work, intensity of secondary X-ray emission has been studied in the case of ultra thin specimens, as a function of :

- 1/ Atomic number of the target
- 2/ Accelerating voltage
- 3/ Proximity of secondary emitting surfaces

An MBX microprobe with a conventional transmission electron microscope attachment has been used. This micro-analyzer was equipped by

- 1/ Fully focussing wave length dispersive spectrometer
- 2/ An energy dispersive spectrometer

A schematic representation of the specimen chamber and spectrometer is drawn on figure 1. Energy dispersive spectrometer is a TRACOR NS 750 ; the 30 mm² silicon diode has a resolution of 170 eV and is located 65 mm from the probe.

Three varieties of specimen have been studied :

- 1/ A 300 angströms gold layer
- 2/ A 300 angströms aluminium layer
- 3/ A spray of iron colloïdal particules on a thin formwar layer

Each specimen has been put on standard specimen holders currently used in electron microscopy : formwar coated cupper grids (window = 120 microns, bars = 50 microns).

RESULTS

1/ SECONDARY X-RAY INTENSITY AS A FUNCTION OF ACCELERATING VOLTAGE AND ATOMIC NUMBER OF THE TARGET

When the probe is localized on the center of the gold or aluminium layer, more precisely at 60 microns of the cupper bar grid, intensity of cupper K α is greatly depending of accelerating voltage and atomic number of the target (figure 2 "dotted line"). On the gold target, and with a 40 kV accelerating voltage, the ratio $\frac{I_{Au K\alpha}}{I_{Cu K\alpha}}$ is <1 when E D S is used. On the other hand, at low accelerating voltage, the same ratio measured in W D S and E D S are not very different in the conditions of figure 1.

2/ INTENSITY OF SECONDARY CHARACTERISTIC RAYS AS A FUNCTION OF THE PROXIMITY OF SECONDARY EMITTING SURFACE

Results obtained with gold and aluminium layers are presented on figure 2 (continuous line). Concerning the iron colloïdal particules, ratio of the Fe K α intensity with the probe on the particule and the

Fe K α intensity with the probe 2 μ m away from the particule, are respectively 7 for E D S and 18 for W D S.

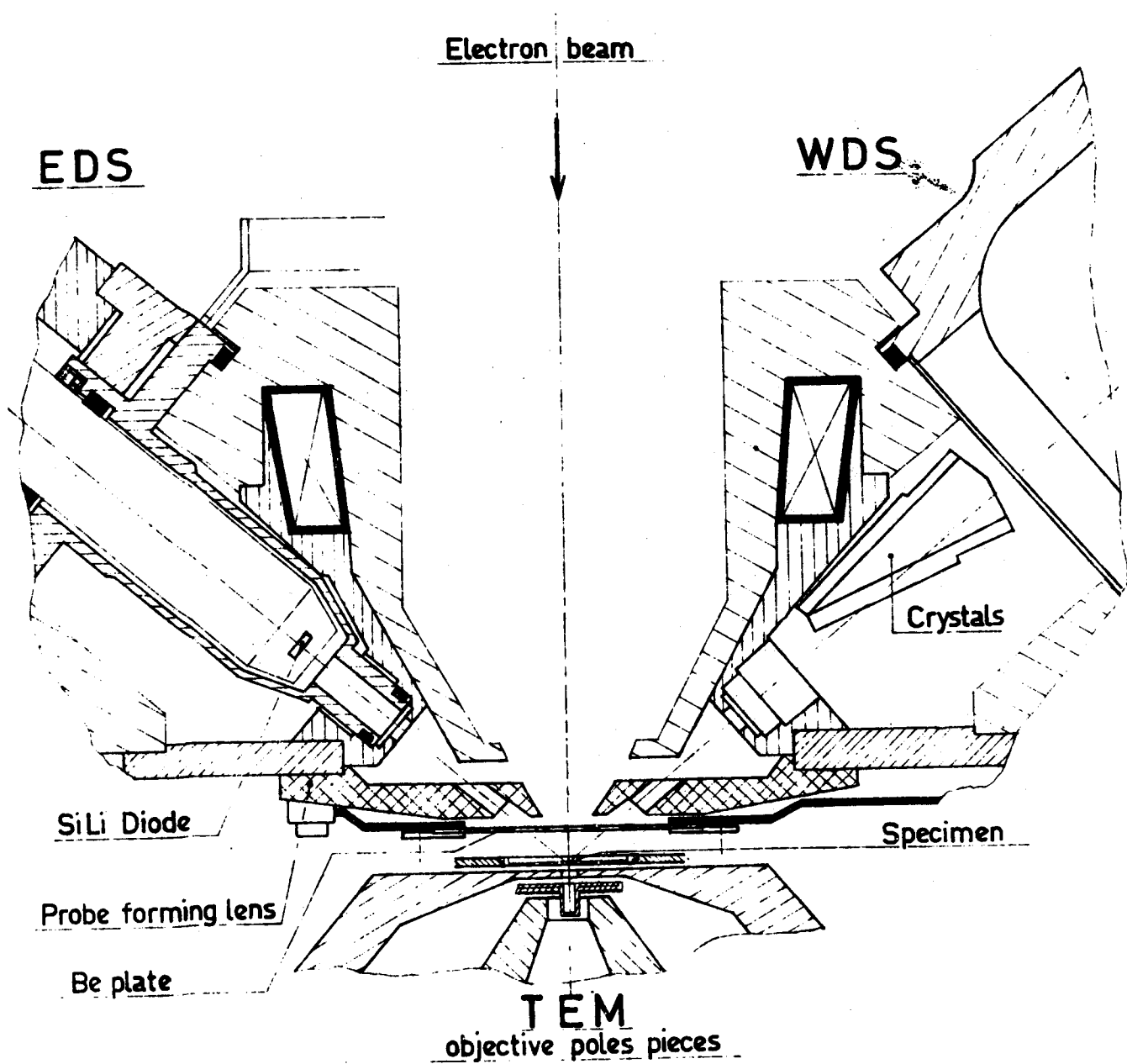
Results presented in section 1/ and 2/ have been obtained in the condition of figure 1, in which a beryllium plate is included in order to eliminate, as much as possible, scattered electrons effects. Without the beryllium plate, at 20 kV intensity of secondary x-rays are not higher in W D S and 10 % higher in E D S. These differences are relatively low and probably due in E D S to the geometric disposition of the diode.

CONCLUSIONS

The secondary X rays (characteristic and continuum) emitted far away from the probe have to be taken in consideration in quantitative and qualitative analysis. This artefact is depending of accelerating voltage, atomic number of the target and geometry of the specimen chamber. In E D S, it also depends of localization of the detector. Quite different results may be obtained with an other disposition. Attenuation of this artefact can be obtained by the use of low atomic number grids, of a beryllium plate, and the choice of an accelerating voltage as low as possible. This attenuation is particularly apparent in E D S.

REFERENCES

- 1/ MORVELAT J.P. and ROUSSIGNOL J.
Etude d'une cause d'erreur en micro-analyse par sonde électronique : l'excitation indirecte de la matrice.
Journal of Physics E : Scientific Instrument (1972) 5 : 332-336
- 2/ MORLEVAT J.P.
Analyse des éléments très légers à la microsonde : quelques causes d'erreurs, exemples d'applications
J. Microscopie (1974), 20 : 108 - 112
- 3/ NICHOLSON W.A.P.
Experience of diffractive and non-diffractive quantitative analysis in the CAMECA microprobe. In " Microprobe analysis as applied to cell and tissues ".
1 vol. Academic Press ed. (1974), 239 - 248

**Fig:1**

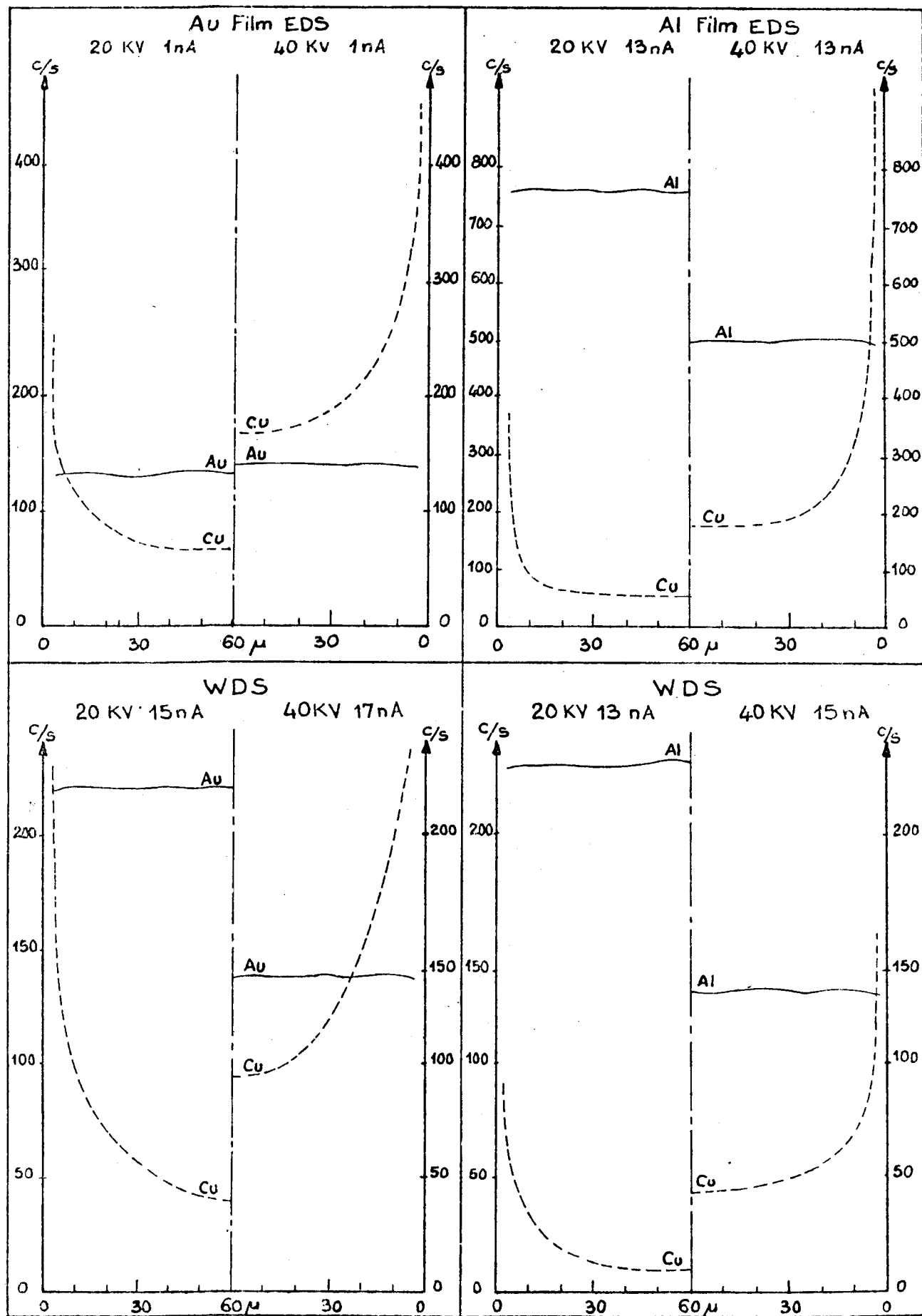


Fig. 2

Minimum Detection Limits In An Automated Microprobe

Joseph D. Geller
JEOL U.S.A. INC.
Medford, MA 02155

"Abstract"

Minimum detectable concentrations, as calculated by the Ziebold equation, are derived from peak and background intensity, counting time, matrix coefficients and the weight percent of the compound standards used. These concentrations are those that could be detected assuming the counting time went to its time-out limit.

The instrumentation used in this paper is computer automated with the system concept aimed at minimizing electron beam exposure of the specimen. This keeps specimen heating and electrical effects to a minimum insuring the highest accuracy analysis.

A newly designed beam blanking device combined with a Faraday cup insure "mathematically" stable incident probe current. This permits immediate operation of the microprobe without warmup stabilization as well as the freedom to alter the beam current to accomodate beam sensitive or low concentration specimens without restandardizing.

Foremost in any quantitative investigation is the precision and accuracy of the analysis. The precision is an indication of the experimental repeatability or random error; and accuracy, a measure of the deviation from the true concentration. The detection limit (Cmdl)¹, the limit at which detection may be guaranteed prior to measurement, is a measure in a sense of both precision and accuracy. At this concentration the instruments capability is being strained in determining even qualitatively whether an element is present or not. The Cmdl is approached when the statistical uncertainty in the "background" is of the same approximate magnitude as the "information" being detected.²

When carrying out quantitative analysis with the wavelength dispersive spectrometer (WDS) Colby³ has stated that trace elements start in the range of 0.1% or less. With energy dispersive spectrometers (EDS) the Cmdl is approximately 0.1%, indicating lower minimum detectable limits with the WDS. Published data⁴ indicate the Cmdl based on cps/unit beam current is similar for WDS and EDS. Beaman and Isasi note, however, that the EDS fails to function properly when the counting rates reach around 10,000 cps due to pulse pile-up, doubling and dead-time problems. On the other hand the WDS works well up to 100,000 cps. In taking advantage of this high count rate by increasing the incident beam current coupled with the high peak/background of the WDS the Cmdl for practical analysis (less than five minutes) are in the range of 60-1000 PPM. The typical peak integrating times for each of ten elements being 30 seconds.

Calculation of the Cmdl

The concentration of the minimum detectable limit directly follows the Ziebold¹ equation.

$$\text{Cmdl} = 3.29 \text{ aW} / (\text{nt P} \cdot \text{P} / \text{B})^{\frac{1}{2}}$$

Where t is the time of measurement, n the number of measurements, P the counting rate in cps for the standard element of concentration W and matrix factor a from the empirical calculation of Ziebold-Ogilvie⁵, and B background cps.

Choice of Standards

The proper choice of standards helps insure the highest accuracy analysis. Standards as close in concentration and composition to the unknown requires the smallest mathematical correction to the counting rate ratio. This is the ratio of counts per second (cps), background subtracted, in the unknown to the standard divided by the concentration

of the standard. The mathematical correction applied increases as the choice of standard worsens decreasing the accuracy.

The factor a of the Ziebold equation is a measure of the matrix effect x-rays undergo in the specimen. The factor is the combined ZAF factor; atomic number, absorption and fluorescence correcting the emerging x-ray flux as if the x-ray of the element being analyzed were not influenced by its host matrix. The a value has been obtained empirically and by numerical calculation.⁶ By running the ZAF equation in reverse inserting unknown or estimated values of the elements and their concentrations the a values fall out. The best choice of a standard then is a matter of matching the a values for the unknown and standard. This also produces the best estimate of the Cmdl.

Matching concentrations in the unknown and standard reduces counting rate uncertainties such as dead-time and pulse shrinkage in the gas flow counter of the WDS and peak ratio nonlinearities in the EDS.

Standards for mineralogical specimens are abundant in a range of a values and concentrations. For metallurgical specimens, however, it is difficult to make close matches due to fewer existing standards necessitating the use of pure standards.

Experimental Data

The choice of operating parameters for a specimen depend strongly on the elements to be analyzed, their concentrations and resistance to electron beam interactions. For geological specimens the Bence-Albee^{7,8} corrections are utilized at a 15kv operating potential with an incident electron (Faraday) current in the range of 50 nanoamperes and a maximum counting time of 30 seconds. These conditions can provide a Cmdl in the range, for instance, of 60-220 PPM for nine elements in 3 minutes with three spectrometers. Table 1* lists the specific parameters for standardization, measured intensities and calculated Cmdl. With modification of the beam current and counting time it is, of course, possible to reduce the Cmdl significantly. Figure 1 shows analyses for a synthetic glass (each analysis requiring three minutes with three spectrometers). The average of three analyses of this specimen are shown where SD is the standard deviation in metal wt. %, C1 the count ratio based on 100% standard, BC the metal oxide before corrections, AC after corrections

and wt. % the wet chemical determination.

For metallurgical specimens the choice of kv and beam current is generally less restrictive than for geological ones. Table II* lists the same type of information as Table I except the standards are pure metals with a corresponding a value of 1.0 (by definition). The analysis (figure 2) was run at 25KV with a beam current of 5 nanoamperes. Colbys Magic IV⁶ correction procedure were used to correct for absorbtion, atomic number and fluorescence. The data is not normalized to 100% concentration. The Al correction is greater than 300% indicating a very poor choice of standards and possibly large uncertainty in the corrected (AC) weight percent.

* Data collected using a JEOL, JXA-50A X-Ray Microanalyzer with Krisel Control automation.

Faraday Cup Measurements

To insure high precision analysis the Faraday beam current should be monitored. Figures 3a and b show the Faraday Cup/beam blanking device just developed. The unit is thermo-electrically operated measuring the beam current after all apertures in the column. The computer control system operates the cup such that the Faraday current is measured and the beam blanked whenever the x-ray scalers are not counting, minimizing electron exposure of the specimen.

The computer measures the current initially and mathematically normalizes it during the analysis. Beam stabilizing devices and instrument warm-up times (usually up to one hour) are not required. Changing filaments and resuming operation without restandardizing is a practical reality.

Figure 4 illustrates the precision of ten analysis. The specimen is a synthetic mineral, WEF-13. The average of ten analyses using the unknown as its own standard is shown. The mathematical correction applied (BC and AC) is negligible by definition. The total is not 100% due to the conversion between Fe_2O_3 and Fe_3O_4 . The standard deviation for these four elements show a worst case deviation of + and - .06% (1.4% relative) concentration for Mg at the 4.24% level. The peak integral for these elements was 20,000 counts. The two sigma limit, $2\sqrt{\text{Pcps}}$, is 1.4% relative illustrating that machine repeatability is within counting statistics. The Peak/Bkg for Mg was 146/1. The background is not statistically significant since it is less than 1% of the peak, however, it is always measured long enough to determine whether or not it is significant.

Conclusion

The precision of analyses are possible and routine to the 1-2% relative level even down to absolute concentrations of 4%. The accuracy of the analysis can be within this level if the corrections applied to the data are minimal.

The use of a Faraday Cup / Beam Blanking Device relax the instrument stability problems making the instrument "mathematically stable".

REFERENCES

1. T.O. Ziebold, Anal. Chem., 39, 858 (1967)
2. R. Woldseth, X-Ray Energy Spectroscopy, Kevex Corp. (1973), p3.7
3. J. Colby, Practical Scanning Electron Microscopy (ed. Goldstein & Yakowitz) Plenum (1975), p.455
4. D. Beaman and J. Isasi, Electron Beam Micronalysis, ASTM (506), p.27
5. T.O. Ziebold and R.E. Ogilvie, Anal. Chem., 36, 322 (1964)
6. J. Colby "Magic IV - A new Improved Version of Magic", Proc. 6th Conf. on Electron Probe Analysis (1971)
7. A. Albee and L. Ray, Anal. Chem., 42, 1408 (1970)
8. A. Albee and L. Ray., J. Geology, 76, 382 (1908)

73F

Element	Peak (cps)	Bkg (cps)	Peak/Bkg	Wt % Std	a	CmdI (PPM)
Ca	1681	6.6	255	12.03	1.073	118
Si	5138	9.7	530	26.59	1.149	110
Mn	505	5.3	95	8.38	1.064	244
Fe	378	5.5	69	5.62	1.116	233
K	1323	4.5	294	12.39	1.128	135
Ti	230	16	14	1.20	1.127	141
Na	406	2.2	185	3.98	1.411	123
Mg	1458	4.9	298	7.30	1.194	79
Al	1240	7	177	4.67	1.194	71

Table I Calculation of the CmdI from appropriate standards used for analyzing the synthetic glass in figure 1.

	MN	FE	K	CA	TI	NA	MG	AL	SI
SD	.01	.25	.07	.25	.09	.04	.14	.27	.34
CI	.08	9.16	1.21	8.38	1.75	1.41	7.63	5.98	18.30
BC	.11	11.78	1.46	11.72	2.92	1.89	12.64	11.29	39.16
AC	.11	11.68	1.42	11.55	2.82	2.19	13.50	11.95	41.33
Wt. %	.11	10.36	1.61	11.68	2.40	2.07	13.10	12.56	41.76

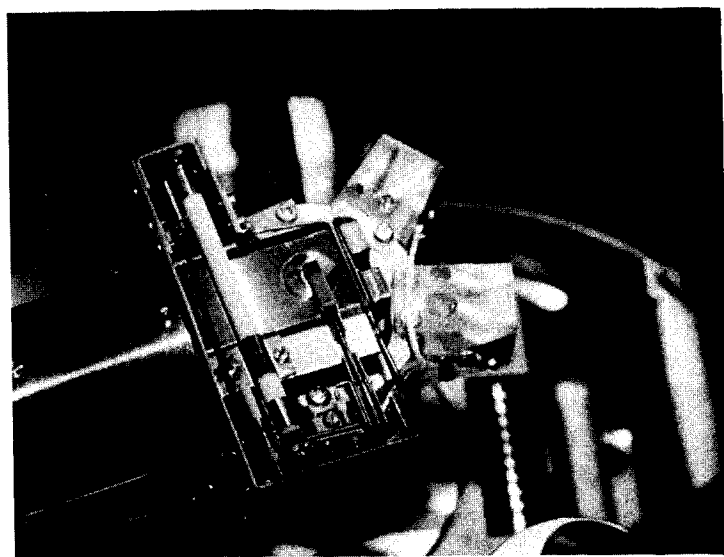
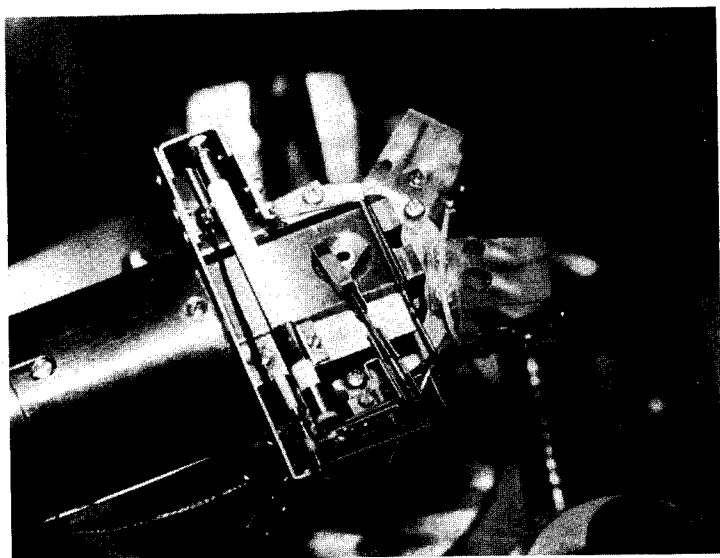
Figure 1 Analysis of a synthetic glass (average of 3 points)

Element	Peak (cps)	Bkg (cps)	Peak/Bkg	Wt % Std	a	CmdI (PPM)
Al	16572	8.1	2033	100	1.0	100
Si	12092	10.4	1162	100	1.0	160
Ti	1478	1.7	835	100	1.0	540
Cr	4495	4.1	1088	100	1.0	270
Fe	6451	9.4	681	100	1.0	286
Co	6859	13.5	506	100	1.0	322
Ni	7654	13.9	549	100	1.0	292
Hf	3499	32.2	108	100	1.0	974

Table II Calculation of the CmdI from pure metallurgical standards used for the analysis in figure 2.

	AL	SI	TI	CR	FE	CO	NI	HF	TOTAL
CI	11.11	.08	.09	3.58	1.03	.43	56.58	1.04	
AC	35.35	.26	.10	3.52	.89	.45	58.23	1.24	100.05

Figure 2 Analysis of an alloyed component.



unblanked position

blanking position

Figure 3 Beam blanking device / Faraday cup mounted in the optical microscope after all apertures

	SI	MG	CA	FE	TOTAL
SD	.25	.06	.27	.16	
CI	20.17	4.24	21.67	13.64	
BC	43.14	7.03	30.32	17.54	
AC	43.14	7.01	30.33	17.55	98.04

Figure 4 Standard deviation (SD) of ten repetitive analyses.

DESIGN, PERFORMANCE, AND APPLICATION OF A 100 kV STEM

by

I. R. M. Wardell

VG Microscopes, Ltd.
The Birches Industrial Estate
Imberhorne Lane
East Grinstead, Sussex, England

The range of analytical techniques available on the VG microscopes 100 kV STEM has been extended. The major innovations include the fitting of an energy dispersive X-ray detector, a wide-angle high-efficiency annular detector, a double-deflection microdiffraction facility and a secondary electron detector for generating a surface topographical image.

X-ray Imaging and Analysis

The design of the objective lens has been modified to permit an energy dispersive X-ray detector to be positioned on the side of the specimen facing the electron beam, at a distance of 15 mm from the specimen. The take-off angle with respect to the incident beam is 76 degrees. With this arrangement and the high currents (circa 10^{-9} Amps) that are available from the instruments' field emission source into a small probe, it is possible to produce X-ray images with better than 100 angstroms definition.

Dark-Field Imaging

The efficiency of producing a dark-field image, in terms of the useful number of dark-field electrons per incident electron

on the specimen, is about 100 times greater in STEM than in TEM. The VG microscopes STEM has been fitted with an annular detector which permits the axial cone of electrons emerging from the specimen to pass through to the energy analyser and bright-field detector. Electrons scattered by the specimen up to an angle of 0.2 radians fall onto a scintillator. This scintillator is coupled to a photomultiplier such that the overall efficiency of detecting electrons is great enough to permit single electron counting and the production of high-quality dark-field images. Results with this detector show that high-quality low-dose images can be formed routinely, which is particularly useful on biological specimens that readily suffer beam damage and require minimum exposure to the beam.

Weak Beam Imaging and Microdiffraction

The introduction of a double deflection coil assembly immediately after the specimen permits a diffracted beam from the specimen to be steered back onto axis and then directed through the energy analyser in place of the original undiffracted beam. In this way energy-analysed weak-beam images can be formed. A series of preselected D.C. excitations on the coils can be chosen so that a rapid interchange between normal bright-field and weak-beam images can be made. Further, by positioning a stationary probe on the specimen and applying a scan-raster waveform to the post-specimen deflection coils a microdiffraction pattern can be obtained from very small areas of the specimen. The probe normally needs to be slightly defocussed such

that a reasonable number of lattice spacings within the specimen are illuminated. The useful minimum diameter from which diffraction patterns can be obtained is in the region of 20 angstroms.

Secondary Electron Imaging

The normal bright and dark-field modes of forming an electron image provide information which is characteristic of the internal structure of a thin specimen. To obtain surface structural information it is necessary to view a secondary electron image. It is preferable to form such an image with those secondary electrons which are emitted from the side of the specimen facing the incident beam so that the resolution tends to be limited by the diffusion of low energy secondary electrons rather than by scatter of the primary beam as it passes through the specimen. A secondary electron detector has been fitted in the objective lens so that a secondary electron image can be viewed at the same time as any one of the standard bright or dark-field images.

Summary

These additional facilities add a new analytical dimension to an instrument that is already capable of providing 3.5 angstroms point-to-point resolution and a 2.7 angstroms lattice resolution.

INVESTIGATION OF DEEP LEVELS IN ZnSe
USING ELECTRON AND PHOTON EXCITATION

C. J. WU and D. B. WITTRY

Departments of Materials Science and Electrical Engineering
University of Southern California
Los Angeles, California 90007

There has been considerable interest in the study of deep level impurities in semiconductors. Traditional techniques such as measurements of photoconductivity, optical absorption or luminescence are most frequently reported in the literature. A new technique using infrared modulated cathodoluminescence and specimen current during electron beam bombardment has been described recently.^{1,2} In this prior work, semi-insulating Cr-doped GaAs and undoped as-grown semi-insulating GaAs crystals were investigated.

In the present work, an attempt was made to use the same technique on single crystal and polycrystalline ZnSe specimens. The spectrum of single crystal ZnSe obtained with this method is shown in Fig. 2(a). One prominent peak with energy of 2.59eV was found in the spectrum. For comparison, a cathodoluminescence spectrum of polycrystalline ZnSe which was recorded using a photomultiplier tube having S-11 sensitivity is also shown. It is apparent that the light-modulation of specimen current drops to zero at an energy close to the absorption edge. Attempts to observe light-modulated specimen current with polycrystalline specimens of ZnSe were unsuccessful. Presumably this was due to a lower specimen resistivity so that the specimen current becomes insensitive to small changes in excess carrier concentration. In order to raise the sensitivity of light-modulation, we used specimens to which contacts had been applied. The specimens used were polycrystalline ZnSe about 3.0 x 2.5 x 2.0 mm thick. The sample was attached to the sample holder by silver paint which served as the bottom contact. Top contacts were made by evaporating 99.99% pure gold ~200 Å thick on the surface. In order to study both surface and bulk effects, the top contacts were made in the form of two half circles about 40 mils in diameter, separated by 4 mils. Phosphor-bronze wires made probe contact to each of the two semicircles.

Measurements made using only the two top contacts indicated electron beam damage of the surface (after bombardment the resistance between these contacts was lower). Other measurements were made of the resistance between the bottom contact and the top two contacts using the circuit shown in Fig. 1, in which the voltage V was measured by a Keithley 610C electrometer. During these measurements, the surface of the specimen between the two top contacts was illuminated by focused monochromatic light alone or in conjunction with simultaneous bombardment by a focused electron beam. The monochromatic light

was obtained using a 150 watt quartzline lamp and a Hilger and Watts D292 plane grating monochromator which was directed into the reflecting objective of the electron probe microanalyzer (EMX-SM) as in previous experiments.^{1,2}

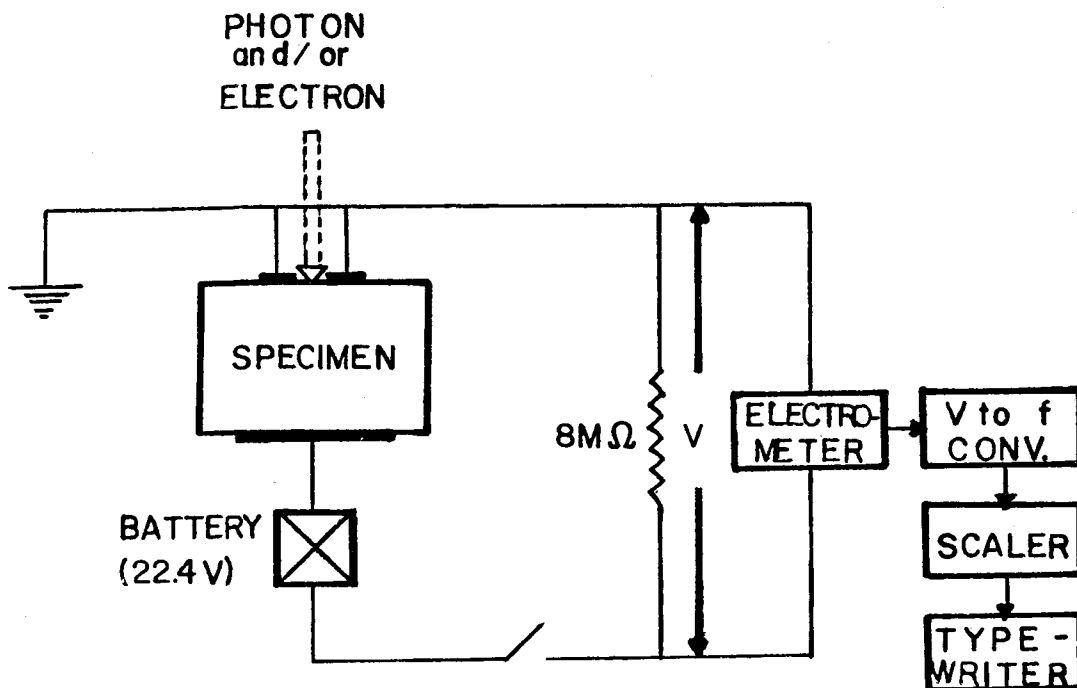
With a negative voltage applied to the bottom contact, the sensitivity of optical modulation was quite high. The typical curves obtained on the polycrystalline ZnSe specimen at room temperature are shown in Fig. 2(b). Two apparent peaks were found at energies of 2.61eV and 2.44eV from the spectrum with electron beam bombardment. However, in the spectrum without electron bombardment, the peak of 2.61eV remained at the same position, but of 2.44eV disappeared. It is evident that some advantage has obtained with primary electron beam bombardment. The peak near the fundamental absorption edge is likely to be due to exciton absorption.³ The prominent structure on the longer wavelength side of the exciton band are either due to defects or impurities. This peak may correspond to the energy level of defects or impurities.⁴ Alternatively, this peak could arise from a threshold for increased photoconductivity followed by a "quenching" of x-ray induced photoconductivity.

It was also observed that the optical modulation is very low with reverse polarity applied to the contacts, i.e., positive bias to the bottom contact. We believe that this indicates strong electron trapping. If the optical radiation is absorbed closer to the top contact, then carriers drifting to this contact may be collected before recombining. In this case, the average current may be determined principally by the $\mu\tau$ product of carriers that drift away from this contact. An analogous case has been reported for solid state x-ray detectors.³ If this interpretation is correct, then it would be possible to measure the $\mu\tau$ product by varying the electric field in the spectrum.

In summary, the techniques described in paper appear to provide much useful information for characterization of semiconductors, namely: evaluation of surface vs bulk effects, enhanced capabilities for study of deep energy levels in low resistivity materials and the possibility of determining the $\mu\tau$ product of excess carriers.

REFERENCES

1. W. N. Lin and D. B. Wittry, Proc. 8th Nat. Conference on Electron Probr Analysis, 73A-73C (1973).
2. W. N. Lin and D. B. Wittry, J. Appl. Phys. (to be published).
3. E. F. Gross and B. V. Novikov, "Photoconductivity", Edited by H. Levinstein, Published by Pergamon Press (1962), pp. 87-100.
4. Hiroji Mitsuhashi, same as in reference 3, pp. 223-226.
5. G. Bertolini, F. Cappellani and G. Restelli, Nuclear Instruments and Methods 112, 219-228 (1973).

**Fig. 1**

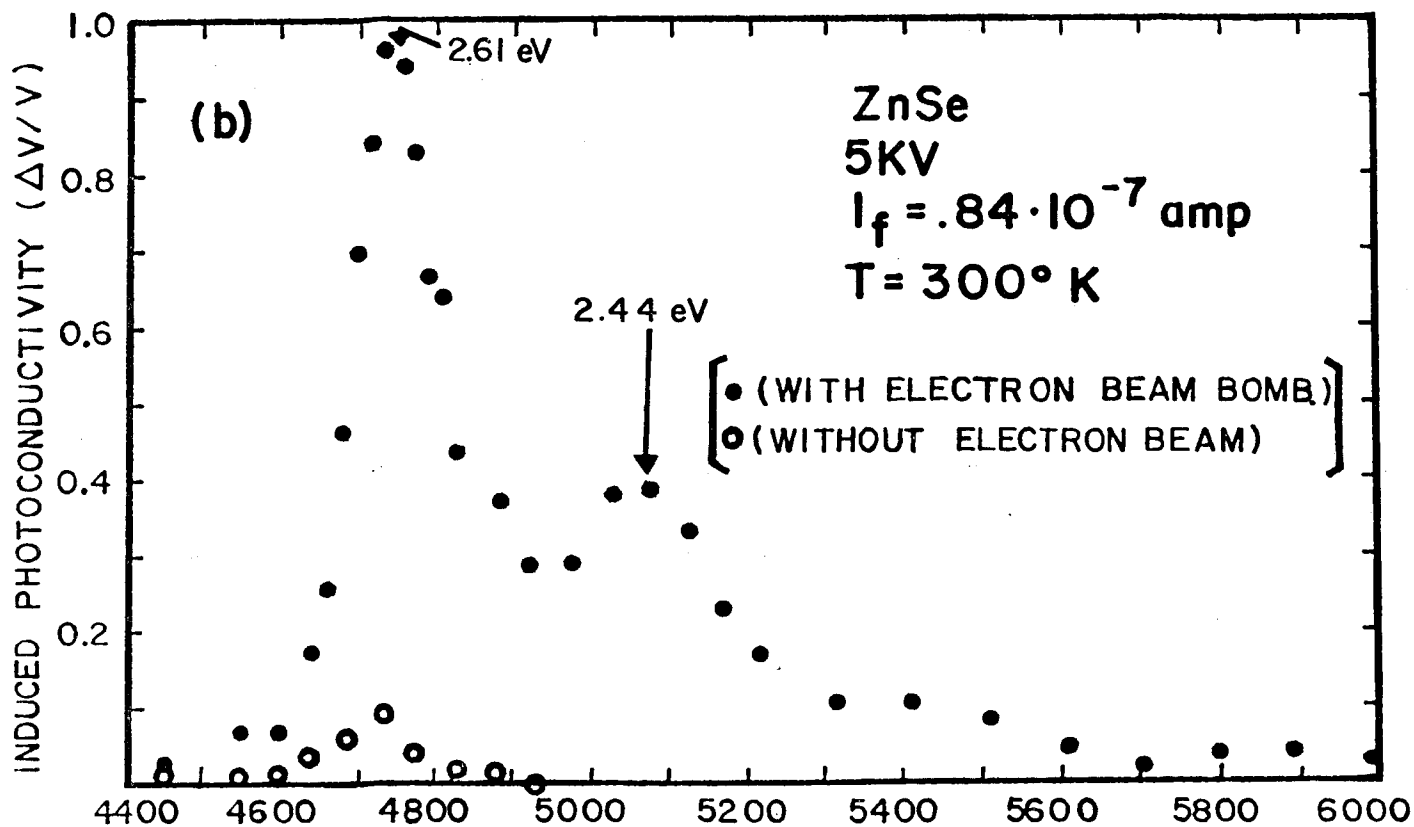
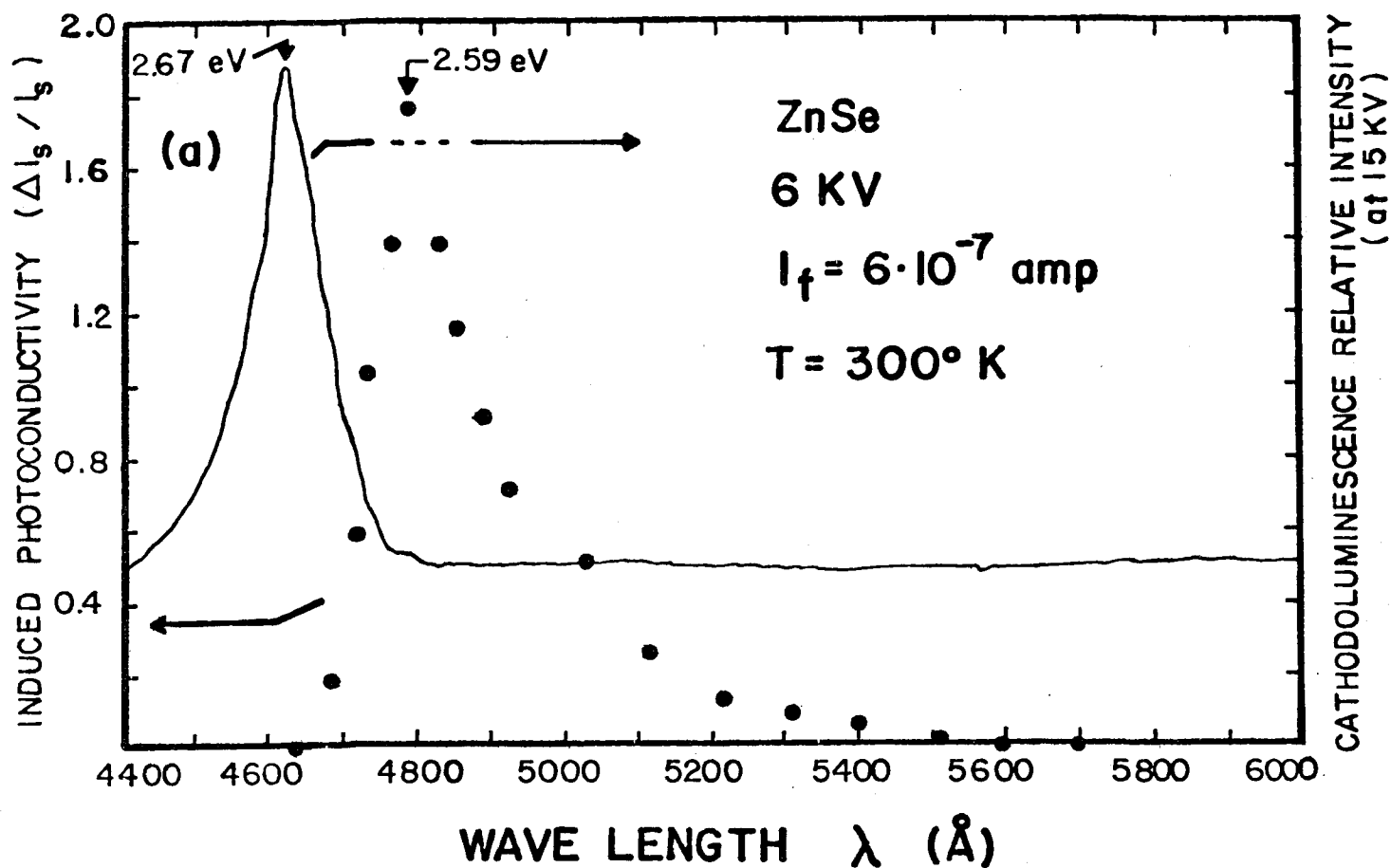


Fig. 2

MICROANALYSIS OF SODIUM EXPOSED STAINLESS STEEL SPECIMENS

A.P. von Rosenstiel , H.B. Zeedijk , B.H. Kolster

Metaalinstituut TNO, Apeldoorn/The Netherlands

Stainless steel specimens of type Wnr. 1.4970, 1.4981 and 1.4988 were exposed to liquid sodium at temperatures between 400 and 700°C for 3090 h in an anisotherm sodium loop. For a description of the loop system see e.g. (1). The exposed specimens were investigated by metallographic techniques, X-ray diffraction, scanning and transmission electron microscopy, electron and ion microprobe techniques and by chemical analysis, as usually applied for sodium exposed AISI 316 specimens (2) (3). Before going into the detailed description of the electron and ion microprobe analyses the results of these investigations can be summarized as follows.

All heated zone specimens showed a surface layer of about 2-4 µm leached in Ni, Cr, Mn and Si and enriched in Fe and Mo with respect to the matrix composition. This layer proved to be ferritic. Ferritic or martensitic grain boundaries were found in a zone up to 20 µm from the specimen surface. Between the ferritic surface layer and the adjacent austenitic matrix, smaller martensitic areas were found for the heated zone specimens of Wns. 1.4981 and 1.4988.

Numerous Mo rich particles (probably Fe_7Mo_6) were found directly on the specimen surface as well as in the ferritic surface layer and in a zone up to 20 µm of the adjacent base material for all heated zone specimens of Wns. 1.4981 and 1.4988. No Mo-rich particles could be detected in the heated zone specimens of Wnr. 1.4970.

All cooled zone specimens showed a surface layer up to 5 µm thick highly enriched in Cr with respect to the base material. The surface layers of the 1.4970 and 1.4983 specimens were determined to be Cr-Fe carbides of type M_{23}C_6 , whereas the surface layer of the 1.4981 specimen was analysed as sigma phase. Neither ferritic grain boundaries nor Mo-rich particles were found in these cooled zone specimens.

Depletion of B, C and N concentrations was found up to a depth of 200 μm under the surface and thus about 10 x deeper than the grain boundary depletion.

Quantitative electron microprobe analyses were performed on taper-sections and on the surfaces of the exposed samples. The ferritic surface layers proved to be of nearly identical composition for the three materials. The ferritic and martensitic grain boundaries under the surface layer showed Ni and Cr concentrations intermediate between the austenitic base material and the ferritic surface layer. The carbides on steel 1.4970 and 1.4988 contained mainly Cr, whereas the σ -phase on steel 1.4981 was free of carbon and contained equal amounts of Cr and Fe.

By means of ion microprobe techniques boron concentrations were measured in the boron containing steel Wnr. 1.4970. In the 200 μm boron depleted zones nearly boron free grain boundaries were observed whereas in the matrix boron was found mainly concentrated at the grain boundaries.

This work was sponsored by "Internationale Atomreaktorbau und Betriebsgesellschaft (Interatom)" Bensberg/W. Germany. The authors are grateful for Interatoms permission to publish the results. They also acknowledge the fruitful discussions with E.D. Grosser and G. Menken of Interatom and the contributions of numerous TNO coworkers.

References:

- (1) B.H. Kolster, J. Nucl. Mat. 55 (1975) p. 155.
- (2) H.B. Zeedijk, J. Jansen and B.H. Kolster, Beitr. Elektronenmikrosp. Direktabb. Oberfl. 6 (1973) p. 87.
- (3) A.P. von Rosenstiel, D.J. Gras, T. Krisch and B.H. Kolster, Beitr. Elektronenmikroskop. Direktabb. Oberfl. 6 (1973) p. 103.

ELECTRON BEAM FURNACE MELTING CONTROL BY THE USE OF AN ENERGY DISPERSIVE SPECTROMETER

F.Borile, E.Olzi, G.Turisini

Electron beam melting technique has reached now days a vast use in modern industries. Very promising engeneering materials such as titanium, niobium tantalium, tungsten, etc., can be melt and refined in ideal conditions. One drawback of this technique however consists in melting alloys containing a number of constituents having a videly varying vapor pressure. In such cases the elements having the highest vapor pressure evaporate at much greater rates and it is therefore difficult to control the alloy composition.

In the present work an energy dispersive spectrometer has been adapted to a Leybold-Heraeus type ES-1/2/20 electron beam melting furnace in order to monitor and control the composition variation of alloys such as Ti-Al-V and Ti-Sn-V. Rate of evaporation established from thermodynamic models will be compared.

USE OF ENERGY DISPERSIVE X-RAY TECHNIQUES
FOR DETECTION AND IDENTIFICATION
OF IMMUNOCHEMICALLY STAINED TUMOR VIRUSES

W. J. Hamilton, Jr.

Developmental Electron Microscopy Laboratory
Frederick Cancer Research Center
(Litton Bionetics, Inc.)
Frederick, Maryland 21701

Electron beam x-ray microanalysis has found a limited application in biological problems. The use of modern techniques for light element analysis such as mylar film windows (1) and windowless detectors (2) are not expected to ameliorate the difficulties. Stoichiometric results of light element analysis of tissues, cells, and biological macromolecules can provide little insight into the fundamental structural and chemical properties of these entities. Biological analyses, therefore, generally have been constrained to situations where heavy metals are present in specimens, such as ecological or toxicological contaminants (3), crystalline inclusions (4), or diffusible ions (5). Successful analysis in cells and tissues of a small number of macromolecules has been accomplished by utilization of the techniques of enzyme cytochemistry (6).

The present experiments were designed as a model system to extend the use of electron microbeam x-ray analysis to the detection of a broad spectrum of biomolecules. The technique developed utilizes the specificity of antibody-antigen reaction for precise discrimination at an exact localization site. These immunological steps are followed by chemical deposition of a heavy metal at the bound antibody site through enzyme catalysis. The heavy metal allows detection and localization of these sites by microbeam x-ray techniques. When all stages of the reaction are carried out under tightly controlled conditions, the reaction product may be studied quantitatively. The model system developed in this work uses an RNA tumor virus adsorbed to a coated grid, immunochemically stained, and critical-point-dried. Preliminary experiments indicate successful application to cellular antigenic macromolecules as well.

MATERIALS AND METHODS

An RNA tumor virus of mice, Rauscher Leukemia Virus (RLV), produced in a JLS-V9 cell culture system was obtained from Dr. G. Shibley (Viral Resources Laboratory, Frederick Cancer Research Center) through Dr. J. Gruber (Chief, Office of Program Resources and Logistics, National Cancer Institute). The virus suspension was adsorbed to glow-discharged, formvar-coated grids, fixed in 2% buffered paraformaldehyde and washed. They were then immunochemically stained by the unlabeled antibody enzyme technique of Sternberger and his co-workers (7). This method consisted of a sequential reaction of antisera. The first antiserum was directed against the target antigen -- in this case,

rabbit antisera to the p30 protein of the Rauscher Leukemia Virus (RARLV/p30). The triple-sandwich was completed by the reaction of goat-antisera to rabbit immunoglobulin G and followed by a soluble complex of rabbit anti-horse radish peroxidase and peroxidase (generously supplied by Dr. L.A. Sternberger, Edgewood Arsenal, Maryland, and obtained from Biological Products Division, Litton Bionetics, Inc., Kensington, Maryland). Following these steps peroxidase enzymatically catalyzed a polymerization reaction and subsequently osmium was deposited. The specimens were critical-point-dried in freons and carbon coated. The x-rays produced by osmium were detected by a 30 mm² solid-state energy-dispersive x-ray detector (Kevex 5100C) in a scanning electron microscope (Etec Autoscan) operated at 20 KV and 100 picoampere beam current. Specimens were also examined by transmission electron microscopy at 50 KV (Hitachi, HU-12A). Controls for the staining procedure were provided by substitution of normal rabbit serum for the antiviral serum with all other steps remaining constant.

RESULTS

Figure 1 illustrates the appearance of the immunochemically stained virus as viewed by TEM. The thick shell of electron dense material deposited by the staining sequence is visible. Figure 2 is the unstained control. Figure 3 illustrates the appearance of the viruses in the secondary electron scanning mode. Figure 4 is the energy-dispersive x-ray spectrum from a single, stained virus particle. The easily discriminated osmium peaks are shown by line markers. On the substrate near the same particle, very low osmium signal is detected (Figure 5). Similarly, a virus particle in the control specimen produces very low x-ray signal from osmium (Figure 6).

DISCUSSION

Immunochemical labeling offers a mechanism for extending the applicability of microbeam analysis methods to a broad range of biological problems. Nearly all biological macromolecules are or can be made antigenic, almost all proteins and certain nucleic acids being the most important. Use of these and similar methods should allow detection of sites on cell surfaces in the SEM and in thin-sections in STEM. Labeling studies of cells and thin-sections for such analyses are currently in progress.

REFERENCES

1. Armagliato, A. and G.G. Bentini. On the Use of a Variable Geometry Proportional Counter for X-rays Microanalysis of Light Elements with an Electron Microscope. Proc. 10th Ann. Conf. Microbeam Anal. Soc.: No. 26, 1975.
2. Barbi, N.C. and J.C. Russ. Analysis of Oxygen on an SEM Using Windowless Energy Dispersive Spectrometer, in Johari, O. and I Corvin, eds., Scanning Electron Microscopy/1975, (Chicago: IITRI), 1975, pp. 85-92.
3. DeNee, P.B., J.L. Abraham, and E.R. Walker. SEM Characterization of Respirable Dust in situ in Lung Tissue Using Ashing and Digestion Techniques. Proc. 10th Ann. Conf. Microbeam Anal. Soc.: No. 51, 1975.

4. Siew, S., R.K. Matta, and M. Johnson. Microanalysis of Crystals in Biological Tissue. Proc. 10th Ann. Conf. Microbeam Anal. Soc.: No. 48, 1975.
5. Garfield, R.E. and A.P. Somlyo. Electron Probe Analysis and Ultrastructure of Cultured, Freeze-Dried Vascular Smooth Muscle. Proc. 10th Ann. Conf. Microbeam Anal. Soc.: No. 44, 1975.
6. Wood, J.G. Positive Identification of Intracellular Biogenic Amine Reaction Product with Electron Microscopic X-Ray Analysis. J. Histochem. Cytochem. 22:1060-67 (1974).
7. Sternberger, L.A. Immunocytochemistry (Englewood Cliffs, N.J.: Prentice Hall) pp. 129-171, 1974.

This work was supported by Public Health Service Contract No. N01-CO-25423 with the Virus-Cancer Program of the National Cancer Institute.

FIGURES

Figure 1: Immunochemical deposition of electron dense osmium on Rauscher Leukemia Virus (RLV). Dense shell of stain is visible external to virus particle. Rabbit anti-RLV/p30, used as primary antiserum in triple-sandwich. Other steps described in text, critical-point-dried and observed by transmission EM at 50 KV. Marker indicates one micrometer.

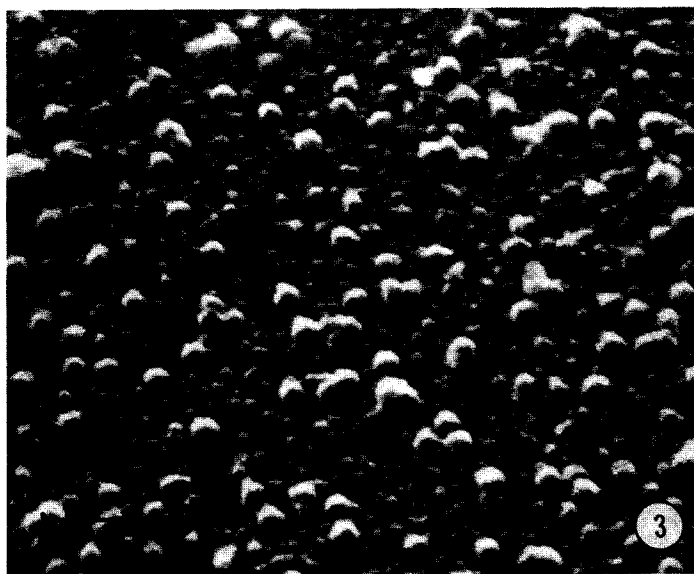
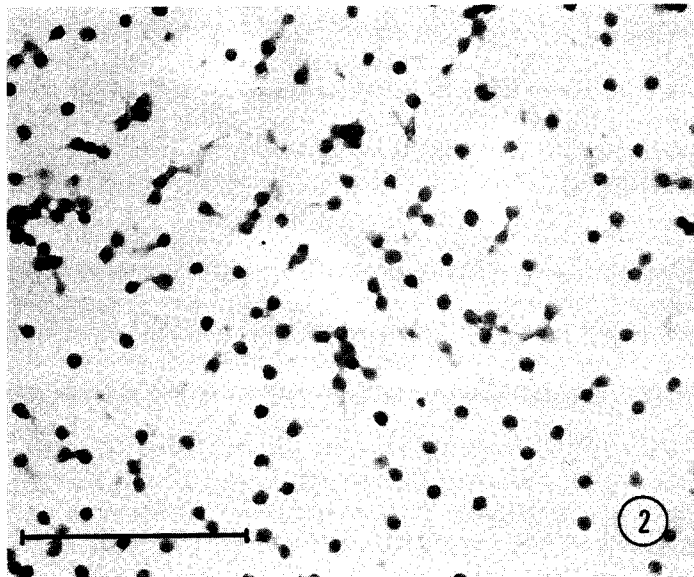
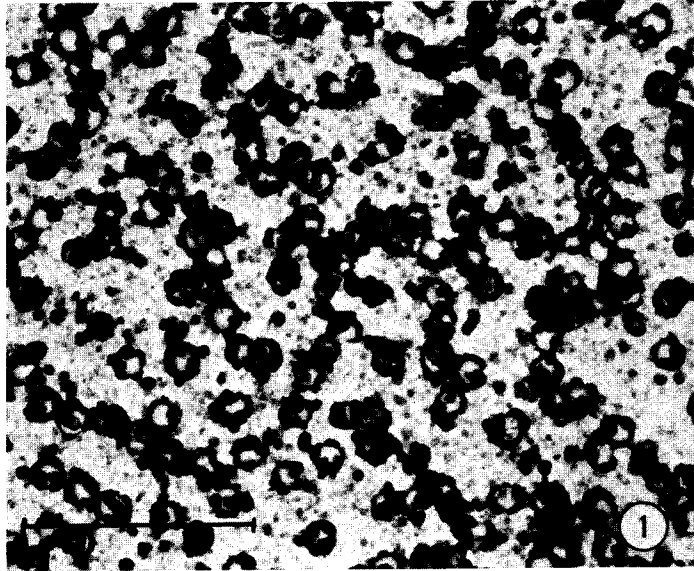
Figure 2: Control preparation of RLV. Normal rabbit serum substituted for anti-RLV antiserum in first step of triple-sandwich. All other steps remained constant. Electron dense stain shell not present. Marker indicates one micrometer.

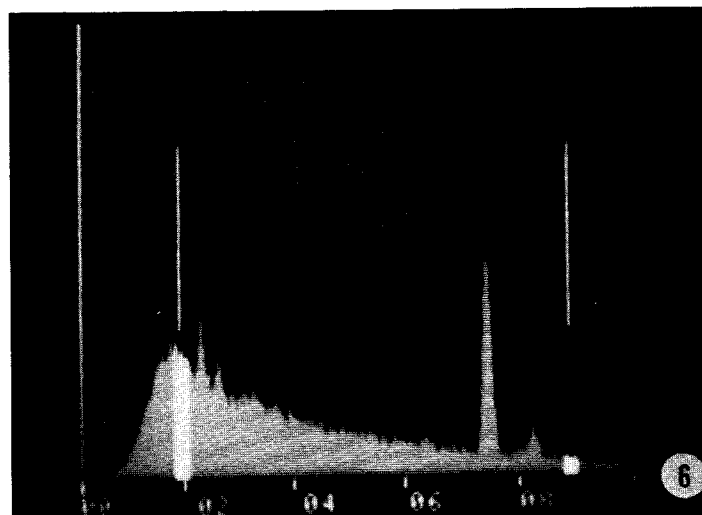
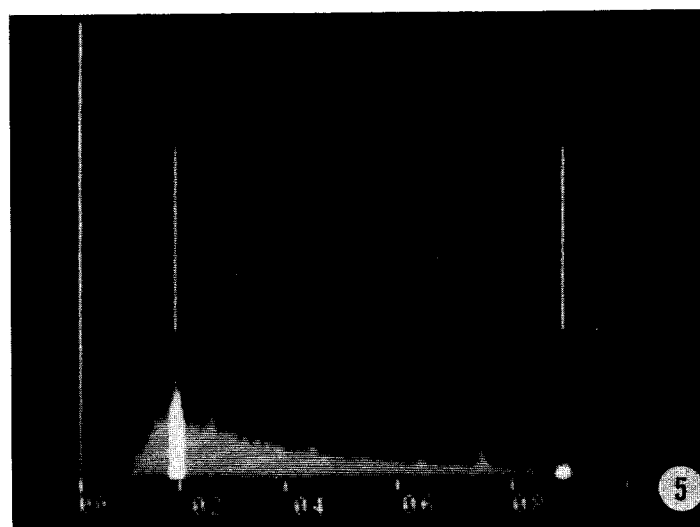
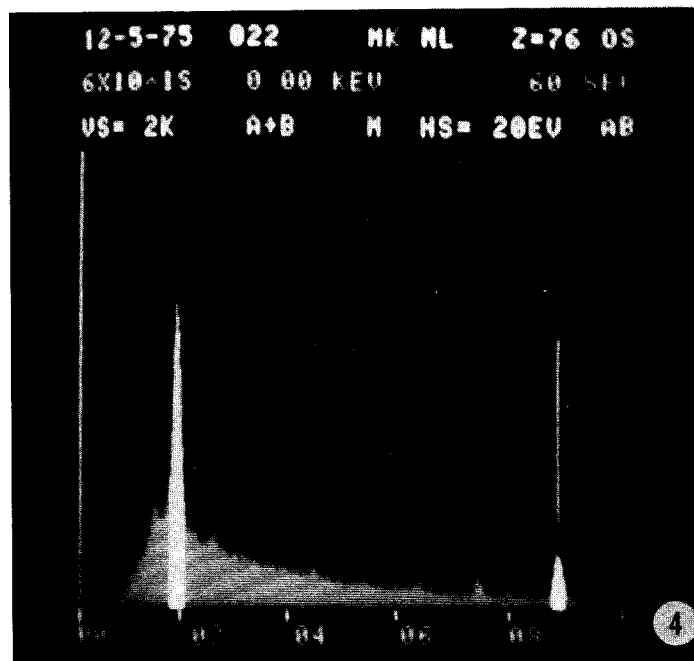
Figure 3: A secondary-electron imaging mode scanning electron micrograph of the stained virus preparation prepared as in Figure 1. Gold coated. Marker indicates one micrometer.

Figure 4: Energy-dispersive x-ray spectrum of virus stained with anti-RLV as in Figure 1. Particles were adsorbed to Formvar-nylon grids and carbon-coated after staining. Intense x-ray peaks of osmium are visible at 1.98 keV and 8.91 keV, the M-beta and L-alpha lines, respectively. Smaller peaks visible are chlorine and sulfur from the particle and iron and nickel from the microscope. Operating conditions: 20 KV accelerating voltage and 100 picoamp beam current.

Figure 5: Energy-dispersive x-ray spectrum of substrate of grid less than three micrometers from particle analyzed in Figure 4. The small osmium signal is expected from electrons and x-rays scattered by substrate toward adjacent particles. Same operating conditions as Figure 4.

Figure 6: Energy-dispersive x-ray spectrum of a particle prepared as in Figure 2. No osmium x-rays are detectable above the background noise--indicating substitution of normal rabbit serum for anti-viral serum eliminated specific staining of the viruses. Large peaks at 7.5 keV and 8.3 keV are produced by x-rays generated by the nickel grid supporting this specimen.





INDEX OF AUTHORS AND THEIR AFFILIATIONS

		<u>Paper Number</u>
Albee, A. L.	Division of Geological and Planetary Sciences, California Institute of Technology, Pasadena, California 91125	38
Anderson, J. R.	Division of Geological and Planetary Sciences, California Institute of Technology, Pasadena, California 91125	38
Amy, J. A.	Electron Optics Laboratory (Code 30333), Naval Weapons Support Center, Crane, Indiana 47522	45
Astill, D. M.	N.E.R.C. Ion Probe Unit, Dept. of Mineralogy & Petrology, University of Cambridge, Madingley Rise, Cambridge CB3 0EZ, England	46
Baillieul, T. A.	Dept. of Geology and Geography, University of Massachusetts, Amherst, Massachusetts 01002	68
Barbi, N. C.	NL Industries-ICD Division, Hightstown, New Jersey 08520	8
Baxter, W. J.	Research Laboratories, General Motors Corporation, Warren, Michigan 48090	31
Beeston, B. E. P.	AEI Scientific Apparatus, Inc., 500 Executive Blvd., Elmsford, N.Y. 10523	16
Bentley, J.	Metals and Ceramics Division, Oak Ridge National Laboratory, Oak Ridge, Tenn. 37830	17
bin-Jaya, R.	University of Sussex, School of Mathematical and Physical Sciences, Falmer, Brighton BN1 9QH, England	34
Blackburn, D. H.	Institute for Materials Research, National Bureau of Standards, Washington, D.C. 20234	27
Blinder, S.	NL Industries-ICD Division, Hightstown, New Jersey 08520	8
Boissel, A.	Department de Biophysique de la Faculte, de Medecine de Creteil and CAMECA, Pairs, France	71

INDEX OF AUTHORS AND THEIR AFFILIATIONS

		<u>Paper Number</u>
Bonventre, J. V.	Biotechnology Resource in Electron Probe Microanalysis, Harvard Medical School, Boston, Massachusetts	61
Borile, F.	CNR-LTM, Via Induno, 10 - Cinisello B., Milano, Italy	77
Brown, J. D.	Metaalinstituut TNO and The University of Western Ontario, London, Canada	40 44
Chambers, W. F.	Sandia Laboratories, Albuquerque, New Mexico 87115	53 54
Chen, C. H.	School of Applied and Engineering Physics, Cornell University, Ithaca, New York 14853	37
Chescoe, D.	AEI Scientific Apparatus Limited, Barton Dock Road, Urmston, Manchester, England	16
Chodos, A. A.	Division of Geological and Planetary Sciences, California Institute of Technology, Pasadena, California 91125	38
Clayton, R. N.	Department of the Geophysical Sciences, and Enrico Fermi Institute, University of Chicago, Chicago, Illinois 60637	41
Cliff, G.	Metallurgy Department, University of Manchester, Manchester, England	25
Colby, J. W.	Bell Telephone Laboratories, 555 Union Boulevard, Allentown, Pennsylvania 12103	T2
Coleman, J. R.	Department of Radiation, Biology and Biophysics, University of Rochester, School of Medicine and Dentistry, Rochester, New York 14642	58 62
Coles, J. N.	N.E.R.C. Ion Probe Unit, Dept. of Mineralogy & Petrology, University of Cambridge, Madingley Rise, Cambridge CB3 0EZ, England	46
Conty, C.	Department de Biophysique de la Faculte de Medecine de Creteil and CAMECA, Paris, France	71
Darr, M. M.	Institute for Materials Research, National Bureau of Standards, Washington, D.C. 20234	27

INDEX OF AUTHORS AND THEIR AFFILIATIONS

		<u>Paper Number</u>
DeNee, P. B.	Appalachian Laboratory for Occupational Safety and Health, National Institute for Occupational Safety and Health, Morgantown, West Virginia	60
Edie, J. W.	Dental Research Laboratory, University of Iowa, Iowa City, Iowa 52240	65
Egerton, R. F.	Department of Physics, University of Alberta, Edmonton, Canada T6G 2J1	36
Elad, E	ORTEC, Inc., Materials Analysis Division, Oak Ridge, Tennessee 37830	2
Everhart, T.E.	University of California, Dept. of Electrical Engineering and Computer Sciences, Berkeley, California 94720	30
Fiori, C. E.	Analytical Chemistry Division, National Bureau of Standards, Washington, D. C. 20234	12 27 29
Fleming, E., III	School of Textiles, North Carolina State University, Raleigh, North Carolina 27607	15
Fralick, R. D.	Applied Research Laboratories, Sunland, California 91040	48
Fraser, H. L.	Dept. of Metallurgy and Mining Engineering, and the Materials Research Laboratory, University of Illinois at Urbana-Champaign, Urbana, Illinois 61801	14
Frederickson, R.G.	Department of Anatomy, School of Medicine, West Virginia University Medical Center, Morgantown, West Virginia	60
Fujisawa, M.	JOEL, Ltd., 1418 Nakagami-cho, Akishima, Tokyo, Japan	69
Galle, P.	Department de Biophysique de la Faculte de Medecine de Creteil and CAMECA, Paris, France	71
Geller, J. D.	JEOL U.S.A., Inc., Medford, Massachusetts 02155	73
Gerlach, R. L.	Physical Electronics Industries, Inc., 6509 Flying Club Drive, Eden Prairie, Minn. 55343	47

INDEX OF AUTHORS AND THEIR AFFILIATIONS

		<u>Paper Number</u>
Glick, P. L.	V. A. Hospital and College of Dentistry, University of Iowa, Iowa City, Iowa 52240	65
Goldstein, J.I.	Metallurgy and Materials Science Dept., Lehigh University, Bethlehem, Pa.	T1 25
Gras, D. J.	Metaalinstituut TNO and The University of Western Ontario, London, Canada	44
Halloran, B. P.	Dept. of Radiation Biology and Biophysics, University of Rochester School of Medicine and Dentistry, Rochester, N.Y. 14642	62
Hamilton, W.J., Jr.	Developmental Electron Microscopy Laboratory, Frederick Cancer Research Center, (Litton Bionetics, Inc.), Frederick, Maryland 21701	78
Harland, C. J.	University of Sussex, School of Mathe- matical and Physical Sciences, Falmer, Brighton BN1 9QH, England	34
Hatfield, W. T.	General Electric Company, Corporate Research and Development, P.O. Box 8, Schenectady, N.Y. 12301	67
Hawkins, D. L.	Department of Geosciences, Purdue University, West Lafayette, Indiana 47907	70
Heinrich, K.F.J.	Analytical Chemistry Division, National Bureau of Standards, Washington, D. C. 20234	12 23 26 27 29 42
Henry, G.	Institut de Recherches de la Siderurgie Francaise (IRSID) - B.P. n° 129 - 78104 St Germain en Laye Cedex - France	43
Hersh, S.	School of Textiles, North Carolina State University, Raleigh, North Carolina 27607	15
Hirata, K.	JEOL, Ltd., 1418 Nakagami-cho, Akishima, Tokyo, Japan	69

INDEX OF AUTHORS AND THEIR AFFILIATIONS

		<u>Paper Number</u>
Hlava, P. F.	Sandia Laboratories, Albuquerque, New Mexico 87115	53 54
Hren, J. J.	Department of Materials Science and Engineering, University of Florida, Gainesville, Florida 32611	13
Hutcheon, I. D.	Enrico Fermi Institute, University of Chicago, Chicago, Illinois 60637	41
Hyman, H.	RCA Corporation, Solid State Division, Somerville, New Jersey	T4
Ingram, F. D.	Department of Internal Medicine, University of Iowa, Iowa City, Iowa 52242	63
Ingram, M. J.	Department of Internal Medicine, University of Iowa, Iowa City, Iowa 52242	63
Isaacson, M.	Department of Physics and the Enrico Fermi Institue, University of Chicago, Chicago, Illinois	7
Jenkins, E. J.	Department of Materials Science and Engineering, University of Florida, Gainesville, Florida 32611	13
Johari, O. M.	Metals Division, IIT Research Institute, 10 West 35th Street, Chicago, Illinois 60616	50
Johnson, D. E.	High Voltage Microscope Laboratory, Department of Zoology and Laboratory of Biophysics, University of Wisconsin, Madison, Wisconsin	7
Johnson, J. M.	Lawrence Livermore Laboratory, University of California, Livermore, California 94550	22
Johnson, P. F.	Department of Materials Science and Engineering, University of Florida, Gainesville, Florida 32611	13
Kane, W. T.	Research and Development Laboratories, Corning Glass Works, Corning, N.Y. 14830	T3

INDEX OF AUTHORS AND THEIR AFFILIATIONS

		<u>Paper Number</u>
Keller, J.	IBM Thomas J. Watson Research Center, Yorktown Heights, New York 10598	21
Kenick, E. A.	Metals and Ceramics Division, Oak Ridge National Laboratory, Oak Ridge, Tennessee 37830	17
Kolster, B. H.	Metaalinstituut TNO, Apeldoorn, The Netherlands	44 76
Kuptsis, J. D.	IBM Thomas J. Watson Research Center, Yorktown Heights, New York 10598	24
Kyser, D. T.	IBM Research Laboratory, San Jose, California 95193	28
Lechene, C. P.	Biotechnology Resource in Electron Probe Microanalysis, Harvard Medical School, Boston, Massachusetts	59 61
Leys, J. A.	3M Central Research Lab., P.O. Box 33221, St. Paul, Minn. 55133	49
Lifshin, E.	General Electric Company, Corporate Research and Development, P. O. Box 8, Schenectady, N.Y. 12301	6
Long, J. V. P.	N.E.R.C. Ion Probe Unit, Dept. of Mineralogy & Petrology, University of Cambridge, Madingley Rise, Cambridge CB3 0EZ, England	46
Lorimer, G. W.	Metallurgy Department, University of Manchester, Manchester, England	25
Lurio, A.	IBM Thomas J. Watson Research Center, Yorktown Heights, N.Y. 10598	21 24
MacDonald, N.C.	Physical Electronics Industries, Inc., 6509 Flying Club Drive, Eden Prairie, Minn. 55343	47
Marinenko, R. B.	Institute for Materials Research, National Bureau of Standards, Washington, D.C. 20234	27
McMahon, C. J.	Department of Metallurgy and Materials Science, University of Pennsylvania, Philadelphia, Pennsylvania 19174	39

INDEX OF AUTHORS AND THEIR AFFILIATIONS

Paper Number

Maitrepierre, P. H.	Institut de Recherches de la Siderurgie Francaise (IRSID) - B.P. n° 129 - 78104 St Germain en Laye Cedex - France	43
Merkle, A. B.	Department of Geology, The University of Nebraska-Lincoln, Lincoln, Nebraska 68508	51
Mitchell, M. V.	IBM System Products Division -- East Fishkill, Hopewell Junction, New York 12533	56
Meyer, H. O. A.	Department of Geosciences, Purdue University, West Lafayette, Indiana 47907	70
Mizuhira, V.	Department of Cell Biology, Medical Research Institute, Tokyo Medical and Dental University, Yushima, Bunkyo-Ku, Tokyo 113, Japan	5
Myklebust, R. F.	Analytical Chemistry Division, National Bureau of Standards, Washington, D. C. 20234	12 23 29 42
Namdar-Irani, R.	Institut de Recherches de la Siderurgie Francaise (IRSID) - B.P. n° 129 - 78104 St Germain en Laye Cedex - France	43
Newbury, D. E.	Analytical Chemistry Division, National Bureau of Standards, Washington, D. C. 20234	23 27 42
Olzie, E.	CNR-LTM, Via Induno, 10 - Cinisello B., Milano, Italy	77
Ong, P. S.	Department of Materials Science and Engineering, University of Florida, Gainesville, Florida 32611	13
Packwood, R. H.	Physical Metallurgy Research Laboratories, CANMET - EMR, 555 Booth Street, Ottawa, Canada	55
Parsons, B. I.	Energy Research Laboratory, CANMET - EMR, 55 Booth Street, Ottawa, Canada	55

INDEX OF AUTHORS AND THEIR AFFILIATIONS

		<u>Paper Number</u>
Phillips, B. F.	Electron Optics Laboratory (Code 30333) Naval Weapons Support Center, Crane, Indiana 47522	45
Ploc, R. A.	Atomic Energy of Canada Limited, Chalk River Nuclear Laboratories, Chalk River, Ontario Canada KOJ 1J0	33
Ramsey, J. N.	IBM System Products Division -- East Fishkill, Hopewell Junction, New York 12533	56
Reed, S. J. B.	Department of Mineralogy and Petrology, Downing Place, Cambridge CB2 3EW, England	4 46
Reuter, W.	IBM Thomas J. Watson Research Center, Yorktown Heights, New York 10598	21 24
Rofes-Vernis, J.	Institut de Recherches de la Siderurgie Francaise (IRSID) - B.P. n° 129 - 78104 St Germain en Laye Cedex - France	43
Rossouw, C. J.	Department of Metallurgy, University of Oxford, Parks Rd., Oxford, England	36
Russ, J. C.	EDAX Laboratories, Prairie View, Illinois 60069	19 52
Schamber, F. H.	Tracor Northern, Inc., 2551 W. Beltline Highway, Middleton, Wisconsin 53562	3
Short, N. A.	Technical Services, Engineering and Research Staff - Research, Ford Motor Company, Dearborn, Michigan	9
Silcox, J.	School of Applied and Engineering Physics, Cornell University, Ithaca, N.Y. 14853	37
Sicignano, A.	Philips Laboratories, Briarcliff Manor, New York 10510	57
Skinner, D. P.	NL Industries-ICD Division, Hightstown, New Jersey 08520	8
Small, J. A.	Institute for Materials Research, National Bureau of Standards, Washington, D. C. 20234	27

INDEX OF AUTHORS AND THEIR AFFILIATIONS

		<u>Paper Number</u>
Smith, J. V.	Department of the Geophysical Sciences, University of Chicago, Chicago, Illinois 60637	41
Solberg, T. N.	Department of the Geophysical Sciences, University of Chicago, Chicago, Illinois 60637	41
Sparrow, G. R.	3M Analytical Systems, 3M Center, St. Paul, Minn. 55133	49
Sprys, J. W.	Technical Services, Engineering and Research Staff - Research, Ford Motor Company, Dearborn, Michigan	9
Spurr, A. R.	Department of Vegetable Crops, University of California, Davies, California 95616	63
Statham, P.	Department of Electrical Engineering and Computer Sciences, University of California, Berkeley, California	10 11
Steele, I. M.	Department of the Geophysical Sciences, University of Chicago, Chicago, Illinois 60637	41
Steele, W. J.	Lawrence Livermore Laboratory, University of California, Livermore, California 94550	22
Sutfin, L. V.	Department of Orthopaedic Surgery, Harvard Medical School, Children's Hospital Medical Center, Boston, Mass. 02115	66
Ternan, M.	Energy Research Laboratory, CANMET - EMR, 555 Booth Street, Ottawa, Canada	55
Thomas, B.	Institut de Recherches de la Siderurgie Francaise (IRSID) - B.P. n° 129 - 78104 St. Germain en Laye Cedex - France	43
Tucker, P.	School of Textiles, North Carolina State University, Raleigh, North Carolina 27607	15
Turisini, G.	CNR-LTM, Via Induno, 10 - Cinisello B., Milano, Italy	77

INDEX OF AUTHORS AND THEIR AFFILIATIONS

		<u>Paper Number</u>
Venables, J. A.	University of Sussex, School of Mathematical and Physical Sciences, Falmer, Brighton BN1 9QH, England	34
vonRosenstiel, A.P.	Metaalinstituut TNO, Apeldoorn, The Netherlands	40 44 76
Walter, E. R.	Research and Development Department, Chemicals and Plastics, Union Carbide Corporation, South Charleston, West Virginia 25303	32
Warner, R. R.	Biotechnology Resource in Electron Probe Microanalysis, Harvard Medical School, Boston, Massachusetts	59
Wells, O. C.	IBM Thomas J. Watson Research Center, P. O. Box 218, Yorktown Heights, New York 10598	35
Whatley, T. A.	Applied Research Laboratories, Sunland, California 91040	48
Whelan, M. J.	Department of Metallurgy, University of Oxford, Parks Road, Oxford, England	36
Wittry, D. B.	Department of Materials Science and Electrical Engineering, University of Southern California, Los Angeles, California 90007	20 75
Woldseth, R.	Kevex Corporation, Burlingame, Calif.	1
Wardell, I. R. M.	VG Microscopes, Ltd., The Birches Industrial Estate, Imberhorne Lane, East Grinstead, Sussex, England	74
Wu, C. J.	Departments of Materials Science and Electrical Engineering, University of Southern California, Los Angeles, California 90007	75
Yagunoff, G. G.	Department of Geology and Geography, University of Massachusetts, Amherst, Massachusetts 01002	68

INDEX OF AUTHORS AND THEIR AFFILIATIONS

		<u>Paper Number</u>
Yakowitz, H.	Metallurgy Division, National Bureau of Standards, Washington, D.C. 20234	23
Zaluzec, N. J.	Department of Metallurgy and Mining Engineering, and the Materials Research Laboratory, University of Illinois at Urbana-Champaign, Urbana, Illinois 61801	14
Zeedijk, H. B.	Metaalinstituut TNO, Apeldoorn, The Netherlands	76